

**NOVEL AIR-COUPLED HEAT EXCHANGERS FOR WASTE  
HEAT-DRIVEN ABSORPTION HEAT PUMPS**

A Thesis  
Presented to  
The Academic Faculty

by

David Forinash

In Partial Fulfillment  
of the Requirements for the Degree  
Master of Science in Mechanical Engineering

Georgia Institute of Technology

August 2015

Copyright © 2015 by David Forinash

**NOVEL AIR-COUPLED HEAT EXCHANGERS FOR WASTE  
HEAT-DRIVEN ABSORPTION HEAT PUMPS**

Approved by:

Dr. Srinivas Garimella, Advisor  
School of Mechanical Engineering  
*Georgia Institute of Technology*

Dr. S. Mostafa Ghiaasiaan  
School of Mechanical Engineering  
*Georgia Institute of Technology*

Dr. Sheldon M. Jeter  
School of Mechanical Engineering  
*Georgia Institute of Technology*

Date Approved: May 21, 2015

## **ACKNOWLEDGEMENTS**

I would first like to thank my advisor, Dr. Srinivas Garimella, for providing me with this opportunity to work on a fulfilling and challenging project. His direction was invaluable in research- and career-related junctures, and I look forward to applying what I have learned from him in future endeavors. I would like to thank the members of the Sustainable Thermal Systems Lab for their technical guidance and camaraderie during my thesis work, particularly Allison Mahvi, Anurag Goyal, Christopher Keinath, Alex Rattner, Malcolm Macdonald, Jared Delahanty, Marcel Staedter, Dhruv Hoysall, Victor Aiello, Subhrajit Chakraborty, and Daniel Kromer. I am fortunate to have spent my graduate school career with such brilliant and inspiring individuals. I am indebted to them for their selfless giving of time and energy to assist me in my work.

I would not have been able to complete this work without the unflinching support of my family. I would especially like to thank my parents, who consistently demonstrate diligence, humility, and charity to others. Lastly, I would like to express my gratitude to Laura, whose patience and unwavering faith sustained me through self-doubt. I hope to learn from her example of courage and generosity.

## TABLE OF CONTENTS

Acknowledgements.....	iii
List of Tables .....	vii
List of Figures.....	ix
List of Symbols and Abbreviations.....	xiv
Summary .....	xviii
CHAPTER 1: Introduction .....	1
1.1 Absorption Heat Pump.....	2
1.2 Air-Coupled Absorption Systems.....	6
1.3 Scope of Present Work.....	8
1.4 Thesis Organization .....	9
CHAPTER 2: Literature Review .....	10
2.1 Recent Developments in Absorption Systems.....	10
2.1.1 Working Fluid Considerations.....	11
2.1.2 Commercial Implementation .....	13
2.1.3 GAX and Unconventional Cycles.....	16
2.1.4 Single-Effect Cycles .....	18
2.2 Absorber and Condenser Design for Absorption Heat Pumps .....	21
2.2.1 Modeling Studies .....	24
2.2.2 Experimental Studies .....	28
2.3 Summary.....	31
CHAPTER 3: Modeling.....	33
3.4 Thermodynamic Cycle Modeling.....	33

3.5	Baseline Cycle Model .....	34
3.5.1	Parametric Analysis .....	43
3.5.2	Ambient Temperature Variation .....	49
3.6	Absorber Modeling .....	50
3.6.1	Round-Tube Corrugated-Fin Segmental Modeling .....	54
3.6.2	Prototype Tube-Array Segmental Modeling .....	93
CHAPTER 4: Experimental Approach .....		106
4.1	Air-Coupled Absorber Fabrication .....	106
4.1.1	Round-Tube Corrugated-Fin Absorber .....	106
4.1.2	Prototype Tube-Array Absorber .....	109
4.2	Air-Coupled Absorption Test Facility .....	113
4.2.1	Ammonia-Water Cycle .....	114
4.2.2	Air-Handling Unit .....	118
4.2.3	Equipment and Instrumentation Overview .....	119
4.3	Experimental Procedures .....	128
4.3.1	Safety Precautions .....	128
4.3.2	Charging Procedure .....	128
4.3.3	Startup and Testing Procedures .....	130
CHAPTER 5: Results and Discussion .....		132
5.1	Comparison of Different Absorber Configurations .....	134
5.2	Round-Tube Corrugated-Fin Absorber .....	136
5.2.1	Overall Heat Transfer Coefficient .....	139
5.2.2	Air Temperature .....	144

5.2.3	Air Flow Rate.....	145
5.2.4	Solution Inlet Temperature .....	148
5.2.5	Solution Flow Rate .....	149
5.2.6	Refrigerant Fraction .....	151
5.2.7	Discussion of Similar Performance .....	152
5.3	Prototype Tube-Array Absorber .....	155
5.3.1	Overall Heat Transfer Coefficient .....	156
5.3.2	Air Temperature.....	157
5.3.3	Air Flow Rate.....	158
5.3.4	Solution Inlet Temperature .....	160
5.3.5	Solution Flow Rate .....	161
5.3.6	Refrigerant Fraction .....	166
5.3.7	Maldistribution Analysis.....	167
CHAPTER 6: Conclusions and Recommendations.....		176
6.1	Conclusions.....	176
6.2	Recommendations.....	178
6.2.1	System-Wide Investigations .....	178
6.2.2	Enhancement of Conventional Heat Exchangers.....	179
6.2.3	Continued Development of Prototype Geometries .....	180
Appendix A: Segmental Heat And Mass Transfer Model Sample Calculations .....		182
A.1	Round-Tube Corrugated-Fin Absorber .....	182
A.2	Prototype Tube-Array Absorber .....	204
References	.....	219

## LIST OF TABLES

Table 2.1 System-level heat pump investigations.....	12
Table 2.2 Component-level absorber and condenser investigations.....	23
Table 3.1 Baseline thermodynamic cycle model inputs .....	34
Table 3.2 Electrical power consumption in baseline cycle model ( $F_{load} = 3.18$ ) .....	42
Table 3.3 Component heat duties and $UA$ values for baseline cycle .....	43
Table 3.4 Component heat duties and $UA$ values for optimized cycle .....	48
Table 3.5 Inlet conditions .....	57
Table 3.6 Round-tube corrugated-fin absorber modeling correlations .....	60
Table 3.7 Predicted air-side heat transfer coefficients for 394-FPM and 551-FPM corrugated-fin absorbers .....	73
Table 3.8 Prototype absorber geometric inputs .....	96
Table 4.1 Designs with steel-wetted configurations considered for ammonia-water absorber.....	110
Table 4.2 Controllable parameters in air-coupled test facility.....	114
Table 4.3 Absorber nominal inlet and outlet conditions in heat pump and single-pressure test facility.....	117
Table 4.4 Equipment and instrumentation used in absorber testing .....	120
Table 5.1 Test matrix for air-coupled absorber testing.....	132
Table 5.2 Uncertainty propagation used in heat transfer rate calculation.....	134
Table 5.3 Heat transfer in each tube bundle for representative maldistributed conditions .....	174
Table A.1 Inlet conditions.....	182

Table A.2 Geometric inputs .....	182
Table A.3 Geometric inputs .....	204
Table A.4 Inlet conditions.....	204



## LIST OF FIGURES

Figure 1.1 Single-effect absorption heat pump with volatile absorbent .....	2
Figure 3.1 Schematic for cycle modeling .....	36
Figure 3.2 “Tornado” diagrams of overall <i>COP</i> (left) and cooling capacity (right) with variations in heat exchanger size ( <i>UA</i> ) .....	44
Figure 3.3 Cooling duty (left axis) and <i>COP</i> (right axis) as a function of concentrated solution flow rate .....	46
Figure 3.4 Cooling duty (left axis) and <i>COP</i> (right axis) as a function of ambient air temperature .....	49
Figure 3.5 Schematic of individual absorber segment.....	51
Figure 3.6 Predicted heat transfer rate (bottom) and average absolute deviation from mean (top) as a function of the number of segments in the 394-FPM absorber...	53
Figure 3.7 Schematic of round-tube corrugated-fin absorbers .....	56
Figure 3.8 Photographs of 551-FPM round-tube corrugated-fin absorber and the 394-FPM and 551-FPM fin densities.....	58
Figure 3.9 Tube-side heat transfer coefficients predicted for 394-FPM corrugated-fin absorber.....	62
Figure 3.10 Taitel-Dukler (1976) flow regime map for round tube 394-FPM corrugated-fin absorption .....	65
Figure 3.11 Segmental frictional pressure drop for 394-FPM round-tube corrugated-fin absorber divided in 220 segments ( $L_{sg} = 0.061$ m).....	66
Figure 3.12 Tube-side components of differential pressure across segment in round-tube 394-FPM corrugated-fin absorber divided in 220 segments ( $L_{sg} = 0.061$ m).....	69

Figure 3.13 Air-side pressure drop in round-tube corrugated-fin absorbers .....	74
Figure 3.14 Schematic of $LMTD_v$ across representative segment .....	80
Figure 3.15 Thermal resistance circuit.....	82
Figure 3.16 Effective annular fin schematic .....	83
Figure 3.17 Thermal resistances during absorption in the 394-FPM corrugated-fin absorber.....	85
Figure 3.18 Segmental (left) and total (right) heat transfer rate as a function of distance along uncoiled tube in the 394-FPM absorber .....	88
Figure 3.19 3-D Plot of solution equilibrium temperature in 394-FPM absorber .....	89
Figure 3.20 Tube arrangement schematic showing approach for predicting effect of air temperature variation .....	91
Figure 3.21 Inlet and outlet air temperatures as a function of the total uncoiled tube length of the absorber.....	92
Figure 3.22 Exploded view of prototype absorber.....	94
Figure 3.23 Close-up photograph of header and distributor before assembly .....	94
Figure 3.24 Photograph of assembled prototype tube-array absorber .....	95
Figure 3.25 Prototype absorber schematic.....	97
Figure 3.26 Tube-side heat transfer coefficient predicted in tube-array absorber .....	98
Figure 3.27 Segmental differential pressure in the first row of the tube-array absorber	100
Figure 3.28 Thermal resistance during absorption in the first row of the tube-array absorber.....	104
Figure 3.29 Temperature profiles across prototype absorber tube rows.....	105
Figure 4.1 Drawing of 394-FPM round-tube corrugated-fin absorber .....	108

Figure 4.2 Drawing of prototype tube-array absorber .....	113
Figure 4.3 Schematic of ammonia-water test facility .....	115
Figure 4.4 Air-handling unit schematic for absorber testing .....	118
Figure 4.5 Photograph of ammonia-water test facility .....	121
Figure 4.6 Rendering (left), exploded photograph (top), and top view (bottom) of separator .....	122
Figure 4.7 Schematic (left) and photograph (right) of mixer.....	123
Figure 4.8 Photograph of absorber in air-handling unit with solution test facility in background.....	124
Figure 4.9 Photograph of absorber outlet with thermocouple locations indicated .....	125
Figure 4.10 Thermal resistance circuit for radiation analysis.....	126
Figure 5.1 Effectiveness values from data and modeling for all absorbers .....	135
Figure 5.2 Energy balance: Comparison of Air-side and Tube-side heat transfer rates .	137
Figure 5.3 Internal, external, and overall heat transfer coefficients as a function of uncoiled length in the 394-FPM and 551-FPM absorbers .....	140
Figure 5.4 Internal, weighted external, and overall heat transfer coefficients as a function of absorber length .....	141
Figure 5.5 Overall heat transfer coefficients for the round-tube corrugated-fin absorbers, determined using total air-side heat transfer area .....	143
Figure 5.6 Heat transfer rate as a function of air temperature for the round-tube corrugated-fin absorbers .....	144
Figure 5.7 Heat transfer rate as a function of air flow rate for the round-tube corrugated-fin absorbers.....	146

Figure 5.8 Air-side differential pressure as a function of volumetric flow rate for the round-tube corrugated-fin absorbers.....	147
Figure 5.9 Heat transfer rate as a function of solution inlet temperature for the round-tube corrugated-fin absorbers .....	148
Figure 5.10 Heat transfer rate as a function of concentrated solution flow rate for the round-tube corrugated-fin absorbers.....	149
Figure 5.11 Tube-side differential pressure as a function of solution flow rate for the round-tube corrugated-fin absorbers.....	150
Figure 5.12 Refrigerant fraction in the 394-FPM absorber .....	152
Figure 5.13 Segmental and total thermal resistances in the 394-FPM and 551-FPM absorbers .....	153
Figure 5.14 Segmental and total heat transfer rate in the absorber for 394-FPM and 551-FPM absorbers .....	154
Figure 5.15 Energy balance between air and tube side for prototype tube-array absorber .....	155
Figure 5.16 Overall heat transfer coefficient as a function of concentrated solution flow rate for the prototype tube-array absorber .....	157
Figure 5.17 Heat transfer rate as a function of air temperature for the prototype tube-array absorber.....	158
Figure 5.18 Heat transfer rate as a function of air flow rate for the prototype tube-array absorber.....	159
Figure 5.19 Air-side differential pressure as a function of air flow rate for the prototype tube-array absorber .....	160

Figure 5.20 Heat transfer rate as a function of solution temperature for the prototype tube-array absorber .....	161
Figure 5.21 Heat transfer rate as a function of solution flow rate for the prototype tube-array absorber.....	162
Figure 5.22 Tube-side differential pressure recorded by pressure transducer before accounting for inlet/outlet losses .....	163
Figure 5.23 Total tube-side differential pressure in the prototype absorber.....	165
Figure 5.24 Prototype heat transfer rates as a function of concentrated solution flow rate, categorized by refrigerant fraction.....	166
Figure 5.25 Thermocouple probes mounted on outer walls of tubes to record variation in wall temperature.....	168
Figure 5.26 Wall temperature measurements across face of tube-array absorber (each line represents one steady-state data point) .....	169
Figure 5.27 Schematic of maldistribution modeling methodology .....	171
Figure 5.28 Pressure drop in each bundle of tubes in maldistribution modeling .....	172
Figure 5.29 Graphs of mass flux (top-left), quality (bottom-left), fraction of incoming liquid (top-right), and number of tube rows (bottom-right) per tube bundle for a representative maldistributed case .....	173
Figure A.1 Corrugated-fin absorber geometry schematic.....	182
Figure A.2 Prototype geometry schematic.....	204

## LIST OF SYMBOLS AND ABBREVIATIONS

### Symbols

<i>A</i>	Area, m <sup>2</sup>
<i>C</i>	Heat capacity rate, W K <sup>-1</sup>
<i>C<sub>p</sub></i>	Specific heat, kJ kg <sup>-1</sup> K <sup>-1</sup>
<i>C<sub>T</sub></i>	Bulk molar concentration, kmol m <sup>-3</sup>
<i>D</i>	Diameter, m; mass diffusivity, m <sup>2</sup> s <sup>-1</sup>
<i>Eu</i>	Euler number
<i>f</i>	Friction factor
<i>Fr</i>	Froude number
<i>g</i>	Gravitational constant, 9.81 m s <sup>-2</sup>
<i>G</i>	Mass flux, kg m <sup>-2</sup> s <sup>-1</sup>
<i>Gz</i>	Graetz number
<i>h</i>	Enthalpy, kJ kg <sup>-1</sup>
<i>H</i>	Height, m
<i>j</i>	Superficial velocity, m s <sup>-1</sup> ; Colburn “ <i>j</i> ” factor
<i>k</i>	Thermal conductivity, W m <sup>-1</sup> K <sup>-1</sup>
<i>K<sub>L</sub></i>	Minor loss coefficient
<i>K<sub>C</sub>, K<sub>E</sub></i>	Contraction, expansion loss coefficient
<i>L</i>	Length, m
<i>M</i>	Molar mass, kg kmol <sup>-1</sup>
<i>ṁ</i>	Mass flow rate, kg s <sup>-1</sup>
<i>N</i>	Number
<i>n</i>	Molar flux of species undergoing absorption, kmol m <sup>-2</sup> s <sup>-1</sup>
<i>Nu</i>	Nusselt number
<i>P</i>	Pressure, kPa
<i>p</i>	Pitch, m
<i>Pr</i>	Prandtl number
<i>q</i>	Quality
<i>Q</i>	Heat duty, W
<i>r</i>	Radius, m
<i>R</i>	Thermal resistance, K W <sup>-1</sup>
<i>Re</i>	Reynolds number
<i>s</i>	Spacing, m
<i>Sc</i>	Schmidt number
<i>Sh</i>	Sherwood number
<i>t</i>	Thickness, m
<i>T</i>	Temperature, °C
<i>U</i>	Overall heat transfer coefficient, W m <sup>-2</sup> K <sup>-1</sup>
<i>u</i>	Velocity, m/s
<i>UA</i>	Overall heat transfer conductance, W K <sup>-1</sup>
<i>v</i>	Specific volume, m <sup>3</sup> kg <sup>-1</sup>
<i>Ṽ</i>	Volumetric flow rate, m <sup>3</sup> s <sup>-1</sup>
<i>W</i>	Width, m
<i>We</i>	Weber number

$x$	Mass concentration of ammonia
$X_{\text{Martinelli}}$	Martinelli parameter

### Abbreviations

<i>AAD</i>	Average absolute deviation
<i>AMTD</i>	Arithmetic mean temperature difference, K
<i>CAT</i>	Closest approach temperature, K
<i>COP</i>	Coefficient of performance
<i>FPM</i>	Fins per meter
<i>LMTD</i>	Log mean temperature difference, K
<i>NTU</i>	Number of transfer units
<i>RH</i>	Relative humidity
<i>VF</i>	Void Fraction

### Greek Symbols

$\alpha$	Heat transfer coefficient, $\text{W m}^{-2} \text{K}^{-1}$
$\beta$	Ratio of tube collar area to fin area allocated to one tube
$\gamma$	Angle of tube inclination, $^{\circ}$
$\Delta$	Differential
$\varepsilon$	Effectiveness
$\eta$	Efficiency
$\theta$	Louver angle (from plane of fin)
$\mu$	Dynamic viscosity, $\text{kg m}^{-1} \text{s}^{-1}$
$\nu$	Kinematic viscosity, $\text{m}^2 \text{s}^{-1}$
$\rho$	Density, $\text{kg m}^{-3}$
$\sigma$	Surface tension, $\text{N m}^{-1}$ ; fin contraction ratio
$\sigma'$	Ratio of cross-sectional flow area to frontal area
$\phi$	Two-phase multiplier
$\phi_{\text{T}}$	Heat transfer correction factor

### Subscripts

abs	Absorption, absorber
accel	Acceleration
air	Air
air,t	Air over tubes
annular	Annular
avg	Average
b	Bulk
bare	Bare
c	Cross-sectional, collar
ch	Channel
col	Column
cond	Conduction
crit	Critical
d	Diagonal
D	Diameter

dec	Deceleration
eff	Effective
entrance	Entrance
equil	Equilibrium
exit	Exit
f,flat	Flat fin
f,wavy	Wavy fin
face	Face
film	Film
fin	Fin
flux	Flux
fr	frontal
fric	Frictional
gl	Glide
grav	Gravitational
h	Hydraulic
H <sub>2</sub> O	Water
holes	Holes
i	Inner
in	Inlet
int	Interface
KL	Kays and London (1984) Parameter
l	Liquid, longitudinal (direction of air flow)
L,UBend	Loss in U-bend
lo	Liquid-only
m	Mean
max	Maximum
min	Minimum
minor	Minor
molar	Molar
NH <sub>3</sub>	Ammonia
NH <sub>3</sub> ,H <sub>2</sub> O	Ammonia-water
o	Outer
out	Outlet
p	Pitch
pass	Pass
r	Ratio
rough	Roughness
row	Row
s	Surface
sens	Sensible
sg	Segment
sol	Solution
t	Transverse (orthogonal to liquid and air flow)
t,col	Tube columns
t,row	Tube rows



TD	Taitel-Dukler parameter
total	Total
tp	Two-phase
tube	Tube
unfin	Unfinned
v	Vapor
vap	Vapor
vo	Vapor-only
w	Water
wav,d	Wave peak-to-valley depth
wav,p	Wave peak-to-valley pitch
wavy	Wavy

## SUMMARY

A detailed investigation of novel air-coupled absorbers for use in a diesel engine exhaust-driven ammonia-water absorption system operating in extreme ambient conditions was conducted. Electrically driven vapor-compression systems are under scrutiny due to the environmental impact of synthetic refrigerants and the exacerbation of electric utility loads during peak demand periods. One alternative to vapor-compression systems is the absorption heat pump that uses environmentally benign working fluids and can be driven by a variety of heat sources, including waste heat and solar thermal processes. Direct air coupling of the absorber and condenser instead of indirect hydronic coupling can reduce absorption system size, complexity, and inefficiency, but materials compatibility issues with ammonia-water and the poor heat transfer properties of air present challenges.

Heat and mass transfer modeling was used to predict the performance of round-tube corrugated-fin and compact tube-array absorbers designed for a 2.64-kW absorption chiller operated in high ambient temperature (51.7°C) conditions. A single-pressure ammonia-water test facility was constructed and used in conjunction with a temperature- and humidity-controlled air-handling unit to evaluate the absorbers at design and off-design operating conditions. Absorber performance was recorded over a range of air temperatures (35-54.4°C), air flow rates (0.38-0.74 m<sup>3</sup> s<sup>-1</sup>), inlet solution temperatures (92-102°C), concentrated solution flow rates (0.006-0.010 kg s<sup>-1</sup>), and concentrated solution concentrations (38-46%). At design conditions, round-tube corrugated-fin absorbers of 394 and 551 Fins Per Meter (FPM) demonstrated comparable performance ( $Q_{394\text{-FPM,exp}} = 4.521 \pm 0.271$  kW;  $Q_{551\text{-FPM,exp}} = 4.680 \pm 0.260$  kW), and measured heat

transfer rates were 0.7-1.9% AAD higher than those predicted through modeling. The measured heat transfer rate in the prototype tube-array absorber was significantly lower than the values predicted at design conditions ( $Q_{\text{prot,exp}} = 2.22 \pm 0.24$  kW;  $Q_{\text{prot,mod}} = 4.33$  kW). Maldistribution of the two-phase flow in the tube array is the probable cause of the disparity between the prototype absorber data and model predictions. Results from this investigation can be used to guide the development of air-coupled heat and mass exchangers for compact absorption heat pumps.

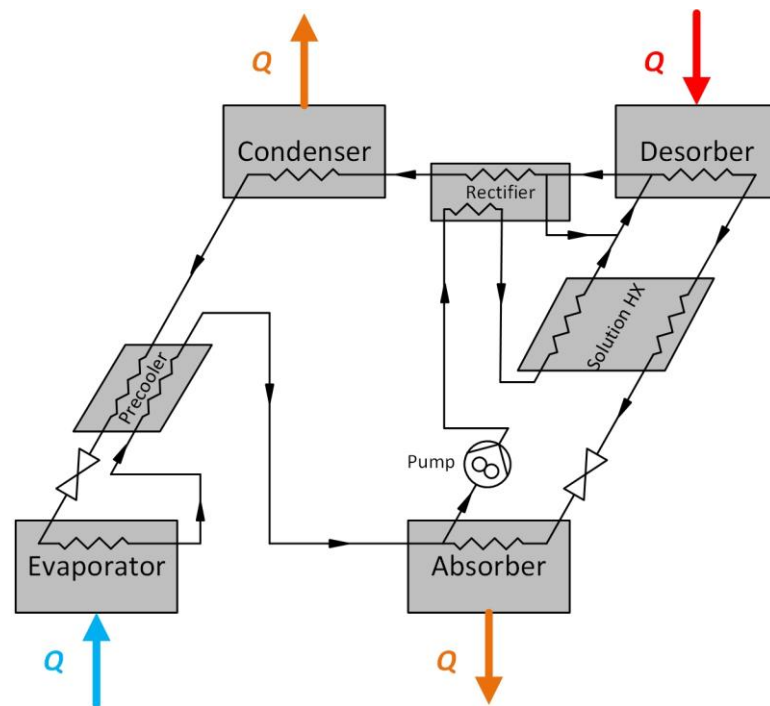
## CHAPTER 1: INTRODUCTION

Residential and commercial space conditioning is typically provided by electrically driven vapor-compression systems, which lead to high loads for electric utilities during the hottest hours of the day. This peak demand can result in power shortages and the use of less efficient power generators that must ramp up quickly to meet such loads. In addition, these systems have relied on the use of synthetic refrigerants that contribute to global climate change. R-134a, which is widely used in commercial, residential, and automotive air conditioning (Venkatarathnam and Murthy, 2012), is facing restrictions for its high global warming potential (GWP). In the European Union, R-134a is scheduled to be phased out of automotive air conditioners by 2017 (Calm, 2008).

Absorption heat pumps, on the other hand, use environmentally benign working fluids and are driven by thermal energy. These systems are being considered for use in space conditioning due to their environmentally benign aspects and their ability to use a variety of thermal inputs such as low-grade waste heat or solar thermal energy. Absorption cycles can help reduce peak electricity consumption because they require minimal electrical input compared to the compressors in vapor-compression heat pumps. These systems have been successfully implemented in large-scale commercial applications, but the larger number of heat and mass exchange components when compared with vapor-compression systems has hindered entry into the residential and light commercial markets. To be viable for small-scale waste heat recovery, the complexity, weight, and volume of the system must be reduced. One potential option is to directly reject heat from the absorber and condenser of the system to ambient air instead

of using hydraulically coupled fluid loops between the working fluid and air. In addition, it is important that these air-coupled components and the remaining heat and mass exchangers of the system are compact to allow for implementation in small-scale and mobile applications. The absorber has been labeled as the "bottleneck" (Beutler *et al.*, 1996) of an absorption system due to the coupled heat and mass transfer that must be accomplished across large transport resistances and small driving temperature differences. A compact and effective air-coupled absorber that addresses this bottleneck is necessary for the implementation of absorption heat pumps in mobile and small-capacity thermally driven space-conditioning applications.

## 1.1 Absorption Heat Pump



**Figure 1.1 Single-effect absorption heat pump with volatile absorbent**

*Figure 1.1* displays a schematic of a single-effect absorption heat pump. The left-hand side of the absorption cycle is identical to that of a vapor-compression system, in

which the refrigerant flows to a condenser for heating applications, through an expansion valve, and to an evaporator for cooling applications. Similar to the vapor-compression system, the absorption system is a two-pressure cycle. The electrically driven compressor, however, is replaced by two heat and mass exchangers, the absorber and desorber. In addition to the condenser, evaporator, absorber, and desorber, the single-effect system that uses working fluids with volatile absorbents such as ammonia-water typically contains a rectifier to increase refrigerant purity, and two recuperative heat exchangers (the solution heat exchanger and refrigerant pre-cooler) to increase the cycle Coefficient of Performance ( $COP$ ).

A binary mixture is used as the working fluid in an absorption heat pump, with one component acting as the refrigerant and the other component as the absorbent. Typical working fluid pairs include lithium bromide-water ( $\text{LiBr-H}_2\text{O}$ ) and ammonia-water ( $\text{NH}_3\text{-H}_2\text{O}$ ) (Ziegler, 2002). The lithium bromide-water fluid pair has been widely used since the 1950s and is typically used in systems with cooling capacities ranging between 35 and 5275 kW (Herold *et al.*, 1996). Disadvantages of lithium bromide-water include the possibility of crystallization, and operation at sub-atmospheric pressures (Srikhirin *et al.*, 2001), which increases the potential for air ingress. At the low temperatures in the evaporator, the vapor pressure of the water in lithium bromide-water cycles is typically well below the ambient pressure ( $P_{\text{vap}} = 0.873 \text{ kPa}$  at  $5^\circ\text{C}$ ). At these pressures, the specific volume of water vapor is very large ( $v_{\text{water,vap}} = 147 \text{ m}^3 \text{ kg}^{-1}$  at  $5^\circ\text{C}$ ), leading to the need for large system components, essentially rendering small-scale applications infeasible. Also, lithium bromide-water systems are typically restricted to

air-conditioning applications due to the relatively high freezing point of the refrigerant (water: 0°C) (Srikhirin *et al.*, 2001).

Ammonia-water has been used as the fluid pair in absorption systems since the late 1800s, and is receiving recent attention due to its environmentally benign aspects (GWP, ODP = 0) (Herold *et al.*, 1996). Ammonia-water absorption differs from that of lithium bromide-water because in this working fluid pair, water is used as the absorbent while ammonia is vaporized and acts as the refrigerant. The low freezing point of ammonia (−77°C) enables low system operating temperatures with applications in heating and cooling (Srikhirin *et al.*, 2001). In addition, the high operating pressure of ammonia-water systems ( $P_{\text{NH}_3\text{-H}_2\text{O}} = 159.3 \text{ kPa}$ ,  $v_{\text{NH}_3\text{-H}_2\text{O}} = 0.85 \text{ m}^3 \text{ kg}^{-1}$  at  $x = 0.998$ ,  $q = 1$ ,  $T = 5^\circ\text{C}$ ) allows for compact component design that is essential for mobile and small-capacity units. However, the use of ammonia-water also presents a variety of design challenges. Unlike lithium bromide in the lithium bromide-water system, the absorbent (water) in the ammonia-water system is volatile and requires the use of a rectifier to purify the refrigerant stream exiting the desorber (Srikhirin *et al.*, 2001). After exiting the rectifier, the refrigerant vapor still contains a small absorbent fraction (typically <1%) that causes a temperature rise during evaporation, which adversely affects the possible cooling temperatures. The toxicity of the refrigerant (ammonia) restricts implementation to well-ventilated areas that may be accessed for occasional maintenance. Fortunately, ammonia levels as low as 5 ppm (ASHRAE, 2010) can be detected by smell, and leaks can be detected and addressed before concentrations approach hazardous long-term exposure levels (300 ppm) (ASHRAE, 2010). Additional refrigerant safety information is reported in ANSI/ASHRAE Standard 34 (ASHRAE, 2007). In terms of material

compatibility, ammonia-water has been shown to corrode aluminum and copper. Therefore, materials for components are generally limited to carbon steel and stainless steel.

*Figure 1.1* is useful in demonstrating the operation of an air-coupled single-effect ammonia-water absorption system. In the ammonia-water system considered here, a concentrated solution is defined as an ammonia-water mixture with a high concentration of ammonia. Conversely, the dilute solution is characterized by a low concentration of ammonia. Heat input is applied to a high-pressure ammonia-water mixture in the desorber (also referred to as the vapor generator in the literature). The ammonia is preferentially vaporized along with a small fraction of water and exits the desorber. This vapor flows to the rectifier where heat is removed by the concentrated solution exiting the absorber and a reflux stream rich in water is condensed out of the refrigerant stream. The refrigerant vapor exiting the rectifier is almost entirely ammonia with a concentration typically >99%. The dilute solution exiting the desorber is recuperatively cooled by the concentrated solution in the solution heat exchanger (SHX) upstream of the absorber. The refrigerant vapor exits the rectifier and flows to the condenser in which heat is rejected to ambient air. For an absorption system in the heating mode, the heat extracted in the condenser and absorber would be the primary output of the system. The subcooled refrigerant flows through a refrigerant pre-cooler to reduce its enthalpy, thereby minimizing flashing across the valve upstream of the evaporator, and increasing the overall system cooling capacity. The expansion valve reduces the refrigerant pressure before vaporization occurs in the evaporator. In the system under consideration here, heat is transferred to the refrigerant from a coupling fluid loop that extracts heat from ambient



air using an air-coupled heat exchanger. This air-coupled heat exchanger serves as the conditioned space heat exchanger and typically uses an antifreeze solution of ethylene or propylene glycol and water. The refrigerant exiting the evaporator is heated in the refrigerant pre-cooler before flowing to the absorber. The absorber mixes the refrigerant and dilute streams and cools the resulting concentrated solution stream to a subcooled liquid state. The heat extracted is a combination of the heat of absorption, heat removed to reach a saturated liquid state, and sensible heat removed to bring the solution to a subcooled state. In the system under consideration here, the heat is transferred directly to the ambient air through forced convection. The concentrated solution exiting the absorber flows through a pump to return to the high pressure before receiving heat in the rectifier and solution heat exchanger in preparation for desorption. To complete the cycle, the concentrated solution is combined with the reflux from the rectifier at the inlet of the desorber.

## **1.2 Air-Coupled Absorption Systems**

There are three locations in the absorption cycle where air coupling is typically used for heat transfer: the evaporator (heat extracted from air), absorber and condenser (heat rejected to air). For air-conditioning applications, an intermediate coupling fluid loop is often used at the evaporator to extract heat from the air that is delivered to the desired space. Because this fluid loop is in the inhabited residential or commercial space, water coupling is preferred over conveying potentially corrosive or hazardous refrigerants through these spaces. For heat rejection in the absorber and condenser, an intermediate fluid that is pumped through single-phase air-coupled components can be used. The intermediate coupling fluid loop requires an additional pump, plumbing, and fluid

inventory. Cycles using these peripheral coupling fluid lines for heat rejection are referred to as indirectly or hydronically coupled absorption systems. Indirect air coupling allows for the use of a non-corrosive intermediate fluid or mixture that reduces material constraints in air-coupled heat exchanger design. Adverse effects include increased system volume, weight, and complexity. Pumping of the coupling fluid also requires electrical input that reduces cycle *COP* and is less readily available than low-grade thermal energy in some environments.

Direct air cooling reduces the total number of components in the cycle and eliminates the need for parasitic pumping of the coupling fluid. The resulting reduction in packaged system size and weight improves the viability of implementation in mobile and small-scale systems. Directly air-cooled absorbers present a variety of design challenges. In comparison to absorption cycles that use cooling towers and the resulting ambient wet bulb temperature as the heat sink, direct dry air-coupled systems require higher absorber operating temperatures because of the poor heat transfer properties of air (Herold *et al.*, 1996). The higher absorber operating temperatures in such dry air-coupled systems require higher solution concentrations, which increase the likelihood of precipitation of the salt in the lithium bromide-water system (Herold *et al.*, 1996). Material compatibility aspects of ammonia-water prevent the use of copper and aluminum in the wetted materials of such components. Corrosion caused by ammonia-water limits heat pump manufacturers to large and simple-to-machine round-tube flat-finned carbon steel heat exchangers, instead of the compact flat-tube louvered-fin geometries that are seen in aluminum automotive radiators. But conventional round-tube heat exchangers typically

present larger tube-side and air-side thermal resistances and also additional flow resistances.

Mini- or microchannel heat exchangers have been shown to effectively transfer heat in a compact volume through high heat transfer coefficients and high surface area-to-volume ratios. Microscale passages are implemented in crossflow air-coupled heat exchangers through the use of extruded multiport rectangular tubes brazed to louvered fins. Because ammonia-water systems require steel wetted surfaces that are not conducive to extrusion, they have not benefited from the reduction in size and improvement in performance that results from the use of compact heat exchangers with a small hydraulic diameter. There is a need for compact air-coupled heat exchangers that are compatible with ammonia-water for small-scale energy recovery.

### **1.3 Scope of Present Work**

The present research aims to improve the understanding of the heat and mass transfer of compact air-coupled absorbers used in ammonia-water absorption systems. A thermodynamic model is developed to predict the performance of an air-coupled single-effect ammonia-water absorption heat pump for use in extreme ambient conditions (51.7°C). The air-coupled absorber inlet conditions and required heat duties are predicted using the cycle model, and a segmental analysis incorporating heat and mass transfer is conducted to predict the performance of round-tube corrugated-fin and novel tube-array absorbers. The components are fabricated and subsequently evaluated at design and off-design operating conditions in an ammonia-water test facility coupled with a temperature- and humidity-controlled air-handling unit. Experimentally obtained heat

exchanger performance is compared with model predictions, and reasons for differences between them are postulated.

#### **1.4 Thesis Organization**

This thesis is organized in several chapters as follows:

Chapter Two presents a review of the literature of air-coupled absorption systems and challenges in the development of compact air-coupled component design and fabrication.

Chapter Three presents a thermodynamic cycle model of the single-effect ammonia-water absorption heat pump under consideration and segmental heat and mass transfer models of the air-coupled absorbers.

Chapter Four presents the fabrication of the novel absorbers as well as the design and construction of an ammonia-water test facility to evaluate the components at typical operating conditions in an air-handling unit.

Chapter Five presents an analysis of absorber performance compared with predictions from models of the round-tube corrugated-fin and novel tube-array designs.

Chapter Six summarizes the present work and discusses the need for future studies in air-coupled absorption systems and the development of compact air-coupled components.

## CHAPTER 2: LITERATURE REVIEW

A review of the literature pertinent to the present study grouped into two categories is presented in this chapter, system-level absorption investigations with an emphasis on air-coupled systems, and component-level investigations of absorbers and condensers for use in absorption heat pumps.

### 2.1 Recent Developments in Absorption Systems

With the rising demand for mobile heat pumps that are independent of the electrical infrastructure required for vapor-compression systems, researchers have developed absorption systems driven by solar energy (De Francisco *et al.*, 2002; Velázquez and Best, 2002; Kim and Ferreira, 2009), natural gas (Lazzarin *et al.*, 1996; Chua *et al.*, 2002; Horuz and Callander, 2004; Wang *et al.*, 2007), micro gas turbines (Moya *et al.*, 2011), and diesel engine exhaust (Keinath *et al.*, 2012). The system-level investigations reviewed here include absorber/condenser indirect cooling through a hydronic loop (Chua *et al.*, 2002; Izquierdo *et al.*, 2008; Moya *et al.*, 2011; Keinath *et al.*, 2012) and direct air cooling (Lazzarin *et al.*, 1996; Chua *et al.*, 2002; De Francisco *et al.*, 2002; Velázquez and Best, 2002; Horuz and Callander, 2004; Wang *et al.*, 2007; Kim and Ferreira, 2009; Llamas-Guillén *et al.*, 2014).

Indirectly cooled systems typically demonstrate lower efficiencies compared to an equivalent directly cooled system due to the additional temperature difference introduced between the working fluid and the heat sink by the intermediate fluid, and also due to the parasitic power required by the hydronic fluid pump. All of the system-level absorption studies reviewed here used conventional, round-tube air coils with flat fins for heat rejection to the ambient. In many cases, the conventional air-coupled heat exchangers

constitute a large portion of the overall system size. Investigations are needed to develop novel compact air-coupled heat exchangers for use as the absorber and condenser. Reduced system size and weight resulting from innovative component design could improve the viability of absorption heat pumps. A list of the system-level heat pump studies reviewed here is provided in *Table 2.1*.

### **2.1.1 Working Fluid Considerations**

With increased environmental concerns and governmental regulations, it is important to identify the working fluids that continue to meet future energy demands. Calm (2008) presented the state of the art in refrigerants based on a historical review of the literature and outlook due to environmental concerns. The review characterized the generational progression of refrigerants from "whatever works" to refrigerants purposed for safety and reliability, ozone generation, and - most recently - global warming. Calm mentions a renewed interest in ammonia as a natural refrigerant to meet new low-GWP regulations. Ammonia is described as a viable refrigerant in industrial and commercial refrigeration systems, despite a concern about its flammability. Calm clarifies that there is no ideal refrigerant and that collective consideration must be given for all environmental issues together when selecting a suitable fluid (2008).

**Table 2.1 System-level heat pump investigations**

<b>Author(s) (Year)</b>	<b>Type of Investigation</b>	<b>System Type Input</b>	<b>System Capacity (kW) Mode</b>	<b>Working Fluids</b>	<b>Absorber/ Condenser Coupling</b>	<b>Method of Cooling</b>
Lazzarin <i>et al.</i> (1996)	Experimental	GAX <i>Natural Gas</i>	10.5-17.5 <i>Cooling</i>	NH <sub>3</sub> -H <sub>2</sub> O	Direct	Air in crossflow over finned round tubes
De Francisco <i>et al.</i> (2002)		Single-Effect <i>Solar Energy</i>	2 <i>Cooling</i>	NH <sub>3</sub> -H <sub>2</sub> O	Direct	Air in natural convection over finned round tubes
Horuz and Callander (2004)		GAX <i>Natural Gas</i>	10.00 <i>Cooling</i>	NH <sub>3</sub> -H <sub>2</sub> O	Direct	Air in crossflow over finned round tubes
Izquierdo <i>et al.</i> (2008)		Single-Effect <i>Heating Oil</i>	4.5 <i>Cooling</i>	LiBr-H <sub>2</sub> O	Indirect	Water in counterflow, pumped to round-tube plain-finned air coil
Llamas-Guillén <i>et al.</i> (2014)		Single-Effect <i>Heating Oil</i>	4.5 <i>Cooling</i>	NH <sub>3</sub> -LiNO <sub>3</sub>	Direct	Falling film inside vertical tubes
Jiang and Garimella (2001)	Modeling	Compression <i>Electricity</i>	10.55 <i>Heating &amp; Cooling</i>	R-22	Indirect	Water in microchannels, pumped to flat-tube louvered-fin air coil
Velázquez and Best (2002)		GAX <i>Solar Energy</i>	10.55 <i>Heating &amp; Cooling</i>	NH <sub>3</sub> -H <sub>2</sub> O	Direct	Air in crossflow over finned round tubes
Chua <i>et al.</i> (2002)		GAX <i>Natural Gas</i>	6.18 <i>Cooling</i>	NH <sub>3</sub> -H <sub>2</sub> O	Direct/ Indirect	Air in crossflow over finned round tubes (solution or water in tubes)
Wang <i>et al.</i> (2007)		Single-Effect <i>Natural Gas</i>	16 <i>Cooling</i>	LiBr-H <sub>2</sub> O	Direct	Flow over packed bed (mixing), flow in finned tubes (heat removal)
Kim and Ferreira (2009)		Half-Effect <i>Solar Energy</i>	12.8 <i>Cooling</i>	LiBr-H <sub>2</sub> O	Direct/ Indirect	Falling film on plate, tube bank/air in crossflow over round finned tube
Keinath <i>et al.</i> (2012)		Single-Effect <i>Diesel Exhaust</i>	2 <i>Heating &amp; Cooling</i>	NH <sub>3</sub> -H <sub>2</sub> O	Indirect	Water in microchannels, pumped to air-coupled heat exchanger
Moya <i>et al.</i> (2011)		Experimental and Modeling	Single-Effect <i>Micro Turbine</i>	17 <i>Cooling</i>	NH <sub>3</sub> -H <sub>2</sub> O	Indirect

It is necessary to understand the advantages and drawbacks of absorption systems driven by ammonia-water mixtures compared to other working fluid pairs. Srihirin *et al.* (2001) presented the state of the art in absorption refrigeration technologies. They commented on the wide application of ammonia-water in absorption systems citing the high latent heat of vaporization and the low freezing point of ammonia ( $-77^{\circ}\text{C}$ ), the low environmental impact of this working fluid pair, and the low cost of the two fluids. They also mentioned the challenges associated with ammonia-water including a high system pressure, the necessity of a rectifier to achieve acceptable refrigerant purities, toxicity, and corrosion in copper alloys. The most common alternative to ammonia-water is lithium bromide-water. Lithium bromide-water systems suffer from the high freezing point of water ( $0^{\circ}\text{C}$ ), near vacuum system operation, risk of crystallization at high concentrations, and high absorbent cost. They identified the absorber as the "most critical component of any absorption refrigeration system" (Srihirin *et al.*, 2001). Cycles evaluated in the literature include single-effect, multi-effect, generator/absorber heat exchange (GAX), diffusion, and combined absorption-refrigeration systems.

### **2.1.2 Commercial Implementation**

Through a review of the literature on sorption heat pump and cooling technologies, Ziegler (2002) identified barriers for absorption systems to be competitive with existing heat pump technology. Despite the advantages of absorption systems due to low noise and vibrations and the possibility of using waste heat, he identified the large footprint, weight, and capital costs of such systems to be obstacles to widespread implementation. Ziegler also noted that the systems must be amenable to mass production for use in small-scale applications. The literature indicates that sorption systems,



particularly those with ammonia-water and lithium bromide-water, will remain relevant in locations with high mid-afternoon demand (Ziegler, 2002). This peak demand is often experienced at the warmest part of the day in which heat rejection to the hot ambient air becomes more challenging. The present study investigates absorption heat pump performance at extreme ambient temperatures to address this concern.

Ammonia-water absorption systems have proven to be reliable and suitable for wide-scale implementation for decades. Lazzarin *et al.* (1996) carried out an analysis of maintenance data gathered during the first 10 years of operation of commercially available ammonia-water absorption chillers. The cooling capacities of the chillers evaluated were between 10.5 and 17.5 kW. The heat pumps included a conventional round-tube finned coil used to reject heat during condensation and absorption. The process of absorption took place in two distinct components: the solution-cooled absorber and the air-cooled absorber. The rate of failure of the heat pump within the first couple years of operation was generally high, but the fault was usually minor. The most common failures were those related to the desorber and to the solution pump. The absorption chillers were noted to demonstrate "appreciable reliability," and no failure caused any injuries to people despite the use of ammonia-water as the working fluid (Lazzarin *et al.*, 1996).

To better understand the current state of batch-produced absorption heat pumps, Horuz and Callander (2004) evaluated the performance of a commercially available 10-kW GAX ammonia-water absorption chiller. An alternative to the conventional single-effect ammonia-water absorption system, the GAX cycle does not include the solution heat exchanger, and a portion of the heat removed from the absorber is transferred to the

desorber. The GAX system typically divides the absorption process between three components in series: a generator cooled absorber (GAX), a solution-cooled absorber (SCA) and an air-cooled absorber (ACA). Conversely, in a non-GAX system, heat is removed from the dilute solution in a solution heat exchanger before mixing with the refrigerant vapor and undergoing heat and mass transfer in the absorber. Although this design allows for mass transfer in three distinct components, it was determined in the non-GAX cycle under consideration here that consolidating the mixing in the air-coupled absorber will reduce total system volume. Horuz and Callander (2004) noted that the air-cooled absorber and air-cooled condenser were combined into a typical cross-flow, round-tube, flat-fin air coil. The system approximately fit in a 1-meter cube in which three of the four sides were composed of the combined absorber and condenser air coil. The absorber and condenser air coils incorporated a typical round-tube flat-fin design.

Commercial absorption heat pumps have demonstrated deteriorating performance with increasing ambient temperature. Izquierdo *et al.* (2008) investigated the performance of a commercially available 4.5 kW air-cooled lithium bromide-water absorption chiller. The combined absorber-condenser in the system is cooled with water that is pumped to a finned-tube coil with air in crossflow. At a volume of 0.61 m<sup>3</sup> and weight of 240 kg, the unit delivered cold water at temperatures between 11°C and 25°C at an average total *COP* of 0.37 during three days of evaluation. With increasing outdoor dry-bulb temperature, the chilled water delivery temperature rose, while the system *COP* and cooling duty decreased. The outdoor dry-bulb temperature spanned from 23°C to 41°C during the investigation. The total system *COP* could be increased through the

elimination of auxiliary component power consumption, such as the water pump used in the indirect cooling of the absorber-condenser.

### **2.1.3 GAX and Unconventional Cycles**

In attempts to increase the efficiency of absorption systems, researchers have developed and evaluated more complex cycles. Velázquez and Best (2002) modeled an air-coupled GAX system using solar energy and natural gas to provide the driving heat. Experimental validation of the hybrid cycle is necessary. The analysis predicted a cooling *COP* of 0.86 with ambient air at 40°C used for heat rejection. The GAX configuration and dual heat sources result in a more complex cycle design compared to the single-effect system; the system featured three stages in both the absorption and desorption processes (Velázquez and Best, 2002). Increased system complexity is likely to increase system capital cost, inhibiting widespread implementation.

Chua *et al.* (2002) developed a thermodynamic model for a single-stage GAX ammonia-water absorption chiller with a cooling duty of 6.2 kW. The heat is applied directly to the system from natural gas combustion, and the absorber is split into an internal recuperative solution-cooled portion and an air-cooled portion. Results of the modeling are likely to deviate from empirical data because the evaporator, refrigerant precooler, solution-cooled absorber, and air-cooled absorber were all treated as isobaric components. Realistically, pressure drop is inevitable in the heat and mass exchangers and will reduce the efficiency of the heat pump. System construction and evaluation would be useful in establishing the validity of these assumptions.

Kim and Ferreira (2009) developed a computer model to simulate the performance of an air-cooled lithium bromide-water absorption chiller with a low

temperature (90°C) heat source. The study included cycle- and component-level modeling for a heat-coupled half-effect parallel-flow absorption cycle. This unconventional three-pressure system was chosen due to its relatively low lithium bromide concentration (44.5 to 57.4 wt. %) and reduced risk of crystallization in the air-coupled components. Air-cooled components that were modeled include a flat-plate falling-film low-pressure absorber, a flat-fin round-tube high-pressure absorber, and a flat-fin round-tube condenser. Kim and Ferreira compared system performance with direct air coupling and indirect coupling using an intermediate water loop. The model predicted a cooling capacity of 12.8 kW and a cooling *COP* of 0.38 for the direct air-cooled chiller at 90°C heat source temperature and 35°C ambient temperature. It is unclear whether or not the *COP* value incorporates the parasitic electrical losses associated with the system fan and two solution pumps. The direct air-cooled chiller was shown to be more efficient than the system using an intermediate water loop; however, it was noted that there were significant practical challenges in the economical fabrication and efficiency of the air-cooled condenser and absorber. Similar obstacles exist for ammonia-water components, which are addressed in the current study.

One benefit of absorption heat pumps is their potential combination with unconventional sources of power generation to meet multiple energy demands. Moya *et al.* (2011) combined a commercially available Capstone C30 micro gas turbine (28 kW power, 60 kW heat) with a Robur ACF 60-00TK air-cooled absorption chiller (17 kW) to produce a tri-generation system for electricity, chilled water, and hot water outputs. The exhaust gas exits the turbine at 275°C and is used to heat thermal oil for the driving input of the absorption chiller. The cooler exhaust gas then flows over a bank of finned tubes in

which water receives heat for domestic applications. The investigation demonstrated the viability of a tri-generation system for large residential and small commercial applications. Ambient temperatures of up to 42°C were recorded, but the chiller capacity was severely limited at these higher temperature data points. An economic analysis revealed long pay back periods for the system (5.2 - 9.6 years, depending on the application) as a result of high system costs and low efficiency compared to typical compression systems. Innovative heat transfer components that are amenable to mass production must be developed to reduce these barriers to implementation.

#### **2.1.4 Single-Effect Cycles**

To reduce parasitic power consumption and improve system *COP*, researchers have attempted heat rejection from the absorber and condenser without forced convection using fans. De Francisco *et al.* (2002) developed and evaluated a prototype ammonia-water heat pump intended to produce 2 kW of cooling using heat from a concentrated solar power system. The absorber and condenser were natural convection-cooled serpentine finned-tube coils. The system demonstrated a *COP* below 0.05 due to component leaks, an underperforming rectifier, and the use of a transfer tank instead of a solution pump. They indicated that forced convection in the absorber and condenser would improve system performance while reducing the overall required heat transfer area. Small-scale fans were speculated to draw little power and could be driven by a small photovoltaic panel. This study demonstrated the challenges inherent in passively-cooled ammonia-water absorption system implementation.

Studies using other working fluid pairs have attempted to address the challenges associated with absorption in a small volume. Wang *et al.* (2007) developed a

thermodynamic model of a gas-fired air-cooled lithium bromide-water absorption system. They attempted to decouple the heat and mass transfer in the absorber by using a packed bed adiabatic absorber for mixing and a separate air cooler for heat removal. The authors claimed that it is difficult to enhance both tube-side heat transfer (for mixing) and air-side heat transfer (for cooling) in the same process. Wang *et al.* recorded total *COP* values that decreased from 1.2 to 0.8 with outside air temperatures increasing from 30°C to 43°C. It is unclear, however, what pressure drop values were used in evaluating component performance, and no information is provided about the volume of the system. Without fan and pump efficiency values and other electrical consumption predictions, it is difficult to compare the calculated *COP* to those from other investigations. Improved system performance is predicted at lower values of solution distribution ratio, but this enhancement brings an increased risk of crystallization. Experimental validation of these modeled results is needed.

In recent years, researchers have focused on the use of low-grade energy that is typically discarded to the atmosphere. Keinath *et al.* (2012) developed a thermodynamic model to simulate the performance of an ammonia-water absorption system driven by waste heat from a diesel engine. The heat pump was designed to deliver a baseline cooling load of 2 kW for space conditioning. Both heating and cooling modes were evaluated across a range of ambient and return air temperatures. Hydronic fluid and microchannel heat exchangers were used to extract heat from the absorber and condenser. Keinath *et al.* (2012) concluded that compact absorption systems can effectively produce space conditioning from diesel exhaust; however, they corroborated the conclusion from Izquierdo *et al.* (2008) and Moya *et al.* (2011) in predicting a significant reduction in

performance at high ambient temperatures. Keinath *et al.* noted a drop in cooling duty from 2.7 to 1.7 kW as ambient temperature increased from 20 to 50°C. To help improve performance at extreme ambient conditions, the authors suggested that delivery temperature can be adjusted.

To improve the viability of low-temperature heat sources, including solar thermal energy, researchers have investigated other working fluids for absorption systems. Llamas-Guillén *et al.* (2014) fabricated a prototype air-cooled ammonia-lithium nitrate chiller and produced 4.5 kW of cooling. The low vapor pressure of lithium nitrate enables separation from ammonia at a relatively low desorber temperature, thereby eliminating the need for a rectifier in the system. This advantage comes at the cost of a risk of crystallization and high mixture viscosity (Llamas-Guillén *et al.*, 2014). The system fabricated by Llamas-Guillén *et al.* included an air-cooled falling-film absorber with 29 finned tubes subjected to downward internal flow of the solution. The absorber was noted to be the largest volume component in the system. The air-cooled condenser was a horizontally-oriented coil with conventional finned round tubes. The system produced 4.5 kW of cooling with *COPs* between 0.3 and 0.4 at ambient temperatures ranging from 25° to 35°C. Opportunities remain to reduce the total system volume into a robust and compact packaged unit for ease of transportation.

Although none of the studies reviewed here used novel compact air-coupled heat exchangers in an absorption heat pump, miniaturization of components has proven beneficial in conventional heating/cooling systems. Jiang and Garimella (2001) integrated system- and component-level models to demonstrate a significant reduction in package size and fluid inventory through the use of compact air-coupled heat exchangers in a

conventional vapor compression system. A model incorporating thermodynamics and heat transfer was developed for a heat pump with typical round-tube air-coupled, microchannel hydronically coupled, and microchannel air-coupled heat exchangers. The investigation indicated that air-coupled microchannel heat exchangers featuring rectangular multiport tubes and louvered fins could be used to reduce system volume by one half compared to a conventional heat pump. Jiang and Garimella (2001) estimated that prototype air-coupled components would reduce refrigerant charge by 20% in comparison with conventional systems. In the heat pumps modeled, R-22 was the refrigerant; therefore, aluminum was selected as the material of fabrication. Additional investigations are required to predict the performance of a compact air-coupled absorber and to verify the model predictions through fabrication and testing.

## **2.2 Absorber and Condenser Design for Absorption Heat Pumps**

In absorption heat pumps, the absorber and condenser serve as the components that reject heat to the environment when the system is operated in the cooling mode. The rejection of this heat can either be done through direct air-coupled components or through the pumping of an intermediate coupling fluid that exchanges heat to the air in a crossflow air-coupled heat exchanger. Directly coupling these components to ambient air presents the heat pump designer with an opportunity to reduce the parasitic pumping power required by the system and thereby increase total *COP*. Air-coupled condensers have long been used in industry, but the use of ammonia-water in the present study restricts the use of off-the-shelf rectangular multiport-tube multi-louvered fin aluminum heat exchangers due to corrosion. Some (Garimella and Wicht, 1995; Garimella *et al.*,



1997) of the investigations reviewed indicate the potential benefits of using compact air-coupled condensers in ammonia-water absorption systems.

Air-coupled absorber design presents a greater set of challenges than those of the condenser (Srikhirin *et al.*, 2001), due to the simultaneous need to reject the heat of absorption and the latent heat of the vapor (Wang *et al.*, 2007) and the underlying mass transfer resistances. A list of the component-level studies reviewed here is shown in *Table 2.2*.

**Table 2.2 Component-level absorber and condenser investigations**

Author(s) (Year)	Type of Investigation	Component	Component Capacity (kW) <i>System Mode</i>	Working Fluids	Absorber/ Condenser Coupling	Geometry
Kim <i>et al.</i> (1997a)	Experimental	Absorber	- <i>Cooling</i>	LiCl/LiBr-H <sub>2</sub> O	Indirect	Falling film on vertical tube, water in horizontal crossflow
Medrano <i>et al.</i> (2002)		Absorber	0.4-1.4 <i>Cooling</i>	LiBr-H <sub>2</sub> O	Indirect	Falling film in vertical tube, water in concentric counterflow
Meacham and Garimella (2002)		Absorber	4.9-16.2 <i>Cooling</i>	NH <sub>3</sub> -H <sub>2</sub> O	Indirect	Falling film over microchannels, water in crossflow
Meacham and Garimella (2004)		Absorber	4.5-15.1 <i>Cooling</i>	NH <sub>3</sub> -H <sub>2</sub> O	Indirect	Falling film over microchannels, water in crossflow
Bourouis <i>et al.</i> (2005)		Absorber	0.3-0.7 <i>Cooling</i>	LiBr-H <sub>2</sub> O (+Salts)	Indirect	Falling film in vertical tube, water in concentric counterflow
Garimella and Wicht (1995)	Modeling	Condenser	20.99 <i>Cooling</i>	NH <sub>3</sub>	Direct	Horizontal flat tubes, air in crossflow over louvered fins
Garimella <i>et al.</i> (1997)		Cooler	26.38 <i>Cooling</i>	EG-H <sub>2</sub> O	Direct	Flat and round tubes, air in crossflow over various fins
Garimella and Coleman (1998)		Condenser	17.92 <i>Cooling</i>	NH <sub>3</sub> -H <sub>2</sub> O	Direct	Flow in horizontal round tubes, crossflow air over various fins
Fernández-Seara <i>et al.</i> (2005)		Absorber	- <i>Cooling</i>	NH <sub>3</sub> -H <sub>2</sub> O	Indirect	Upward flow in tubes of shell-and-tube, counterflow water
Fernández-Seara <i>et al.</i> (2007)		Absorber	- <i>Cooling</i>	NH <sub>3</sub> -H <sub>2</sub> O	Direct	Upward flow in staggered tube array, crossflow air over flat fins
Ferreira <i>et al.</i> (1984)	Experimental and Modeling	Absorber	1.1 <i>Cooling</i>	NH <sub>3</sub> -H <sub>2</sub> O	Indirect	Upward flow in tube, methanol in concentric counterflow
Castro <i>et al.</i> (2009)		Absorber	0.6-1.4 <i>Cooling</i>	NH <sub>3</sub> -H <sub>2</sub> O	Direct	Falling film/upward flow, air in crossflow over flat fins
Nagavarapu and Garimella (2013)		Absorber	3-10 <i>Cooling</i>	NH <sub>3</sub> -H <sub>2</sub> O	Indirect	Falling film over horizontal water-carrying microchannels

Of the studies reviewed, the majority involved indirect coupling (*e.g.*, hydronic fluid pumped to an air coil) to reject this heat from the absorber. Indirect cooling typically occurs in a vertical tube in falling-film mode (downward) or bubble mode (upward). Falling-film absorbers have been demonstrated on the outside of the tube (Kim *et al.*, 1997a) as well as on the inside of a vertical tube (Medrano *et al.*, 2002; Bourouis *et al.*, 2005; Castro *et al.*, 2009). Upward, bubble flow during absorption has been explored by Ferreira *et al.* (1984) and Castro *et al.* (2009). Alternative indirectly cooled absorber designs include shell-and-tube (Fernández-Seara *et al.*, 2005) and falling film with counterflow vapor over a compact bank of small coolant channels (Meacham and Garimella, 2002; Meacham and Garimella, 2004; Nagavarapu and Garimella, 2013). The investigations that include direct coupling to air are primarily numerical studies without experimental validation. The study by Castro *et al.* (2009) demonstrated an air-coupled absorber experimentally; in this instance, a conventional, flat-finned round-tube air coil was used. The present study expands upon the experimental validation of air-coupled absorbers and proposes compact absorber geometries that could serve as alternatives to large, conventional air coils.

### **2.2.1 Modeling Studies**

To investigate the feasibility of novel compact air-coupled components in an absorption system, Garimella and Wicht (1995) conducted an analysis of a rectangular-tube multi-louvered fin heat exchanger for ammonia condensation. A computer model was developed to predict the performance and required size of the condenser based on various tube, fin, and louver geometries as well as tube-side pass arrangements. The previous literature on round tubes was adapted for the two-phase heat transfer and

pressure drop in flat tubes with cooling air in cross flow. Garimella and Wicht (1995) concluded that the use of flat tubes and multi-louvered fins enabled flexibility in heat exchanger design while providing substantial reduction in size and weight. The flat tubes were shown to reduce flow area obstruction (along with drag and fan power requirements) in comparison with conventional round tubes. Although carbon steel was chosen for ammonia-water compatibility, it was noted that typical compact air-coupled heat exchangers of this design are made with aluminum. Considerable manufacturing challenges, including the machining of flat steel tubes and the bonding of aluminum fins to steel tubes, must be overcome before these heat exchangers can be applied to an ammonia-water absorption system.

In a subsequent study, Garimella *et al.* (1997) developed a model to predict and compare the performance of rectangular-tube multi-louvered fin heat exchangers with the performance of conventional round-tube heat exchangers with flat, wavy, annular, and louvered fins. The model was limited to single-phase flow. In these components, hydronic fluid flowed in the tubes and transferred heat to air in cross flow. The space and weight requirements of the novel heat exchanger were compared with those of typical round-tube heat exchangers at equivalent heat duties. Garimella *et al.* investigated a variety of internal flow arrangements including fully serpentine, fully parallel, combination serpentine-parallel, and multiple-row cross-counter flow configurations. It was concluded that flat-tube multi-louvered fin heat exchangers match the pressure drop and heat transfer performance of conventional round-tube heat exchangers at a significantly reduced overall mass and size. Of the round-tube air-coupled designs that were investigated (flat, wavy, annular, louvered), the component with wavy fins resulted

in the highest air-side heat transfer coefficient and lowest overall mass. It should be noted that the material used in the flat tube and multi-louvered fin design was aluminum while copper tubing and aluminum fins were specified for the conventional heat exchangers.

Garimella and Coleman (1998) developed a model to predict the performance of an air-coupled multi-row ammonia-water condenser at realistic absorption heat pump conditions. This two-phase model accounted for the non-isothermal behavior of the binary fluid mixture and predicted the performance of conventional round-tube air coils with flat, wavy, annular, and louvered fins. Carbon steel was chosen as the tube material, while aluminum was specified for the fins. Variations in mixture concentration, saturation pressure, and air temperature were investigated to predict the performance of such condensers over a wide range of operating conditions. Garimella and Coleman concluded that a round-tube wavy-fin heat exchanger provided the greatest heat transfer within the allowable pressure drop and size constraints out of the readily available air-coupled carbon steel heat exchangers.

Vertical tube absorbers, in both falling-film and bubble modes, have been investigated thoroughly in the literature. Ferreira *et al.* (1984) developed a model to predict the heat and mass transfer in an ammonia-water solution flowing upward in a tubular bubble absorber. The predicted heat and mass exchange was then compared with data obtained from experiments on a single tube. Heat was transferred from cocurrent liquid and vapor solution to methane in concentric counterflow. Tube internal diameters of 10, 15.3, and 20.5 mm were investigated, and the Sherwood relation was modified to produce empirical mass transfer coefficient correlations. In addition, Ferreira *et al.* (1984)

developed an expression to estimate the height required for absorption in a vertical tube bubble absorber, which is particularly useful for absorption heat pumps.

Fernández-Seara *et al.* (2005) conducted a heat and mass transfer analysis of a cocurrent vertical tube absorber. Ammonia vapor and dilute ammonia-water solution flow upward in the tubes of a shell-and-tube heat exchanger while cooling water flows downward around baffles on the shell side. The model accounted for a variety of flow patterns during absorption, and a parametric study indicated that adjustments in the diameter and length of the tubes had a large impact on absorber performance. An experimental investigation is needed to validate the predictions of this model.

Fernández-Seara *et al.* (2007) also modeled heat and mass transfer in an air-cooled vertical tube absorber. Absorption was designed to occur in the upward flow of ammonia-water in a staggered vertical tube array with air in cross flow over flat external fins. The dilute solution exiting the desorber was mixed with ammonia-water vapor in a premixer before entering the air-cooled absorber. As expected, the model predicted that a higher fin density, lower air temperature, and higher air velocity reduced the required length of tubing to complete the absorption process. Fernandez-Seara *et al.* also showed an increase in the absorption length with decreasing tube diameter, but this was with the total ammonia-water mass flow rate and the number of tubes held constant. The study also indicated that absorption in the tubes farthest downstream from the air inlet was reduced because of the heating of the air occurring in the first tube rows exposed to air flow. Fernandez-Seara *et al.* concluded that the air-side heat transfer coefficient had the most significant effect on the component performance.

Castro *et al.* (2009) developed models to predict the performance of air-coupled falling-film and bubble absorbers and validated the models with experiments. They reasoned that air cooling of the absorber and condenser is necessary to reduce system size, complexity, and capital cost. The falling-film and bubble absorbers consisted of round vertical finned tubes with downward cocurrent liquid and vapor (falling-film mode) or upward cocurrent liquid and vapor (bubble mode). Heat is removed by air in crossflow in both modes of operation through flat fins. A variety of assumptions were incorporated in the modeling include negligible pressure gradients in the falling film, no convection in the radial direction, spherical vapor bubbles, and no break-up or coalescence of bubbles. They reported reasonable agreement between modeling and experiments (<15% difference in most cases) in component cooling capacity, but the bubble-flow model was validated with data from a water-cooled, rather than air-cooled, absorber. It is unclear whether these data can be used to validate the model. They concluded that bubble absorption was typically more effective than falling-film absorption, particularly at low flow rates at which the wetted area is small (Castro *et al.*, 2009).

### **2.2.2 Experimental Studies**

Experimental investigations of absorber performance in the literature are limited, and there is a notable absence of studies with direct heat rejection to the air. A primary focus in recent studies has been on lithium bromide-water heat pumps and the prevention of crystallization at low delivery temperatures. Attempts to reduce tube-side thermal resistance in component design through the use of mini- or microchannel tubes have resulted in inconsistent liquid and vapor distribution. Challenges remain for researchers

to accomplish both the miniaturization of flow channels required for the improvement of flow regime and even distribution of the liquid and vapor streams.

Kim *et al.* (1997a) designed a set of experiments to compare the performance of a vertical falling-film absorber in an open-cycle absorption refrigeration system with lithium bromide-water and lithium chloride-water used as the working fluid pair. The open-cycle is different from the closed system in that the dilute solution is generated by evaporating water using solar radiation, and exhausting it to the atmosphere instead of condensing it. As a result, a conventional closed-cycle desorber and condenser are absent in the open-cycle system. Kim *et al.* (1997a) demonstrated a higher absorption rate with lithium bromide than with lithium chloride, resulting in smaller and less expensive components. A cost analysis showed the cost of the two absorbent candidates to be a hindrance for implementation, due to the large volume of strong solution that would be required to provide cooling when solar radiation is insufficient to generate water vapor. As part of an effort to develop a compact lithium bromide-water absorption chiller, Medrano *et al.* (2002) designed an air-cooled absorber featuring vertical finned tubes with internal cocurrent falling film and water vapor flow. An experimental evaluation of the design was carried out with counterflowing cooling water in a concentric tube instead of air cooling used to complete the absorption process. To account for the differing heat transfer characteristics between cooling air and water, relatively high temperature (35°C) water was used to transfer heat from the lithium bromide-water solution. Results of the experiment showed that there is no significant difference between the mass absorption flux in a falling film on the inner wall compared to a falling film on the outer wall of a vertical tube. Medrano *et al.* demonstrated increased absorption with higher solution flow



rates, lower cooling water temperatures, and higher operating pressures in the absorber. It was concluded that absorber performance was very sensitive to cooling water temperature, and it was suggested that the concentration of the lithium bromide-water solution could be raised to help drive the absorption process. It should be noted, however, that higher concentrations of lithium bromide (along with an increased absorber operating temperature) would increase the risk of crystallization occurring in the system. In a follow-up study, Bourouis *et al.* (2005) added four additional salts to the lithium bromide-water solution in an attempt to increase the solubility of lithium bromide in water. The absorber was able to operate at higher solution concentrations and a higher absorption flux, but the heat and mass transfer coefficients were slightly lower than the values recorded in a typical concentration absorber configuration. Concerns to be addressed include the long-term consequences of the use of these salts in heat pump operation.

Meacham and Garimella (2002) fabricated and demonstrated the performance of a miniaturized heat and mass exchanger for use in absorption heat pumps. An absorber with a design load of 19.28 kW was evaluated in which liquid ammonia-water solution flows in falling-film mode over an array of small diameter tubes while vapor flows upward. The average absorber duty recorded during testing was 12.78 kW. One explanation offered for the discrepancy in the predicted and actual performance is the use of a single-pressure test facility in which the vapor entering the absorber was representative of desorber outlet conditions rather than evaporator outlet conditions. In addition, maldistribution of flow within the tube array was noted as a possible cause for suboptimal performance. In a follow-up study, Meacham and Garimella (2004)

experimentally investigated the performance of an ammonia-water absorber that demonstrated loads up to 15 kW in a compact volume ( $0.162 \times 0.157 \times 0.150$  m). The component featured liquid solution in a falling film over microchannel coolant tubes with vapor flowing upward to maximize vapor-solution contact. This absorber demonstrated superior performance compared to the first prototype developed by them due to improvements in solution distribution and wetting caused by improvements in the drip tray geometry. The study incorporated flow visualization of the solution in falling-film mode over small microchannel tubes as a confirmation of the flow distribution and the droplet formation and redistribution. Meacham and Garimella (2004) emphasized the need for a segmental heat and mass transfer model of the component for better comparison with the data.

Nagavarapu and Garimella (2013) evaluated the performance of an absorber composed of a bank of coolant-carrying microchannel tubes with falling-film ammonia-water solution and counter-current vapor. They confirmed the findings of Meacham and Garimella (2002, 2004) through the demonstration of large absorber duties in a compact package. In contrast to previous studies, Nagavarapu and Garimella (2013) evaluated the absorber in a complete two-pressure absorption facility over a range of realistic design conditions. Due to a lack of relevant solution heat transfer coefficient correlations in the literature, they recommended the development of a new model for ammonia-water absorption in falling films over microchannel tubes.

### **2.3 Summary**

The above discussion of the literature indicates the complexity of choices faced by heat pump manufacturers in terms of working fluids, cycle designs, and coupling

options for heat addition and rejection. Large system size, high cost, crystallization, and a relatively high ( $0^{\circ}\text{C}$ ) refrigerant freezing point hinder lithium bromide-water systems. Ammonia-water systems, however, require a rectifier, present material compatibility challenges, and potential health hazards due to toxicity and flammability. Researchers have investigated increasingly complex cycles with the aim of improving system efficiency and viability, but their efforts are counteracted by the rising capital and maintenance costs of such cycles. Modeling studies frequently predict the gains in performance in directly over indirectly cooled systems, but few of those studies are validated experimentally due to the challenges associated with test facility design and the use of air as a working fluid. The studies that have addressed compact component design experimentally have demonstrated the inherent difficulties in attempting to simultaneously reduce internal thermal resistance, promote liquid and vapor mixing, and minimize pressure drop.

The present investigation builds upon the work of previous investigators through the modeling and experimental validation of direct air-coupled heat exchangers for waste heat driven absorption cooling systems. The specific modeling and experimental efforts are described in the following chapters.

## CHAPTER 3: MODELING

The development of a thermodynamic cycle model to predict absorption system performance at a variety of ambient conditions and segmental heat and mass transfer models for the design of the absorber are described in this chapter. The design models address round-tube corrugated-fin and prototype tube-array configurations. The results from the models are compared with data from air-coupled heat exchanger testing in Chapter 5. Detailed sample calculations for the segmental models are provided in Appendix A.

### 3.4 Thermodynamic Cycle Modeling

A thermodynamic cycle model is developed in the *Engineering Equation Solver (EES)* software platform to predict the performance of the heat pump and establish the inlet and outlet conditions for the air-coupled components under consideration in this study. The absorption system is designed to deliver 2.64 kW of cooling air at a delivered air temperature of 19.5°C using exhaust gas from a diesel generator as the heat source. At the design conditions, the exhaust gas enters the heat pump at a temperature of 398.9°C with a specific heat of 1.005 kJ kg<sup>-1</sup> K<sup>-1</sup> and a flow rate of 0.0255 kg s<sup>-1</sup>. To evaluate the performance in hot, arid climates, the inlet air to the absorber and condenser is assumed to be at 51.67°C and 18% relative humidity. To obtain an accurate indication of the cycle cooling capacity and *COP*, conservative estimates are used for the pressure drop, Closest Approach Temperature (*CAT*), and effectiveness values for individual components. First, a baseline cycle model is developed in which these estimates are used to predict system performance at design conditions. A parametric study is then conducted to determine the impact of adjustments in various model inputs on cycle cooling capacity and *COP*. Based

on the parametric study, adjustments are made to optimize cycle performance while maintaining realistic values for component performance. An ambient temperature study is conducted to predict the performance of the system over a range of outdoor conditions.

### 3.5 Baseline Cycle Model

For preliminary performance predictions, a baseline cycle model is developed using the inputs shown in *Table 3.1*.

**Table 3.1 Baseline thermodynamic cycle model inputs**

Desorber Coupling		Component Performance		Power Consumption	
$T_{\text{gas,in}}$ (°C)	398.9	$\Delta P_{\text{abs}}$ (kPa)	6.895	$\dot{m}_{\text{conc}}$ (kg s <sup>-1</sup> )	0.008
$\dot{m}_{\text{gas}}$ (kg s <sup>-1</sup> )	0.0255	$\Delta P_{\text{cond}}$ (kPa)	13.79	$\eta_{\text{fan}}$ (-)	0.5
$C_p$ (kJ kg <sup>-1</sup> K <sup>-1</sup> )	1.005	$\Delta P_{\text{evap}}$ (kPa)	6.895	$\eta_{\text{fan,motor}}$ (-)	0.4
$\Delta T_{\text{ineq,des}}$ (°C)	10	$\Delta P_{\text{fan,abs}}$ (kPa)	0.062	$\eta_{\text{pump}}$ (-)	0.9
Conditioned Space Coupling		$\Delta P_{\text{fan,cond}}$ (kPa)	0.062	$\eta_{\text{pump,motor}}$ (-)	0.6
$T_{\text{CS,air,in}}$ (°C)	32.22	$\Delta T_{\text{evap}}$ (°C)	2.5	$\Delta P_{\text{PG,pump}}$ (kPa)	68.95
$T_{\text{CS,air,out}}$ (°C)	19.50	$\Delta T_{\text{ineq,rect}}$ (°C)	3	$F_{\text{load}}$ (-)	3.18
$RH_{\text{CS,in}}$ (-)	0.50	$\Delta T_{\text{sub,abs}}$ (°C)	2	$Q_{\text{controls}}$ (kW)	0.075
$\dot{V}_{\text{CS,air}}$ (m <sup>3</sup> s <sup>-1</sup> )	0.151	$\Delta T_{\text{sub,cond}}$ (°C)	2		
$x_{\text{PG}}$ (-)	0.16	$RH_{\text{abs,in}}$ (-)	0.18		
$\dot{m}_{\text{PG-H}_2\text{O}}$ (kg s <sup>-1</sup> )	0.0957	$RH_{\text{cond,in}}$ (-)	0.18		
$P_{\text{atm}}$ (kPa)	101.3	$T_{\text{abs,air,in}}$ (°C)	51.67		
		$T_{\text{cond,air,in}}$ (°C)	51.67		
		$\dot{V}_{\text{abs,air}}$ (m <sup>3</sup> s <sup>-1</sup> )	0.354		
		$\dot{V}_{\text{cond,air}}$ (m <sup>3</sup> s <sup>-1</sup> )	0.354		

The inlet exhaust gas conditions (398.9°C, 0.0255 kg s<sup>-1</sup>, 1.005 kJ kg<sup>-1</sup> K<sup>-1</sup>) are chosen to be representative of the output from a 10 kW diesel generator. The inlet

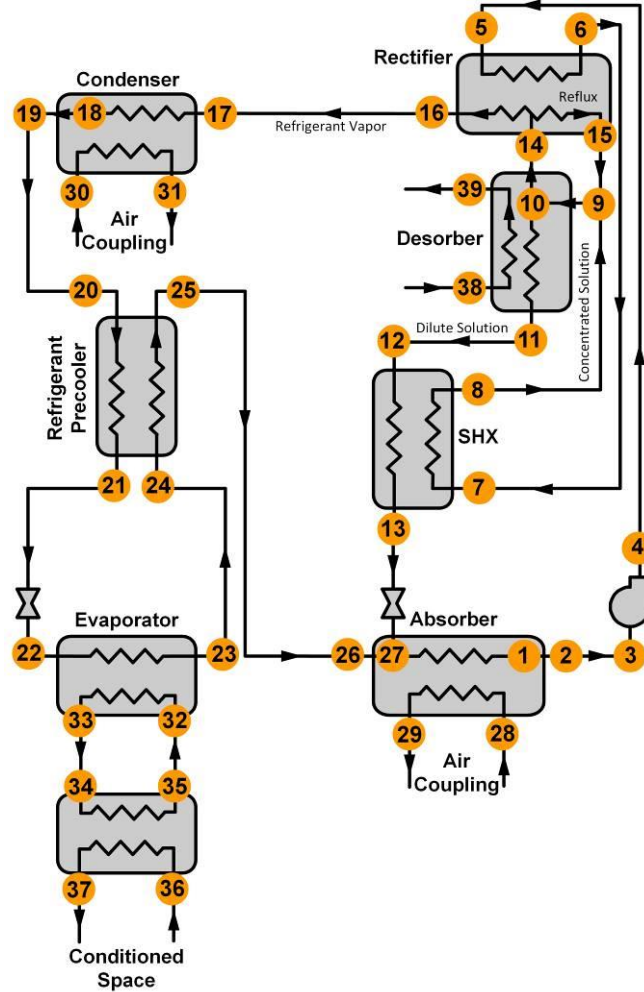
(32.22°C, 0.5 RH, 0.151 m<sup>3</sup> s<sup>-1</sup>) and outlet (19.5°C) air conditions for the conditioned space heat exchanger correspond to the cooling air return and supply temperatures, respectively, for the severe ambient field conditions under consideration in the present study. The hydronic fluid flowing in the conditioned space heat exchanger contains a 0.16 mass fraction of propylene glycol to prevent freezing, and is pumped at a rate of 0.0957 kg s<sup>-1</sup>. The flow rates of the propylene glycol-water solution internally and air externally are specified to maximize cooling without excessive pump and fan power consumption.

For an accurate prediction of total system efficiency, the pressure loss in the heat and mass exchangers should also be taken into account. Two-phase flow takes place in the absorber, condenser, and evaporator, which typically leads to large pressure losses. The pressure loss is expected to be small in the single-phase recuperative components (the refrigerant precooler and the solution heat exchanger). The selection of allowable pressure drop values in the heat and mass exchangers is based on a tradeoff between the benefits of high heat and mass transfer coefficients, penalties in saturation temperature drop due to pressure drop and the corresponding decrease in driving temperature difference, and pumping power. The absorber and evaporator pressure losses are each assumed to be 6.895 kPa. The pressure drop in the condenser is higher (13.79 kPa) because of the high-side pressure, the vapor inlet condition, and the small condenser volume (0.30 height × 0.51 length × 0.07 width) required for implementation in a mobile, small-capacity system.

Pump and fan efficiencies change with flow rate and differential pressure, which are likely to vary during heat pump operation; however, reasonable values are established

for cycle modeling at design conditions. The efficiency values do not affect the system cooling capacity or cooling  $COP$ . The values are used to estimate electricity consumption that reduces the overall system efficiency. The fan efficiency value (0.5) for the absorber and condenser is within a range of efficiencies (0.25 to 0.80) expected for fans with impeller diameters less than 0.51 m (Cermak *et al.*, 2013). The pump efficiency depends on the type and geometry of pump; a representative value of 0.9 was used here.

A schematic of the cycle modeled in this study is shown in *Figure 3.1*. A brief description of the cycle modeling procedure is provided here.



**Figure 3.1 Schematic for cycle modeling**

In the system under consideration here, the absorber and condenser reject heat to air in parallel. Although it would be possible to draw air in series across the absorber and condenser, the first component would receive air at 51.7°C while the second would receive the air exiting the first coil at a higher temperature with a non-uniform profile. In addition, the static pressure rise required across the fan would be the sum of the air differential pressures for both the absorber and condenser. In parallel flow across the two components, the air differential pressure is lower than in the case of air flow in series, but a higher flow rate is required to maintain the same air velocity with a larger air flow area. With the same fan or set of fans drawing air over both heat exchangers in parallel, any differences in flow area or air-side differential pressure between the absorber and condenser affect the distribution of the air flow between the two. Air is drawn in parallel in the present investigation to ensure that both components receive ambient air at 51.7°C. This helps ensure a high driving temperature difference between the inlet air and the incoming working fluid (absorber: 97.5°C; condenser: 75.0°C).

Throughout the cycle, it is estimated that there are no heat losses or pressure drops ( $\Delta h, \Delta P = 0$ ) in the plumbing between components. In the actual system, minor pressure losses and heat losses in the plumbing between components are inevitable; however, these factors are not expected to dramatically reduce performance with the use of appropriately sized plumbing and insulation. Conservative pressure drop values are specified for each heat and mass exchanger. Assumed component differential pressures are shown in *Table 3.1*.

Cycle modeling begins at the exit of the rectifier [16] at which point the refrigerant is assumed to be a saturated vapor ( $q = 1$ ) with an ammonia concentration of



0.998 at the high-side pressure. This pressure is established by a chosen *CAT* between the saturated refrigerant [18] and the outlet air temperature [31]. The mass flow rate can be initially assumed, but the actual value is established based on the required system cooling capacity and the enthalpy change in the evaporator. Because the refrigerant is a binary-mixture, three properties are used to determine all remaining fluid properties. The refrigerant flows into the condenser [17] and is condensed to a saturated liquid condition [18]. With temperature, concentration and quality known at the saturated liquid state, the high-side pressure is determined. The outlet air temperature of the condenser [31] can be predicted from the inlet air temperature [30] using an expected condenser duty. The *CAT* value is then used to predict the saturation temperature in the condenser [18] from the outlet air temperature [31]. Although for detailed design purposes, it is not adequate to use the *CAT* to characterize the performance of a cross-counterflow heat exchanger, this parameter is used in the initial cycle modeling for simplicity. For the air-coupled components (the absorber, condenser, and conditioned space heat exchanger), the effectiveness is later computed using the  $\varepsilon$ -*NTU* method, at which point, the *CAT* specification is removed. Conservative values of the air-side and solution-side pressure drop in the condenser are specified. The refrigerant then flows through the refrigerant pre-cooler [20, 21], where it rejects heat to the vapor stream exiting the evaporator.

After flowing through an isenthalpic expansion valve in which the pressure is reduced, the refrigerant enters the evaporator [22]. During vaporization, the refrigerant extracts heat from a propylene glycol-water loop [32, 33] that flows to the conditioned space heat exchanger [34, 35]. A *CAT* is assumed in the evaporator to determine the inlet refrigerant temperature [22] from the propylene-glycol water temperature exiting the

evaporator [33]. The low-side pressure can be determined at the evaporator inlet using the temperature, enthalpy, and concentration. Due to the presence of ammonia and water in the solution, the saturation temperature changes during the evaporation process. This changing saturation temperature, *i.e.*, the temperature glide, is limited to 2.5°C to prevent excessive rise in the refrigerant temperature, which would decrease the available cooling. The resulting outlet temperature establishes the evaporator outlet condition [23] completely. The 2.5°C temperature glide is based on a parametric study in which the effect of temperature glide on *COP* and cooling capacity was predicted. While a low temperature glide is desirable to achieve low cooling temperatures, a very small temperature glide would limit the evaporation that would be possible, leading to substantially incomplete evaporation. The specific value of the temperature glide is based on these tradeoffs. The effect of variation in evaporator temperature glide on system performance is discussed in 3.5.1. The initial estimate of the refrigerant mass flow rate is adjusted in subsequent modeling to ensure that the evaporator is providing the necessary cooling capacity. Based on these considerations, the inlet and outlet conditioned space heat exchanger air temperatures are 32.22°C and 19.35°C, respectively. The temperature of the propylene glycol-water entering the conditioned space heat exchanger [34] can be determined using the exiting air temperature [37] and a chosen *CAT* value. Upon exiting the evaporator, the refrigerant flows to the refrigerant pre-cooler [24] in which it receives heat from the high-side liquid phase [20] to [21].

The dilute solution enthalpy and mass flow rate entering the absorber [13] must be initially assumed. The dilute solution [13] and refrigerant [26] streams combine at the inlet of the absorber to form a fully mixed two-phase concentrated solution [27] stream.

Heat removal from this stream [27  $\rightarrow$  2] leads to absorption, change of phase to the liquid phase, and subcooling [2]. The rejected heat raises the ambient air temperature from [28] to [29].

The subcooled solution then flows through the pump [3, 4] to arrive at the high-side pressure. Heat is received from the refrigerant vapor in the rectifier [5, 6]. The concentrated solution exiting the rectifier flows to the solution heat exchanger [7, 8] in which it receives heat from the dilute solution leaving the desorber [12, 13]. A *CAT* value between the high-side inlet to the precooler [20] and the low-side outlet from the precooler [25] is used to specify the performance of the solution heat exchanger. The concentrated solution then combines [9] with the reflux exiting the rectifier [15] before entering the desorber [10]. The temperature of the exhaust gas exiting the desorber [39] can be determined from the inlet gas temperature [38] and the desorber duty. A *CAT* value in the desorber is specified to establish the solution temperature inlet [10] based on the exiting gas temperature [39]. The solution entering the desorber [10] is split into saturated vapor [14] and saturated liquid [11] streams due to desorption. Finally, the refrigerant vapor enters the rectifier [14] and is cooled to increase refrigerant purity [16] through the preferential condensation of a water-rich stream from the vapor [15]. The 3°C rectifier inequilibrium temperature accounts for the mass transfer resistance between the rectifier vapor inlet [14] and the exiting water-rich stream [15]. A species balance between the rectifier inlet [14] and outlet [15, 16] streams establishes the concentration of the exiting vapor [16]. At this point, the cycle is closed, and the initially assumed concentration (0.998) is replaced by the value calculated from the rectifier species balance, thus achieving model closure. Mass, species, and energy balances ( $\dot{m}$ ,  $h$ ,  $x$ ) are

ensured at all mixing [27, 9] and separating [10, 14] state points. The heat transfer rate is calculated in each internal flow component (desorber, rectifier, precooler, evaporator, solution heat exchanger) using the *LMTD* method and in each air-coupled component (condenser, absorber, conditioned space heat exchanger) using the  $\varepsilon$ -*NTU* method. The initially established *CAT* values in crossflow heat exchangers are replaced by  $\varepsilon$  values. From these *LMTD* and  $\varepsilon$  values, the *UA* values for all components are calculated. All baseline parameters (*UA* values, evaporator temperature glide, rectifier inequilibrium temperature, air and solution flow rates) are then varied in parametric studies, and their effects on system performance are investigated.

An overall energy balance of the heat pump ensures that the heat entering the solution in the desorber, pump, and conditioned space heat exchanger is equal to the heat removed from the absorber and condenser. The system cooling *COP* is calculated as the ratio of heat removed from the conditioned space to the heat provided by the diesel exhaust gas.

$$COP_{\text{cooling}} = \frac{Q_{\text{evap}}}{Q_{\text{des}}} = \frac{2.644 \text{ kW}}{4.876 \text{ kW}} = 0.542 \quad (3.1)$$

For this waste heat recovery application, it is also important to account for the parasitic electrical draws needed to run the solution pump, propylene glycol-water pump, control system, and air-coupled heat exchanger fans. Therefore, the overall *COP* is calculated as the ratio of the heat removed from the conditioned space to the desorber heat input and the parasitic power requirements.

$$COP_{\text{overall}} = \frac{Q_{\text{evap}}}{Q_{\text{des}} + Q_{\text{consumed}}} = \frac{2.644 \text{ kW}}{4.876 + 1.193 \text{ kW}} = 0.436 \quad (3.2)$$

**Table 3.2 Electrical power consumption in baseline cycle model ( $F_{load} = 3.18$ )**

Component	Expression	$Q$ (W)	$Q_{load}$ (W) = $F_{load}Q$
Absorber Fan	$Q_{fan,abs} = \frac{\Delta P_{fan,abs} \cdot \dot{V}_{air,abs}}{\eta_{fan} \cdot \eta_{motor}}$	110	351
Condenser Fan	$Q_{fan,cond} = \frac{\Delta P_{fan,cond} \cdot \dot{V}_{air,cond}}{\eta_{fan} \cdot \eta_{motor}}$	110	351
Controls	$Q_{controls} \approx 75 \text{ W}$	75	239
PG-Water Pump	$Q_{motor,PG} = \frac{\dot{V}_{PG-H_2O} \cdot \Delta P_{PG,pump}}{\eta_{pump,PG} \cdot \eta_{motor,PG}}$	37	119
Solution Pump	$Q_{motor,soln} = \frac{\dot{m}_3 v_3 (P_4 - P_3)}{\eta_{pump,soln} \cdot \eta_{motor,soln}}$	42	135
<b>Total Electrical Power Consumption (<math>Q_{consumed}</math>):</b>			<b>1193</b>

The system in consideration here is a compact and mobile system that can be easily implemented to utilize waste heat from a diesel generator. As a result, it is important to minimize the electrical draw of the system, which requires additional infrastructure. To appropriately weigh the cost of the electrical inputs of the system, each predicted electrical input is multiplied by a site-to-source conversion factor ( $F_{load} = 3.18$ ) (Ryan *et al.*, 2010) before being added to the desorber heat duty in the calculation of the overall *COP*. This conversion factor approximates the thermodynamic penalty of converting energy from a primary energy source to upgraded electricity. A breakdown of the total electrical power required by the system,  $Q_{consumed}$ , is shown in *Table 3.2*.

The baseline cycle model discussed above predicts the size required (*UA*) for each heat/mass exchanger along with the predicted inlet and outlet fluid conditions. *Table 3.3* shows the resulting capacity and *UA* values for the system components based on the specified *CAT* and  $\epsilon$  inputs. Also shown in *Table 3.3* is the resulting cooling duty and overall *COP* values.

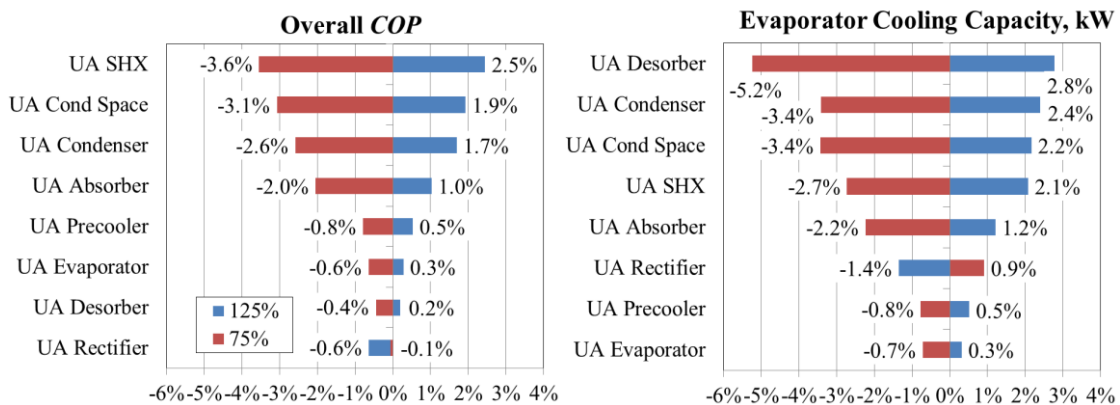
**Table 3.3 Component heat duties and  $UA$  values for baseline cycle**

<b>Component</b>	<b><math>Q</math> (kW)</b>	<b><math>UA</math> (kW K<sup>-1</sup>)</b>	<b><math>\varepsilon</math> (-)</b>	<b><math>CAT</math> (K)</b>
Condenser	2.45	0.179	0.52	-
Precooler (RHX)	0.34	0.025	-	4.7
Evaporator	2.64	0.846	-	3.0
Conditioned Space Heat Exchanger	2.64	0.277	0.64	-
Absorber	5.10	0.362	0.89	-
Rectifier	1.51	0.044	-	18.3
Desorber	4.88	0.052	-	70.0
Solution Heat Exchanger (SHX)	2.18	0.074	0.93	-
<b>Flow Rates</b>	<b><math>\dot{m}</math> (kg s<sup>-1</sup>)</b>		<b><math>\dot{V}</math> (m<sup>3</sup> s<sup>-1</sup>)</b>	
Concentrated Solution	0.008		-	
Absorber Air	-		0.354 m <sup>3</sup> s <sup>-1</sup>	
Condenser Air	-		0.354 m <sup>3</sup> s <sup>-1</sup>	
		<b><math>COP_{cooling}</math></b>	<b>0.542</b>	
		<b><math>COP_{overall}</math></b>	<b>0.436</b>	

### 3.5.1 Parametric Analysis

To determine the modeling parameters that are most influential in system performance, a parametric study is conducted in which input parameters are adjusted to  $\pm 25\%$  of their baseline values. The resulting system cooling capacity and overall  $COP$  are recorded, and adjustments are made based on these results to optimize system performance. Parameters considered in these analyses include component  $UA$  values, temperature glide, and solution and air-side flow rates. “Tornado” diagrams showing the impact of heat exchanger size adjustments on cooling duty and overall  $COP$  are shown in *Figure 3.2*.

The components in *Figure 3.2* are shown in order of their influence on the cycle overall *COP* (left) and evaporator cooling capacity (right). For example, an increase in the size of the solution heat exchanger (SHX) would most effectively increase system *COP* while increasing the size of the desorber would most effectively increase overall cooling capacity. Although it would be ideal to substantially increase all heat transfer areas for improved performance, system volume and weight would increase beyond reasonable limits for the application. The corresponding capital costs for system fabrication would also be prohibitive. It should be noted that increasing the size of the rectifier would decrease the overall *COP* while reducing total cooling capacity. This degradation in performance is a result of the reduced flow rate of the refrigerant stream exiting the rectifier if the size is increased further. An excess of cooling increases the subcooled reflux flow rate and decreases the exiting refrigerant vapor flow rate. Despite increased refrigerant purity, the decrease in refrigerant flow rate adversely affects system performance. With the exception of the rectifier, an increase in the size of any heat/mass exchanger would make a smaller impact on system performance than an equivalent

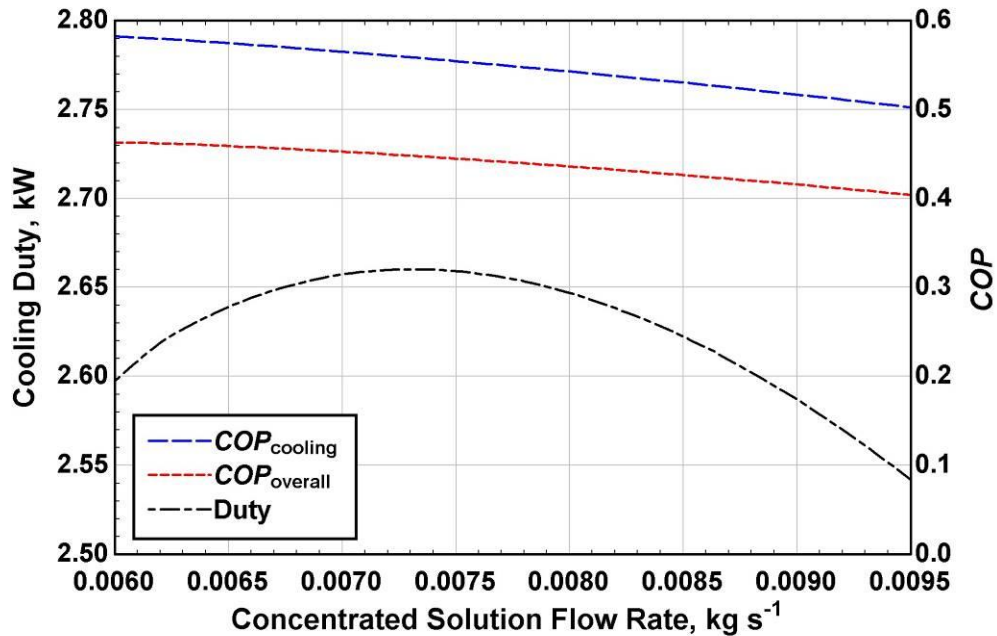


**Figure 3.2 “Tornado” diagrams of overall *COP* (left) and cooling capacity (right) with variations in heat exchanger size (UA)**

reduction in component size. This demonstrates the expected diminishing benefits of further increases in component heat transfer areas beyond the chosen values.

A parametric study is also conducted on the effects of variations in air flow rates in the absorber and condenser, the propylene glycol-water flow rate in the evaporator, and the concentrated solution flow rate on system performance. Increases in the air flow rate in the absorber and condenser, as well as increases in the hydronic pump speed in the evaporator result in increases in system cooling capacity and a reduction in overall *COP* as a result of increased fan and pump power consumption. Air flow rates in the absorber were varied between 0.266 and 0.443 m<sup>3</sup> s<sup>-1</sup>, resulting in increased cooling capacity (2.629 to 2.654 kW) and reduced overall *COP* (0.440 to 0.431). Over the same range, condenser air flow rates yielded cooling capacities ranging from 2.622 kW to 2.657 kW and overall *COP* values from 0.439 to 0.431. Increasing the hydronic pump flow rate from 7.10×10<sup>-5</sup> m<sup>3</sup> s<sup>-1</sup> to 1.18×10<sup>-4</sup> m<sup>3</sup> s<sup>-1</sup> increased cooling capacity (2.620 to 2.656 kW) and decreased overall *COP* (0.434 to 0.435). These effects are relatively insignificant compared to the effect of concentrated solution flow rate on system performance (*Figure 3.3*).





**Figure 3.3 Cooling duty (left axis) and  $COP$  (right axis) as a function of concentrated solution flow rate**

Increases in the solution flow rate from the baseline value decrease both the cooling and overall  $COP$ . Higher solution flow rates lead to a greater heat input into the desorber for an equivalently sized component, but the increase in refrigerant generation and cooling duty is not commensurately higher. This leads to the decrease in overall system efficiency. The cooling capacity, however, indicates an optimal range of concentrated solution flow rates. When the concentrated solution flow rate is decreased, the temperature of the solution exiting the desorber increases, and the refrigerant fraction increases. The higher temperature of the solution increases the water fraction in the desorbed vapor, which increases the rectifier load. The resulting lower refrigerant purity and the lower concentrated solution flow rate decrease the cooling capacity. This effect is demonstrated by the drop in cooling capacity predicted when  $\dot{m}_{conc} < 0.007 \text{ kg s}^{-1}$  in *Figure 3.3*. On the other hand, high concentrated solution flow rates ( $> 0.008 \text{ kg s}^{-1}$  in

*Figure 3.3*) result in a lower desorber outlet temperature and the generation of less refrigerant vapor. The input heat is used more to sensibly heat the solution rather than to desorb vapor. This reduction in refrigerant flow reduces the amount of heat that can be received from the conditioned space by the evaporator. The parametric study also includes the effect of adjustments in evaporator temperature glide and inequilibrium temperatures in the desorber and rectifier. Temperature glide values from 1.88 to 3.13°C result in reducing cooling capacity values from 2.656 to 2.631 kW and overall *COP* values from 0.437 to 0.434. The cooling capacity is predicted to decrease at temperature glides below 1°C as a result of the reduced utilization of the enthalpy of vaporization due to incomplete evaporation. Increasing desorber inequilibrium temperature values from 7.5 to 12.5°C results in reduction in cooling capacity (2.650 to 2.638 kW) and overall *COP* (0.439 to 0.432). Increasing rectifier inequilibrium temperature had negligible impact on cooling capacity (+0.02%) and overall *COP* (−0.05%).

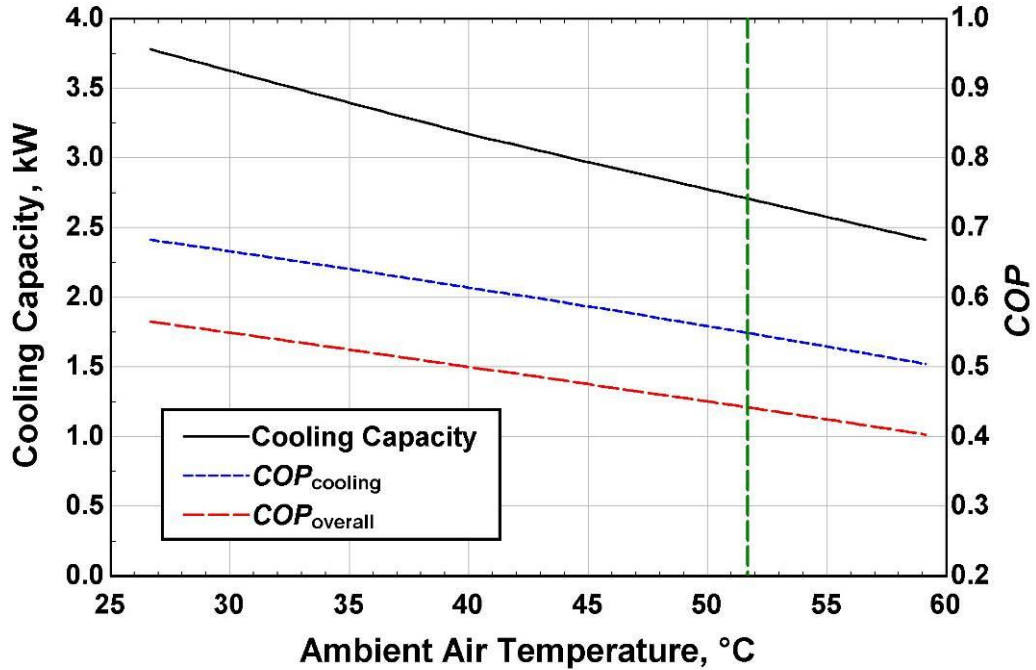
**Table 3.4 Component heat duties and  $UA$  values for optimized cycle**

<b>Component</b>	<b><math>Q</math> (kW)</b>	<b><math>UA</math> (kW K<sup>-1</sup>)</b>	<b><math>\varepsilon</math> (-)</b>	<b><math>CAT</math> (K)</b>
Condenser	2.53	<b>0.188 (5%↑)</b>	0.54	
Precooler (RHX)	0.34	0.025	-	5.1
Evaporator	2.71	0.846		3.0
Conditioned Space Heat Exchanger	2.71	<b>0.299 (8%↑)</b>	0.66	-
Absorber	5.15	<b>0.380 (5%↑)</b>	0.90	-
Rectifier	1.50	0.044	-	18.4
Desorber	4.94	<b>0.055 (5%↑)</b>	-	68.9
Solution Heat Exchanger (SHX)	2.20	0.074	-	5.9
<b>Flow Rates</b>	<b><math>\dot{m}</math> (kg s<sup>-1</sup>)</b>		<b><math>\dot{V}</math> (m<sup>3</sup> s<sup>-1</sup>)</b>	
Concentrated Solution	0.008		-	
Absorber Air	-		0.354 m <sup>3</sup> s <sup>-1</sup>	
Condenser Air	-		0.354 m <sup>3</sup> s <sup>-1</sup>	
		<b><math>COP_{cooling}</math> 0.549</b>		
		<b><math>COP_{overall}</math> 0.442</b>		

Based on the results of the parametric study, changes are made to the component sizes and concentrated solution flow rate to optimize system performance. The  $UA$  values of the desorber, condenser, absorber, and conditioned space heat exchanger are increased slightly to improve system cooling capacity and efficiency. Compared to the baseline model, the adjustments result in a 2.5% increase in cooling capacity (2.634 to 2.710 kW) and 1.3% and 1.4% increases in cooling  $COP$  (0.542 to 0.549) and overall  $COP$  (0.436 to 0.442) values, respectively. Values selected for the optimized cycle based on the parametric study are shown in *Table 3.4*. Bolded  $UA$  values demonstrate adjustments that were made to heat exchanger heat transfer area.

### 3.5.2 Ambient Temperature Variation

A parametric analysis on the effect of ambient air temperature on system performance is also conducted. *Figure 3.4* shows a plot of the system cooling capacity and *COP* values as a function of ambient air temperature.



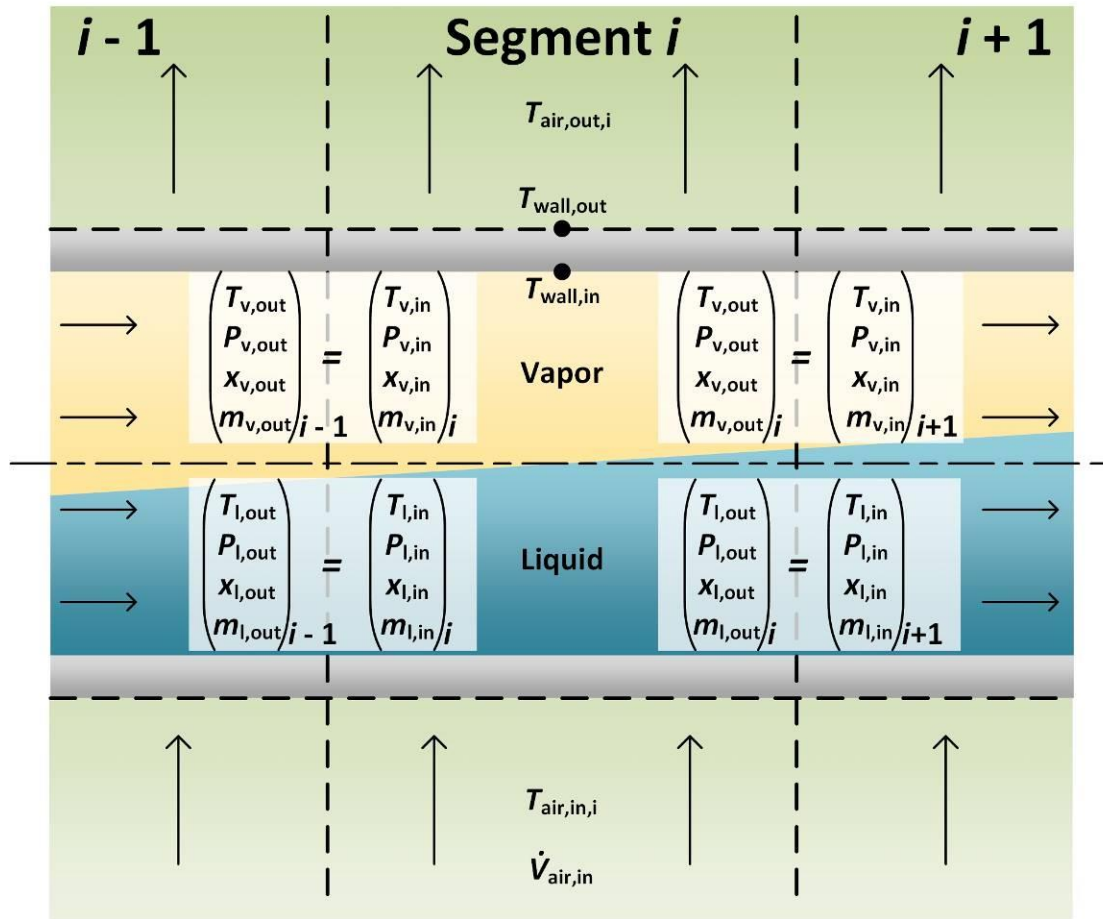
**Figure 3.4 Cooling duty (left axis) and *COP* (right axis) as a function of ambient air temperature**

As expected, the cooling duty of the heat pump and the efficiency decreases with increasing ambient temperature. While the design condition was an ambient temperature of 51.7°C, if the system were operated at more typical residential ambient conditions of an outdoor temperature of 35°C, the cooling capacity and overall *COP* would increase from 2.710 to 3.396 kW and from 0.442 to 0.525, respectively. The operating conditions for the absorber obtained from this system model were used to design the absorber using a segmental heat and mass exchange model described next.

### 3.6 Absorber Modeling

A segmental numerical model is developed in the *Engineering Equation Solver (EES)* software platform to predict the performance of the air-coupled absorbers. Three absorber configurations are considered, including two conventional round-tube corrugated-fin air coils with carbon steel tubing and one prototype absorber consisting of a dense array of small diameter unfinned stainless steel tubes. All three designs feature heat rejected to air in crossflow from round tubes. The heat and mass transfer analyses for the conventional and prototype absorbers are similar, with adjustments made for differences in tube geometry, solution flow pattern, and air-side heat transfer and pressure drop characteristics.

For air-coupled heat exchangers, the heat transfer coefficient on the air side is typically constant across the length of the tube, but the heat and mass transfer processes vary dramatically for fluids undergoing phase change. During the condensation process, there is a transition in flow regimes that affects the liquid-vapor interface available for heat transfer (and mass transfer in the case of mixtures). Additionally, as the void fraction of the solution decreases, the reduction in shear force between the liquid and vapor increases the internal thermal resistance. In absorbers, concentration gradients in both the liquid and vapor phases and the respective resistances affect transport across the interface. Significant changes in phase distributions and velocities, and the temperature gradients in the binary mixture necessitate a discretized approach to the modeling of phase change. The modeling effort here divides the heat exchanger into several segments to properly account for the variation in the heat and mass transfer processes during absorption. *Figure 3.5* shows a representative segment.

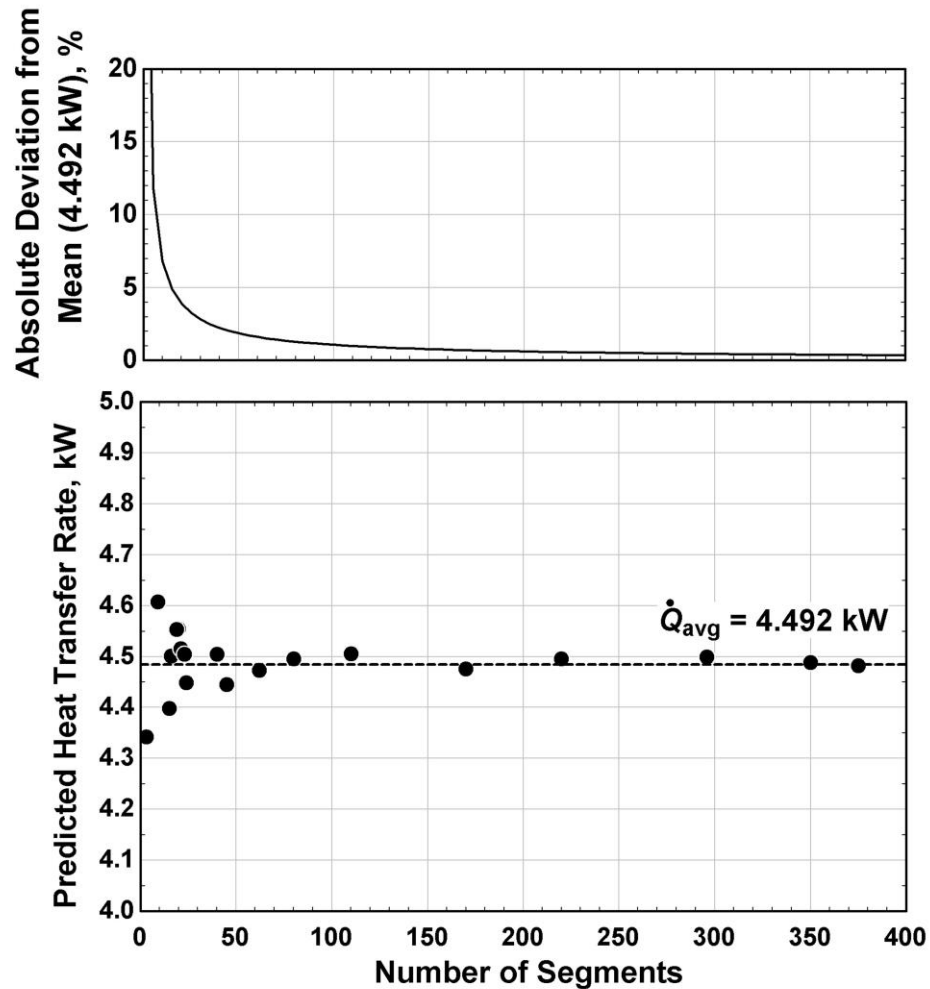


**Figure 3.5 Schematic of individual absorber segment**

A uniform length for each segment, or the total number of segments into which the heat exchanger should be divided, is specified. Initial values are assumed for the fluid outlet properties, and the resulting average properties are used in the prediction of the heat and mass transfer in a given segment. Iteration allows for the initially assumed output conditions to be adjusted such that a solution for all parameters is reached. The calculated outlet conditions are set as the inlet conditions in the subsequent segment, and the process continues along the length of the heat exchanger.

A grid refinement study is used to determine an appropriate number of segments to ensure computational efficiency without significantly reducing modeling accuracy. To

determine the sufficient number of segments, the heat transfer rate in the absorber is predicted using 3 to 375 segments (*Figure 3.6*). For the 394-FPM absorber, the predicted heat transfer rate asymptotically approaches a mean value of 4.492 kW with an increasing number of segments. Low numbers of segments ( $N_{sg} < 25$ ) result in an over- or under-prediction of absorber heat transfer rate (−14% to 11%). *Figure 3.6* also shows the average absolute deviation from this mean (4.492 kW) as a function of number of segments. The approximate error in absorber duty predictions is less than 1% when the number of segments is larger than 105. In the present study, 200 or more segments are used during modeling, corresponding to errors smaller than 0.6%.



**Figure 3.6 Predicted heat transfer rate (bottom) and average absolute deviation from mean (top) as a function of the number of segments in the 394-FPM absorber**

Ammonia-water mixture properties required for the heat and mass exchange calculations are determined using the procedure outlined by Nagavarapu (2012). A brief summary is provided here. Thermodynamic properties ( $C_p$ ,  $h$ ,  $P$ ,  $q$ ,  $T$ ,  $v$ ) are determined in the *Engineering Equation Solver* (EES) software package using ammonia-water mixture correlations from Ibrahim and Klein (1993). These correlations rely on the combination of independent pure component properties. Transport vapor properties ( $D_v$ ,  $k_v$ ,  $\mu_v$ ), for pure components are determined from the Chapman-Enskog kinetic theory



(Mills, 1999), and the procedure of Wilke (1950) is used for vapor properties of mixtures. Liquid properties,  $k$ ,  $\mu$ , and  $\sigma$  are determined from empirical correlations of Meacham (2002) based on graphical data from Herold *et al.* (1996). Finally, The liquid diffusion coefficient ( $D_l$ ) is based on an expression from Frank *et al.* (1996) using the concentration and temperature of the solution. A detailed discussion of all ammonia-water property calculations with equations is provided in Nagavarapu (2012).

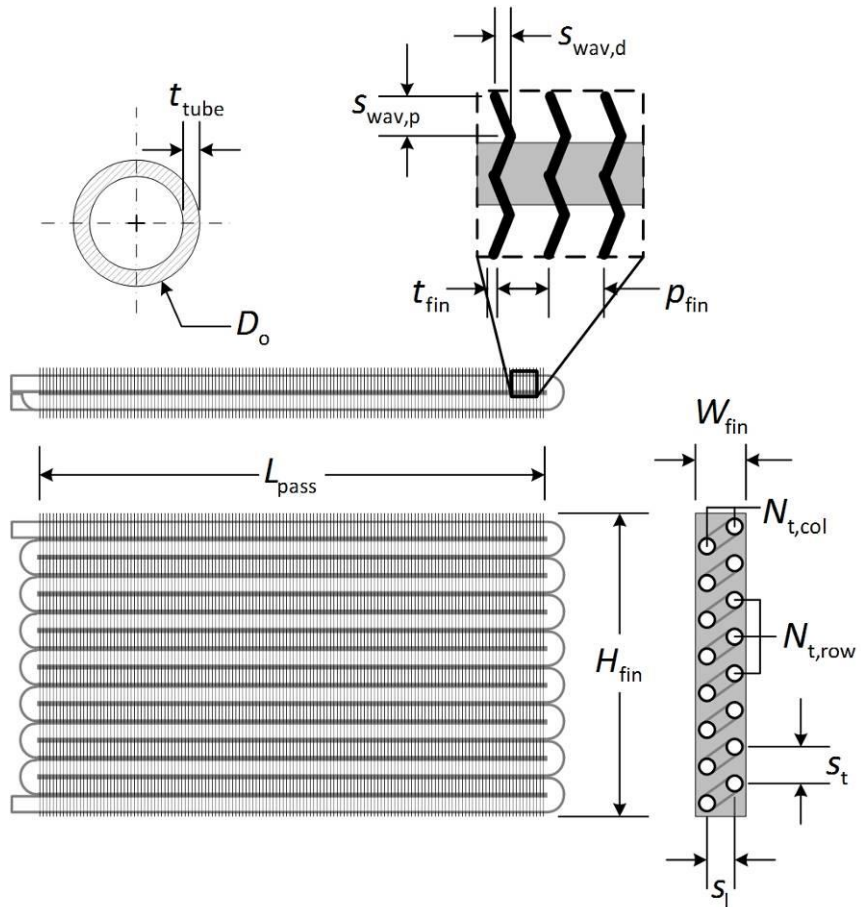
A discussion of the modeling of the two absorber designs follows. Detailed sample calculations for the segmental analyses can be found in Appendix A.

### **3.6.1 Round-Tube Corrugated-Fin Segmental Modeling**

The conventional absorber consists of one 13.41 m long, 13.4 mm inner diameter tube that serpentine over a  $0.61 \times 0.42$  m flow area. The flow of the solution is therefore not divided into multiple parallel paths but remains contained in this single tube. The bundle is oriented horizontally in 2 columns of 11 rows (22 passes) in a staggered arrangement with tight U-bends at the end of each pass. Corrugated, or wavy, fins are press-fitted onto the tubes at a specified spacing. The wavy fin surface enhances air-side heat transfer. A schematic of the conventional absorbers is shown in *Figure 3.7*, and inlet conditions are provided in *Table 3.5*. Geometric inputs for the 394-FPM absorber are also provided in *Table 3.5*.

The sizing of all air-coupled absorbers is based on their predicted performance at the inlet conditions specified from cycle modeling of the heat pump system. However, the testing of the absorbers is conducted in a single-pressure test facility that enables more direct control of absorber conditions and a greater range of conditions than those possible in a two-pressure heat pump system. Therefore, the inlet conditions used during

testing differ from those specified in cycle modeling. For direct comparison of experiments to modeling, the inlet conditions used in modeling are the same as those used during testing in the single-pressure test facility. As shown in *Table 3.5*, the refrigerant vapor inlet concentration is lower than the value specified in cycle modeling ( $0.877 < 0.988$ ). Providing a 0.988 concentration vapor stream would require a rectifier, condenser and evaporator in the system, which is not practical for dedicated absorber measurements. Similarly, the vapor inlet temperature, without the presence of the evaporator and refrigerant pre-cooler in the system, is higher than the value specified in cycle modeling ( $97.6^{\circ}\text{C} > 57.2^{\circ}\text{C}$ ). The absorber is, however, tested at the same overall cooling duty as the value obtained from cycle modeling (5.15 kW). A detailed comparison of the heat pump and single-pressure inlet conditions with discussion is presented in Chapter 4.



**Figure 3.7 Schematic of round-tube corrugated-fin absorbers**

**Table 3.5 Inlet conditions**

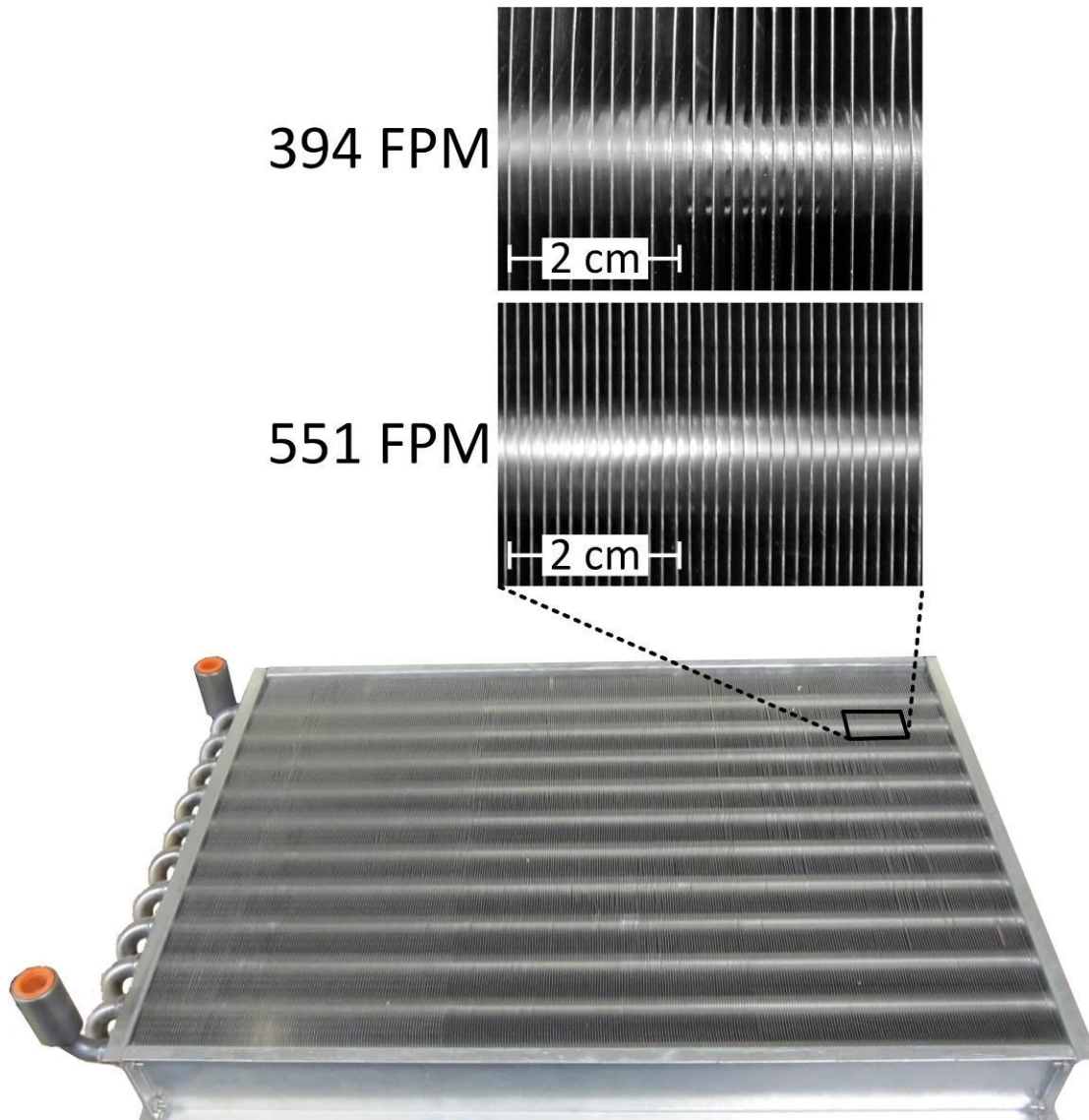
<b>Refrigerant Vapor Inlet Conditions</b>	
$T_{v,in}$ (°C)	97.60
$P_{v,in}$ (kPa)	591.8
$x_{v,in}$ (-)	0.877
$\dot{m}_{v,in}$ (kg s <sup>-1</sup> )	$2.32 \times 10^{-3}$
<b>Dilute Solution Inlet Conditions</b>	
$T_{l,in}$ (°C)	97.49
$P_{l,in}$ (kPa)	591.8
$x_{l,in}$ (-)	0.235
$\dot{m}_{l,in}$ (kg s <sup>-1</sup> )	$5.68 \times 10^{-3}$
<b>Inlet Air Conditions</b>	
$\dot{V}_{air}$ (m <sup>3</sup> s <sup>-1</sup> )	0.425
$T_{air,in}$ (°C)	51.67
$P_{air,in}$ (kPa)	101.3
$RH_{air,in}$ (-)	0.18

**Geometric inputs**

<b>Tube-Side Geometry</b>	
$L_{sg}$ (m)	0.025
$D_o$ (m)	0.016
$t_{tube}$ (m)	$1.25 \times 10^{-3}$
$L_{pass}$ (m)	0.610
$N_{t,row}$ (-)	11
$N_{t,col}$ (-)	2
$s_t$ (m)	0.038
$s_1$ (m)	0.033
$\epsilon_{rough}$ (m)	$1.0 \times 10^{-5}$
Tube material	Carbon steel
<b>Air-Side Geometry</b>	
$H_{fin}$ (m)	0.419
$W_{fin}$ (m)	0.066
$t_{fin}$ (m)	$2.41 \times 10^{-4}$
$p_{fin}$ (m)	$2.54 \times 10^{-3}$ $1.81 \times 10^{-3}$
$s_{wav,d}$ (m)	$2.79 \times 10^{-3}$
$s_{wav,p}$ (m)	$8.20 \times 10^{-3}$
Fin material	Aluminum

The round-tube corrugated-fin absorbers investigated here are determined to be the most effective and compact conventional air coils that fit within the volume and pressure drop requirements of the mobile heat pump application under consideration here. Corrugated fins are selected based on the work by Garimella *et al.* (1997) in which wavy (*i.e.*, corrugated) fins are predicted to transfer more heat than plain, lanced, and annular fins in the same mass and pressure drop budgets. The segmental model is used to determine the various geometric features (tube diameter, tube length, fin density). The

designed heat exchanger was fabricated by Super Radiator Coils. A photograph of one of the round-tube corrugated-fin absorbers is shown in *Figure 3.8*.



**Figure 3.8 Photographs of 551-FPM round-tube corrugated-fin absorber and the 394-FPM and 551-FPM fin densities**

Two conventional heat exchangers with different fin densities are chosen: 394 and 551 Fins Per Meter (FPM) pressed onto a round tube bank. All other geometric features, including air-side face area, are kept constant for these two heat exchangers.

For simplicity, the following discussion focuses on the 394-FPM corrugated-fin absorber. The analysis is identical for the 551-FPM air coil with the appropriate fin pitch adjustment.

The prediction of absorption in the conventional heat exchangers depends on various heat transfer and pressure drop correlations from the literature. Several factors are considered in the choice of which correlations are most relevant for the present heat exchangers, such as the range of applicability, the breadth of the database used in developing the correlation, and the validation of the correlations by subsequent investigations. These correlations, along with the recommended ranges of application, are shown in *Table 3.6*. The reasons for the selection of these heat transfer and pressure drop coefficients over others are discussed in the following discussion as each aspect of the modeling is introduced.

**Table 3.6 Round-tube corrugated-fin absorber modeling correlations**

	<b>Correlation</b>	<b>Applicable Range</b>	<b>Present Conditions</b>	<b>Notes</b>
<b>Tube-Side Heat Transfer</b>	Shah (1979)	$11 \leq G_{sol} \leq 211 \text{ kg m}^{-2} \text{ s}^{-1}$ $0.5 \leq Pr_1 \leq 13$ $0.007 \leq D_i \leq 0.04 \text{ m}$	$G_{sol} = 56.85 \text{ kg m}^{-2} \text{ s}^{-1}$ $Pr_1 = 2.15 - 4.26$ $D_i = 0.014 \text{ m}$	Horizontal and vertical, circular
<b>Tube-Side Pressure Drop</b>	Friedel (1979)	Adiabatic, air-water, air-oil, steam, R11, R12, R22, R113, N <sub>2</sub> , NH <sub>3</sub> , Ne, Na	Condensing absorbing NH <sub>3</sub> -H <sub>2</sub> O	Horizontal and vertical, circular and rectangular
<b>Air-Side Heat Transfer</b>	Kim <i>et al.</i> (1997b)	$500 \leq Re_{D,Kim} \leq 6000$ $1 \leq N_{t,col} \leq 4$ $1.16 \leq (s_t/s_1) \leq 1.33$ $0.15 \leq (s/D_c) \leq 0.33$ $1.44 \leq (s_{wav,p}/s_{wav,d}) \leq 10.0$ $0.23 \leq (s_{wav,d}/s) \leq 1.21$	$Re_{D,Kim} = 2518 - 2629$ $N_{t,col} = 2$ $(s_t/s_1) = 1.16$ $(s/D_c) = 0.10 - 0.14$ $(s_{wav,p}/s_{wav,d}) = 2.94$ $(s_{wav,d}/s) = 1.21 - 1.78$	Indicated range is for staggered tube arrangements
<b>Air-Side Pressure Drop</b>	$\Delta P_t$ : Zukauskas <i>et al.</i> (1968) $\Delta P_{f,flat}$ : Gray and Webb (1986) $\Delta P_{f,wavy}$ : Webb and Gupte (1990)	$1 \leq N_{t,col} \leq 8$ $1.97 \leq (s_t/D_o) \leq 2.55$ $1.70 \leq (s_1/D_o) \leq 2.58$ $0.08 \leq (s/D_o) \leq 0.64$	$N_{t,col} = 2$ $(s_t/D_o) = 2.4$ $(s_1/D_o) = 2.08$ $(s/D_o) = 0.10 - 0.14$	Factor of 1.9 used to predict wavy fin pressure drop from flat fin pressure drop

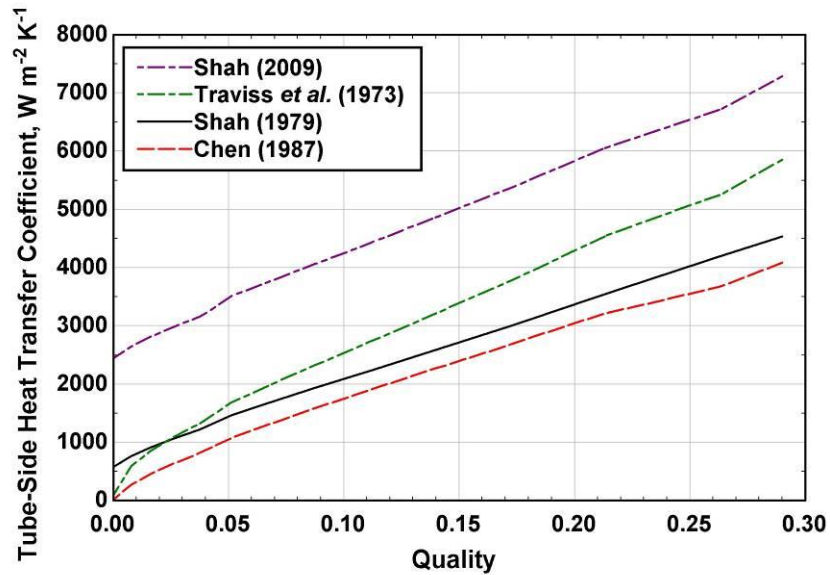
### **3.6.1.1. Tube-Side Heat Transfer**

The heat transfer in any given segment is a combination of the sensible heat removed from the vapor and the latent heat removed from the condensation of the ammonia-water solution. The concentration of ammonia in the vapor is higher near the liquid-vapor interface than in the bulk vapor flow due to the preferential condensation of water, the less volatile component. The result is a concentration gradient in the vapor that lowers the interface temperature, thereby limiting the tube-side heat transfer. The concentration gradient must be traversed across a mass transfer resistance that impedes the heat transfer process. The heat and mass transfer are interrelated and cannot be accounted for independently; however, they are presented sequentially here. First, the determination of tube-side heat transfer is discussed. Then, the method used to predict the effect of the concentration gradient on the heat transfer process is discussed in the section pertaining to mass transfer (Section 3.6.1.6).

The correlation from Shah (1979) was used in the present modeling of tube-side heat transfer. This heat transfer correlation is commonly used in industry for condensation of a variety of refrigerants in horizontal, vertical, and inclined round tubes. The correlation is based on 474 data points with a large range of saturation temperatures, reduced pressures, Reynolds numbers, and heat fluxes (Shah, 1979). It is important to note that the correlation does not predict condensation in mixtures, and no data from the condensation of ammonia are used in its formulation. One of the first widely used condensation heat transfer correlations was developed by Traviss *et al.* (1973) for annular flow (Carey, 1992). However, annular flow is not expected for substantial regions of the heat exchanger at the present flow conditions. Chen *et al.* (1987) developed a



comprehensive film condensation correlation from analytical and theoretical results from previous investigations. Their predicted heat transfer coefficient for horizontal tubes is independent of gravity (Carey, 1992), and they stated that their correlation may be inaccurate for cocurrent flow near the inlet and outlet of the tube (Chen *et al.*, 1987). Shah provided a revised heat transfer correlation with a wider range of applicability ( $4 < G_{\text{sol}} < 820 \text{ kg m}^{-2} \text{ s}^{-1}$ ,  $0.002 \text{ m} < D_i < 0.049 \text{ m}$ ) in 2009, but the predictions from this correlation are well above those of the other correlations considered. The heat transfer coefficient predicted by Shah (1979) applied to the present absorber design is shown in *Figure 3.9*, along with the other condensation correlations for comparison (Traviss *et al.*, 1973; Chen *et al.*, 1987; Shah, 2009).



**Figure 3.9 Tube-side heat transfer coefficients predicted for 394-FPM corrugated-fin absorber**

For the present application, the two-phase mixture enters the absorber at a nominal quality of 0.29 and a mass flux of  $56.9 \text{ kg m}^{-2} \text{ s}^{-1}$ . The heat transfer coefficient predicted

by all these correlations decreases significantly with decreasing quality as a result of transitions into less favorable flow regimes.

The Shah (1979) correlation is based on a multiplier applied to the liquid-only heat transfer coefficient from Dittus and Boelter (1930) in terms of the quality and reduced pressure.

$$\alpha_{lo} = 0.023 \frac{k_l}{D_i} \left( \frac{G_{sol} D_i}{\mu_l} \right)^{0.8} Pr_l^{0.4} \quad (3.3)$$

$$\alpha_{Shah} = \alpha_{lo} \left[ (1 - q_{sol})^{0.8} + \frac{3.8 q_{sol}^{0.76} (1 - q_{sol})^{0.04}}{(P_{sol}/P_{crit})^{0.38}} \right] \quad (3.4)$$

The fluid properties used above ( $k_l, \mu_l, Pr_l$ ) are at the average liquid conditions across the segment, determined through iteration. The solution mass flux is  $G_{sol}$ , while  $q_{sol}$  refers to the average quality of the solution across the segment. The critical pressure for ammonia-water is approximated as a molar average of the critical pressures of ammonia and water.

$$P_{crit} = x_{mol,NH_3} P_{crit,NH_3} + x_{mol,H_2O} P_{crit,H_2O} = 17396 \text{ kPa} \quad (3.5)$$

In many cases, the design conditions modeled results in the solution reaching a saturated liquid state before the outlet of the absorber. In the subcooled region that followed, the Churchill (1977 (b)) correlation is used to predict the single-phase heat transfer coefficient in the solution.

### **3.6.1.2. Tube-Side Flow Regime**

The flow regime map proposed by Taitel and Dukler (1976) is commonly used to predict the evolving flow pattern in horizontal two-phase flow. The Martinelli parameter,

based on the liquid and vapor pressure gradients along the direction of flow, is plotted on the x-axis.

$$\left(\frac{dP}{dz}\right)_l = \frac{-2f_l G_{sol}^2 (1-q_{sol})^2}{\rho_l D_i} \quad (3.6)$$

$$\left(\frac{dP}{dz}\right)_v = \frac{-2f_v G_{sol}^2 q_{sol}^2}{\rho_v D_i} \quad (3.7)$$

$$X_{\text{Martinelli}} = \sqrt{\frac{(dP/dz)_l}{(dP/dz)_v}} \quad (3.8)$$

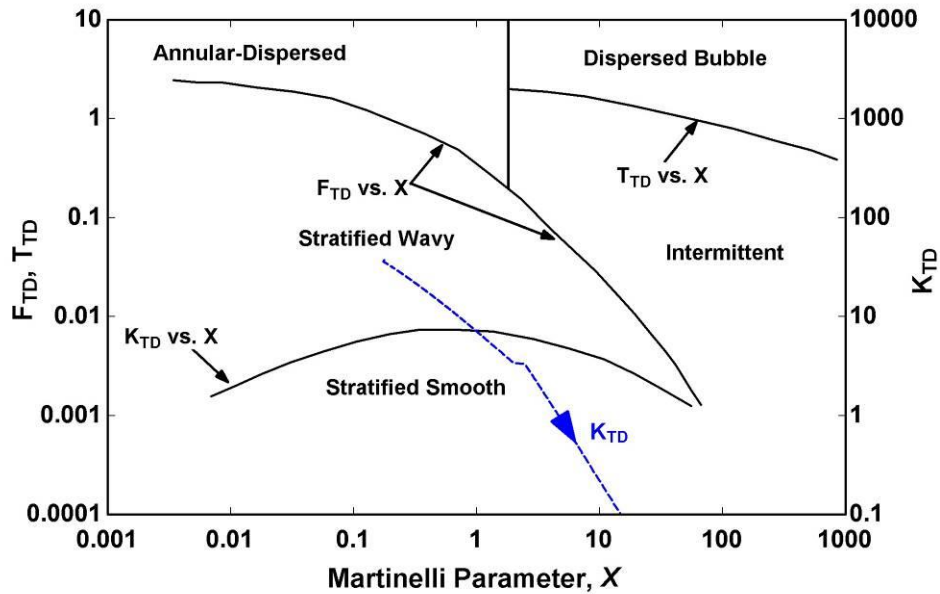
The Taitel-Dukler parameters  $K_{\text{TD}}$ ,  $F_{\text{TD}}$ , and  $T_{\text{TD}}$  are used to identify the transition between the stratified-to-wavy-flow, wavy-annular/wavy-intermittent flow, and bubbly-to-intermittent flow regimes, respectively.

$$K_{\text{TD}} = \sqrt{\frac{\rho_v j_v^2 j_l}{v_l (\rho_l - \rho_v) D_i g}} \quad (3.9)$$

$$F_{\text{TD}} = \sqrt{\frac{\rho_v j_v^2}{(\rho_l - \rho_v) D_i g}} \quad (3.10)$$

$$T_{\text{TD}} = \sqrt{\frac{-dP/dz_l}{(\rho_l - \rho_v) g}} \quad (3.11)$$

A view of the three parameters plotted on the Taitel-Dukler map during absorption in the present case indicates that  $K_{\text{TD}}$ , the stratified-to-wavy-flow parameter, is relevant for the round-tube corrugated-fin design in consideration. This transition from stratified wavy to stratified smooth flow during absorption is shown in *Figure 3.10*.



**Figure 3.10 Taitel-Dukler (1976) flow regime map for round tube 394-FPM corrugated-fin absorption**

The Taitel-Dukler flow regime map indicates that the solution is in the stratified regime throughout absorption. The relatively low vapor-liquid shear is expected to result in low heat transfer rates. Absorption that begins in the annular flow regime, on the other hand, would experience high interfacial area and vapor-liquid shear.

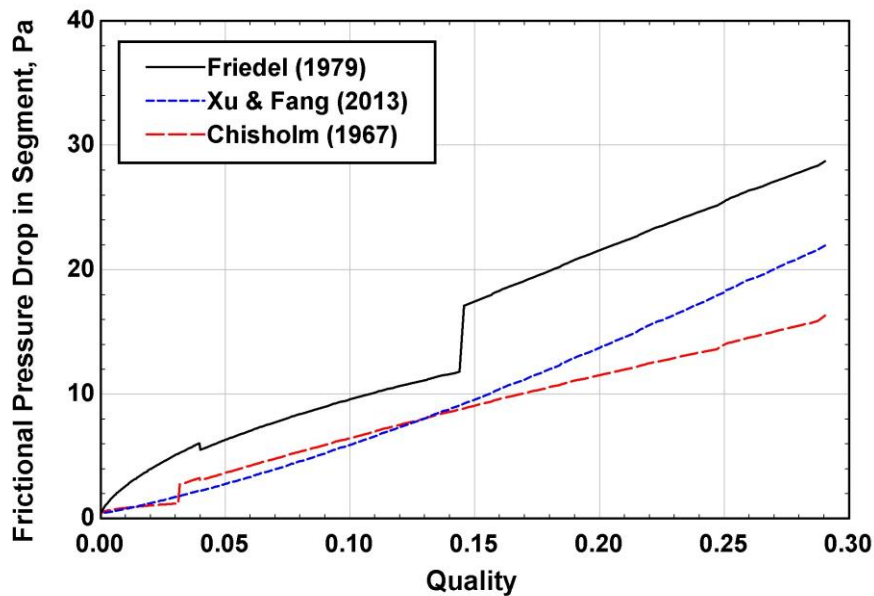
### **3.6.1.3. Tube-Side Pressure Drop**

The total solution pressure drop in each segment is a sum of the frictional, deceleration, gravitational, and minor components. A positive pressure drop value ( $\Delta P_{sol,sg} > 0$ ) corresponds to a decrease in solution pressure between the inlet and outlet of the segment.

$$\Delta P_{sol,sg} = \Delta P_{fric,Friedel} + \Delta P_{dec} + \Delta P_{grav} + \Delta P_{sol,minor} \quad (3.12)$$

The tube-side frictional pressure drop is determined by the Friedel (1979) correlation, which applies to a variety of fluids for horizontal and vertical flow of both

single- and two-component mixtures in adiabatic channels. The correlation is based on approximately 25,000 data points (Friedel, 1979), and it has long been used for two-phase pressure drop predictions. Although the data used to compile the correlation includes ammonia and water studies, none of the studies involve an ammonia-water mixture. It should be noted that the correlation is specifically for adiabatic flow, although there is considerable condensation occurring in the present case. *Figure 3.11* shows the segmental frictional pressure drop predicted in the 394-FPM corrugated-fin absorber. For comparison, the segmental frictional pressure drop during absorption is shown for the Xu and Fang (2013) and Chisholm (1967) correlations on the right axis. The Chisholm (1967) correlation is based on data from air-water mixtures, and the Xu and Fang (2013) correlation is a comprehensive correlation for refrigerants in small (0.1-10.1 mm) diameter tubes.



**Figure 3.11 Segmental frictional pressure drop for 394-FPM round-tube corrugated-fin absorber divided in 220 segments ( $L_{sg} = 0.061$  m)**

In *Figure 3.11*, the frictional pressure drop in a segment decreases as the quality decreases (from right to left on the x-axis). This is a result of the decreasing vapor velocity as the vapor fraction decreases. The values for the segmental pressure drop are dependent on the number of segments; only the magnitude of the values in relation to one another should be considered. The transition at  $q = 0.15$  in the Friedel (1979) correlation in *Figure 3.11* reflects the change in liquid-only friction factor associated with the transition to laminar flow.

The frictional pressure drop predicted by the Friedel (1979) correlation is determined from the liquid-only two-phase multiplier.

$$C_{F1} = (1 - q_{\text{sol}})^2 + q_{\text{sol}}^2 \left( \frac{\rho_l}{\rho_v} \right) \left( \frac{f_{\text{vo}}}{f_{\text{lo}}} \right) \quad (3.13)$$

$$C_{F2} = q_{\text{sol}}^{0.78} (1 - q_{\text{sol}})^{0.224} \left( \frac{\rho_l}{\rho_v} \right)^{0.91} \left( \frac{\mu_v}{\mu_l} \right)^{0.19} \left( 1 - \frac{\mu_v}{\mu_l} \right)^{0.7} \quad (3.14)$$

$$\phi_{\text{lo,Friedel}} = \sqrt{C_{F1} + \frac{3.24 C_{F2}}{Fr^{0.045} We^{0.035}}} \quad (3.15)$$

$$\left( \frac{dP}{dz} \right)_{\text{Friedel}} = \phi_{\text{lo,Friedel}}^2 \left( \frac{2 f_{\text{lo}} G_{\text{sol}}^2}{\rho_l D_i} \right) \quad (3.16)$$

$$\Delta P_{\text{fric,Friedel}} = \left( \frac{dP}{dz} \right)_{\text{Friedel}} \cdot L_{\text{sg}} \quad (3.17)$$

The implementation of the equations above requires the determination of the Froude number, Weber number, and liquid- and vapor-only friction factors.

$$\rho_{\text{tp}} = \left( \frac{q_{\text{sol}}}{\rho_v} + \frac{1 - q_{\text{sol}}}{\rho_l} \right)^{-1} \quad (3.18)$$

$$Fr = \frac{G_{\text{sol}}^2}{g D_i \rho_{\text{tp}}^2} \quad (3.19)$$

$$We = \frac{G_{\text{sol}}^2 D_i}{\rho_{\text{tp}} \sigma_1} \quad (3.20)$$

$$\text{If } Re_{j_o} < 2000: f_{j_o} = 16/Re_{j_o}; \text{ Else: } f_{j_o} = 0.079 Re_{j_o}^{-0.25} \quad (3.21)$$

where j = l,v for liquid or vapor

The differential pressure resulting from deceleration of the flow during condensation requires an approximation of the void fraction of the solution. The void fraction here is in the form presented by Butterworth (1975), with constants from Lockhart and Martinelli (1949).

$$VF_{\text{in/out}} = \left[ 1 + 0.28 \left( \frac{1 - q_{\text{sol,in/out}}}{q_{\text{sol,in/out}}} \right)^{0.64} \left( \frac{\rho_v}{\rho_l} \right)^{0.36} \left( \frac{\mu_l}{\mu_v} \right)^{0.07} \right]^{-1} \quad (3.22)$$

$$\Delta P_{\text{dec}} = G_{\text{sol}}^2 \left[ \frac{q_{\text{sol,out}}^2}{\rho_v VF_{\text{out}}} - \frac{(1 - q_{\text{sol,out}})^2}{\rho_l (1 - VF_{\text{out}})} \right] - G_{\text{sol}}^2 \left[ \frac{q_{\text{sol,in}}^2}{\rho_v VF_{\text{in}}} - \frac{(1 - q_{\text{sol,in}})^2}{\rho_l (1 - VF_{\text{in}})} \right] \quad (3.23)$$

Although flow in the heat exchanger is primarily horizontal, U-bends at the end of each pass curve downward, inducing a minor pressure drop and a gravitational pressure rise. In the present model, the minor loss and gravitational rise in one U-bend are attributed equally to the segments in that pass. For example, if there are ten segments in each pass (220 total segments), the model predicts that the U-bend minor loss in any given segment is one-tenth of the minor loss that results from flow through one U-bend. Therefore, the minor loss associated with U-bends in any segment is the minor loss associated with one U-bend  $\left( [1/2] K_{L,\text{UBend}} \rho_{\text{sol,equl}} u_{\text{sol}}^2 \right)$  multiplied by the fraction of the length of the segment over the length of the pass  $\left( L_{\text{sg}}/L_{\text{pass}} \right)$ :

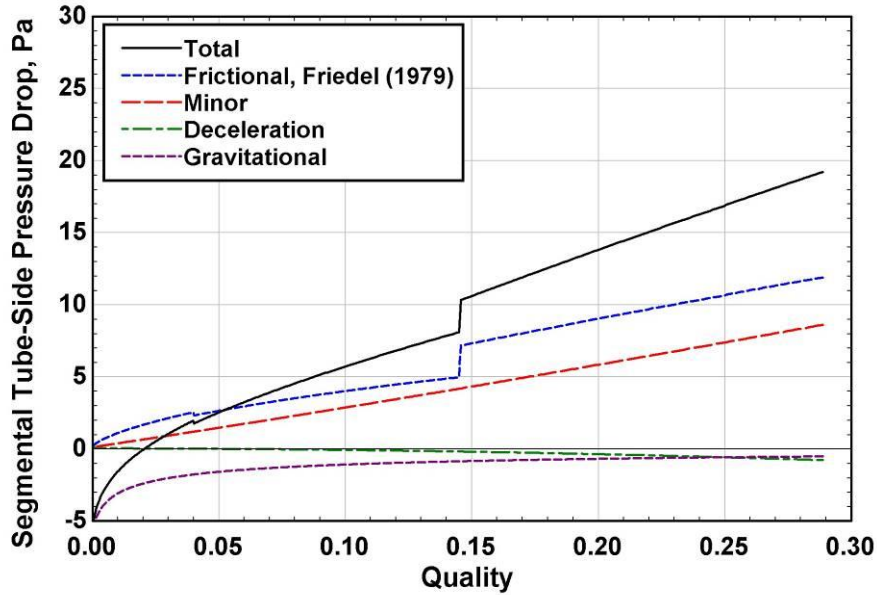
$$\Delta P_{\text{sol,minor}} = \frac{1}{2} K_{L,\text{UBend}} \rho_{\text{sol,equl}} u_{\text{sol}}^2 \left( \frac{L_{\text{sg}}}{L_{\text{pass}}} \right) \quad (3.24)$$

For the gravitational component of the differential pressure, the angle of tube inclination,  $\gamma$ , is approximated such that the total drop in the height of flow in the absorber corresponds to the vertical distance between the coil inlet and outlet. In the corrugated-fin absorbers, the height of the flow drops; therefore, the angle of inclination is specified as  $-1.7^\circ$ .

$$\gamma = \tan^{-1} \left[ -s_t \left( \frac{N_{t, \text{row}} - 0.5}{L_{\text{total}}} \right) \right] \quad (3.25)$$

$$\Delta P_{\text{grav}} = \left[ (1 - VF) \rho_l + VF \cdot \rho_v \right] g \sin(\gamma) L_{\text{sg}} \quad (3.26)$$

Figure 3.12 shows the total segmental pressure drop predicted during absorption and the breakdown of the various pressure differential sub-components.



**Figure 3.12 Tube-side components of differential pressure across segment in round-tube 394-FPM corrugated-fin absorber divided in 220 segments ( $L_{\text{sg}} = 0.061$  m)**

The transition near  $q = 0.15$  in the frictional pressure drop reflects the change in liquid-only friction factor associated with the transition to laminar flow. Because the



value of the pressure drop depends on the number of segments chosen during modeling, only the relative magnitudes are of primary importance. The frictional component of the differential pressure has the largest impact on the total change in pressure, whereas deceleration has negligible significance. As expected, the pressure rise due to gravity increases as the quality of the solution decreases. Near the end of the absorption process, this gravitational component causes the total differential pressure to become negative.

#### **3.6.1.4. Air-Side Heat Transfer**

Several studies on air-side heat transfer are available in the literature; however, the wide variety of geometrical parameters in finned air coils leads to predictions that are limited in application to narrow ranges of geometries. Heat transfer over an unfinned bank of tubes has been thoroughly studied; however, there is no universal correlation to account for innovative fin designs featuring lanced, louvered, and corrugated surfaces. For corrugated or wavy fins, studies have not been able to account for wide ranges of fin densities, fin thicknesses, peak-to-valley pitches, and peak-to-valley depths. The majority of studies incorporate at most a handful of air coil geometries.

The correlation by Kim *et al.* (1997b) is determined to be the most comprehensive study for corrugated fin-and-tube heat exchangers and is used in the present investigation. The correlation includes data from 41 wavy fin geometries from Beecher and Fagan (1987) and Wang *et al.* (1997). It predicts 92% of their heat transfer database within  $\pm 10\%$ . It should be noted that the aggressive density of fins in the 394-FPM and 551-FPM absorbers falls just outside the range of applicability suggested by Kim *et al.* (1997b). The 394-FPM absorber ( $s/D_c = 0.14$ ) and 551-FPM absorber ( $s/D_c = 0.10$ ) have fin spacing to collar diameter ratios outside the range:  $0.15 \leq (s/D_c) \leq 0.33$ . The

551-FPM coil also has a wave depth-to-spacing ratio ( $s_{\text{wav,d}}/s=1.78$ ) beyond the window of applicability of this correlation:  $0.23 \leq (s_{\text{wav,d}}/s) \leq 1.21$ . Nevertheless, these are the largest ranges of application found in the literature. The Colburn “ $j$ ” factor is used to predict the heat transfer coefficient according to Kim *et al.* (1997b).

$$\begin{aligned}
 N \geq 3: j_N = j_3 &= 0.394 \text{Re}_{\text{D,Kim}}^{-0.357} \left( \frac{s_t}{s_1} \right)^{-0.272} \left( \frac{s}{D_c} \right)^{-0.205} \left( \frac{s_{\text{wav,p}}}{s_{\text{wav,d}}} \right)^{-0.558} \left( \frac{s_{\text{wav,d}}}{s} \right)^{-0.133} \\
 N = 1, 2; \text{Re}_{\text{D,Kim}} \geq 1000: j_N = j_3 &\left( 0.978 - 0.010 N_{\text{t,col}} \right) \\
 N = 1, 2; \text{Re}_{\text{D,Kim}} < 1000: j_N = j_3 &\left( 1.350 - 0.162 N_{\text{t,col}} \right)
 \end{aligned} \tag{3.27}$$

$$Nu_{\text{Kim}} = j_N \left( \text{Re}_{\text{D,Kim}} \text{Pr}_{\text{air}}^{1/3} \right) \frac{D_h}{D_c} \tag{3.28}$$

These expressions require the Reynolds number according to Kim *et al.* (1997b), the hydraulic diameter ( $D_h$ ), the collar diameter ( $D_c = D_o + 2t_{\text{fin}}$ ), and the spacing between fins ( $s = p_{\text{fin}} - t_{\text{fin}}$ ). Intermediate calculations include the fin contraction ratio ( $\sigma = s/[s + t_{\text{fin}}]$ ), the mean velocity ( $u_m$ ), the max velocity ( $u_{\text{max}}$ ), and geometric parameters  $\beta$  and  $\theta$ , as defined below.

$$u_m = \frac{u_{\text{fr}}}{\sigma(1-\beta)}; u_{\text{fr}} = \frac{\dot{V}_{\text{air}}}{L_{\text{pass}} H_{\text{fin}}} \tag{3.29}$$

$$u_{\text{max}} = \dot{V}_{\text{air}} / A_c; A_c = (H_{\text{fin}} - N_{\text{t,row}} D_o) L_{\text{pass}} \left( 1 - \frac{t_{\text{fin}}}{p_{\text{fin}}} \right) \tag{3.30}$$

$$\text{Re}_{\text{D,Kim}} = \text{Re}_h \left( \frac{D_c}{D_h} \right) \left( \frac{u_{\text{max}}}{u_m} \right) \tag{3.31}$$

$$D_h = \frac{2s(1-\beta)}{(1-\beta)\sec\theta + 2s\beta/D_c} \tag{3.32}$$

$$\beta = \frac{\pi D_c^2}{4s_t s_l} \quad (3.33)$$

$$\sec \theta = \sqrt{(s_{\text{wav,p}}^2 + s_{\text{wav,d}}^2)} / s_{\text{wav,p}} \quad (3.34)$$

Another corrugated-fin tube bank correlation based on data from Beecher and Fagan (1987) was developed by Webb and Gupte (1990). *Table 3.7* compares heat transfer coefficients predicted by Kim *et al.* (1997b) and Webb and Gupte (1990) for the 394-FPM round-tube corrugated-fin absorber. Single values for the heat transfer coefficient are shown here because the air-side heat transfer remains relatively unchanged across the face of the heat exchanger in the present application. Also listed are heat transfer coefficients based on a variety of convective flow cases, including flow over plain-fin tubes, a finless tube bank, internal flow through a rectangular duct (between fins), and external flow over a cylinder. These correlations are not recommended for use in the present absorber design; however, they are useful for demonstrating the heat transfer enhancement expected from wavy fins. As expected from the literature (Garimella and Coleman, 1998), the corrugated-fin correlations predict heat transfer coefficients significantly higher than the value proposed for flat fins by Gray and Webb (1986). The wavy-fin coefficient calculated using the Kim *et al.* (1997b) correlation is 61% higher than the flat fin correlation prediction. This increase in heat transfer coefficient from flat to wavy fins agrees with the “55% to 70% increase” recorded by Wang *et al.* (1997).

**Table 3.7 Predicted air-side heat transfer coefficients for 394-FPM and 551-FPM corrugated-fin absorbers**

Geometry	Reference	Predicted Heat Transfer Coefficient ( $\text{W m}^{-2} \text{K}^{-1}$ )	
		394-FPM	551-FPM
Corrugated-fin tube bank	Kim <i>et al.</i> (1997b)	72.3	76.5
Plain-fin tube bank	Gray and Webb (1986)	45.0	45.5
Tube bank	Zukauskas <i>et al.</i> (1968)	41.0	42.0
Internal flow through rectangular channels	Kakaç <i>et al.</i> (1987)	47.6	69.4
External flow over cylinder (no fins)	White (1991)	46.8	47.8
External flow over cylinder (no fins)	Hilpert (1933)	43.3	44.2
Minimum cross-sectional air flow area ( $A_c$ )			
		0.135 $\text{m}^2$	0.129 $\text{m}^2$
Contraction ratio of flow area ( $A_c/A_{fr}$ )			
		0.528	0.506
Air velocity at minimum air flow area ( $u_{\max}$ )			
		3.149 $\text{m s}^{-1}$	3.287 $\text{m s}^{-1}$

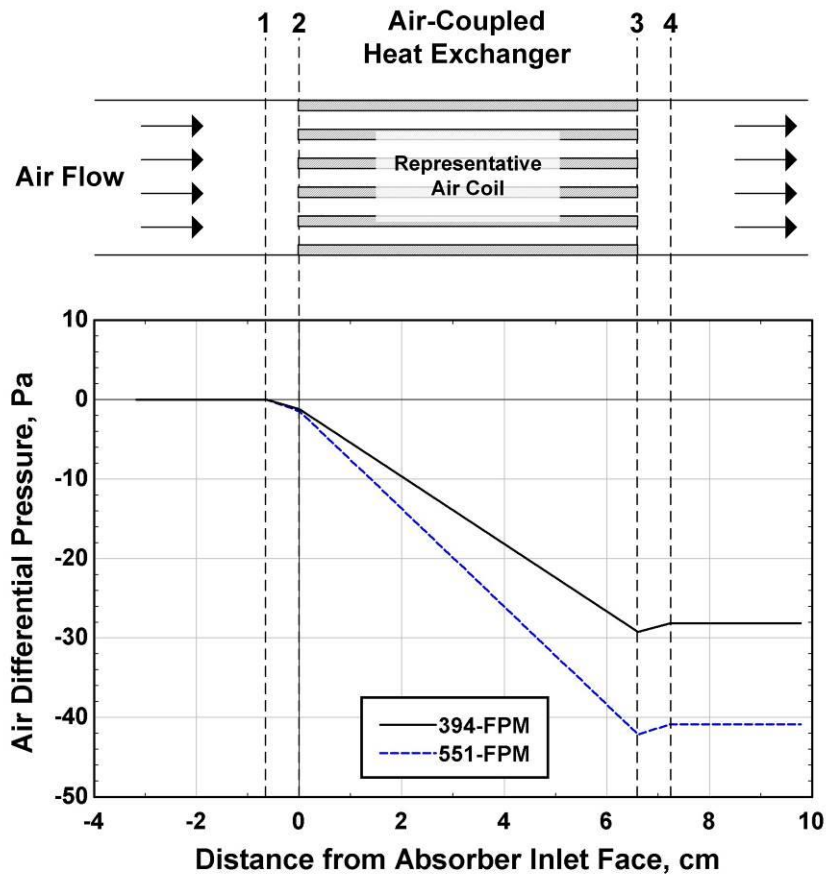
The Kim *et al.* (1997b) correlation, used for the present modeling, predicts a 5.8% increase in heat transfer coefficient as a result of the reduced fin pitch between the 394-FPM and 551-FPM absorbers. This increase corresponds to an increase in air velocity (3.149 to 3.287  $\text{m s}^{-1}$ ) as a result of reduced air flow area (0.135 to 0.129  $\text{m}^2$ ) in the 551-FPM absorber compared to the 394-FPM absorber. Although the air-side heat transfer area is 38% higher with the higher fin density (16.24 compared to 11.70  $\text{m}^2$ ), the increase in air velocity is marginal (4%) due to the low fin thickness ( $2.41 \times 10^{-4}$  m).

### **3.6.1.5. Air-Side Pressure Drop**

The total pressure drop across the round-tube corrugated-fin absorbers is comprised of four components: the contraction at the entrance, the friction losses in the core, the acceleration in the core, and the exit expansion.

$$\Delta P_{\text{air}} = \Delta P_{\text{air,entrance}} + \Delta P_{\text{air,fric}} + \Delta P_{\text{air,accel}} + \Delta P_{\text{air,exit}} \quad (3.35)$$

Figure 3.13 plots the predicted decrease in pressure for the 394-FPM and 551-FPM coils as a function of length in the direction of air flow. The entrance/exit, frictional, and acceleration terms account for 0.6%, 96.0%, and 3.3% of the total air-side pressure drop, respectively.



**Figure 3.13 Air-side pressure drop in round-tube corrugated-fin absorbers**

The entrance [1→2 in Figure 3.13] and exit [3→4] portions of the differential pressure correspond to the contraction and expansion of the flow area, respectively. Meanwhile, the variations in pressure due to friction and acceleration take place in the core of the heat exchanger [2→3]. As expected the predicted pressure drop is greater in the 551-FPM absorber than in the 394-FPM absorber. It should be noted that although

shown as a linear drop, the pressure drop in the core varies as the air flows over portions of fins and tubes. The length indicated for flow contraction and expansion shown in *Figure 3.13* is for illustrative purposes only; in the heat exchanger, contractions and expansion occurs at specific locations.

When combined, entrance and exit effects account for a marginal portion (4.3% and -3.7%, respectively) of the total air-side pressure drop. Following the procedure from Kays and London (1984), entrance and exit losses are only based on the change in air flow area caused by the fins. The contraction and expansion of the air flow over the tubes is accounted for in the frictional pressure drop analysis described below. The frictional pressure drop term, which includes frictional effects over both the fins and tubes, accounts for 96% of the total air-side pressure drop.

The pressure decreases during contraction of the flow area and rises during expansion. Contraction and expansion loss coefficients,  $K_c$  and  $K_e$  are used to account for irreversibilities due to changes in flow area caused by the fins. Values for the coefficients can be found in Kays and London (1984) as a function of Reynolds number and the ratio of the flow area within the fins to the frontal flow area ( $\sigma'_{KL}$ ). The finned-to-frontal flow area ratio for the 394-FPM and 551-FPM absorbers is 0.905 and 0.867, respectively.

$$\sigma'_{KL} = \frac{L_{\text{pass}} (1 - t_{\text{fin}} / p_{\text{fin}}) H_{\text{fin}}}{L_{\text{pass}} H_{\text{fin}}} \quad (3.36)$$

$$\Delta P_{\text{air,entrance}} = \frac{G_{\text{air}}'^2}{2\rho_{\text{air,in}}} (1 - \sigma_{KL}'^2 + K_c) \quad (3.37)$$

$$\Delta P_{\text{air,exit}} = -\frac{G_{\text{air}}'^2}{2\rho_{\text{air,in}}} (1 - \sigma_{KL}'^2 - K_e) \left( \frac{\rho_{\text{air,in}}}{\rho_{\text{air,out}}} \right) \quad (3.38)$$

The frictional pressure drop in the core of the heat exchanger is typically the dominant portion of the total change in pressure for coils with minor reduction in flow area. The pressure decreases due to friction across the fins and the bank of tubes.

$$\Delta P_{\text{air,fric}} = \Delta P_{\text{air,t}} + \Delta P_{\text{air,f,wavy}} \quad (3.39)$$

The portion of the frictional pressure drop attributed to flow over a bank of tubes is determined using the correlation from Zukauskas *et al.* (1968). Coefficients used in determining Euler number ( $A_{\text{Eu}}$ ,  $B_{\text{Eu}}$ ,  $C_{\text{Eu}}$ ,  $D_{\text{Eu}}$ ,  $E_{\text{Eu}}$ ) and the correction factor for 10 or fewer tube rows ( $C_z$ ) may be found in Hewitt (1990).

$$a_t = S_t/D_o; b_t = S_1/D_o; k_1 = (a_t/b_t)^{-0.048} \quad (3.40)$$

$$Eu = k_1 \left( A_{\text{Eu}} + \frac{B_{\text{Eu}}}{\text{Re}_{D,Z}} + \frac{C_{\text{Eu}}}{\text{Re}_{D,Z}^2} + \frac{D_{\text{Eu}}}{\text{Re}_{D,Z}^3} + \frac{E_{\text{Eu}}}{\text{Re}_{D,Z}^4} \right); Eu_z = C_z Eu \quad (3.41)$$

$$s_{\text{min}} = \text{Min}(s_t, s_d); s_d = \sqrt{s_1^2 + (s_t^2/4)} \quad (3.42)$$

$$f_{\text{air,tube}} = Eu_z N_{t,\text{col}} \left( \frac{s_{\text{min}} - D_o}{\pi D_o} \right) \quad (3.43)$$

$$A_{\text{tube,bare}} = N_{\text{pass}} \pi D_o (L_{\text{pass}} - t_{\text{fin}} N_{\text{fins}} L_{\text{pass}}) \quad (3.44)$$

$$\Delta P_{\text{air,t}} = \frac{1}{2} f_{\text{air,tube}} \rho_{\text{air}} u_{\text{max}}^2 \left( \frac{A_{\text{tube,bare}}}{A_c} \right) \quad (3.45)$$

Following the approach by Webb and Gupta (1990) and Garimella and Coleman (1998), the present investigation approximates the air-side pressure drop over wavy fins by augmenting the flat-fin predicted pressure drop (Gray and Webb, 1986) by a factor of 1.9.

$$\Delta P_{\text{air,f,flat}} = \frac{1}{2} f_{\text{air,fin}} \rho_{\text{air}} u_{\text{m}}^2 \left( \frac{A_{\text{fin,total}}}{A_c} \right) \quad (3.46)$$

$$\Delta P_{\text{air,f,wavy}} = 1.9\Delta P_{\text{air,f,flat}} \quad (3.47)$$

The friction factor for air over flat fins is predicted by Gray and Webb (1986).

$$f_{\text{air,fin}} = 0.508(\text{Re}_{\text{D,Z}})^{-0.521} (s_t/D_o)^{1.318} \quad (3.48)$$

$$\text{Re}_{\text{D,Z}} = \frac{\rho_{\text{air}} u_{\text{max}} D_o}{\mu_{\text{air}}} \quad (3.49)$$

The final portion of the pressure drop accounts for the acceleration or deceleration of the flow with heating or cooling.

$$\Delta P_{\text{air,accel}} = \frac{G_{\text{air}}^2}{2\rho_{\text{air,in}}} \left( \frac{\rho_{\text{air,in}}}{\rho_{\text{air,out}}} - 1 \right) \quad (3.50)$$

The total air-side pressure drop predicted for the 394-FPM corrugated-fin absorber at design conditions was 28.1 Pa, compared to 40.8 Pa for the 551-FPM absorber. The total air-side pressure drop in the 394-FPM absorber (28.1 Pa) consists of the inlet contraction (1.2 Pa, 4.3%), friction in the core (27.0 Pa, 96.0%), acceleration in the core (0.9 Pa, 3.3%), and exit expansion (−1.0 Pa, −3.7%).

### **3.6.1.6. Mass Transfer**

Near the liquid-vapor interface, the less volatile component of the mixture (water) preferentially condenses out of the ammonia-water vapor, resulting in a concentration gradient in both the liquid and vapor phases. The concentration in the vapor near the interface is higher than the bulk vapor concentration, while the liquid concentration near the interface is lower than the bulk liquid concentration. In the present case, the liquid layer is assumed to be well mixed such that the presence of the concentration gradient in the liquid phase is considered negligible. This assumption is particularly valid when the liquid film is thin. Predictions based on this assumption are expected to deviate slightly



from experiments at very low qualities (at the end of the absorption process), but mass transfer has less of an effect on heat transfer as these low qualities (Bell and Ghaly, 1973).

The concentration gradient in the vapor phase is due to the mass transfer resistance that impedes heat transfer. The Silver-Bell-Ghaly method is used in the present model to predict the effect of the concentration gradient in the vapor on condensation (Silver, 1947; Bell and Ghaly, 1973). The internal thermal resistance to heat transfer can be separated into the thermal resistance in the condensate film and the resistance in the bulk vapor, which includes the effect of the concentration gradient.

$$R_{in} = R_{in, \text{film}} + R_{in, \text{vap}} \quad (3.51)$$

$$R_{in, \text{film}} = \frac{1}{\alpha_{sol} \pi D_i L_{sg}} \quad (3.52)$$

$$R_{in, \text{vap}} = q_{sol} C_{p,v} \frac{\Delta T_{gl}}{\Delta h_m} \frac{1}{\alpha_v \pi D_i L_{sg}} \quad (3.53)$$

The condensate layer (film) resistance is calculated using  $\alpha_{sol}$ , the heat transfer coefficient according to Shah (1979). This specifies the thermal resistance between the interface and inner wall temperatures. The thermal resistance in the vapor accounts for the degradation in heat transfer as a result of mass transfer, and it consists of the thermal resistance in the vapor multiplied by the quality and the ratio of the sensible heat duty removed from the vapor to the total enthalpy change during condensation ( $C_{p,v} \Delta T_{gl} / \Delta h_{fg}$ ). The quality ( $q_{sol}$ ) in the vapor thermal resistance term corresponds to the transport length scale in the vapor. With decreasing void fraction, the effective diameter of the vapor flow reduces, thereby decreasing the mass transfer resistance. The magnitude of the degradation in heat transfer resulting from the concentration gradient corresponds to the

zeotropic characteristics of the mixture ( $\Delta T_{gl}/\Delta h_{fg}$ ) because of the significant effect of sensible heat removal on total heat transfer. This vapor thermal resistance characterizes heat transfer between the bulk vapor and interface temperatures. The vapor heat transfer coefficient used in this resistance is determined using the correlation from Churchill (1977 (b)).

$$\alpha_v = Nu_v k_v / D_i \quad (3.54)$$

For the first 25.4-mm segment modeled in the 394-FPM absorber ( $q = 0.29$ ), the vapor-phase thermal resistance accounting for mass transfer degradation on heat transfer is predicted to be 48% ( $0.19 \text{ K W}^{-1}$ ) of the internal thermal resistance ( $0.40 \text{ K W}^{-1}$ ) and 16.5% of the total thermal resistance ( $1.14 \text{ K W}^{-1}$ ) between the bulk vapor and the air. This effect decreases with quality along the length of tube in the absorber. A plot of this variation in thermal resistance as a function of the length is provided in a subsequent section on the thermal resistance circuit (*Figure 3.17*).

To determine the vapor outlet conditions the procedure described by Colburn and Drew (1937) for the determination of the sensible heat transfer between the liquid film and the vapor is used here.

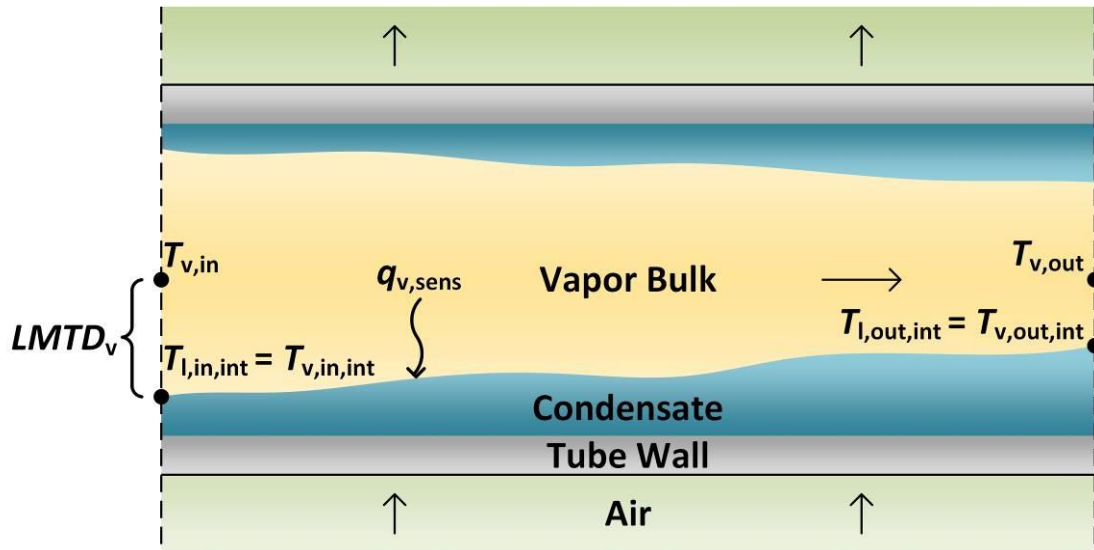
$$q_{v,\text{sens}} = \alpha_v \left( \frac{\phi_T}{1 - e^{-\phi_T}} \right) A_{\text{int}} LMTD_v \quad (3.55)$$

The vapor heat transfer coefficient calculated previously is used here, along with the correction factor for sensible heat affected by mass transfer, shown in the parentheses. This correction factor adjusts the sensible heat removed from the vapor due to the difference between the interface and bulk vapor temperatures that results from the concentration gradient. The heat transfer correction factor uses the parameter,  $\phi_T$ , which

is calculated as a function of the molar specific heats and condensing fluxes of ammonia and water.

$$\phi_T = (n_{\text{NH}_3} C_{p,\text{NH}_3,\text{molar}} + n_{\text{H}_2\text{O}} C_{p,\text{H}_2\text{O},\text{molar}}) / \alpha_v \quad (3.56)$$

The log mean temperature difference is calculated between the bulk vapor and interface temperatures across each segment, as shown in *Figure 3.14*.



**Figure 3.14 Schematic of  $LMTD_v$  across representative segment**

$$LMTD_v = [(T_{v,in} - T_{l,in,int}) - (T_{v,out} - T_{l,out,int})] / \ln \left( \frac{T_{v,in} - T_{l,in,int}}{T_{v,out} - T_{l,out,int}} \right) \quad (3.57)$$

At the liquid-vapor interface, the liquid and vapor temperatures are equal ( $T_{l,int} = T_{v,int}$ ). The sensible heat removed from the vapor to the interface can now be determined to find the outlet vapor temperature.

$$q_{v,sens} = \dot{m}_v C_{p,v} (T_{v,in} - T_{v,out}) \quad (3.58)$$

The Nusselt and Schmidt numbers in the vapor can be combined to determine the vapor mass transfer coefficient,  $\beta_v$ , using the Chilton and Colburn heat and mass transfer analogy.

$$\left(\frac{Nu_v}{Sh_v}\right)^3 = \frac{Pr_v}{Sc_v} \quad (3.59)$$

$$Sh_v = \frac{\beta_v D_i}{D_{NH_3H_2O,v}} \quad (3.60)$$

The total ammonia and water condensing flux can now be determined using the bulk molar concentration ( $C_T$ ), fraction of condensing ammonia ( $z$ ), and vapor and interfacial molar concentrations ( $x_{v,molar}$ ,  $x_{v,int,molar}$ ).

$$C_T = P_v / RT_v \quad (3.61)$$

$$n_{NH_3} = z \cdot n_{total} \quad (3.62)$$

$$n_{total} = \beta_v C_T \ln\left(\frac{z - x_{v,int,molar}}{z - x_{v,molar}}\right) \quad (3.63)$$

$$M_{v,int} = \left(\frac{x_{v,int}}{M_{NH_3}} + \frac{1 - x_{v,int}}{M_{H_2O}}\right)^{-1}; \quad x_{v,int,molar} = x_{v,int} M_{v,int} / M_{NH_3} \quad (3.64)$$

The mass concentration of the vapor at the interface  $x_{v,int}$  is known from  $T_{v,int} = T_{l,int}$ ,  $P_{v,int}$ , and  $q_{v,int} = 0$ . At this point, the mass flux of condensing ammonia and water can be determined.

$$m_{flux,NH_3} = n_{NH_3} M_{NH_3} \quad (3.65)$$

$$m_{flux,H_2O} = n_{H_2O} M_{H_2O} \quad (3.66)$$

The calculation of mass flow rate of the condensing ammonia and water requires an interfacial area, approximated using the void fraction.

$$D_{int} = \sqrt{VF \cdot D_i^2} \quad (3.67)$$

$$A_{int} = \pi D_{int} L_{sg} \quad (3.68)$$

$$\dot{m}_{abs,NH_3} = m_{flux,NH_3} A_{int} \quad (3.69)$$

$$\dot{m}_{\text{abs,H}_2\text{O}} = m_{\text{flux,H}_2\text{O}} A_{\text{int}} \quad (3.70)$$

Finally, these mass flow rates are used to determine the outlet mass flow rate of liquid and satisfy the mass exchange between the liquid and vapor across the segment.

$$\dot{m}_{\text{l,out}} = \dot{m}_{\text{l,in}} + \dot{m}_{\text{abs,NH}_3} + \dot{m}_{\text{abs,H}_2\text{O}} \quad (3.71)$$

$$\dot{m}_{\text{l,in}} + \dot{m}_{\text{v,in}} = \dot{m}_{\text{l,out}} + \dot{m}_{\text{v,out}} \quad (3.72)$$

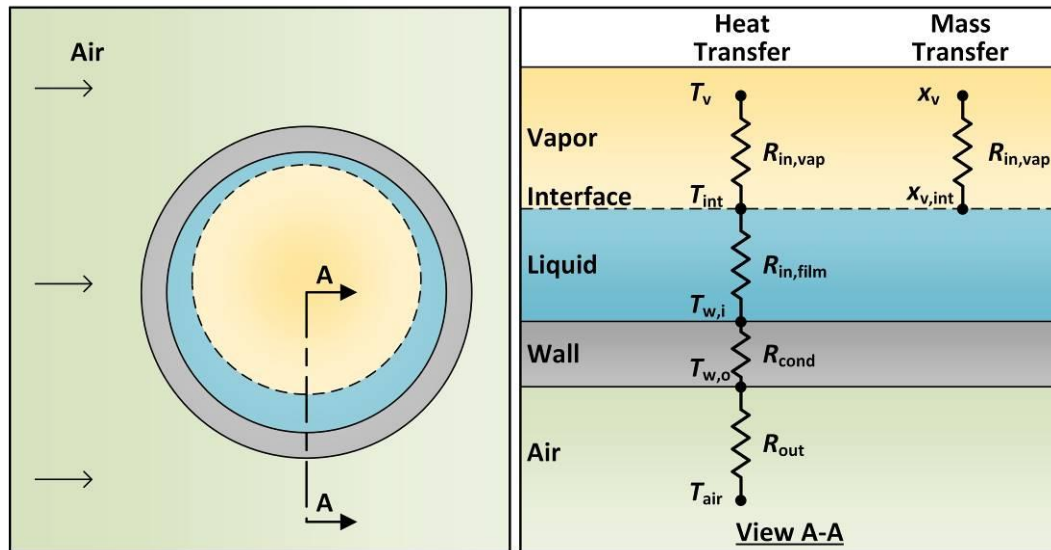
$$\dot{m}_{\text{l,out}} x_{\text{l,out}} = \dot{m}_{\text{l,in}} x_{\text{l,in}} + \dot{m}_{\text{abs,NH}_3} \quad (3.73)$$

$$\dot{m}_{\text{l,in}} x_{\text{l,in}} + \dot{m}_{\text{v,in}} x_{\text{v,in}} = \dot{m}_{\text{l,out}} x_{\text{l,out}} + \dot{m}_{\text{v,out}} x_{\text{v,out}} \quad (3.74)$$

### 3.6.1.7. Thermal Resistance Circuit

The thermal resistance between the refrigerant and the air is composed of the internal thermal resistance (with vapor and condensate film components), conductive resistance (inner to outer tube wall), and external resistance (outer tube wall to bulk air).

The thermal resistance circuit is shown in *Figure 3.15*.



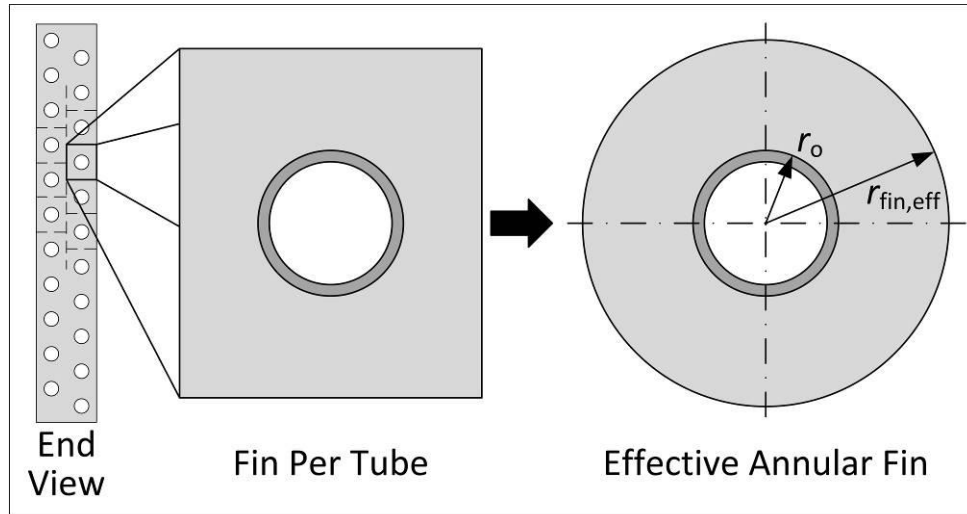
**Figure 3.15 Thermal resistance circuit**

$$R_{\text{total}} = R_{\text{in,vap}} + R_{\text{in,film}} + R_{\text{cond}} + R_{\text{out}} \quad (3.75)$$

The internal thermal resistance here is calculated using the Silver-Bell-Ghaly method to account for the degradation of heat transfer due to the mass transfer resistance in the vapor. Discussion of the liquid film and vapor resistances is included in the previous section. The conductive thermal resistance is calculated as follows:

$$R_{\text{cond}} = \frac{\ln(D_o/D_i)}{2k_{\text{tube}}\pi L_{\text{sg}}} \quad (3.76)$$

To calculate the external thermal resistance, the effective annular fin radius ( $r_{\text{fin,eff}}$ ) is determined (Figure 3.16).



**Figure 3.16 Effective annular fin schematic**

The fin sheet is idealized as being apportioned among the tubes such that each tube has an equivalent fin area. The area of fin per tube can then be used to find the radius of an annular fin with the same area.

$$A_{\text{annular,fin}} = \frac{\pi}{4} (D_{\text{fin,eff}}^2 - D_o^2) = \left[ \frac{H_{\text{fin}} W_{\text{fin}}}{N_{\text{pass}}} - \left( \frac{\pi}{4} \right) D_o^2 \right] \quad (3.77)$$

$$r_{\text{fin,eff}} = \frac{D_{\text{fin,eff}}}{2} \quad (3.78)$$

The external thermal resistance depends on the fin efficiency and overall surface efficiency,  $\eta_{\text{fin}}$  and  $\eta_o$ , respectively. The fin efficiency for a circular fin is found in Incropera *et al.* (2011).

$$r_o = D_o/2 \quad (3.79)$$

$$m_{\text{fin}} = \sqrt{\frac{2\alpha_{\text{air}}}{k_{\text{fin}}t_{\text{fin}}}} \quad (3.80)$$

$$C_2 = \frac{2m_{\text{fin}}r_o}{(m_{\text{fin}}r_{\text{fin,eff}})^2 - (m_{\text{fin}}r_o)^2} \quad (3.81)$$

$$\eta_{\text{fin}} = C_2 \frac{K_1(m_{\text{fin}}r_o)I_1(m_{\text{fin}}r_{\text{fin,eff}}) - I_1(m_{\text{fin}}r_o)K_1(m_{\text{fin}}r_{\text{fin,eff}})}{I_0(m_{\text{fin}}r_o)K_1(m_{\text{fin}}r_{\text{fin,eff}}) - K_0(m_{\text{fin}}r_o)I_1(m_{\text{fin}}r_{\text{fin,eff}})} \quad (3.82)$$

$I, K$ : Modified Bessel functions

The surface efficiency characterizes an array of fins over a base and is calculated using the ratio of the finned area to the total area (fins and tube) in a segment (Incropera *et al.*, 2011).

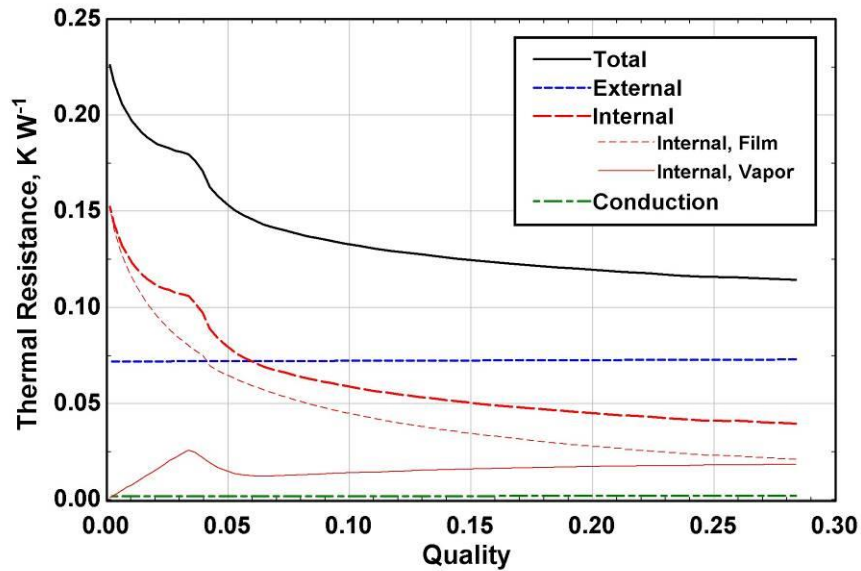
$$\eta_o = 1 - \left( \frac{A_{\text{fin,sg}}}{A_{\text{total,sg}}} \right) (1 - \eta_{\text{fin}}) \quad (3.83)$$

The absorber  $UA$  value is determined from the sum of the thermal resistances.

$$R_{\text{out}} = \frac{1}{\eta_o \alpha_{\text{air}} A_{\text{total,sg}}} \quad (3.84)$$

$$UA = 1/R_{\text{total}} \quad (3.85)$$

A view of the magnitude of the internal, conductive, and external thermal resistances during absorption can provide insight into the governing resistances to the absorption process (*Figure 3.17*).



**Figure 3.17 Thermal resistances during absorption in the 394-FPM corrugated-fin absorber**

The total thermal resistance is composed of the external, internal, and conduction resistances (bold lines), but the sub-components of the internal resistance (thin lines) have been plotted to show the effect of mass transfer. During absorption, the wall conduction thermal resistance ( $0.0075\text{-}0.0083\text{ K W}^{-1}$ ) and external thermal resistance ( $0.283\text{-}0.304\text{ K W}^{-1}$ ) remain relatively unchanged. When absorption begins (from the right going left in *Figure 3.17*), the external thermal resistance is limiting the heat transfer. As absorption nears completion, the flow regime becomes unfavorable, and the tube-side thermal resistance rises rapidly primarily due to the rising film resistance. For  $q < 0.06$  in *Figure 3.17*, the heat transfer is limited by the tube-side resistance. The rise in the vapor resistance with decreasing quality from 0.06 to 0.03 corresponds to the diminishing vapor heat transfer coefficient at low qualities. Eventually, the vapor flow becomes laminar ( $Re_v < 2200$ ) with decreasing quality, and the Nusselt number predicted by Churchill (1977 (b)) assumes a constant value of 4.36, corresponding to laminar flow



in a circular tube with uniform heat flux. This transition to laminar flow in the vapor takes place at  $q = 0.034$ , where the vapor heat transfer coefficient takes on a constant value ( $\alpha_v \approx 10.7 \text{ W m}^{-2} \text{ K}^{-1}$ ). With a constant heat transfer coefficient and diminishing quality, the vapor resistance drops ( $q < 0.034$  in *Figure 3.17*).

The effectiveness-*NTU* (Number of Transfer Units) method is used to relate the heat exchanger *UA* value to the heat that is transferred in a given segment. First, the minimum heat capacity rates between the tube and air sides must be determined. The mass flow rate of air in a segment is determined using the fraction of the segmental air flow area over the total air flow area (*Fraction<sub>sg</sub>*).

$$\dot{m}_{\text{air,sg}} = \dot{m}_{\text{air}} \text{Fraction}_{\text{sg}}; \dot{m}_{\text{air}} = \dot{V}_{\text{air}} \rho_{\text{air,in}} \quad (3.86)$$

$$\dot{C}_{\text{air}} = \dot{m}_{\text{air,sg}} C_{p,\text{air}} \quad (3.87)$$

$$\dot{C}_{\text{sol}} = \dot{m}_{\text{sol}} \left[ \frac{(h_{\text{sol,in}} - h_{\text{sol,out}})}{(T_{\text{sol,in}} - T_{\text{sol,out}})} \right] \quad (3.88)$$

$$\dot{C}_{\text{min}} = \min(\dot{C}_{\text{air}}, \dot{C}_{\text{sol}}) \quad (3.89)$$

The heat capacity rate of the solution is estimated using the ratio of the enthalpy change over the temperature change. This effective specific heat accounts for the phase change that is occurring during the absorption process. The number of transfer units can now be calculated.

$$NTU = UA / \dot{C}_{\text{min}} \quad (3.90)$$

As the number of segments increases, the mass flow rate of air in any given segment decreases due to the diminishing fraction of air flow area in the segment. This results in a decreasing  $\dot{C}_{\text{air}}$ . On the solution side, however, the latent heat removed from the solution during absorption leads to a high effective specific heat, usually resulting in a comparatively much larger  $\dot{C}_{\text{sol}}$ . In most cases, this results in the air side having the

minimum heat capacity rate in such segments. For example, for the first 25.4-mm segment in the 394-FPM absorber, the heat capacity rate in the air is  $0.91 \text{ W K}^{-1}$ , compared to  $176.4 \text{ W K}^{-1}$  in the solution. The air side may be considered unmixed due to the fins preventing airflow in the lateral direction. The following effectiveness- $NTU$  expression can be used to find the effectiveness of a crossflow heat exchanger in which the minimum heat capacity rate fluid (air) is unmixed (Incropera *et al.*, 2011).

$$\varepsilon = \frac{1}{C_r} \left( 1 - \exp \left[ -C_r \left( 1 - e^{-NTU} \right) \right] \right) \quad (3.91)$$

This expression corresponds to a single-pass crossflow heat exchanger. Although the corrugated-fin absorbers exhibit multiple passes, the segmental approach considers one tube or pass at a time in crossflow, justifying the use of this single-pass expression. The heat transfer rate in the segment can be determined from the effectiveness and the maximum possible heat transfer rate.

$$q_{\max} = \dot{C}_{\min} (T_{l,\text{in,int}} - T_{\text{air,in}}) \quad (3.92)$$

$$\varepsilon = q_{\text{sg}} / q_{\max} \quad (3.93)$$

Finally, the outlet solution enthalpy can be calculated and substituted for the inlet enthalpy in the following segment. The outlet air temperature is also calculated.

$$q_{\text{sg}} = \dot{m}_{\text{sol}} (h_{\text{sol,in}} - h_{\text{sol,out}}) \quad (3.94)$$

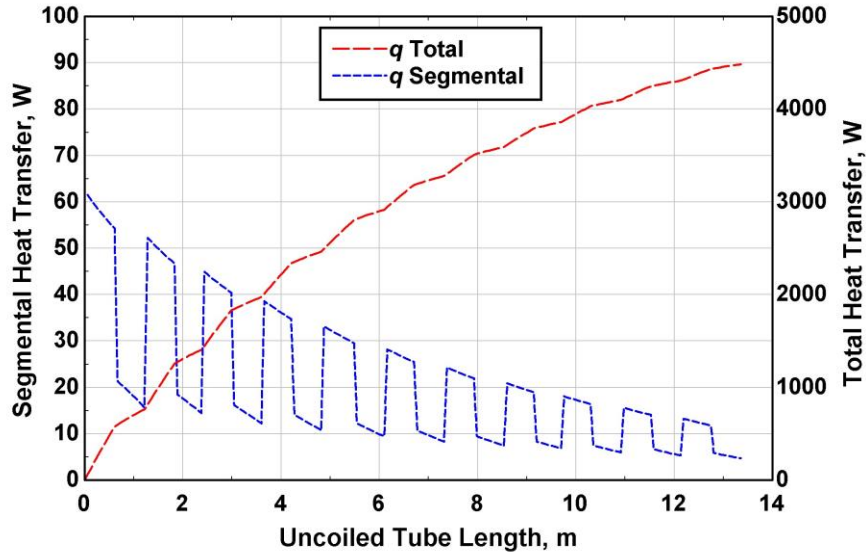
$$q_{\text{sg}} = \dot{m}_{\text{air,sg}} C_{p,\text{air}} (T_{\text{air,out}} - T_{\text{air,in}}) \quad (3.95)$$

An approximated solution temperature can be used to find the inner and outer wall temperatures.

$$q_{\text{sg}} = (T_v - T_{w,i}) / R_{\text{in}} \quad (3.96)$$

$$q_{\text{sg}} = (T_v - T_{w,o}) / (R_{\text{in}} + R_{\text{cond}}) \quad (3.97)$$

Tube conductivity values are obtained at the average of the inner and outer wall temperatures ( $T_{w,i}$ ,  $T_{w,o}$ ) using thermal conductivity data from Touloukian *et al.* (1970), implemented in the *Engineering Equation Solver* software platform. The segmental and total heat transfer rates in the 394-FPM absorber are shown in *Figure 3.18*.

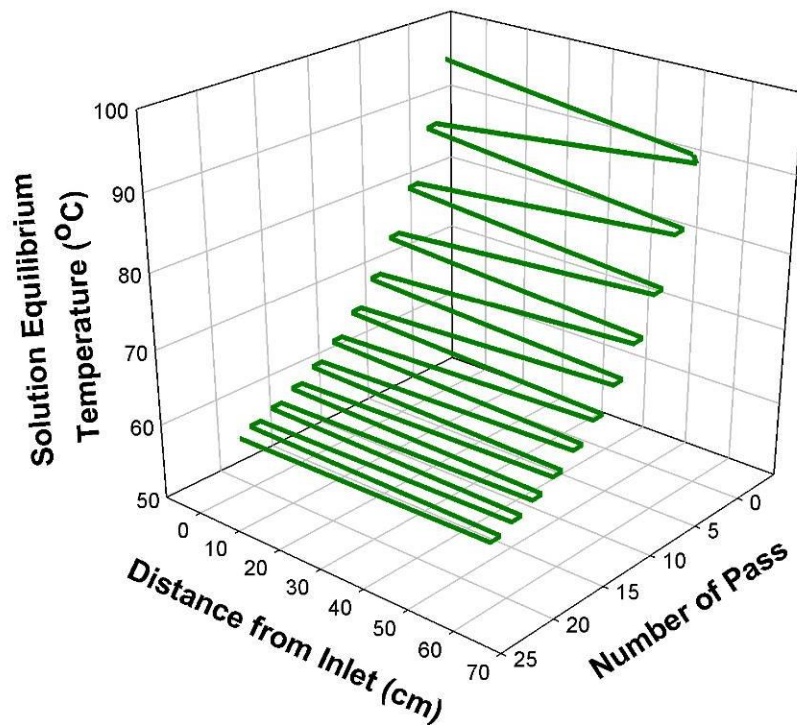


**Figure 3.18 Segmental (left) and total (right) heat transfer rate as a function of distance along uncoiled tube in the 394-FPM absorber**

The x-axis corresponds to the length along the absorber tubing, as if the coil were unwound into one straight tube. The segmental heat transfer (blue) decreases along the uncoiled length of the tube as a result of the diminishing driving temperature difference between the solution and the air and due to the transition to unfavorable flow regimes. The serrations in the segmental heat transfer demonstrate the changing heat transfer rate between the frontal and rear passes, which receive air at different temperatures. Each frontal tube row receives unheated inlet air ( $51.7^{\circ}$ ), leading to a high heat transfer rate compared to the rear tube rows, which receive heated inlet air ( $57\text{-}80^{\circ}\text{C}$ ) that results in a reduced driving temperature difference. This effect is discussed further in the next

subsection that addresses the corresponding temperature variations. The total heat transfer (red) is the sum of the segmental heat transfer rates, and approaches 4.496 kW for the 394-FPM absorber.

A three-dimensional plot of the solution equilibrium temperature during absorption is shown in *Figure 3.19*. The plot demonstrates the decrease in solution temperature across each pass as the flow serpentine down the absorber.



**Figure 3.19** 3-D Plot of solution equilibrium temperature in 394-FPM absorber

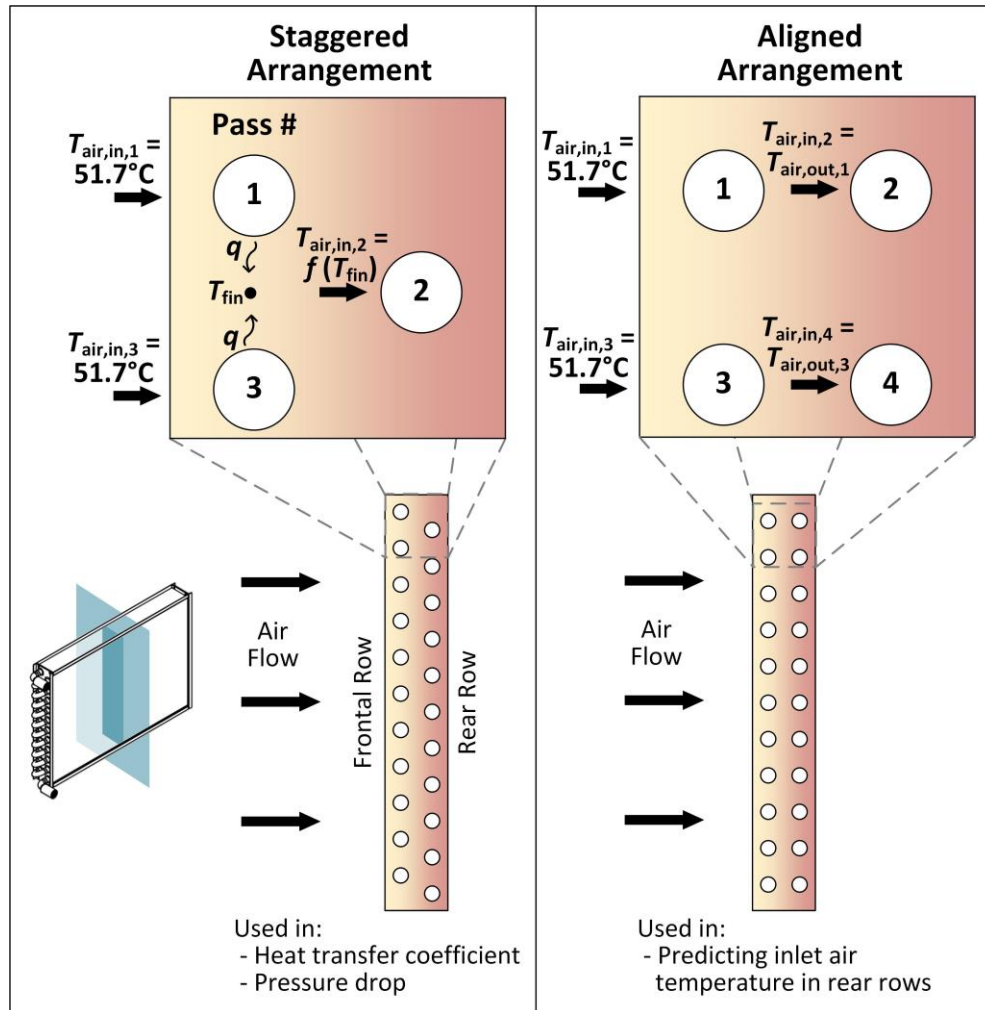
### **3.6.1.8.      *Temperature Variation in Segmental Modeling***

The air-side heat transfer and pressure-drop predictions used here account for the number of tube rows/columns, tube spacing, fin spacing, wavy fin patterning, and the staggered arrangement of tube rows. Staggered and aligned tube arrangements are shown *Figure 3.20*. Although the heat transfer coefficient includes the effect of two tube rows in

the airflow direction, the analysis described above does not address the variation in inlet air temperature resulting from the frontal or rear positioning of the tube row. The first row of tubes, exposed to unheated inlet air, is expected to have the same inlet air temperature (51.7°C). The rear tube row is downstream (33 mm) from the frontal row, and is expected to have higher inlet air temperatures as a result of heat received from upstream tube and finned surfaces.

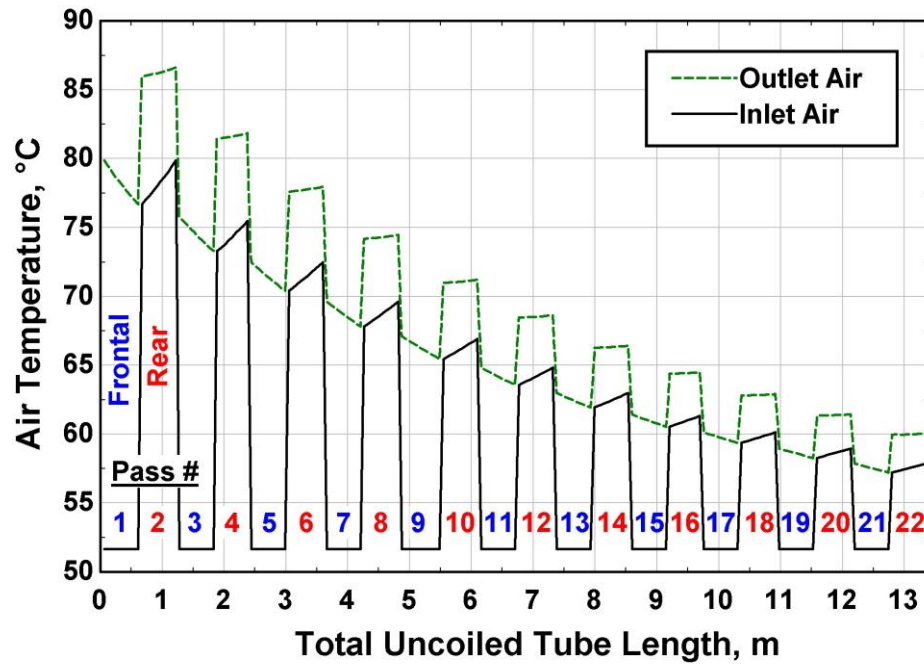
Due to the serpentine flow of solution, the air temperature in the core is expected to vary laterally and vertically across the face area. In the staggered arrangement, a prediction of the inlet air temperature in the rear row requires an estimation of the upstream fin temperature (*Figure 3.20*). At a particular location, this upstream fin temperature is dependent on heat exchange from the adjacent upper and lower frontal tubes, as well as from the rear tube. Accurate predictions of the air temperature approaching the rear tube in a particular segment necessitates information from surrounding tube rows (*i.e.*, previous and upcoming segments). An estimation of the effect of this air temperature variation on heat transfer rate is included in the present analysis. It is assumed that the inlet air to a segment in the rear row is at the air exit temperature from the segment in the previous (frontal) pass at the same lateral position.

In the present analysis, the inlet air temperature between passes is based on an absorber with an aligned arrangement of tubes, as shown in *Figure 3.20*.



**Figure 3.20 Tube arrangement schematic showing approach for predicting effect of air temperature variation**

The predicted heat transfer rate accounting for air temperature variation using an aligned bank of tubes is expected to be a good approximation of the heat transfer in the 394-FPM and 551-FPM absorbers. Half of the passes receive unheated inlet air ( $51.7^{\circ}\text{C}$ ), while the rear passes receive air at the temperature exiting the frontal passes. The inlet air to a segment in a rear tube row uses the outlet air temperature calculated from a segment in the previous frontal pass, located at the same lateral position along the width of the face area (Figure 3.21).



**Figure 3.21 Inlet and outlet air temperatures as a function of the total uncoiled tube length of the absorber**

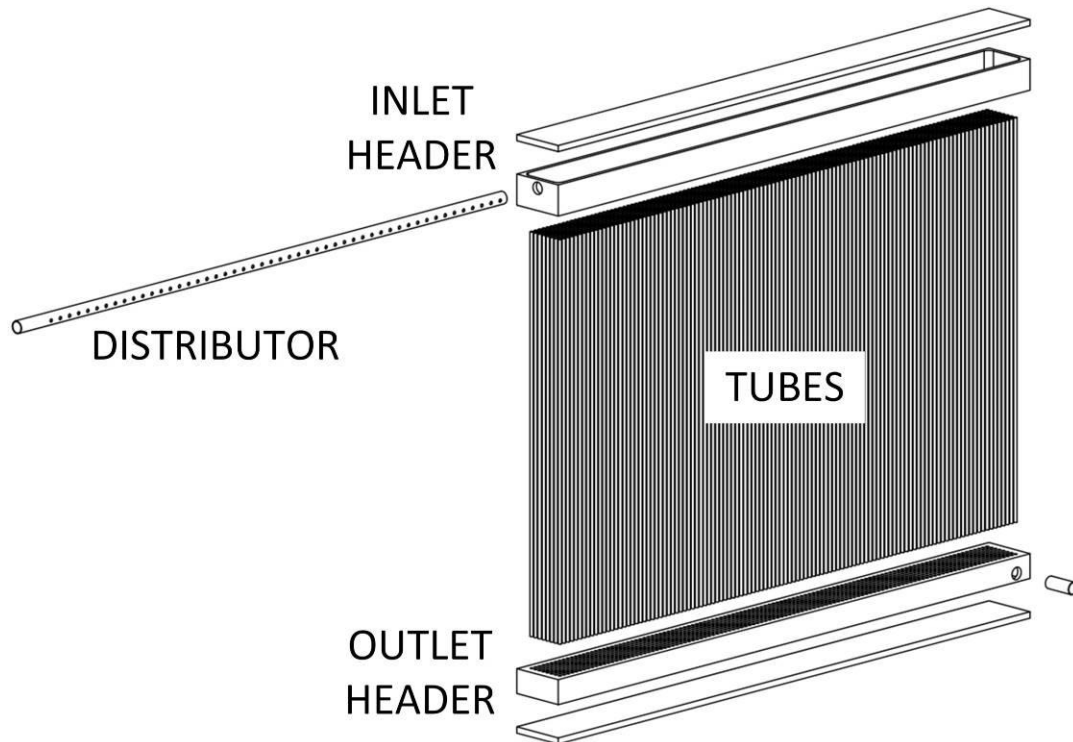
The odd-numbered passes correspond to frontal tubes, which receive incoming air at 51.7°C. The even-numbered passes correspond to rear tubes that are exposed to the same air temperature profile exiting the previous pass; this is evident in the equivalent slopes of the frontal row outlet air temperature and subsequent rear inlet air temperature shown in *Figure 3.21*. This method accounts for lateral and vertical variation in air temperature entering the rear tube row. The heat transfer rate in the 394-FPM absorber using the present in-line tube-array assumption is predicted to be 4.496 kW. Because the inlet air to the rear tube row is expected to be cooler in reality than the air exiting the frontal tube row, this assumption may slightly under-predict absorber performance. Nevertheless, this in-line air temperature assumption is expected to be a better predictor of performance (4.496 kW) than the uniform fresh-air (5.030 kW) and preheated (4.284

kW) assumptions. The in-line air temperature method described above is used in the comparisons with data presented in Chapter 5.

### **3.6.2 Prototype Tube-Array Segmental Modeling**

The prototype tube-array absorber is designed to reduce hydraulic diameter and internal thermal resistance using wetted materials compatible with ammonia-water. With a width of 0.634 m, a height of 0.387 m, and a depth of 0.057 m, the air flow area is similar to that of the conventional absorber flow area ( $W = 0.610$  m,  $H = 0.419$  m,  $D = 0.066$  m). The absorber includes a finless bank of 912 stainless tubes with a 2.159 mm inner diameter (3.175 mm *OD*). The  $8 \times 114$  tube array delivers heat to air in crossflow in a single pass. The external surface areas of the conventional and prototype absorber are  $11.70 \text{ m}^2$  and  $3.52 \text{ m}^2$ , respectively. To help reduce problems with flow distribution, the absorber is oriented for vertical flow with the flow tubes designed to protrude the same distance (6.4 mm) into the header. An inlet distributor tube carries the two-phase flow into the header and distributes it across the inlet header. The entering flow splits into tubes in the array, rejects heat in downward flow, and recombines in the outlet header. An exploded view of the absorber (*Figure 3.22*), a close-up view of the header and distributor before assembly (*Figure 3.23*), and a photograph of the assembled component (*Figure 3.23*) are provided.

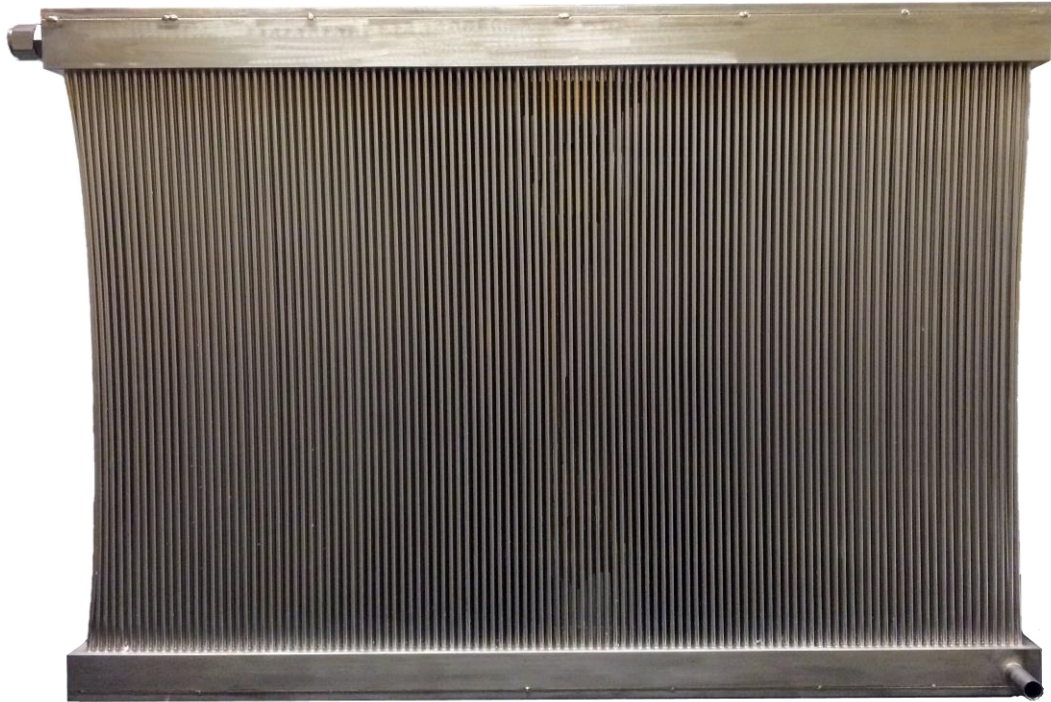




**Figure 3.22 Exploded view of prototype absorber**



**Figure 3.23 Close-up photograph of header and distributor before assembly**



**Figure 3.24 Photograph of assembled prototype tube-array absorber**

The heat and mass transfer analysis for the prototype tube-array absorber is similar to the procedure listed above for the round-tube corrugated-fin heat exchanger. The design features eight rows of tubes in the air-flow (longitudinal) direction. A thorough analysis requires that the air outlet temperature from each row be used as the inlet air temperature for the subsequent row.

In addition, the total flow rate and vapor/liquid fraction of incoming liquid and vapor must be evenly distributed between all tubes in the bank. The segmental model developed here treats each tube row in the air flow direction independently. The first tube row encountered by the air is divided into  $\geq 200$  segments vertically beginning at the top of the tube. The heat and mass transfer is determined across the length of the heat exchanger, and the total heat transfer rate in the tube row is calculated. The outlet air temperatures from the first row are then input as the inlet air temperature for the second

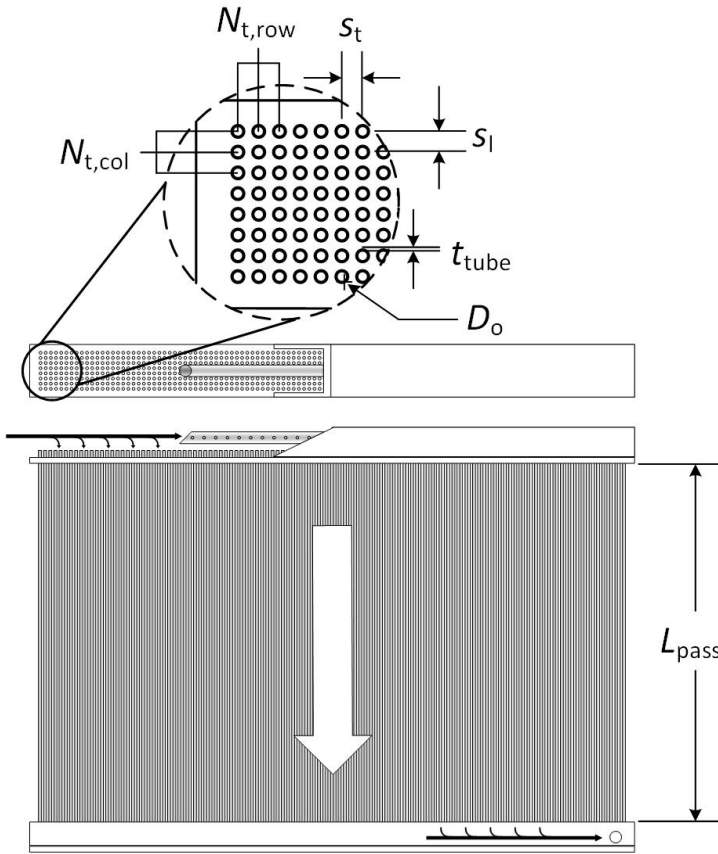
row, and the segmental analysis continues. The total heat transfer rate in the absorber is the sum of the heat transfer rates in the eight rows. The model assumes even distribution of liquid and vapor in all of the tubes and does not account for any heat of absorption that may occur in the inlet or outlet headers. The inlet air is also assumed to have a uniform temperature and flow rate. Geometric inputs and inlet conditions (Table 3.8), as shown in Figure 3.25, are used to begin the modeling process. The inlet conditions correspond to the single-pressure test facility design conditions, as discussed in the discussion of the conventional absorber modeling.

**Table 3.8 Prototype absorber geometric inputs**

Geometry	
$L_{sg}$ (m)	0.025
$D_o$ (m)	$3.175 \times 10^{-3}$
$t_{tube}$ (m)	$5.08 \times 10^{-4}$
$L_{pass}$ (m)	0.387
$N_{t,row}$ (-)	114
$N_{t,col}$ (-)	8
$s_t$ (m)	$5.588 \times 10^{-3}$
$s_l$ (m)	$5.588 \times 10^{-3}$
$\varepsilon_{rough}$ (m)	$1.0 \times 10^{-5}$
Inner Surface Area	2.40 m <sup>2</sup>
Outer Surface Area	3.52 m <sup>2</sup>
Mass	26.1 kg
Header Material	303 SS
Tube Material	304 SS

**Prototype absorber inlet conditions**

Refrigerant Vapor Inlet Conditions	
$T_{v,in}$ (°C)	97.60
$P_{v,in}$ (kPa)	591.8
$x_{v,in}$ (-)	0.877
$\dot{m}_{v,in,total}$ (kg s <sup>-1</sup> )	$2.32 \times 10^{-3}$
Dilute Solution Inlet Conditions	
$T_{l,in}$ (°C)	97.49
$P_{l,in}$ (kPa)	591.8
$x_{l,in}$ (-)	0.235
$\dot{m}_{l,in,total}$ (kg s <sup>-1</sup> )	$5.68 \times 10^{-3}$
Inlet Air Conditions	
$\dot{V}_{air}$ (m <sup>3</sup> s <sup>-1</sup> )	<b>0.425</b>
$T_{air,in}$ (°C)	<b>51.67</b>
$P_{air,in}$ (kPa)	<b>101.3</b>
$RH_{air,in}$ (-)	<b>0.18</b>



**Figure 3.25 Prototype absorber schematic**

### **3.6.2.1. Tube-Side Heat Transfer**

The segmental analysis predicts the performance of each of the eight tube rows independently; thus, the liquid and vapor entering the absorber header must be divided appropriately.

$$\dot{m}_{l,in} = \dot{m}_{l,in,total} / N_{t,col} \quad (3.98)$$

$$\dot{m}_{v,in} = \dot{m}_{v,in,total} / N_{t,col} \quad (3.99)$$

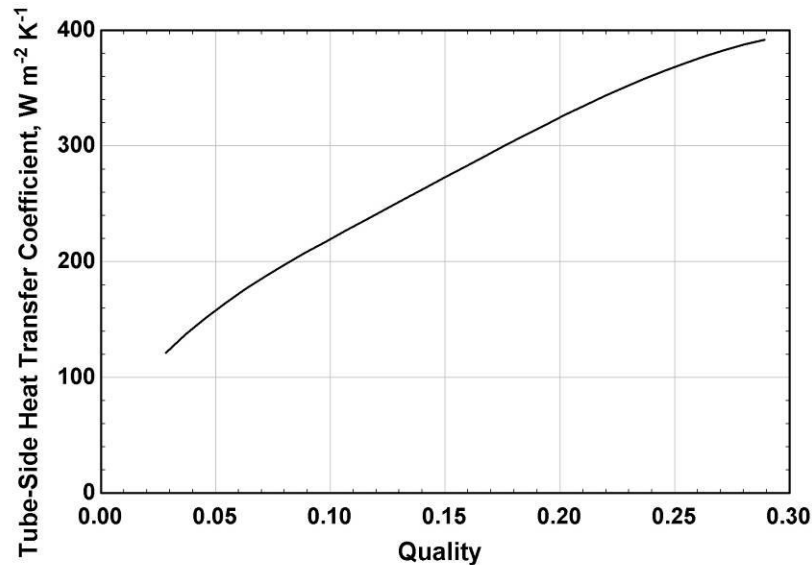
In addition, the solution flow area ( $A_1$ ) and surface area in contact with air ( $A_{total,sg}$ ) must incorporate the area available across the entire row of 114 tubes.

$$A_1 = \frac{\pi}{4} N_{t,row} D_1^2 \quad (3.100)$$

$$A_{\text{bare,tube,sg}} = \pi D_o L_{\text{sg}} N_{\text{t,row}} \quad (3.101)$$

$$A_{\text{total,sg}} = A_{\text{bare,tube,sg}} \quad (3.102)$$

The remaining tube-side heat transfer calculations are identical to those described in Section 3.6.1.1. The solution mass flux used in the liquid-only heat transfer coefficient calculations is determined using the internal flow area for the entire tube row (3.100). The liquid-only heat transfer coefficient is then inserted into the Shah (1979) correlation. It should be noted that the multitude of flow paths in the tube-array condenser results in a mass flux below the range recommended by Shah (1979).



**Figure 3.26 Tube-side heat transfer coefficient predicted in tube-array absorber**

Figure 3.26 shows the reduction in tube-side heat transfer coefficient during absorption. The coefficient is plotted as a function of the quality along the length of the tube-array absorber. The model predicts that the solution will not reach the saturated liquid condition given the designed absorber heat transfer area.

### **3.6.2.2. Tube-Side Pressure Drop**

The internal pressure drop predicted in the prototype tube-array absorber is composed of frictional, deceleration, and gravitational components. There is also a drop in pressure expected due to the contraction of flow in the header to the individual tube ports. Similarly, the solution expands into an outlet header at the exit of the tubes. Yin *et al.* (2002) conducted an investigation of single-phase pressure drop measurements in microchannel heat exchangers in which an array of tubes protrude into an inlet and outlet header. In that study, the drop in pressure expected during the contraction of the flow into the tube was determined using the ratio of the header cross-sectional area to a single microchannel tube area,  $\gamma_{\text{hdr,tube}}$ .

$$\Delta P_{\text{con,hdr,tube}} = \frac{G_{\text{sol}}^2}{2\rho_{\text{in}}} (\xi_{\text{con}} + 1 - \gamma_{\text{hdr,tube}}^2) \quad (3.103)$$

The ratio of the header area to a single microchannel,  $\gamma_{\text{hdr,tube}}$ , is 0.003. A similar expression was used to determine the pressure rise during expansion in the outlet header by Yin *et al.* (2002). A quick calculation shows that in the present case, the mass flux is sufficiently low ( $2.396 \text{ kg m}^{-2} \text{ s}^{-1}$ ) to neglect the pressure drop due to contraction into and expansion from the tubes ( $\Delta P_{\text{con,hdr,tube}} \approx 0.3 \text{ Pa}$ ). The ratio of the header cross-sectional area to the solution flow area in the entire tube array is 2.76. The pressure changes associated with the expansion from the inlet tube to the header and the contraction from the outlet header to the outlet tube are also negligible. Thus, only the frictional, deceleration, and gravitational components of pressure drop are included.

$$\Delta P_{\text{sol,sg}} = \Delta P_{\text{fric,Friedel}} + \Delta P_{\text{dec}} + \Delta P_{\text{grav}} \quad (3.104)$$

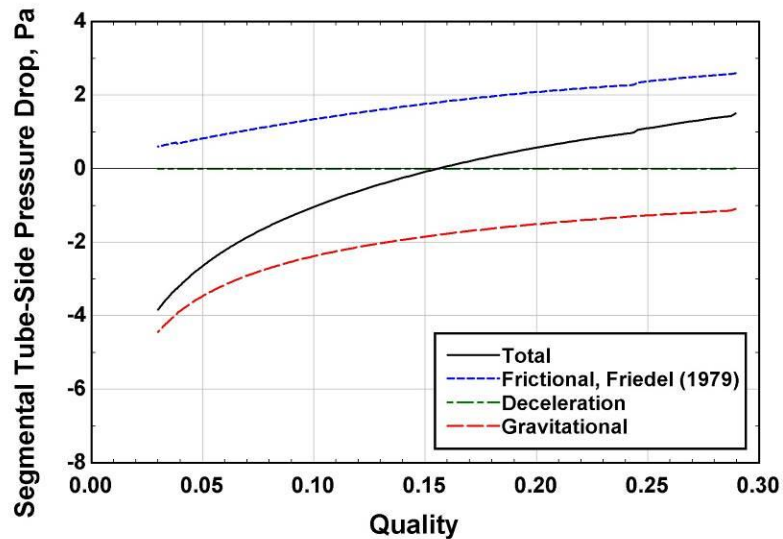
The two-phase multiplier used in calculating the frictional component of the pressure drop must be determined for downward vertical, rather than horizontal, flow. Friedel (1979) provides the following expressions, including a parameter adjusted for vertical downward flow,  $C_{F2,down}$ .

$$C_{F1} = (1 - q_{sol})^2 + q_{sol}^2 \left( \frac{\rho_l}{\rho_v} \right) \left( \frac{f_{vo}}{f_{lo}} \right) \quad (3.105)$$

$$C_{F2,down} = q_{sol}^{0.8} (1 - q_{sol})^{0.29} \left( \frac{\rho_l}{\rho_v} \right)^{0.9} \left( \frac{\mu_v}{\mu_l} \right)^{0.73} \left( 1 - \frac{\mu_v}{\mu_l} \right)^{7.4} \quad (3.106)$$

$$\phi_{lo,Friedel,down} = \sqrt{C_{F1} + \frac{48.6 C_{F2,down} Fr^{0.03}}{We^{0.12}}} \quad (3.107)$$

All other aspects of the pressure drop calculations remain the same as those outlined in the corrugated-fin absorber discussion. Due to the low flow rates in the tubes, the frictional component of the pressure drop is minor compared to the gravitational component (*Figure 3.27*).



**Figure 3.27 Segmental differential pressure in the first row of the tube-array absorber**

The differential pressure in each segment depends on the length of the segment; *Figure 3.27* is intended for the comparison of the different components of pressure drop. The negative pressure drop values indicate that the pressure is actually rising during some portions of the heat exchanger. The model predicts that the pressure at the outlet of the tube-array absorber will be approximately 246 Pa higher than the pressure at the inlet.

### **3.6.2.3. Air-Side Heat Transfer**

Without fins, the tube-array absorber relies on the increased flow velocity of air in a dense bank of tubes for air-side heat transfer. The Zukauskas (1973) correlation for flow over a bank of tubes is used. The maximum velocity of air is calculated at the minimum flow area:  $u_{\max} = \dot{V}_{\text{air}}/A_c$ . The minimum flow area ( $A_c$ ) is defined as the open air flow area between the tubes:  $A_c = (W_{\text{face}} - N_{\text{t, row}} D_o) H_{\text{face}} = 0.106 \text{ m}^2$  where  $W_{\text{face}}$  is the width of the available flow area 0.635 m. The Reynolds number can then be used to select inputs for the Nusselt number calculation.

$$\text{Re}_{D,Z} = \rho_{\text{air}} u_{\max} D_o / \mu_{\text{air}} \quad (3.108)$$

$$\text{If } (\text{Re}_{D,Z} < 100): C = 0.8, m = 0.4$$

$$\text{If } (100 < \text{Re}_{D,Z} < 1,000): C = 0.683, m = 0.446$$

$$\text{If } (1,000 < \text{Re}_{D,Z} < 200,000): C = 0.27, m = 0.63$$

$$\text{Else } (\text{Re}_{D,Z} > 200,000): C = 0.021, m = 0.84$$

$$Nu_{D, \text{Nr} > 20} = C \text{Re}_{D,Z}^m \text{Pr}_{\text{air}}^{0.36} \left( \frac{\text{Pr}_{\text{air}}}{\text{Pr}_s} \right)^{1/4} \quad (3.110)$$

Finally, a correction factor can be applied for fewer than 20 tube rows in the direction of air flow. Values of  $C_2$  can be looked up at a given number of tube rows (Zukauskas, 1973).



$$Nu_{D,Nr<20} = C_2 Nu_{D,Nr>20} \quad (3.111)$$

$$\alpha_{\text{air,Zukauskas}} = (Nu_{D,Nr<20} k_{\text{air}}) / D_o \quad (3.112)$$

The resulting air-side heat transfer coefficient is approximately  $94.5 \text{ W m}^{-2} \text{ K}^{-1}$ ; this varies slightly with the air temperature through the tube array. The predicted air-side heat transfer coefficient for the prototype is 31% higher than the value predicted for the 394-FPM corrugated-fin absorber ( $72.3 \text{ W m}^{-2} \text{ K}^{-1}$ ).

#### **3.6.2.4. Air-Side Pressure Drop**

For an unfinned bank of tubes in crossflow, the entrance and exit effects of contraction and expansion are typically already accounted for in the frictional pressure drop correlations (Kays and London, 1984). The air-side pressure drop then consists only of frictional and acceleration components.

$$\Delta P_{\text{air}} = \Delta P_{\text{air,fric}} + \Delta P_{\text{air,accel}} \quad (3.113)$$

The acceleration component of the differential pressure is calculated in the same manner as described for the round-tube corrugated-fin absorbers. The frictional pressure drop consists only of the friction over the bank of tubes ( $\Delta P_{\text{air,fric}} = \Delta P_{\text{air,t}}$ ), determined again using the correlation from Zukauskas *et al.* (1968). The predicted air-side pressure drop in the tube-array absorber is approximately 19.6 Pa, compared to 27.2 Pa in the 394-FPM corrugated-fin absorber (−28% change).

#### **3.6.2.5. Mass Transfer**

The Silver-Bell-Ghaly method is used to calculate the heat transfer resistance resulting from the concentration gradient in the vapor, as described in the conventional

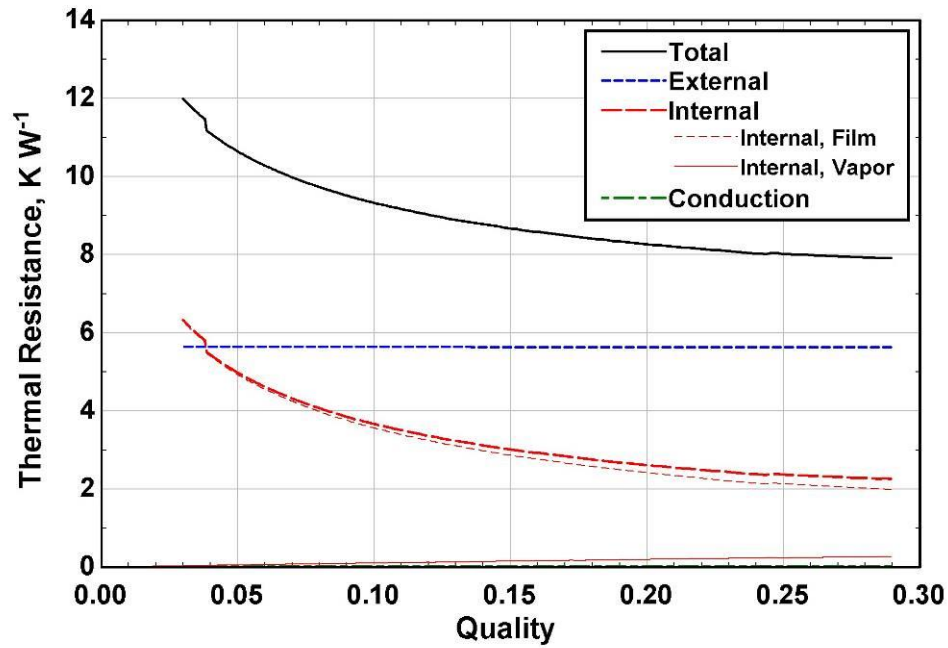
absorber modeling section. The sensible heat from the vapor is calculated following the procedure from Colburn and Drew (1937), which yields the outlet vapor conditions. The Chilton and Colburn heat and mass transfer analogy is used to determine the condensing flux of the ammonia and water in each segment.

### **3.6.2.6. Thermal Resistance Circuit**

The thermal resistance circuit presented in 3.6.1.7 also applies here, with the surface efficiency term absent in the external thermal resistance ( $R_{\text{out}} = 1/\alpha_{\text{air}} A_{\text{total,sg}}$ ). In the prototype absorber, the absence of fins enables the mixing of the air, while the parallel flow of solution in the tube array prevents mixing internally. Therefore, a different effectiveness- $NTU$  correlation is used here than the expression shown in the corrugated-fin absorber modeling (Incropera *et al.*, 2011).

$$\varepsilon = 1 - \exp\left(-C_r^{-1} \left[1 - \exp(-C_r \cdot NTU)\right]\right) \quad (3.114)$$

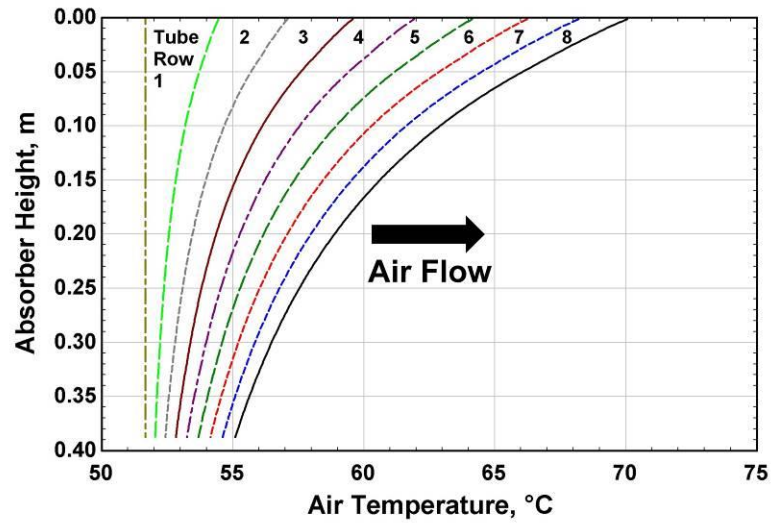
The resulting thermal resistances during absorption are shown in *Figure 3.28*.



**Figure 3.28 Thermal resistance during absorption in the first row of the tube-array absorber**

According to the model, the high internal resistance region is absent because complete absorption and the corresponding low qualities are not achieved in this absorber. The heat transfer of the prototype is predicted to be limited by the air side throughout absorption.

*Figure 3.29* demonstrates the evolving temperature profile of the air over the tube banks. The air at the top of the absorber receives the most heat due to the high-temperature solution entering the tubes at the top.



**Figure 3.29 Temperature profiles across prototype absorber tube rows**

Chapter 5 presents a comparison of the model predictions with the data from experiments on the conventional and prototype absorbers.

## CHAPTER 4: EXPERIMENTAL APPROACH

The fabrication of the air-coupled absorbers, the design and construction of the air-coupled test facility, and a brief description of the experimental procedures are presented in this chapter.

### 4.1 Air-Coupled Absorber Fabrication

During the design and fabrication of the air-coupled absorbers, consideration was given to the cost of machining and assembly, material compatibility, internal pressure, total mass, and anticipated tube-side and air-side pressure drop. A novel tube-array prototype absorber was fabricated and compared to a conventional corrugated-fin round-tube air coil. Both components were custom designed to fit in a compact small-capacity absorption heat pump operating at extreme ambient conditions.

#### 4.1.1 Round-Tube Corrugated-Fin Absorber

Following the modeling procedure discussed in Chapter 3, the conventional absorber was designed to most effectively reject heat to the ambient. Two air coils were fabricated with fin densities of 10- and 551-FPM to determine the impact of additional air-side heat transfer area on absorber performance. This predicted improvement in the higher fin density absorber was accompanied by additional air-side pressure drop and weight. The different air-side pressure drop and heat duties for the two fin densities allows the heat pump designer to choose a fin density that would result in the needed heat rejection for an acceptable fan power consumption.

The round-tube corrugated-fin absorbers were fabricated by Custom Air Coolers, a division of Super Radiator Coils. Discussions with the air coil manufacturer were held

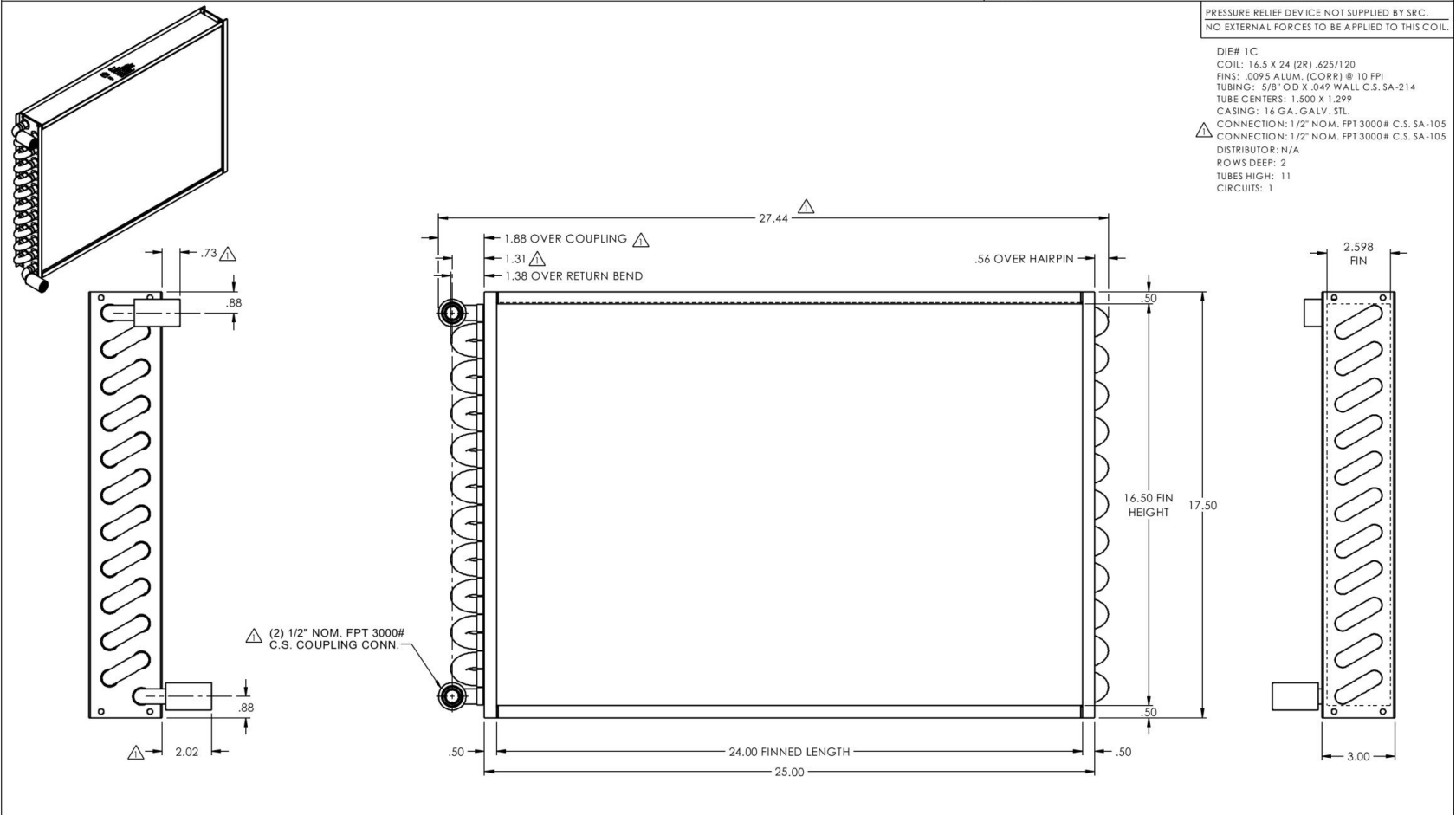
to determine the maximum possible fin density (551-FPM), minimum tube spacing (based on minimum bending radius), and the availability of fin patterns. Based on these manufacturing constraints, engineering drawings are shown in *Figure 4.1*, and the air coils were fabricated. *Figure 4.1* contains the drawing of the 394-FPM absorber; the 551-FPM absorber is identical except for the adjusted fin pitch. Upon receipt, each coil was pressure tested to 4482 kPa, beyond the operating pressure (592 kPa), to ensure the absence of leaks upon charging.

BUILT IN ACCORDANCE WITH ASME SECTION VIII, DIVISION 1, 2010/2011 ADDENDA - UM STAMP

MAX. ALLOWABLE WORKING PRESSURE: 500 PSIG @ 200°F NDE REQUIREMENTS: NONE  
 MIN. DESIGN METAL TEMPERATURE: -20°F @ 500 PSIG PWHT REQUIREMENTS: NONE  
 PRESSURE TEST: HYDROSTATIC @ 650 PSIG CORROSION ALLOWANCE: NONE

PRESSURE RELIEF DEVICE NOT SUPPLIED BY SRC.  
 NO EXTERNAL FORCES TO BE APPLIED TO THIS COIL.

DIE# 1C  
 COIL: 16.5 X 24 (2R) .625/120  
 FINS: .0095 ALUM. (CORR) @ 10 FPI  
 TUBING: 5/8" OD X .049 WALL C.S. SA-214  
 TUBE CENTERS: 1.500 X 1.299  
 CASING: 16 GA. GALV. STL.  
 CONNECTION: 1/2" NOM. FPT 3000# C.S. SA-105  
 CONNECTION: 1/2" NOM. FPT 3000# C.S. SA-105  
 DISTRIBUTOR: N/A  
 ROWS DEEP: 2  
 TUBES HIGH: 11  
 CIRCUITS: 1



TOLERANCES: X.XXX +/- 0.13 ANGULAR +/- .1° X.XXX +/- 0.06 [ ] = +/- .005 NON-CUMULATIVE UNLESS OTHERWISE STATED		TC 1 APPD DFT REV#	CHANGED COUPLING FROM 3/4" REVISION	11-1-13 DATE	ENGINEERED AIR-COOLED HEAT EXCHANGERS A Division Of Super Radiator Coils	customaircoolers.com 2822 S. 21ST STREET PHOENIX, ARIZONA 85034	DATE: 10-23-13 DESIGNED BY: PM APPROVED BY:	DESCRIPTION: 16.5 X 24 (2R) .625/120 CONDENSER CUSTOMER: GEORGIA TECH	DWG NO. B46-12297 REV.1
--	--	-----------------------	--	-----------------	--	---	---	--	----------------------------


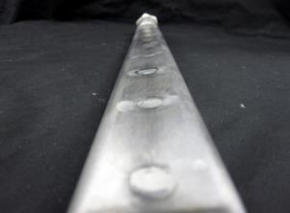
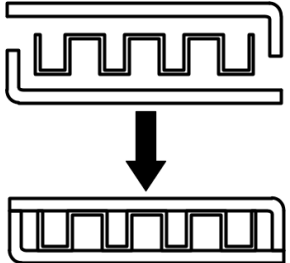
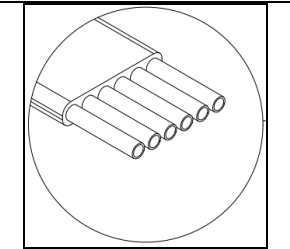
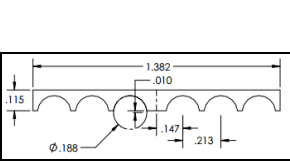

Figure 4.1 Drawing of 394-FPM round-tube corrugated-fin absorber

#### **4.1.2 Prototype Tube-Array Absorber**

A novel air-coupled absorber was developed in an attempt to enhance heat transfer through a reduction in hydraulic diameter and internal thermal resistance. *Table 4.1* lists the air-coupled absorber designs considered. Initial designs were focused on developing geometries that resembled the compact flat-tube louvered fin air coils used in automotive condensers. Such compact flat-tube geometries are typically fabricated in aluminum, which would corrode in contact with ammonia-water mixtures. Round carbon steel tubes were flattened in an attempt to obtain flat tubes for brazing with louvered fins. Without internal structural support through webbing or other similar features, these flattened tubes were susceptible to bloating under an applied internal pressure. To improve the capability of the flat carbon steel tube to withstand internal pressures, holes were drilled, and carbon steel pins were welded intermittently along the length of the flat tubes. The result was reduced and intermittent tube bloating upon pressurization. It was determined that the welding of these support pins did not effectively solve the problem of deformation and required an additional fabrication step that would increase component cost with perhaps decreased reliability.



**Table 4.1 Designs with steel-wetted configurations considered for ammonia-water absorber**

Proposed Design	Image	Advantages	Disadvantages
Flattened carbon steel tubes with brazed louvered fins		<ul style="list-style-type: none"> <li>• Use of pre-existing fabrication techniques</li> </ul>	<ul style="list-style-type: none"> <li>• Significant tube bloating under applied internal pressure</li> </ul>
Flattened carbon steel tubes with welded pins for support, brazed to louvered fins		<ul style="list-style-type: none"> <li>• Improved internal pressure withstanding capability</li> </ul>	<ul style="list-style-type: none"> <li>• High labor and fabrication cost</li> <li>• Intermittent swelling of tube</li> </ul>
Brazing of carbon steel shims with internal fins, brazed to external louvered fins		<ul style="list-style-type: none"> <li>• Effective heat transfer-to-flow area ratio</li> <li>• Likely to maintain shape with internal pressure</li> </ul>	<ul style="list-style-type: none"> <li>• Risk of leak along continuous brazed tube seam</li> <li>• Potential poor fin-to-shim contact</li> </ul>
Casting of small-diameter carbon/stainless steel tubes in aluminum, brazed to louvered fins		<ul style="list-style-type: none"> <li>• Effective heat transfer to flow area ratio</li> <li>• Ability to withstand internal pressure</li> </ul>	<ul style="list-style-type: none"> <li>• Very high set-up cost</li> <li>• Two steps: channel casting and assembly brazing</li> </ul>
Riveting of small-diameter carbon/stainless steel tubes in aluminum, brazed to louvered fins		<ul style="list-style-type: none"> <li>• Ability to withstand internal pressure</li> </ul>	<ul style="list-style-type: none"> <li>• Milling, riveting, and brazing</li> <li>• Potentially poor contact area</li> </ul>
Brazing dense array small-diameter stainless steel tubes, no fins		<ul style="list-style-type: none"> <li>• No fins to increase air-side heat transfer area</li> </ul>	<ul style="list-style-type: none"> <li>• One-step assembly</li> <li>• Pre-existing fabrication methods</li> </ul>

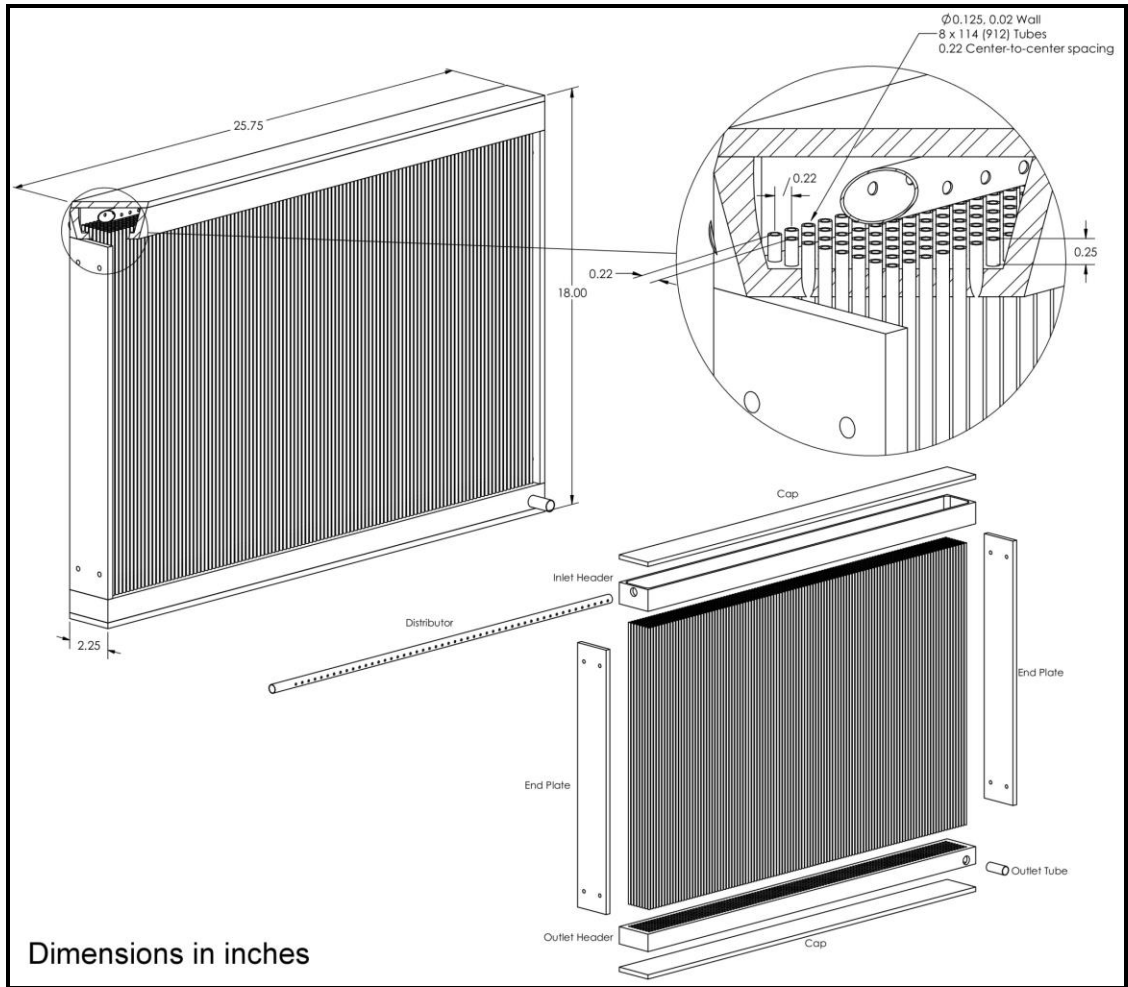
The intermittent swelling of the tube indicated the need for continuous internal ribbing along the length of the tube for structural support. One potential solution is the brazing of straight fins between two carbon steel shims to assemble individual ribbed channels. It was decided that the risk of leaks along the continuous brazed seam of the tubes, combined with the multi-step assembly process, did not merit further investigation.

Two designs combined the internal pressure withstanding capability of round tubes with the thermal conductivity and machinability of aluminum. It was proposed that a row of round carbon or stainless steel tubes could be cast in a shim of aluminum, or riveted between shims with milled grooves. However, the cost to set up a mold and procedure for the casting of aluminum was excessive. Meanwhile, the riveted aluminum shims required a time-intensive series of assembly steps: the milling of the aluminum shims, the assembly and riveting of the individual stacks, and the brazing of the channels to the inlet and outlet header. In addition, a thermal grease or paste would be required to help reduce contact resistance between the carbon or stainless steel tubes and aluminum shims.

Finally, it was determined that the brazing of a dense array of small-diameter carbon steel tubes without fins combined the advantages of: a single brazing step for assembly, the use of conventional manufacturing techniques, the high internal pressure capabilities of small diameter round tubes, and a higher predicted air-side heat transfer coefficient over the bank of tubes when compared to the conventional absorber ( $\alpha_{\text{air,prot}} = 94.5 \text{ W m}^{-2} \text{ K}^{-1}$ ;  $\alpha_{\text{air,conventional}} = 72.3 \text{ W m}^{-2} \text{ K}^{-1}$ ).

Initial designs of the tube-array absorber incorporated cylindrical or semi-cylindrical headers that would effectively withstand the operating pressure with minimal

wall thickness. Discussions with machining vendors indicated that it would be difficult to drill consistent holes through a contoured surface, or to produce a smooth plane on the edge of the cylindrical shell required for brazing the header cap. It was determined that the headers would instead be machined out of rectangular blocks of stainless steel. The brazing of the tubes into the header requires capillary action of the brazed alloy, which requires a consistent and appropriately-sized gap between the tube outer surface and hole wall. Due to the limited acceptable variation in gap size, a computerized numerical control (CNC) mill was used to machine the inlet and outlet headers. Rectangular pressure vessel calculations were used to determine the required header wall and cap thicknesses. The tubes were specified to protrude by an equal height into the header to allow the buildup of a liquid pool that would promote the even distribution of liquid in the tube array. The spacing of the tubes was determined based on the allowable air-side pressure drop and the feasibility of brazed alloy application during assembly. A nickel-based brazing alloy was used during bonding for compatibility with ammonia-water. The prototype absorber was designed to fit with framing within the footprint ( $0.71 \times 0.46 \times 0.08$  m) of the conventional corrugated-fin absorbers. Prototype absorber drawings are shown in *Figure 4.2*.



**Figure 4.2 Drawing of prototype tube-array absorber**

## 4.2 Air-Coupled Absorption Test Facility

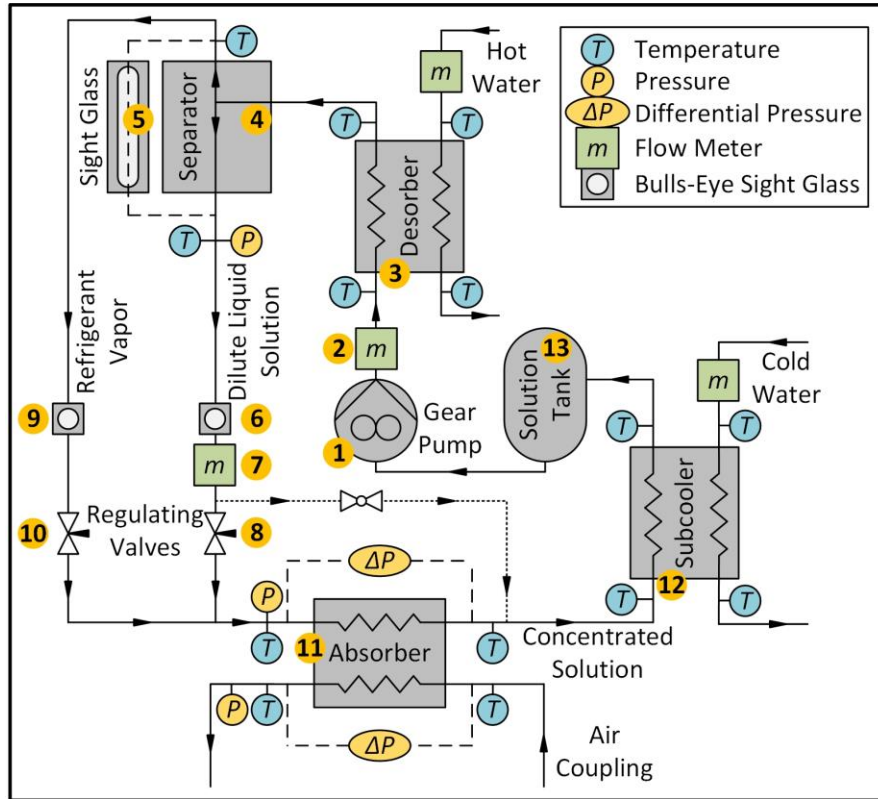
An air-coupled test facility was designed and constructed to test the absorbers at design conditions. To simulate a range of ambient and solution conditions during heat pump operation, the test facility was designed to facilitate the variation of parameters shown in *Table 4.2*.

**Table 4.2 Controllable parameters in air-coupled test facility**

	<b>Name</b>	<b>Description</b>	<b>Means of Adjusting</b>
Air	$T_{\text{air,in}}$	Inlet air temperature	Air handling unit steam/chiller coils
	$\dot{V}_{\text{air,in}}$	Inlet air velocity	Air handling unit fan speed
Solution	$T_{\text{sol,in}}$	Absorber solution inlet temperature	Heater set point temperature (desorber coupling fluid inlet)
	$\dot{m}_{\text{conc}}$	Concentrated solution flow rate	Solution pump speed
	$x_{\text{conc}}$	Concentrated solution concentration	Amount of charge in system

#### 4.2.1 Ammonia-Water Cycle

Evaluation of the absorbers at the exact conditions expected in the heat pump requires the construction of a full two-pressure absorption system. Such a facility would include all heat pump components and introduce significant complexity in the system start-up and shut-down procedures. It would be difficult to directly adjust absorber inlet conditions without indirectly affecting the other system parameters. Absorption chiller control through ambient and conditioned space heat exchange would at best provide indirect control of the absorber conditions, and also restrict the range of possible test conditions to a much small envelope. It was therefore determined for the present investigation that a single-pressure ammonia-water cycle would enable greatest control over absorber inlet conditions without unnecessary complexity (*Figure 4.3*).



**Figure 4.3 Schematic of ammonia-water test facility**

A brief discussion of the ammonia-water test facility and its operation is provided here. Water flows in a loop parallel to the ammonia-water loop and is heated using an electric circulation heater (Watlow CBDNF29R3S). The hot water transfers heat to ammonia-water in the counterflow desorber (Exergy 00677-3 RW) [3 in *Figure 4.3*]. The ammonia-water mixture exits the desorber in cocurrent liquid and vapor streams with low and high concentrations of ammonia, respectively. A separator [4] is used to split the liquid and vapor flow streams, and a sight glass [5] plumbed in parallel is used to verify the liquid level in the separator. The dilute liquid and refrigerant vapor independently flow through Bulls-eye sight glasses [6, 9] for visual confirmation of the state. A regulating valve on each line [8, 10] (Swagelok SS-3NRS4, SS-6NRS8) enables the control of the liquid level in the separator [4]. The liquid and vapor streams combine

before entry into the absorber [11] in which heat is rejected to air in crossflow. Depending on the performance of the absorber, the exiting solution can be in a two-phase or subcooled state. A subcooler (FlatPlate FPN3X8-14) [12] removes heat from the solution exiting the absorber to condense any remaining vapor. A solution tank [13] is used to maintain a liquid inventory upstream of the gear pump (Tuthill TXS2.6EEET3WNB3OCO) [1] to prevent dry-out. The solution flows to the inlet of the desorber to complete the cycle. Flow meters (MicroMotion CMF025M319NU) are located on the dilute [7] and concentrated [2] solution streams, and pressure transducers are located at the separator liquid outlet (Omega PX409-500AI) and absorber inlet (Omega PX409-750AI). The mass flow rate of the refrigerant vapor can be deduced from the difference between the concentrated and dilute solution flow rates. Type-T thermocouples (Omega TMQSS-125G-6: 1°C or 0.75% accuracy) are located between all heat exchangers in the system. Differential pressure transducers are located on the tube side (Omega PX409-015DWUI) and air side (Dwyer 607-3) of the absorber. Accuracy specifications and operating ranges for instrumentation are provided in *Table 4.4* in the discussion of the equipment and instrumentation (4.2.3).

Because a single-pressure test facility was designed, some of the solution inlet conditions to the absorber are different than those specified for the heat pump (*Table 4.3*).

**Table 4.3 Absorber nominal inlet and outlet conditions in heat pump and single-pressure test facility**

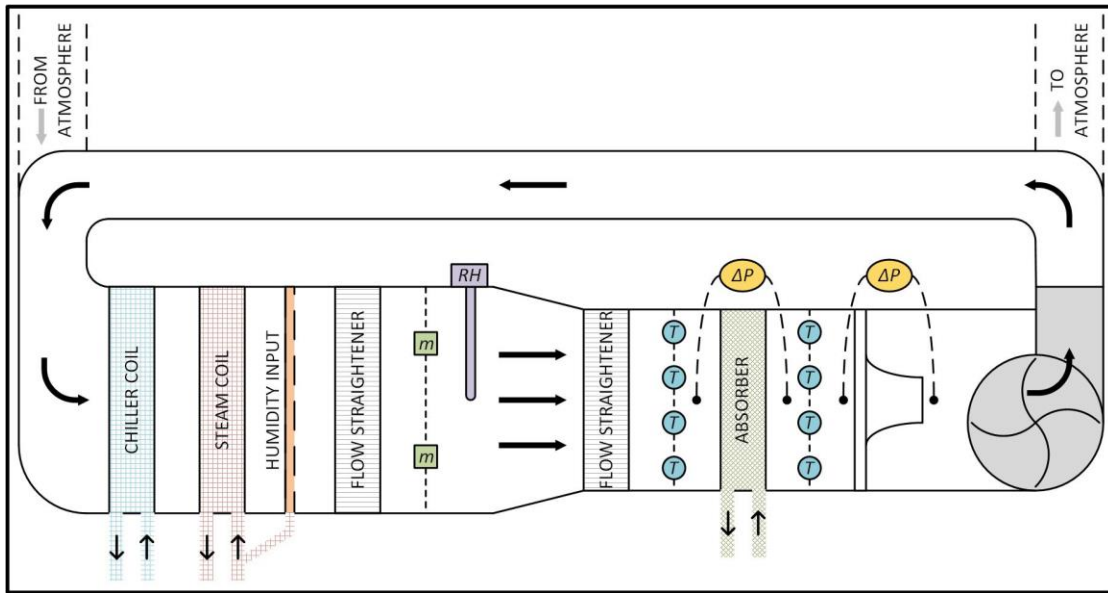
		<b>Heat Pump Conditions</b>	<b>Single-Pressure Facility Conditions</b>
<b>Refrigerant Vapor Inlet</b>	$\dot{m}_{v,in}$ (kg s <sup>-1</sup> )	0.00247	0.00232
	$x_{v,in}$ (-)	<b>0.998</b>	<b>0.877</b>
	$T_{v,in}$ (°C)	<b>57.2</b>	<b>97.6</b>
	$h_{v,in}$ (kJ kg <sup>-1</sup> )	1401	1633
<b>Dilute Solution Inlet</b>	$\dot{m}_{l,in}$ (kg s <sup>-1</sup> )	0.00553	0.00568
	$x_{l,in}$ (-)	<b>0.164</b>	<b>0.235</b>
	$T_{l,in}$ (°C)	97.5	97.5
	$h_{l,in}$ (kJ kg <sup>-1</sup> )	331	264
<b>Concentrated Solution Outlet</b>	$\dot{m}_{out}$ (kg s <sup>-1</sup> )	0.008	0.008
	$x_{out}$ (-)	0.421	0.421
	$T_{out}$ (°C)	56.2	56.2
	$h_{out}$ (kJ kg <sup>-1</sup> )	17	17
<b>Absorber Duty, <math>\dot{Q}_{abs}</math> (kW)</b>		<b>5.149</b>	<b>5.149</b>

Without rectification of the vapor exiting the desorber, the vapor entering the absorber in the present test facility has a lower concentration than in the heat pump (0.877 compared to 0.998). This higher water fraction reduces the mass transfer that can occur in the absorber. To evaluate the absorber for the same total cooling capacity, this decreased mass transfer during testing is accounted for by the larger driving  $\Delta T$  for heat transfer. The inlet vapor temperature, for example, is 97.6°C, compared to 57.2°C in the heat pump. Although the conditions during testing were not identical to those expected during heat pump operation, the absorber was evaluated for the same total heat duty. It is expected that performance in this test facility under these modified operating conditions will still provide good guidance for operation under heat pump operating conditions.



## 4.2.2 Air-Handling Unit

Adjacent to the ammonia-water loop was a previously constructed air-handling unit that preconditions the temperature and humidity of the incoming air. A schematic of the air-handling unit is shown in *Figure 4.4*.



**Figure 4.4** Air-handling unit schematic for absorber testing

A brief discussion of the air-handling unit operation is provided here. A variable-speed fan is used to draw air across a series of measurement and flow preparation devices. The air first encounters a round-tube finned coil that circulates chilled city water for any necessary pre-cooling. The flow can then be heated in crossflow over a steam-carrying air coil. Additionally, a series of ports along the face of the flow area permit the adjustment of humidity through the addition of steam. A flow straightener with an extruded honeycomb-like structure helps promote unidirectional flow. The air then flows over an array of thermal dispersion flow meters (Ebtron GP1 Type B) and a relative humidity sensor (Johnson Controls HE-67P2-0N00P). The flow area is then reduced to match the face area of the air-coupled heat exchanger being tested. The air flows through

a second flow straightener before reaching the inlet face of the absorber. Thermocouple arrays upstream and downstream of the absorber are used to record approximate temperature profiles. The upstream and downstream array each included 16 type-T thermocouple wires (Omega TT-T-30: 1°C or 0.75% accuracy) in a 4×4 grid. Additional details of the thermocouple arrays are provided in Section 4.2.3. A differential pressure transducer (Dwyer 607-3) is mounted with ports just upstream and downstream of the absorber. The differential pressure is also recorded across a nozzle downstream of the absorber (Dwyer 607-4), which can be used to validate the air flow rates measured by the thermal dispersion flow meters. Finally, the air reaches the variable-speed induced draft fan. Automated vents in the ducting can be opened or closed to permit recirculation of air, or air can be drawn from and rejected to the atmosphere. For greater control of the inlet air conditions to the absorber, the air-handling unit was operated in recirculation mode during testing in this study.

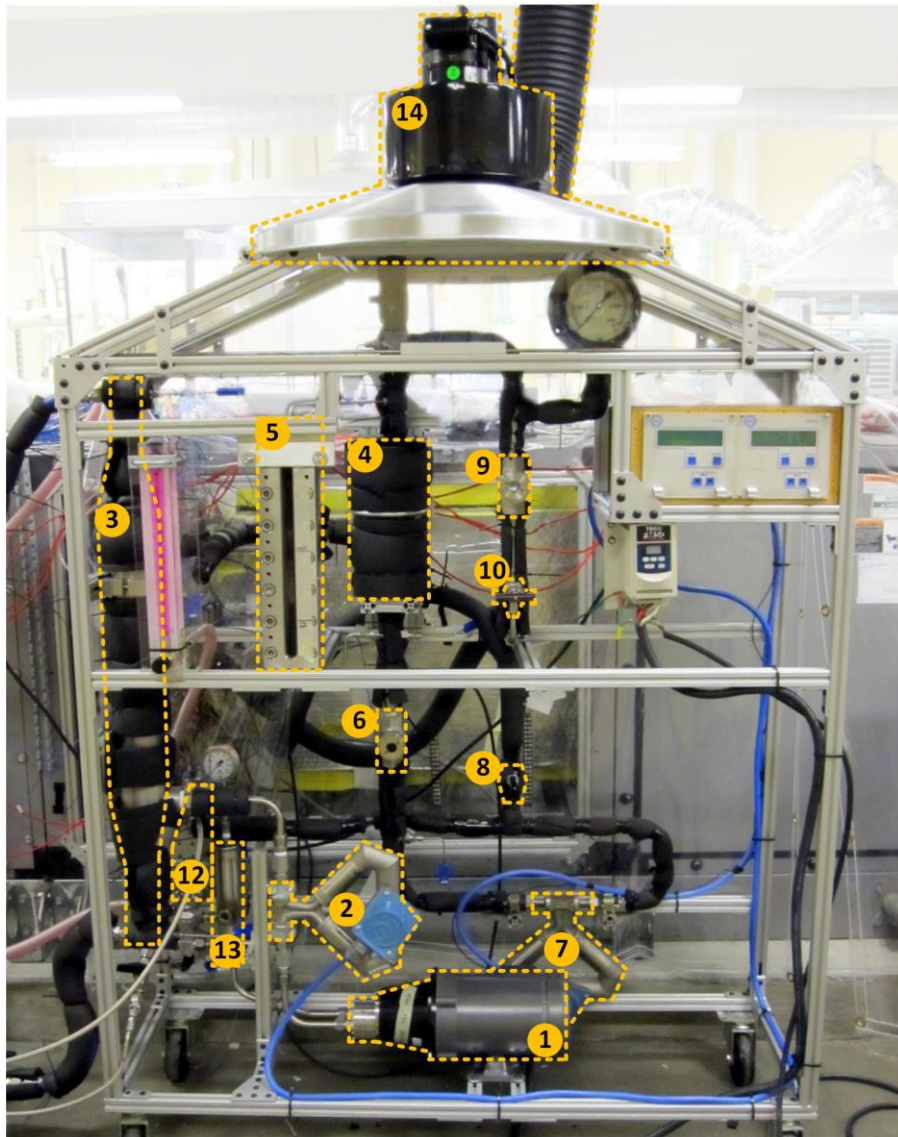
### **4.2.3 Equipment and Instrumentation Overview**

A list of equipment and instrumentation used in the present investigation is provided in *Table 4.4*.

**Table 4.4 Equipment and instrumentation used in absorber testing**

<b>Fluid Loop</b>	<b>Name</b>	<b>Figure Label</b>	<b>Vendor</b>	<b>Model</b>	<b>Range</b>	<b>Accuracy</b>
<b>Ammonia-Water</b>	Solution Gear Pump	1	Tuthill	TXS2.6EEET3WN B3OCO	-	-
	Concentrated Flow Meter	2	MicroMotion	CMF025M319NU	0.60 kg s <sup>-1</sup>	0.1% Reading
	Desorber Shell-and-Tube Separator	3	Exergy	00677-3 RW	5.171 MPa	-
	Separator Sight Glass	4	In-House	Custom	600 psi	-
	Separator Sight Glass	5	PresSure Products	Seven LL Reflex	650 psi	-
	Dilute/Vapor Sight Glass	6/9	PresSure Products	-	600 psi	-
	Dilute Flow Meter	7	MicroMotion	CMF025M319NU	0.60 kg s <sup>-1</sup>	0.1% Reading
	Dilute Regulating Valve	8	Swagelok	SS-3NRS4	-	-
	Vapor Regulating Valve	10	Swagelok	SS-6NRS8	-	-
	Subcooler	12	FlatPlate	FPN3X8-14	300 psi	-
	Solution Tank	13	Stone Mountain Technologies	Custom	-	-
	Fume Hood	14	Vent-A-Kiln	1332-500	0.19 m <sup>3</sup> s <sup>-1</sup>	-
	Tube-Side Differential Pressure Transducer	-	Omega	PX409-015DWUI	103.4 kPa	1% FS
	Separator Absolute Pressure Transducer	-	Omega	PX409-500AI	3.447 MPa	0.5% FS
	Absorber Absolute Pressure Transducer	-	Omega	PX409-750AI	5.171 MPa	0.5% FS
Type-T Thermocouple Probes	-	Omega	TMQSS-125G-6	-270-400°C	1°C or 0.75%	
<b>Air</b>	Air-Side Differential Pressure Transducer	-	Dwyer	607-3	249 Pa	0.5% FS
	Nozzle Differential Pressure Transducer	-	Dwyer	607-4	498 Pa	0.5% FS
	Absolute Air Pressure Transducer	-	Omegadyne	PX02K1-26A5T	88.04-108.4 kPa	0.1% FS
	Humidity Sensor	-	Johnson Controls	HE-67P2-0N00P	0-100%	2% FS
	Air Thermal Dispersion Flow Meter	-	Ebtron	GP1 Type B	25.4 m s <sup>-1</sup>	2% Reading
	Inlet and Outlet Type-T Thermocouple Arrays (4×4 grids)	-	Omega	TT-T-30	0-150°C	1°C or 0.75%
	Air Nozzle	-	Helander Metal Spinning	0.356 m bore	-	-
	Flow Straighteners	-	Air Monitor	1.22×0.76 m, 0.61×0.61 m	-	-
<b>Water</b>	Water Absolute Pressure Transducer	-	Rosemount	2088: A3S2BA1M7	5.516 MPa	0.075% FS
	Water Flow Meter	-	Rosemount	8711: ASA30FR1E5G1	12 m s <sup>-1</sup>	0.25% Reading
	Water Circulation Heater	-	Watlow	CBDNF29R3S	10.5 kW	-
	Water Gear Pump	-	Concentric Rockford	1070089	-	-
<b>All</b>	Data Acquisition System	-	National Instruments	cDAQ-9178	-	-

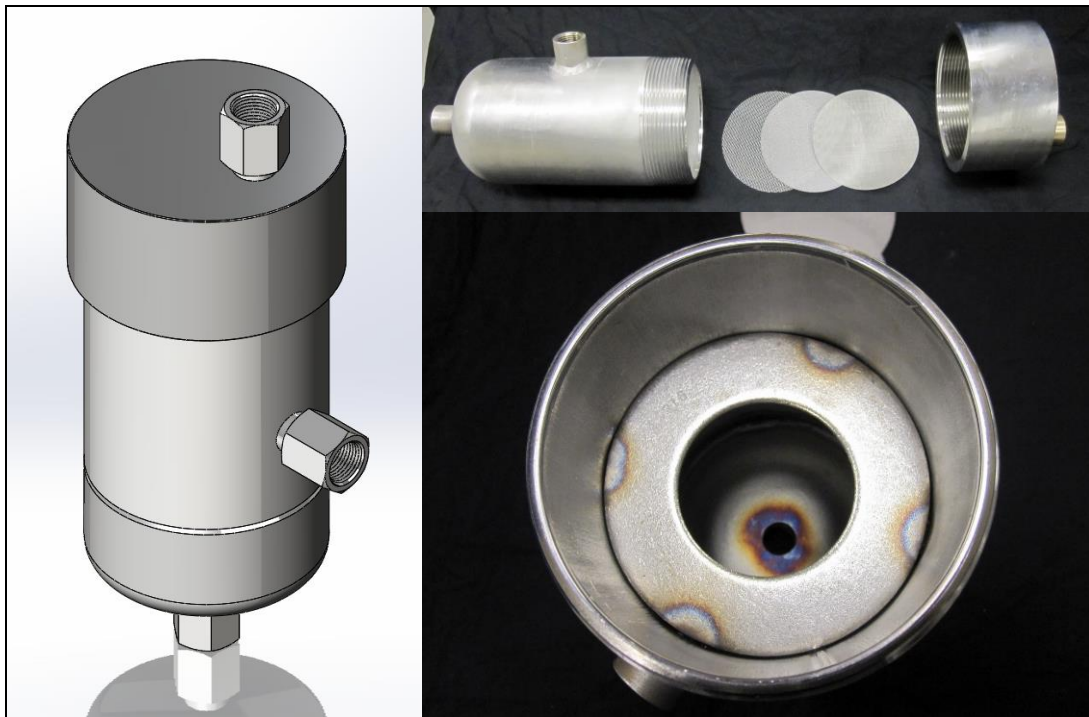
A photograph of the ammonia-water loop is shown in *Figure 4.5*. Immediately in the background of the ammonia-water test facility is the air-handling unit in which the absorber is mounted. Flexible stainless steel hoses lined with PTFE were used to bring the refrigerant vapor and dilute liquid streams to the absorber ports in the air-handling unit.



**Figure 4.5 Photograph of ammonia-water test facility**

A simple water loop is positioned adjacent to the facility shown in *Figure 4.5*. A circulation heater is used to heat water used in the desorption of ammonia-water. The

water loop is pressurized to raise the saturation temperature and prevent vaporization. Hot water enters at the top of the tube side of a shell-and-tube heat exchanger [3 in *Figure 4.5*], fabricated by Exergy (00677-3 RW). Ammonia-water flowing upward in the shell of the heat exchanger collects heat in counterflow and flows to the separator [4] as cocurrent liquid and vapor. The separator was positioned vertically such that the outlet of the desorber was level with the center of the separator. The desorber was intentionally flooded during operation, and the rising vapor bubbles collected in the top of the separator. The separator was designed and fabricated for the current facility (*Figure 4.6*).

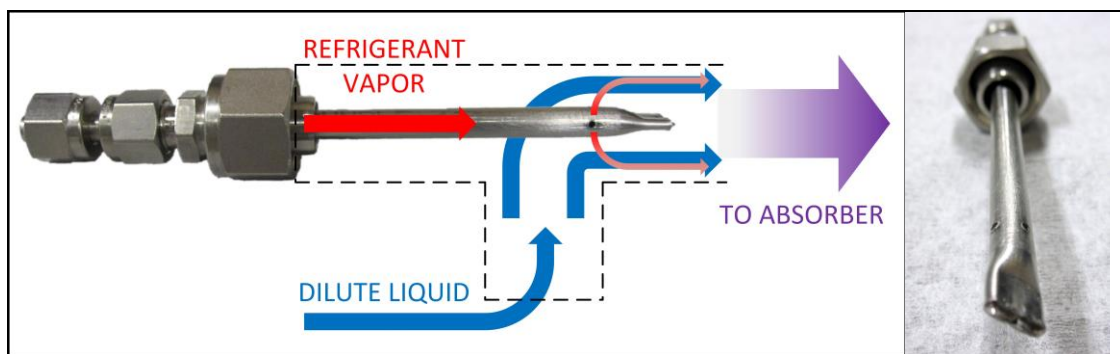


**Figure 4.6 Rendering (left), exploded photograph (top), and top view (bottom) of separator**

The separator consists of a 114-mm outer diameter pipe and cap with welded-on NPT fittings for the inlet (center), vapor outlet (top), and liquid outlet (bottom). The diameter was calculated to be larger than the maximum diameter (39.9 mm) in which liquid slugs are predicted to rise with vapor bubbles. Also, a series of mesh screens of different

opening sizes (0.18-0.86 mm) were mounted on a washer above the inlet in the separator to prevent liquid entrainment in the vapor. The sight glass parallel to the separator [5], fabricated by PresSure Products was used to ensure a liquid level in the separator. Bulls-eye sight glasses on the liquid [6] and vapor [9] provide additional visual confirmation of single-phase flow in the lines. Swagelok regulating valves [8, 10] were positioned to regulate the pressure drop across the liquid and vapor lines and adjust the height of the liquid level in the separator.

To inject the vapor into the liquid flow before entry to the absorber, a simple mixer was fabricated (*Figure 4.7*).



**Figure 4.7 Schematic (left) and photograph (right) of mixer**

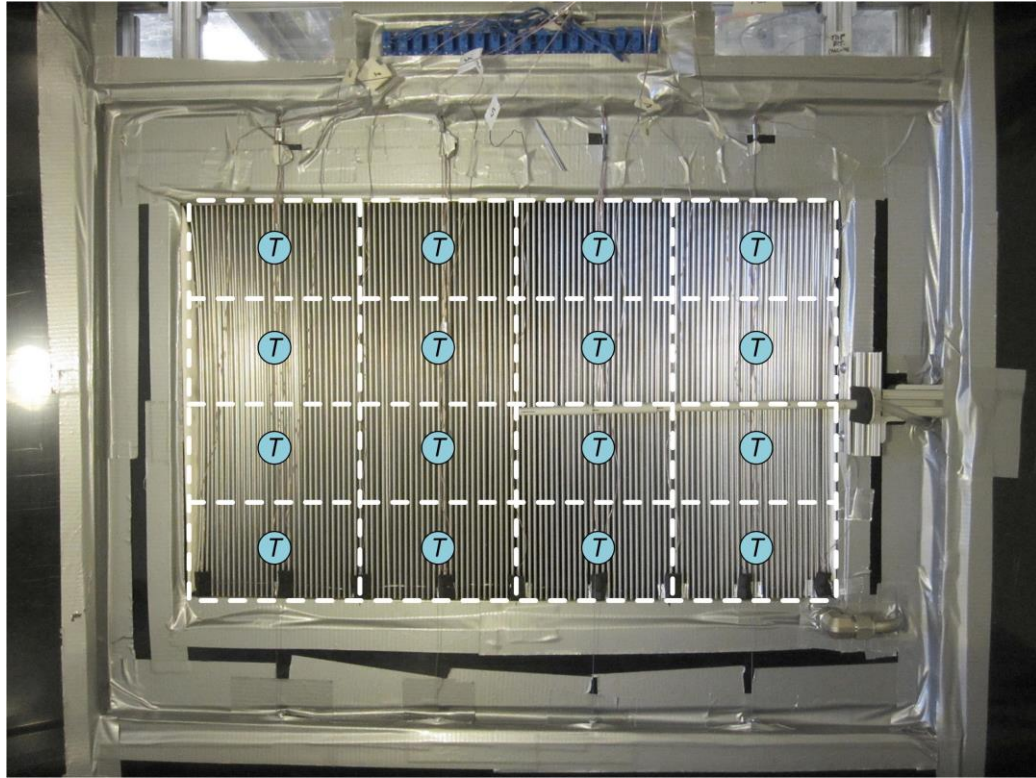
The vapor line was reduced in diameter to a 6.35-mm tube and positioned in the center of a 12.7-mm bore-through tee. The end of the 6.35-mm vapor tube was crimped, and 1.75-mm holes were drilled for the exit of refrigerant vapor. The vapor, therefore, was injected into the liquid stream in the center of the tee joint, and the combined stream continued to the absorber.

Flexible hosing carries the solution to and from the absorber that is mounted in the air-handling unit (*Figure 4.8*).



**Figure 4.8 Photograph of absorber in air-handling unit with solution test facility in background**

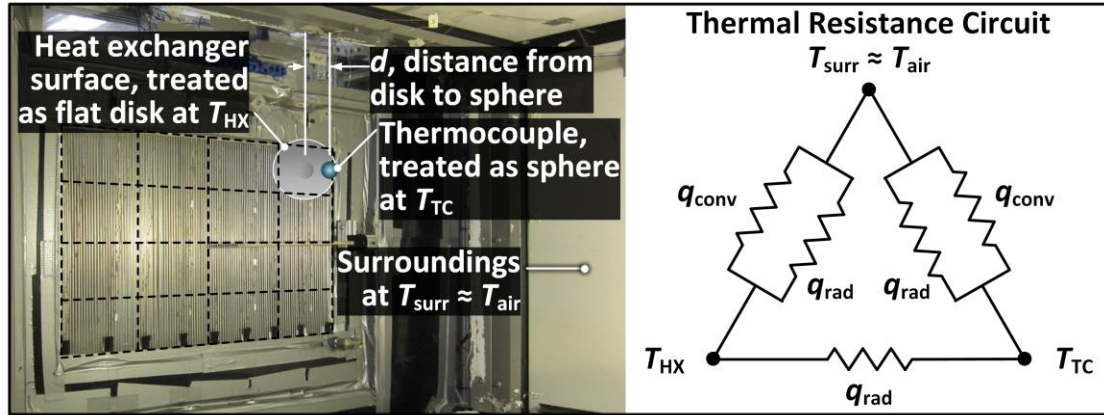
Thermocouple arrays were installed immediately upstream and downstream of the absorber. To prevent the disruption of air flow by the temperature measurements, 0.254-mm thermocouple wire was used in the thermocouple arrays. First, four lengths of structural 0.51-mm stainless steel wire were stretched vertically across the face of the absorber. Then, the soldered thermocouple wires were mounted on the structural wire such that each thermocouple bead was in the center of one-sixteenth of the flow area (*Figure 4.9*). The thermocouples were spaced approximately 0.02 m from the absorber surface to prevent any heat transfer through conduction.



**Figure 4.9** Photograph of absorber outlet with thermocouple locations indicated

An approximate calculation is used to predict the effect of radiation on air-side thermocouple measurements. A thermal resistance circuit is formed between the temperatures of the heat exchanger surface ( $T_{HX}$ ), thermocouple ( $T_{TC}$ ), and surroundings ( $T_{surr}$ ), as shown in *Figure 4.10*. At steady state conditions, the temperatures of the surroundings and of the air are assumed to be equal.





**Figure 4.10 Thermal resistance circuit for radiation analysis**

The temperature of the thermocouple is predicted based on the temperature of the surroundings, the temperature of the heat exchanger surface, and an assumption of steady-state temperatures ( $\sum q_{TC} = 0 \text{ W}$ ). The following conservative assumptions are used to predict the maximum effect of radiation on thermocouple readings: all surfaces act as blackbodies ( $\epsilon = 1$ ), the heat exchanger surface temperature is set to  $92.1^\circ\text{C}$  (the hottest outer tube wall temperature predicted from cycle modeling), and the temperature of the surroundings and air are set to  $51.7^\circ\text{C}$ . The heat exchanger surfaces and thermocouples have actual emissivities less than 1.0, and the tube wall temperature is predicted to be an average of  $68.1^\circ\text{C}$  across the length of the 394-FPM absorber. The heat transfer rate due to radiation from the surface of the absorber to the thermocouple can be estimated as follows:

$$q_{\text{HX,TC,rad}} = \frac{\sigma_B (T_{\text{HX,K}}^4 - T_{\text{TC,K}}^4)}{A_{\text{TC}} F_{\text{TC,HX}}} \quad (4.1)$$

The surface area of the thermocouple is labeled as  $A_{\text{TC}}$ , and the view factor ( $F_{\text{TC,HX}}$ ) is determined from Naraghi and Chung (1982), assuming that the heat exchanger surface acts as a disk that is a nominal distance from a sphere (the thermocouple bead). This

expression is also used to determine the heat transfer through radiation from the heat exchanger surface to the surroundings and from the thermocouple to the surroundings.

The convective heat transfer components shown in *Figure 4.10* can be determined from  $q = \alpha_{\text{conv}} A \Delta T$ , using temperature differences between the heat exchanger surface and surroundings and between the thermocouple and surroundings. The convective heat transfer coefficient used for the thermocouple is determined from flow over a sphere ( $\alpha_{\text{TC}} = 176.9 \text{ W m}^{-2} \text{ K}^{-1}$ ) (Incropera *et al.*, 2011). For flow over the heat exchanger, the 394-FPM absorber convective heat transfer coefficient from segmental modeling is used ( $\alpha_{\text{TC}} = 72.3 \text{ W m}^{-2} \text{ K}^{-1}$ ). With expressions for all of the radiative and convective resistances specified, the temperature of the thermocouple can be determined from the temperatures of the heat exchanger surface (92.1°C) and surroundings (51.7°C), assuming an energy balance across the thermocouple node (*i.e.*, the heat received by the thermocouple is equal to the heat leaving the thermocouple). Due to radiation received from the face of the heat exchanger, the thermocouple temperature is predicted to be 52.35°C at these conditions, 0.68°C higher than the air temperature. The actual discrepancy between air and thermocouple temperatures will be less than this value, due to the blackbody and hot wall temperature (92.1°C) assumptions. At the average outer wall temperature (68.1°C) determined from segmental modeling of the 394-FPM absorber, the predicted thermocouple temperature is 51.91°C. These air-side thermocouple readings are used to check the energy balance between the tube and air sides, but the overall heat transfer rate presented in Chapter 5 is calculated using tube-side measurements. Therefore, the effect of radiation on thermocouple measurements is not expected to substantially affect the results.

## **4.3 Experimental Procedures**

### **4.3.1 Safety Precautions**

Due to the toxicity and flammability of ammonia, care was taken to minimize the risk of injury during testing. The ammonia-water test facility was surrounded by a curtain when charged with ammonia, and a fume hood was mounted on the top of the facility. If a leak were to occur, the ammonia would be primarily contained within the curtained facility and funneled into the fume hood for safe venting. The laboratory was equipped with ammonia sensors, and gas masks were kept on-hand in the event of a rapid leak. During facility discharging, a large tank of water was used to slowly and safely absorb ammonia for disposal. Protective eyewear was used throughout test facility construction and absorber testing. Care was taken to prevent rises in pressure that approached the working pressure limits of the hosing and other equipment.

### **4.3.2 Charging Procedure**

A brief discussion of the charging and discharging procedures is provided here. Before charging the facility with ammonia, it is essential that all non-negligible leaks be eliminated. In the present work, pressure testing takes place using water, nitrogen (bubble testing), and occasionally using a small volume of charged refrigerant and a refrigerant detector. Once the system has maintained pressure over a sustained period of time, charging is permitted. Water is added to the system, followed by ammonia. A vacuum pump is used to evacuate the ammonia-water loop, typically to an absolute pressure less than 8 kPa, and a tank of distilled water is connected to the low system charge ports. Once the system and the hose connecting the water tank to the facility are evacuated, the vacuum pump is turned off, and a valve opening allows the entry of water into the

system. The water tank is mounted on a scale during charging to measure the amount of water leaving the tank. After the desired mass of water is added to the system (~2 kg in the present study), the charging line is closed, and the water tank is disconnected from the facility. The tank of ammonia is placed on the charging scale and covered by the curtain. After securely connecting the ammonia tank to the test facility, the hose between the ammonia tank and test facility is evacuated. Now, the tank is opened slowly, with the operator carefully checking for signs of leakage. The ammonia is allowed to fill the connecting hose. After the scale is zeroed, the valve between the facility and the hose is slowly opened to permit the flow of ammonia into the facility. Due to the large drop in pressure between the ammonia tank and the facility, frost may form on the charging lines of the facility. The valve is closed to allow for the defrosting of the equipment before more ammonia is added to the system. Once the desired mass of ammonia is added to the system (~0.9 kg in the present study), the valve between the ammonia tank and facility is closed, along with the ammonia tank. A hose branching off this charging hose is then inserted into a volume of water for the absorption of ammonia remaining in the hosing. Once all of the ammonia is evacuated from the hosing, the charging hose is carefully disconnected. All hoses exposed to ammonia are kept in a tank of water or under a fume hood until no traces of ammonia are detectable.

The discharge process includes the slow release of ammonia from the system through a hose submerged in a large volume of water. The water absorbs ammonia so that it can be disposed of properly. The system is flushed with water and air to flush all flow paths to remove as much ammonia as possible.

### **4.3.3 Startup and Testing Procedures**

When starting up the ammonia-water test facility and air-handling unit, it is important that all fluids are circulated before the addition of heat. The water pump, ammonia-water pump, and wind tunnel fan are turned on. Once flow meters verify the movement of fluid and all system temperatures and pressures are displaying accurately, the heater is activated. The set point temperature in the heater is raised gradually, with the operator keeping careful track of the water and ammonia-water pressures. Once vapor generation begins, the operator allows the flow of cooling water through the subcooler to prevent pump dry-out in case two-phase solution exits the absorber. Once the system reaches the design temperature in the solution, the air temperature is raised through the flow of steam in the heating coil in the air-handling unit. The user continues monitoring all system temperatures and pressures as the air temperature rises to the required absorber inlet temperature. Regulating valves on the vapor and liquid lines are used to adjust the vapor fraction flowing into the absorber as well as the height of the liquid level in the separator. Visual confirmation of single-phase flow in the vapor and liquid streams is possible in the Bulls-eye sight glasses. The operator also visually confirms liquid inventory in the solution tank to prevent pump dry-out. Data are collected upon achievement of steady state, after no upward or downward trend is seen in temperature or pressure readings over a three-minute time period. Readings are taken over a five-minute timeframe to account for any minor oscillatory behavior.

To end a session of testing, the heat input in the heater and steam flow are discontinued first. While the fan and pumps continue operating, the chilled water in the subcooler and air-handling unit chiller coil are used to expedite the cooling process. Once

the system temperatures reach safe values ( $<40^{\circ}\text{C}$ ), the pumps and fan are turned off. It may take up to thirty minutes for cool down due to the thermal mass of the facility.

Chapter 5 presents the matrix of conditions tested in the present study and an analysis of absorber performance compared with predictions from models of the round-tube corrugated-fin and novel tube-array absorbers.

## CHAPTER 5: RESULTS AND DISCUSSION

The performance of the round-tube corrugated-fin and prototype tube-array absorbers is discussed in this chapter. The data are compared directly with predictions from the models, and potential explanations are provided for discrepancies between the model predictions and the data. The test matrix for absorber evaluation is shown in *Table 5.1*. The test conditions were selected to represent absorber conditions during heat pump operation. To address performance at different ambient conditions, the inlet air temperature was varied. Testing was also conducted at different air flow rates to assess the effect on absorber duty and fan power. During system operation, solution inlet conditions at the absorber depend on factors such as the performance of other heat and mass exchangers in the system, variations in refrigerant charge, and system heat source and conditioned space temperatures. Therefore, the effects of variations in inlet solution temperature to the absorber are investigated. Concentrated solution flow rate was also varied to investigate the effect of solution pump performance. Finally, the volume of ammonia charged to the system was also varied enable testing at different concentrated solution concentrations.

**Table 5.1 Test matrix for air-coupled absorber testing**

Variable	Unit	Test Number											
		01	02	03	04	05	06	07	08	09	10	11	12
$T_{\text{air,in}}$	$^{\circ}\text{C}$	51.7	35	43.3	54.4	51.7	51.7	51.7	51.7	51.7	51.7	51.7	51.7
$\dot{V}_{\text{air,in}}$	$\text{m}^3 \text{s}^{-1}$	0.42	0.42	0.42	0.42	0.38	0.47	0.42	0.42	0.42	0.42	0.42	0.42
$T_{\text{sol,in}}$	$^{\circ}\text{C}$	97.6	97.6	97.6	97.6	97.6	97.6	92	102	97.6	97.6	97.6	97.6
$\dot{m}_{\text{conc}}$	$\text{g s}^{-1}$	8	8	8	8	8	8	8	8	6	10	8	8
$x_{\text{conc}}$	%	42	42	42	42	42	42	42	42	42	42	38	46

The shaded fields in *Table 5.1* represent values that are different from design conditions. For example, the inlet air temperature is 51.7°C in the design condition, but the absorber is also evaluated at off-design inlet air conditions (35°C, 43.3°C, 54.4°C).

An uncertainty propagation analysis is conducted on the data in the present study. The calculation of the solution concentrations, heat transfer rates, effectiveness values, and overall heat transfer coefficients depends on errors in estimations of a variety of measurements, including temperatures, pressures, and flow meters. The method of uncertainty propagation proposed by Taylor and Kuyatt (1994) is used here. The uncertainty ( $u$ ) in a calculated variable ( $y$ ) is a sum of the products of the partial derivatives and uncertainties in the variables used in its calculation [ $y = f(x_1, x_2, x_3, \text{etc.})$ ]:

$$U_y^2 = \left( \frac{\partial y}{\partial x_1} U_{x_1} \right)^2 + \left( \frac{\partial y}{\partial x_2} U_{x_2} \right)^2 + \left( \frac{\partial y}{\partial x_3} U_{x_3} \right)^2 + \dots \quad (5.1)$$

The uncertainties of all measurement devices (Type-T thermocouples, pressure transducers, flow meters) are reported in Chapter 4. As an example of the uncertainty propagation method, the uncertainty of the tube-side heat transfer rate of one data point is presented as a result of its constituent measurement uncertainties (*Table 5.2*).



**Table 5.2 Uncertainty propagation used in heat transfer rate calculation**

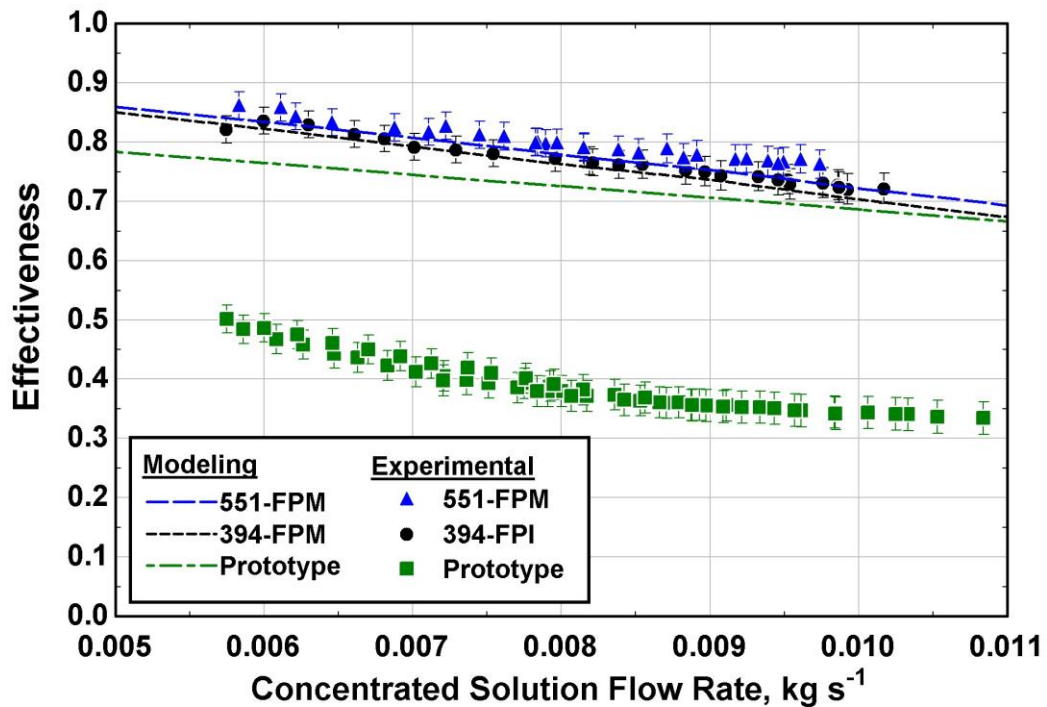
Partial Derivative	% Uncertainty (of total)
$\dot{Q}_{\text{sol,HX}} = 4.682 \pm 0.30 \text{ kW } (\pm 6.4\%)$	
$(\partial \dot{Q}_{\text{sol,HX}} / \partial \Delta P_{\text{sol,HX}}) = -0.05023$	0.02%
$(\partial \dot{Q}_{\text{sol,HX}} / \partial \dot{m}_{\text{conc}}) = 2.965$	0.01%
$(\partial \dot{Q}_{\text{sol,HX}} / \partial P_{\text{sep}}) = -0.04604$	14.72%
$(\partial \dot{Q}_{\text{sol,HX}} / \partial P_{\text{sol,HX}}) = 0.05024$	39.43%
$(\partial \dot{Q}_{\text{sol,HX}} / \partial T_{\text{sep,liq,out}}) = 0.1148$	14.66%
$(\partial \dot{Q}_{\text{sol,HX}} / \partial T_{\text{sep,vap,out}}) = 0.04359$	2.11%
$(\partial \dot{Q}_{\text{sol,HX}} / \partial T_{\text{sol,HX,out}}) = -0.1617$	29.05%

The uncertainty propagation was implemented in the *Engineering Equation Solver* (EES) software platform. The uncertainty of the measurement devices is presented in tabular form in Chapter 4.

## 5.1 Comparison of Different Absorber Configurations

The round-tube corrugated-fin and prototype tube-array absorbers in consideration are designed for the heat pump modeled in Chapter 3. The absorbers are designed to occupy the same approximate face area, accounting for space required for inlet/outlet tubes, headers, and framing. Including headers, the tube-array absorber is contained in a slightly larger face ( $0.71 \times 0.46 \text{ m}$ ) than the corrugated-fin absorber ( $0.69 \times 0.44 \text{ m}$ ), but the tube-array depth is 57.2 mm compared to the 76.2 mm deep corrugated fins. The area available for air flow is 3.7% smaller in the prototype than in the conventional heat exchanger. The similarity in volume and flow area of the absorbers permits their comparison for use in the heat pump under consideration here.

With the same inlet air and solution conditions, the maximum possible heat transfer in the designs ( $\dot{Q}_{\max}$ ) is equal. The maximum possible heat transfer rate is calculated based on the minimum heat capacity rate ( $\dot{C}_{\min}$ ) and the difference between the inlet air and inlet solution temperatures used for the tests. Effectiveness values predicted by the models and data from the experiments for all absorbers at all concentrated solution flow rates are presented in *Figure 5.1*.



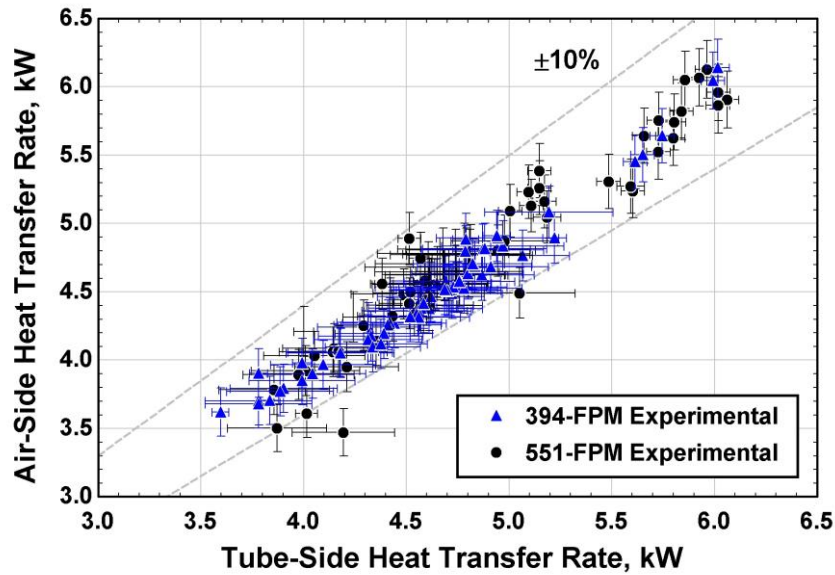
**Figure 5.1 Effectiveness values from data and modeling for all absorbers**

In general, good agreement is seen in effectiveness between data and modeling for the corrugated-fin absorbers. The measured effectiveness values are 1.5% and 2.7% higher (AAD) than the predicted effectiveness values for the 394-FPM and 551-FPM absorbers, respectively. This discrepancy could be due to the modeling of the temperature variation as an in-line, rather than staggered, tube array. The staggered tube array is expected to

demonstrate cooler rear row air temperatures than an equivalent aligned tube array, allowing higher overall heat transfer. For the prototype tube-array absorber, however, the measured effectiveness values were an average of 46.2% lower than the values predicted through modeling, most likely due to the maldistribution of liquid and vapor in the tube array. This large discrepancy between the data and the modeling is discussed in-depth in Section 5.3. Discussion of these data and the corresponding model predictions follows.

## **5.2 Round-Tube Corrugated-Fin Absorber**

The heat transfer rate in the absorber can be measured across the air flow or across the solution. In the present study, the heat transfer rate in the solution was used for comparisons with data due to non-uniformities in air temperature and velocity. In addition, it is difficult to get a well-mixed temperature representative of the entire air stream. The solution-side thermocouples provide a localized and well-mixed temperature measurement. The air-side heat transfer rate is compared to the solution-side heat transfer rate in *Figure 5.2*.



**Figure 5.2 Energy balance: Comparison of Air-side and Tube-side heat transfer rates**

The heat transfer rate on the air side is calculated using an average of all 16 upstream and 16 downstream thermocouple measurements for the inlet and outlet air temperatures, respectively. A uniform profile is assumed for the mass flow rate of the air such that the flow rate of air over each thermocouple was one-sixteenth of the total incoming flow rate. For the corrugated-fin absorber testing, the heat transfer rate determined using the air flow meters and temperature measurements is an average of 1.9% lower (92 W) than the heat transfer rate determined using tube-side measurements across all data points. The standard deviation of the difference between the heat transfer rates is 0.14 kW, or 3.57% of the tube-side heat transfer rate. The average uncertainties in the tube-side and air-side heat transfer rates are  $\pm 0.202$  kW and  $\pm 0.185$  kW, respectively.

Good agreement is observed between the data and predictions from modeling for the round-tube corrugated-fin absorbers. For the 394-FPM absorber at design conditions, the experimentally measured heat transfer rate is approximately 0.7% higher than the

value predicted by the model (*e.g.*,  $Q_{394\text{-FPM,exp}} = 4.521 \pm 0.271$  kW;  $Q_{394\text{-FPM,mod}} = 4.490$  kW). The 551-FPM absorber model demonstrated a total heat transfer rate 1.9% higher than the modeled value ( $Q_{551\text{-FPM,exp}} = 4.680 \pm 0.260$  kW;  $Q_{551\text{-FPM,mod}} = 4.591$  kW) at design conditions. Despite a 37.7% difference in heat transfer area exposed to air between the 394-FPM and 551-FPM designs, the two corrugated-fin absorbers performed almost identically. A discussion of the similarity in the performance between the two different fin densities is presented in Section 5.2.7. Although it appears that the 551-FPM design has a slightly higher heat transfer rate than the 394-FPM design, the difference is generally within the range of uncertainty.

The absorber model ignored solution subcooling, and also assumed well-mixed solution conditions in each segment. In reality, there will be a small concentration gradient in the liquid film, which will manifest as a temperature gradient that limits heat transfer. In addition, the model assumes an equal temperature distribution across the inlet air flow. During testing, however, there were temperature differences across the face of the absorber, with an average temperature spread of 6.02°C across all data points. This variation in temperature is probably due to maldistribution in the air flow rate and temperature, in part due to differences in preconditioning by the heating/cooling coils upstream of the absorber. Maldistribution in air flow rate across the face area can be attributed to boundary layers at the duct walls and unavoidable obstructions in the flow area such as ducting vanes, thermal dispersion flow meters, and temperature/humidity sensors. The inlet air temperatures reported here represent an average of the inlet 4×4 thermocouple array, recorded over five minutes of steady-state data collection. The same averaging is performed on the outlet 4×4 thermocouple array.

### 5.2.1 Overall Heat Transfer Coefficient

The segmental heat transfer conductance ( $UA_{sg}$ ) of the absorbers may be determined from the sum of the internal convection, tube conduction, and external thermal resistances:

$$UA_{sg} = [R_{in} + R_{cond} + R_{out}]^{-1} = \left[ \frac{1}{\alpha_{in} A_{i,sg}} + \frac{\ln(D_o/D_i)}{2k_{tube} \pi L_{sg}} + \frac{1}{\alpha_{air} \eta_0 A_{total,sg}} \right]^{-1} \quad (5.2)$$

For the 394-FPM absorber, the model predicts segmental internal thermal resistances ranging from 0.165 to 0.426 K W<sup>-1</sup>, external resistances between 0.283 and 0.304 K W<sup>-1</sup>, and conduction resistances  $\leq 0.008$  K W<sup>-1</sup>. The internal heat transfer coefficient used here effectively combines heat transfer in the vapor (with the accompanying mass transfer resistance) and in the liquid film.

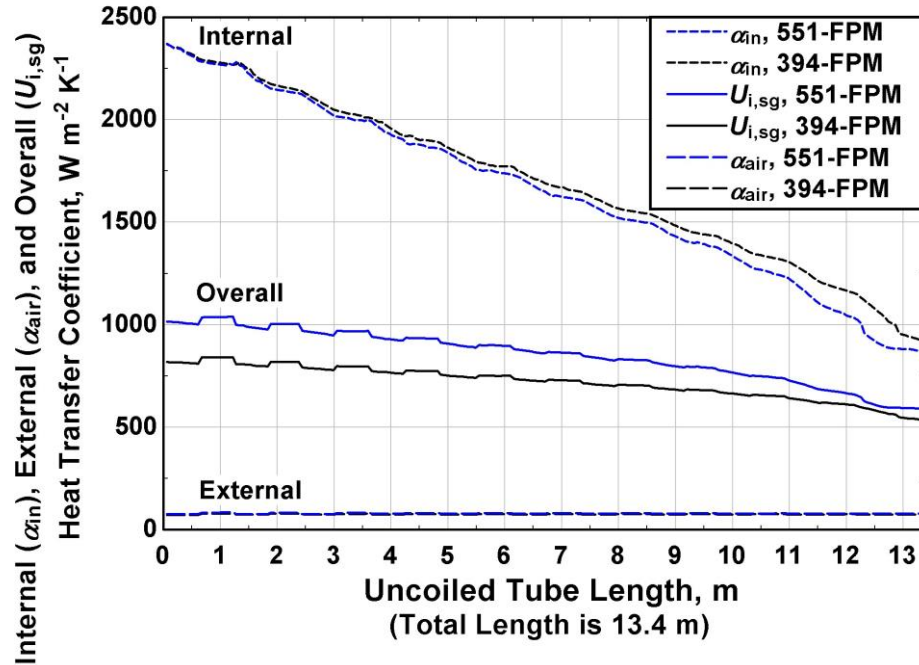
$$\alpha_{in} = [A_{i,sg} R_{in}]^{-1} = [A_{i,sg} (R_{in,vap} + R_{in,film})]^{-1} = \left[ q_{sol} C_{p,v} \frac{\Delta T_{gl}}{\Delta h_m} \frac{1}{\alpha_v} + \frac{1}{\alpha_{sol}} \right]^{-1} \quad (5.3)$$

The quality ( $q_{sol}$ ) in the vapor thermal resistance term corresponds to the transport length scale in the vapor. With decreasing void fraction, the effective diameter of the vapor flow decreases, thereby decreasing the mass transfer resistance. Heat is transferred to the air over an effective external surface area: the product of the surface efficiency with the total tube-and-fin surface area exposed to air ( $\eta_0 A_{total,sg}$ ). The surface efficiencies in the two absorbers ranged from 0.840 to 0.846.

The internal overall heat transfer coefficient ( $U_{i,sg}$ ) is determined from the conductance using the segmental internal heat transfer area ( $A_{i,sg} = \pi D_i L_{sg}$ ):

$$U_{i,sg} A_{i,sg} = UA_{sg} \quad (5.4)$$

Tube conduction thermal resistance is minimal; therefore,  $U_{i,sg}$  is effectively set by the internal and external heat transfer coefficients  $[U_i \approx f(\alpha_{in}, \alpha_{out})]$ . The internal, external, and overall heat transfer coefficients in each segment are plotted along the length of the absorber in *Figure 5.3*.

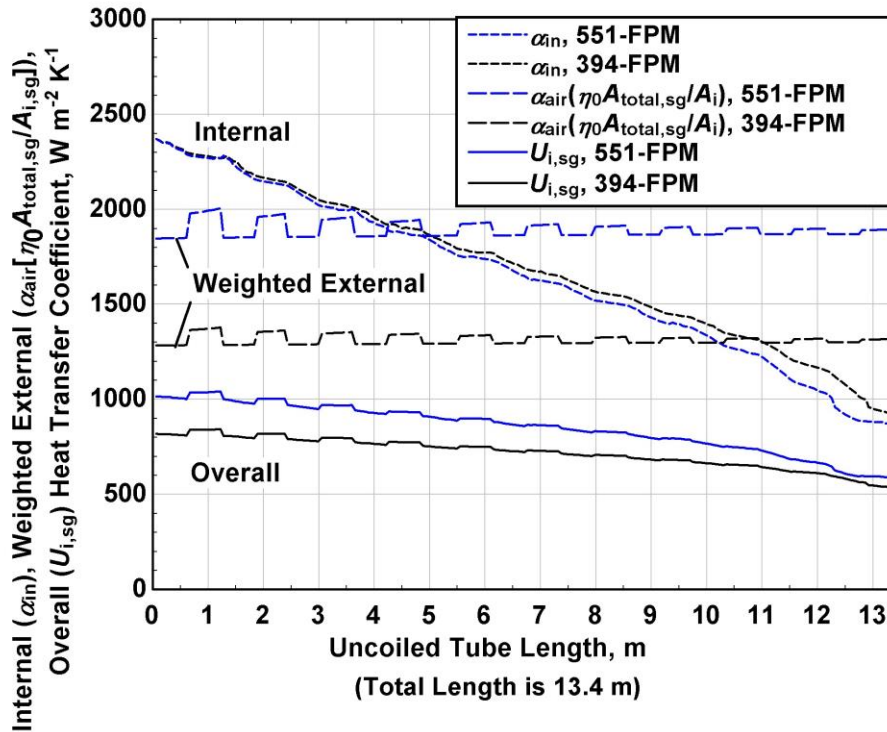


**Figure 5.3 Internal, external, and overall heat transfer coefficients as a function of uncoiled length in the 394-FPM and 551-FPM absorbers**

The serrations in heat transfer coefficient curves correspond to the variations in air-side transport properties between the front and rear tube rows due to differences in local air temperature. For example, the air-side heat transfer coefficient in the 394-FPM absorber rises from 72.44 to 77.69 between the first pass and second pass (0.67 m in *Figure 5.3*) due to a rise in incoming air temperature from 51.7 to 76.7°C. This temperature rise corresponds to a 11.9% decrease in air density (1.061 to 0.935 kg m<sup>-3</sup>) and a 13.5% increase in air velocity (3.149 to 3.574 m s<sup>-1</sup>). The overall heat transfer coefficient ( $U_i$ ) is predicted to be greater (14.9% on average) in the 551-FPM absorber than in the 394-FPM

absorber throughout the heat exchanger. This occurs because greater fin area increases  $UA$  for fixed  $A_i$  ( $U_i = UA / A_i$ ). The total external heat transfer area for the 394-FPM absorber is  $11.70 \text{ m}^2$ , while it is  $16.24 \text{ m}^2$  for the 551-FPM absorber.

As indicated earlier, internal and external thermal resistances are of similar order, and both significantly affect absorber performance. The relative effects of internal and external thermal resistances on  $U_i$  can be understood better by weighting the external heat transfer coefficient by the effective external-to-internal area ratio  $\left[ \alpha_{\text{air}} \left( \eta_0 A_{\text{total,sg}} / A_{i,\text{sg}} \right) \right]$ . The ratio of the effective external area to the internal area ( $\eta_0 A_{\text{total,sg}} / A_{i,\text{sg}}$ ) is 17.75 and 24.17 in the 394-FPM and 551-FPM absorbers, respectively. The internal, weighted external, and overall heat transfer coefficients are plotted in *Figure 5.4*.

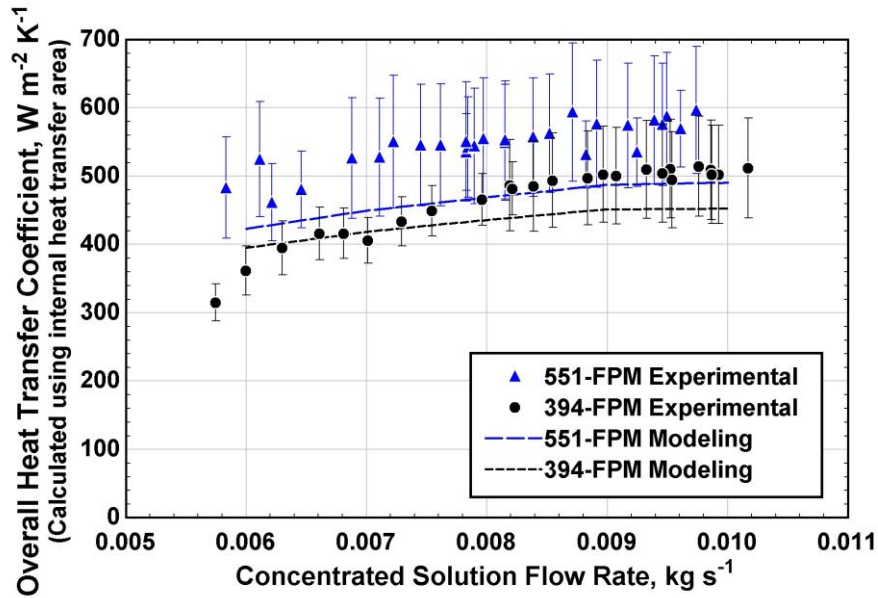


**Figure 5.4 Internal, weighted external, and overall heat transfer coefficients as a function of absorber length**



The increased fin density in the 551-FPM absorber, compared to the 394-FPM absorber, results in reduced air-side thermal resistance (narrower fin channels), and an increase in the air heat transfer coefficient (72.3 to 76.4 W m<sup>-2</sup> K<sup>-1</sup>, +5.7%) and the weighted external heat transfer coefficient (1283 to 1847 W m<sup>-2</sup> K<sup>-1</sup>, +44.0%) in the first 0.061 m segment. The internal heat transfer coefficient predicted for the 551-FPM absorber is slightly lower (3.5% on average) than the value predicted in the 394-FPM absorber because a less favorable flow regime is reached at the lower exit quality predicted in the 551-FPM absorber ( $q = 0.030$ , compared to  $q = 0.036$ ). The internal heat transfer coefficient decreases from 2370 to 915.7 W m<sup>-2</sup> K<sup>-1</sup> in the 394-FPM absorber and from 2369 to 872.6 W m<sup>-2</sup> K<sup>-1</sup> in the 551-FPM absorber, as shown in *Figure 5.4*. During absorption, the internal thermal resistance rises due to the reduced liquid-vapor shear at low qualities. After a certain length of tubing in the absorber, the internal thermal resistance is predicted to be dominant. In *Figure 5.4*, these transitions can be seen at 4.3 m in the 551-FPM absorber and 11 m in the 394-FPM absorber. Nevertheless, the reduction in external thermal resistance with increased fin density is more substantial than the increase in internal resistance, resulting in a larger overall heat transfer coefficient in the 551-FPM absorber.

The total heat transfer rate and outlet solution conditions predicted in the model are used to determine the overall heat transfer coefficient ( $U_i$ ) for comparison with data. The predicted and experimental values of overall heat transfer coefficient, as a function of concentrated solution flow rate, are shown in *Figure 5.5*.



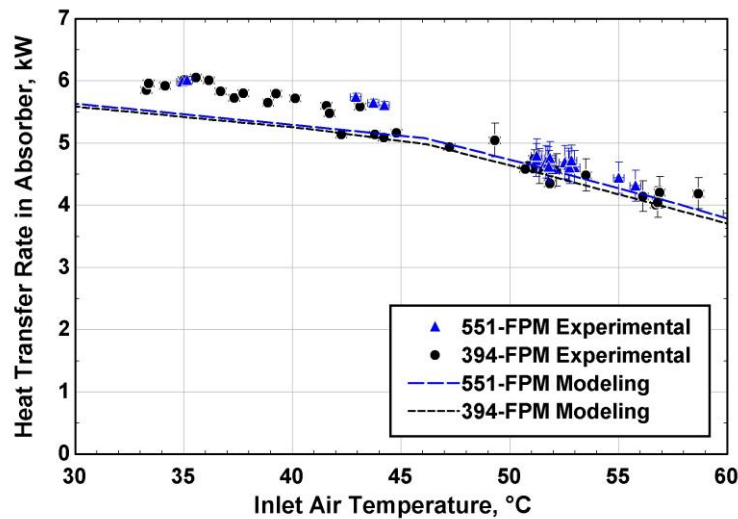
**Figure 5.5 Overall heat transfer coefficients for the round-tube corrugated-fin absorbers, determined using total air-side heat transfer area**

In both the model predictions and the data, the overall heat transfer coefficient based on the tube inner diameter increases with concentrated solution flow rate as a result of the increased liquid-vapor shear. The measured overall heat transfer coefficient values ranged from 315.0 to 514.2  $\text{W m}^{-2} \text{K}^{-1}$  and from 461.6 to 596.8  $\text{W m}^{-2} \text{K}^{-1}$  for the 394-FPM and 551-FPM absorbers, respectively, with average uncertainties of 56.9  $\text{W m}^{-2} \text{K}^{-1}$  ( $\pm 13.7\%$ ) and 81.0  $\text{W m}^{-2} \text{K}^{-1}$  ( $\pm 15.3\%$ ). The measured overall heat transfer coefficient was 6.6% higher on average than predicted values for the 394-FPM absorber and 16.9% higher than predicted values for the 551-FPM absorber. One potential explanation for this discrepancy in the 551-FPM absorber is that the present fin wave depth to fin spacing ratio  $\left[ \left( s_{\text{wav,d}}/s \right)_{551\text{-FPM}} = 1.78 \right]$  is outside the range recommended for use in the air-side heat transfer coefficient correlation proposed by Kim *et al.* (1997b)  $\left[ 0.23 \leq \left( s_{\text{wav,d}}/s \right) \leq 1.21 \right]$ . Also, the model predictions rely on air temperature variation

predicted in an in-line, rather than staggered, tube bank. This assumption is expected to decrease the predicted overall heat transfer coefficient, contributing to the discrepancy between data and the model predictions.

### 5.2.2 Air Temperature

The inlet air temperature determines the driving temperature difference between the working fluid solution and the air; therefore, it has a considerable effect on the heat transfer rate in the absorber (*Figure 5.6*).



**Figure 5.6 Heat transfer rate as a function of air temperature for the round-tube corrugated-fin absorbers**

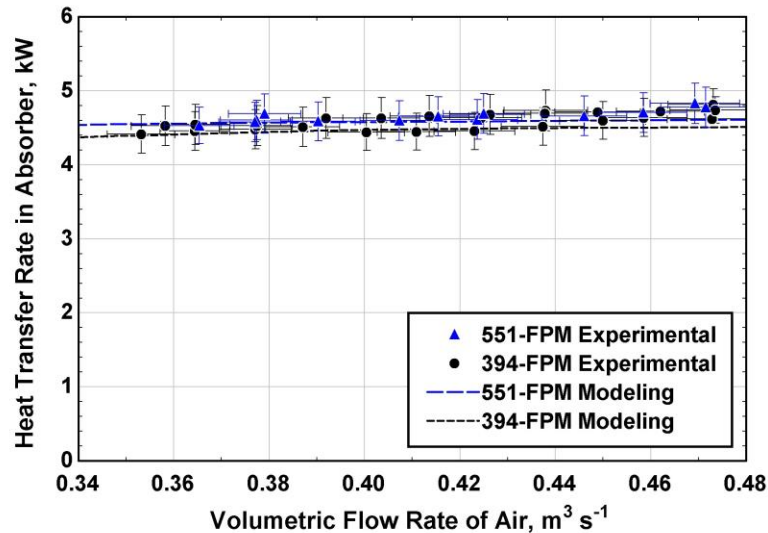
Both the model and the experiments demonstrate the decrease in absorber heat duty with increasing ambient air temperature as a result in the reduction of the driving temperature difference between the solution and the air. For the 394-FPM absorber, heat transfer rates ranged from 3.871 to 6.061 kW with uncertainties between  $\pm 0.052$  and  $\pm 0.271$  kW across the range of inlet air temperatures considered. The 551-FPM demonstrated heat transfer rates between 4.315 and 6.015 kW with uncertainties ranging from  $\pm 0.055$  to  $\pm 0.271$  kW.

The Average Absolute Deviation (AAD) between the modeling and the experiments is 4.9% for the 394-FPM absorber and 4.6% for the 551-FPM absorber across the range of air temperatures evaluated. According to predictions from the model, the solution reaches saturation at approximately 5.06 kW of heat rejection. At temperatures above  $\sim 45^{\circ}\text{C}$ , the model predicts a slightly larger difference in the performance of the two different fin density absorbers. This difference is due to the higher enthalpy change during phase change compared to the subcooled region. At lower temperatures, both absorbers are predicted to reach the subcooled liquid phase in which very little heat transfer occurs; the total heat transfer rates are then very similar. At air temperatures below  $45^{\circ}\text{C}$ , the discrepancy between model and predictions becomes more pronounced. This is believed to be a result of the temperature variation assumption of an aligned tube array used during modeling. This assumption would over-predict the temperature of the air entering the rear row of tubes, causing an under-prediction in performance. This under-prediction is expected to be most significant at low inlet air temperatures.

### **5.2.3 Air Flow Rate**

The flow rate of air over the corrugated-fin absorbers for the range investigated has a minor impact on the total heat transfer rate (*Figure 5.7*). The marginal influence of air flow rate is most likely due to the tube-side thermal resistance resulting from the stratified flow regime, as shown in the Taitel-Dukler flow regime map in Chapter 3. For example, when the 394-FPM absorber is modeled using 220 segments, the internal thermal resistance increases from 0.04 to 0.15  $\text{K W}^{-1}$  during absorption, while the external thermal resistance stays constant at 0.07  $\text{K W}^{-1}$ . The internal thermal resistance is the limiting resistance when  $q < 0.06$ , corresponding to approximately 68% of the total

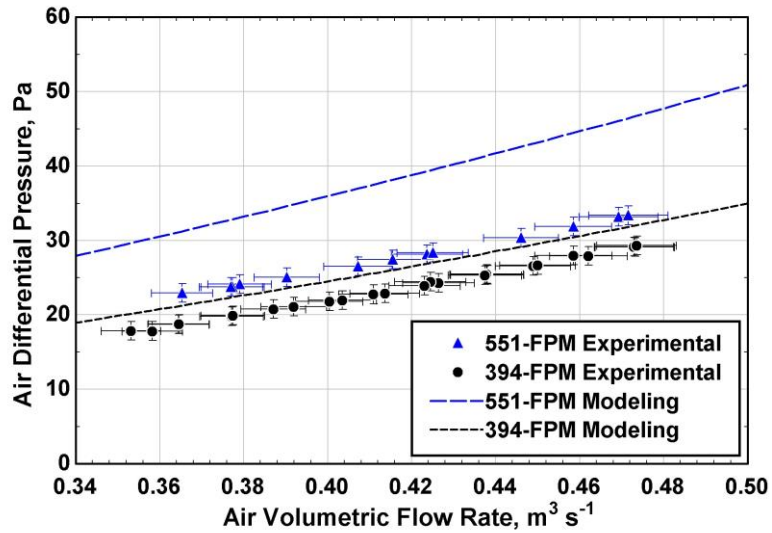
uncoiled length of the conventional absorber. Based on this finding, opportunities may exist to minimize electrical power consumption by the absorber fans without a large degradation in heat transfer rate.



**Figure 5.7 Heat transfer rate as a function of air flow rate for the round-tube corrugated-fin absorbers**

The volumetric flow rate of air was varied between 0.353 and 0.474  $\text{m}^3 \text{s}^{-1}$ , with uncertainties between  $\pm 0.007$  and  $\pm 0.009 \text{ m}^3 \text{s}^{-1}$ . A marginal increase in heat transfer rate with air-side flow rate is demonstrated by both the data and the model. Across the range of air-side flow rates, experimental heat transfer rates are 2.6% and 1.5% higher (AAD) than those predicted from modeling for the 394-FPM and 551-FPM absorbers. The heat transfer rates range from 4.415 to 4.814 kW (uncertainties from  $\pm 0.056$  to  $\pm 0.276$  kW) in the 394-FPM absorber, and from 4.530 to 4.830 kW ( $\pm 0.246$  to  $\pm 0.274$  kW) in the 551-FPM absorber.

Although the change in air-side pressure drop with flow rate was similar for the data and the model predictions, the model over-predicted the air-side pressure drop (Figure 5.8).

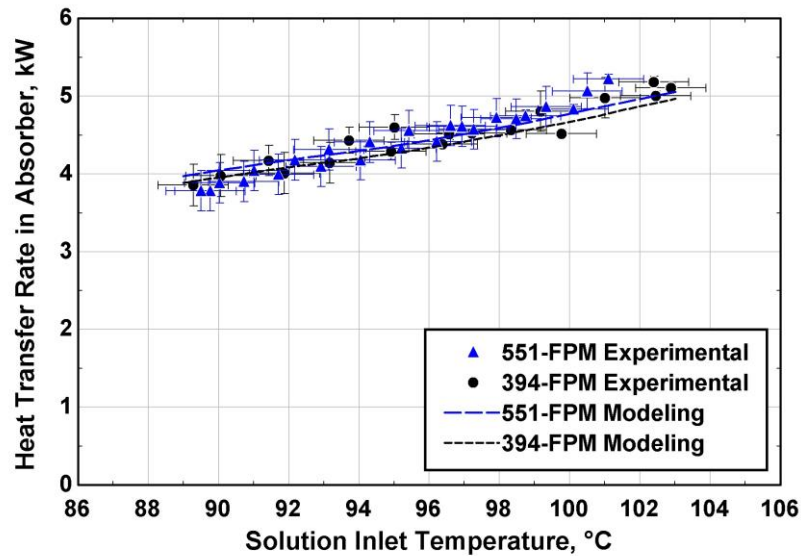


**Figure 5.8 Air-side differential pressure as a function of volumetric flow rate for the round-tube corrugated-fin absorbers**

A positive value for differential pressure in *Figure 5.8* represents a pressure drop between the inlet and the outlet of the air. Differential pressure readings ranged between 17.83 and 29.30 Pa in the 394-FPM absorber, and 22.96–33.36 Pa in the 551-FPM absorber, with an average uncertainty of  $\pm 1.25$  Pa. Over the range of air flow rates tested, the 394-FPM differential pressure was 10.5% (AAD) lower than model predictions, while the 551-FPM absorber differential pressure was 27.9% lower than predictions. The fin and tube spacing falls within the range of application specified by Gray and Webb (1986), but the most comparable heat exchanger used in the correlation database was used only for heat transfer predictions, not friction factor. Additional investigations of air-side pressure-drop correlations over wavy fins are necessary for a correlation that accounts for wave depth and pitch in the air-side pressure drop calculation. As mentioned in Chapter 3, the friction in the core is the largest component of the air-side pressure drop (96%), while the inlet contraction, acceleration in the core, and exit expansion account for 4% of the total air-side pressure drop.

## 5.2.4 Solution Inlet Temperature

During heat pump operation, the temperature of the incoming two-phase ammonia-water is likely to vary with changes in ambient, conditioned space, and heat source conditions. The effect of this variation on absorber heat duty is shown in *Figure 5.9*.



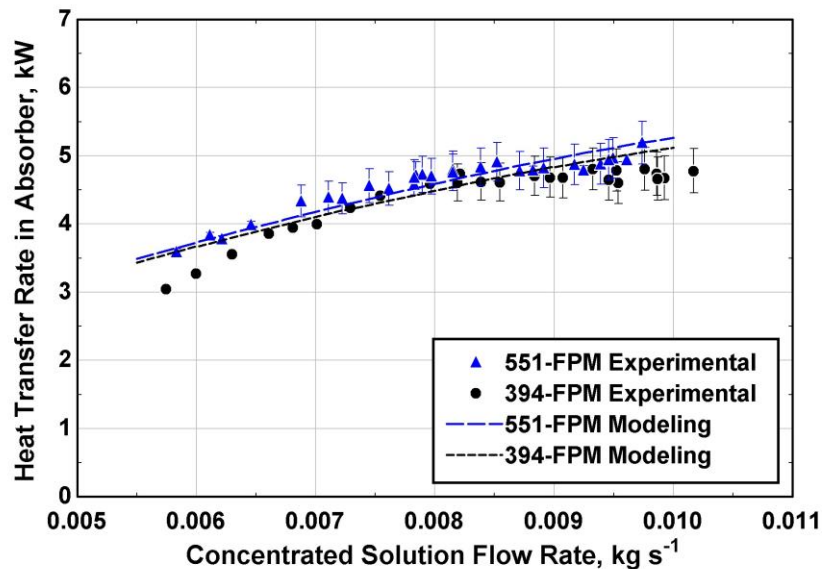
**Figure 5.9 Heat transfer rate as a function of solution inlet temperature for the round-tube corrugated-fin absorbers**

The solution inlet temperature was varied between  $89.3 \pm 1.0$  and  $102.9 \pm 1.0$  °C, resulting in increasing heat transfer rates in the 394-FPM ( $3.856 \pm 0.269$  to  $5.185 \pm 0.067$  kW) and 551-FPM ( $3.780 \pm 0.260$  to  $5.221 \pm 0.058$  kW) absorbers. As solution inlet temperature decreases, the refrigerant fraction accompanying the dilute solution to the absorber decreases due to the reduced vaporization of the ammonia-water mixture in the test facility desorber. This reduction in the fraction of incoming refrigerant vapor reduces the amount of mixing and heat rejection that can take place in the absorber. In addition, the driving temperature difference between inlet fluid streams (air and solution) decreases.

Experimental heat transfer rates in the 394-FPM and 551-FPM absorbers are on average 2.1% and 0.08% higher than predictions across the range of inlet solution temperatures considered.

### 5.2.5 Solution Flow Rate

Changes in concentrated solution flow rate significantly affect absorber performance (*Figure 5.10*).



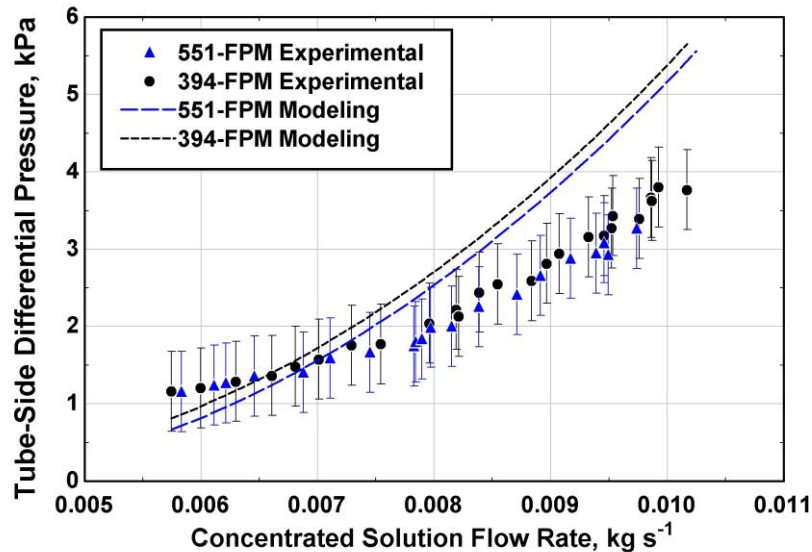
**Figure 5.10 Heat transfer rate as a function of concentrated solution flow rate for the round-tube corrugated-fin absorbers**

The concentrated solution flow rate ranges from 0.0057 to 0.0102 kg s<sup>-1</sup> with uncertainties of  $\pm 0.1\%$ . Heat transfer rates vary from  $3.047 \pm 0.039$  to  $4.812 \pm 0.315$  kW in the 394-FPM absorber, and from  $3.595 \pm 0.041$  to  $5.194 \pm 0.312$  kW in the 551-FPM absorber. The heat rejected to ambient air in the absorber increases with increasing solution flow rate. The increasing solution flow rate increases the solution-side heat transfer coefficient and also decreases the temperature drop in the solution for a given heat duty, thereby increasing the driving temperature difference, both of which lead to an



increasing heat duty. However, at much higher flow rates, the available heat sink is unable to support complete absorption, leading to a two-phase solution outlet, which could damage the solution pump. Overall, the measured heat transfer rate was 3.7% (AAD) lower than the value predicted in the 394-FPM absorber and 0.6% higher than the value predicted in the 551-FPM absorber across the range of solution flow rates.

The tube-side pressure drop as a function of concentrated solution flow rate is shown in *Figure 5.11*. Measured tube-side pressure drop values ranged from  $1.162 \pm 0.517$  to  $3.803 \pm 0.517$  kPa in the 394-FPM absorber, and from  $1.158 \pm 0.517$  to  $3.268 \pm 0.517$  kPa in the 551-FPM absorber.



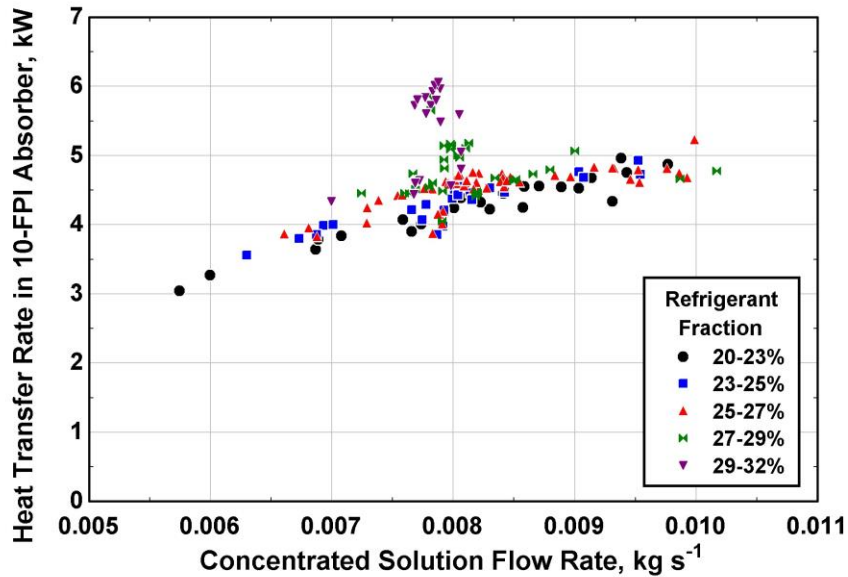
**Figure 5.11 Tube-side differential pressure as a function of solution flow rate for the round-tube corrugated-fin absorbers**

Over the range of flow rates considered, the 394-FPM absorber pressure drop is 17.7% (AAD) lower than predictions and the 551-FPM measured pressure drop is 11.1% lower than predictions. The average uncertainty in both the 394-FPM and 551-FPM tube-side pressure drop reading is  $\pm 0.517$  kPa. This difference in the pressure drop of the 394-

FPM and 551-FPM absorbers is due to overall absorber performance. The gravitational pressure rise in the absorber is more significant at lower qualities (discussed in Chapter 3), and the 551-FPM absorber is expected to contain a higher fraction of liquid across its length ( $0.030 < q < 0.29$ ) than the 394-FPM absorber ( $0.036 < q < 0.29$ ). This gravitational pressure rise counteracts the frictional pressure drop across the length of the heat exchanger. Although the magnitude of the pressure drop measured across the absorber is comparable to the value predicted through modeling, the model predicts a greater rate of differential pressure increase with increasing solution flow rate. The slope does vary with the value of the minor loss coefficients; values in the present study were selected from Cengel and Cimbala (2006).

#### **5.2.6 Refrigerant Fraction**

During air-coupled testing, refrigerant fraction was varied through the adjustment of the liquid/vapor regulating valves, alterations to the amount of ammonia charged in system, and changes in desorber inlet coupling fluid temperature. A plot of the heat transfer rates observed as a function of concentrated solution flow rate for a range of refrigerant fractions in the 394-FPM absorber is shown in *Figure 5.12*.



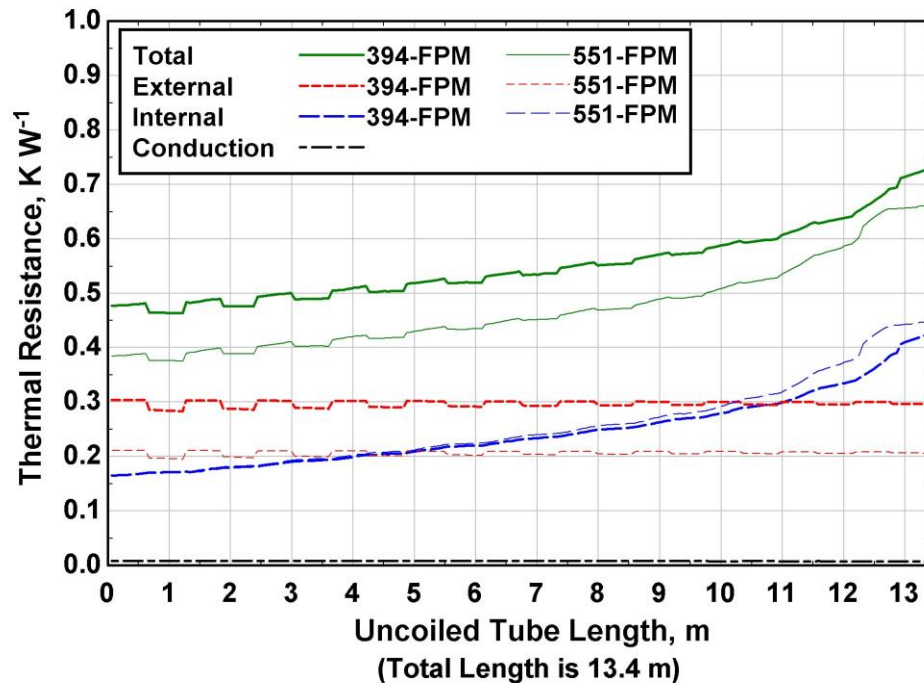
**Figure 5.12 Refrigerant fraction in the 394-FPM absorber**

The high refrigerant fractions (27-32%) correspond to the high heat transfer rates that were recorded at low inlet air temperatures (<45°C) and high inlet solution temperatures (>100°C). High solution temperatures in the test facility desorber enabled a higher rate of vapor generation; therefore, refrigerant fraction was higher.

### **5.2.7 Discussion of Similar Performance**

One should consider carefully the similarity in performance between the two fin densities, demonstrated in modeling and in experiments. The 551-FPM design incorporates 37.7% more total air-side heat transfer area than the 394-FPM absorber, yet the model predicts only about 100 W of additional heat transfer (4.596 vs 4.496 kW). First, the internal and external thermal resistances comprise nearly equivalent fractions of the total thermal resistance. The individual thermal resistances (internal, conduction, external) and total thermal resistance for the 394-FPM and 551-FPM absorbers are shown in *Figure 5.13*. The oscillations in thermal resistances are caused by the varying inlet air

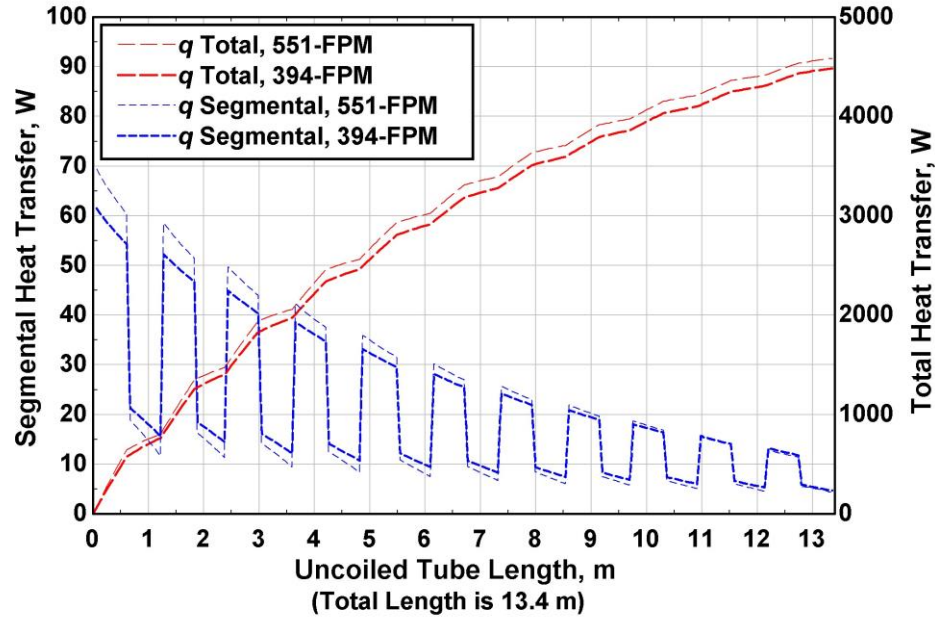
temperatures between the frontal and rear tube rows in the serpentine absorbers. The internal thermal resistance rises throughout the absorption process, thereby diminishing the role of fins in aiding heat transfer along the length of the heat exchanger. At a given length of uncoiled absorber tubing, the internal thermal resistance in the 551-FPM absorber is higher than in the 394-FPM absorber (*Figure 5.13*). This is caused by the unfavorable flow regime encountered at low qualities, which are reached at an earlier length in the 551-FPM absorber than in the 394-FPM absorber. As shown by the diminishing gap between the total heat transfer rates in the absorbers in *Figure 5.14*, the 394-FPM absorber compensates for the lower absorption rates in the initial regions of the absorber by better performance near the exit.



**Figure 5.13 Segmental and total thermal resistances in the 394-FPM and 551-FPM absorbers**

The internal thermal resistance plays a less prominent role at higher qualities. At these higher qualities, the flow regime is more favorable, and the external thermal resistance

contributes more to the overall thermal resistance. This explains the deviation in performance in the two absorbers predicted when the solution exits in a two-phase state.

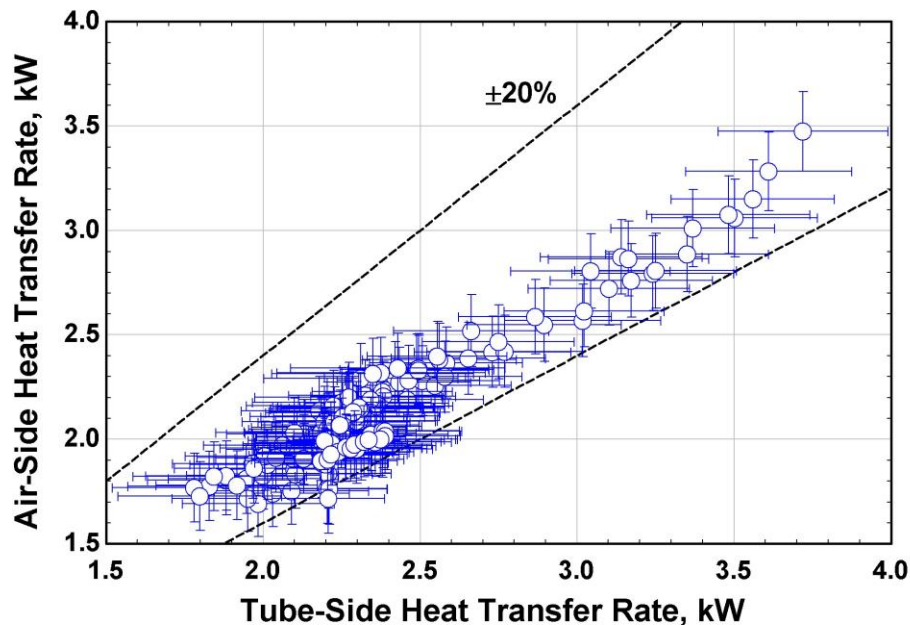


**Figure 5.14 Segmental and total heat transfer rate in the absorber for 394-FPM and 551-FPM absorbers**

The heat transfer rate along the length of the absorber is useful in interpreting the comparable performance of the two fin densities (*Figure 5.14*). The total heat transfer rate (right axis) is a summation of the segmental heat transfer rates (left axis). The disparity in segmental heat transfer rate, which is significant at the beginning of absorption, quickly diminishes. The serrations in the segmental and total heat transfer rates are due to the inlet air temperature changes between the frontal and rear tube rows in the corrugated-fin absorbers. The heat pump designer has the option to use the 394-FPM design to reduce fan power consumption and increase system performance without a significant impact on absorber heat transfer rate.

### 5.3 Prototype Tube-Array Absorber

The prototype tube-array absorber attempts to reduce the internal thermal resistance seen in conventional absorbers, as described in Chapter 4. This reduction in hydraulic diameter is made possible through dense tube spacing and the elimination of fins. Although the model predicted a reduction in internal thermal resistance and a heat transfer rate of 4.30 kW, the heat transfer rate measured experimentally was only  $2.22 \pm 0.24$  kW at design conditions. The significant disparity between predictions and testing is believed to be the result of maldistribution of the two-phase flow entering the tube array; the model assumed even distribution of liquid and vapor across all tubes. A maldistribution analysis predicted a significant reduction in heat transfer rate for a variety of distribution conditions. The maldistribution analysis is presented after the discussion of the measured data. The energy balance for all data points is shown in *Figure 5.15*.



**Figure 5.15** Energy balance between air and tube side for prototype tube-array absorber

Across all data points, the heat transfer rate measured using air-side thermocouples and the flow meters is 9.4% lower on average than the heat transfer rate measured on the tube side. The probable cause of the imbalance is heat loss from the absorber headers and inlet and outlet tubes. Insulation surrounding the headers and inlet/outlet tubing is used to minimize this heat loss. Uncertainties range from  $\pm 0.055$  to  $\pm 0.342$  kW and from  $\pm 0.138$  to  $\pm 0.191$  kW in the tube-side and air-side heat transfer rates, respectively.

### **5.3.1 Overall Heat Transfer Coefficient**

*Figure 5.16* demonstrates the substantial difference between the overall heat transfer coefficient predicted by the model and the measured values over the range of concentrated solution flow rates considered. The measured overall heat transfer coefficient ranges from  $17.24 \pm 1.71$  to  $18.97 \pm 2.92$   $\text{W m}^{-2} \text{K}^{-1}$ , compared to predicted values between  $35.77$  and  $55.59$   $\text{W m}^{-2} \text{K}^{-1}$ . The negligible impact of solution flow rate on heat transfer coefficient in the absorber suggests that the performance is not primarily inhibited by internal thermal resistance. It is possible that poor distribution of the two-phase flow in the tube array could limit the interfacial area available for absorption, thereby decreasing the heat transfer rate. This effect is discussed in further detail in the section on maldistribution analysis (5.3.7).

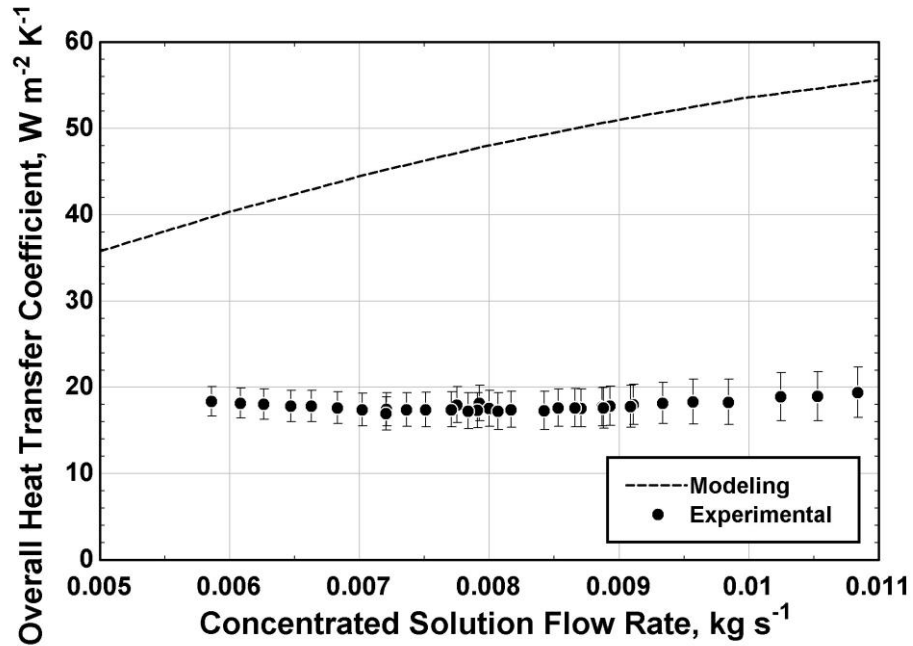
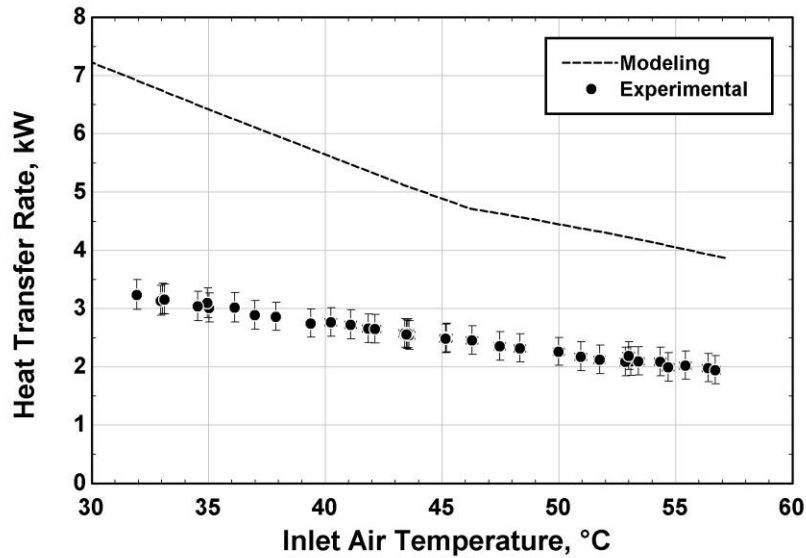


Figure 5.16 Overall heat transfer coefficient as a function of concentrated solution flow rate for the prototype tube-array absorber

### 5.3.2 Air Temperature

Ambient conditions have a large impact on the performance of the prototype absorber (*Figure 5.17*). Measured heat transfer rates decrease from  $3.241 \pm 0.258$  to  $1.950 \pm 0.241$  kW as air temperatures rise ( $31.93 \pm 0.25$  to  $56.68 \pm 0.25^\circ\text{C}$ ). The maximum possible heat transfer rate decreases as the temperature difference between the inlet solution and air is decreased. This is expected to affect viability of the absorption heat pump in severe ambient conditions.



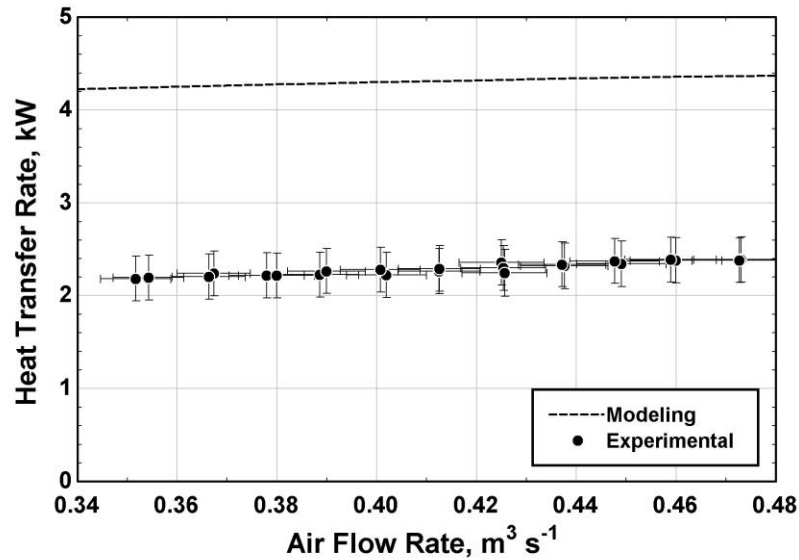


**Figure 5.17 Heat transfer rate as a function of air temperature for the prototype tube-array absorber**

The heat transfer rate in the absorber decreases with rising temperature because of the diminishing solution-to-air temperature difference. The measured heat transfer rate is 50.5% (AAD) lower than model predictions. The model predicts two-phase flow exiting the absorber at temperatures above  $\sim 46^{\circ}\text{C}$ , indicated by the change in slope of the heat transfer rate values.

### 5.3.3 Air Flow Rate

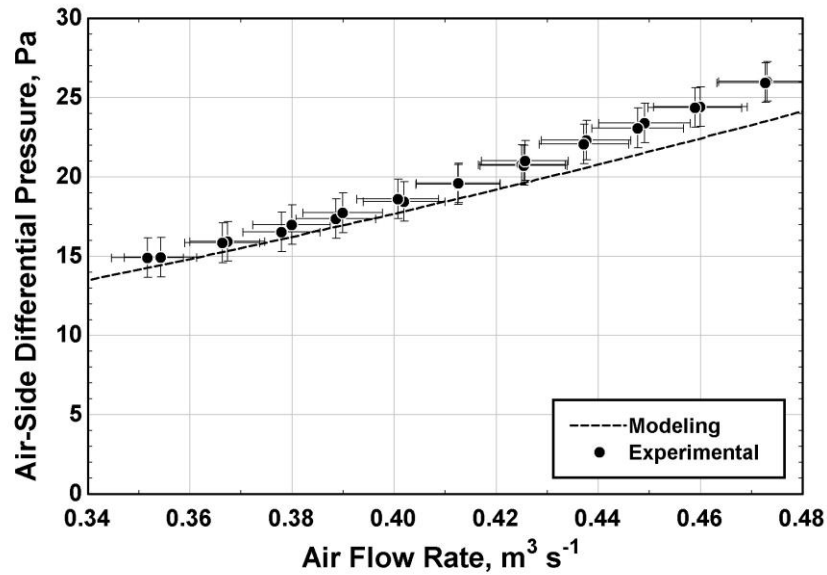
Modeling and data show that increasing the flow rate of the air only marginally increases the heat transfer rate in the absorber (*Figure 5.18*). Heat transfer rates increase from  $2.184 \pm 0.243$  to  $2.388 \pm 0.240$  kW with increasing air flow rates ( $0.352 \pm 0.009$  to  $0.473 \pm 0.009$   $\text{m}^3 \text{s}^{-1}$ ).



**Figure 5.18 Heat transfer rate as a function of air flow rate for the prototype tube-array absorber**

Testing demonstrated heat transfer rates significantly lower (47.0%) than those predicted from modeling. The maldistribution analysis in Section 5.3.7 demonstrates similar reduction in performance.

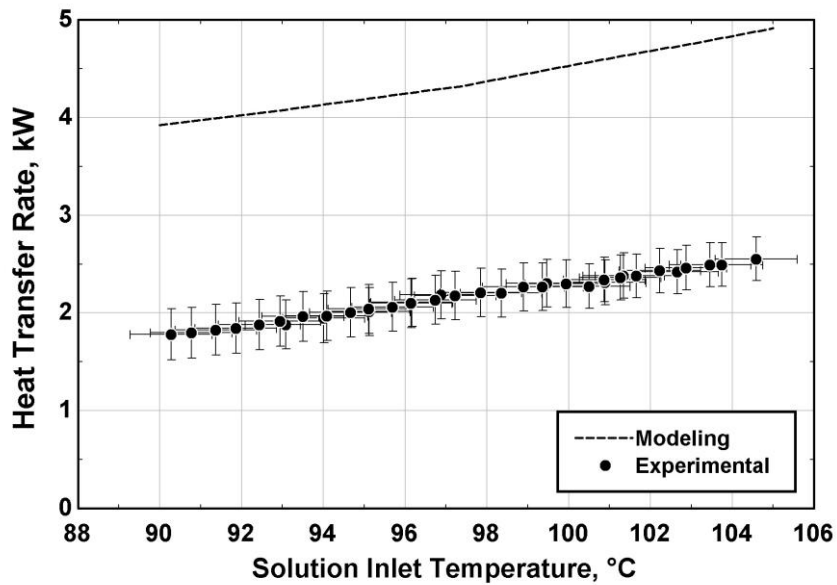
Good agreement is shown between the air-side pressure drop predicted by the model and the measured values (*Figure 5.19*). Measured air-side pressure drop values range from  $14.91 \pm 1.25$  to  $26.02 \pm 1.25$  Pa. The measured pressure drops are slightly higher (6.0%) than those predicted by the model. The frictional pressure drop correlation by Zukauskas *et al.* (1968) for crossflow air over a bank of tubes therefore appears to work well even for small diameter (3.18-mm OD) tubes.



**Figure 5.19 Air-side differential pressure as a function of air flow rate for the prototype tube-array absorber**

### **5.3.4 Solution Inlet Temperature**

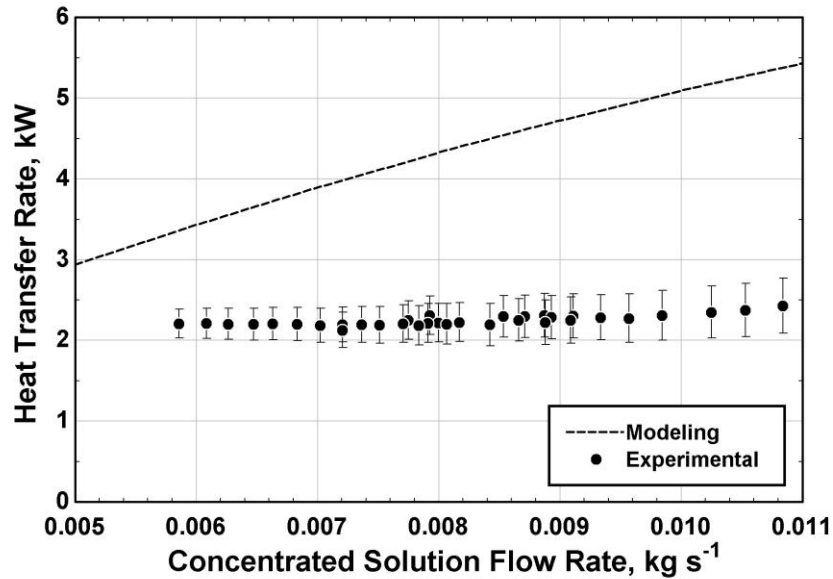
Over the range of solution temperatures considered ( $90.28 \pm 1.0$  to  $104.6 \pm 1.0^\circ\text{C}$ ), the prototype absorber demonstrated heat transfer rates significantly lower (50.6% AAD) than model predictions (*Figure 5.20*). It is expected that improvement in flow distribution would reduce the disparity in heat transfer rate by providing additional interfacial area for heat and mass transfer. The measured heat transfer rate increased from  $1.780 \pm 0.260$  to  $2.554 \pm 0.222$  kW with increasing absorber inlet temperature.



**Figure 5.20 Heat transfer rate as a function of solution temperature for the prototype tube-array absorber**

### **5.3.5 Solution Flow Rate**

The model predicts a substantial increase in heat transfer rate with rising solution flow rates (*Figure 5.21*). During testing, the flow rates of dilute and refrigerant streams were increased proportionally with concentrated solution flow rate. *Figure 5.21* presents data points over a range of concentrated solution flow rates with the same refrigerant fraction.



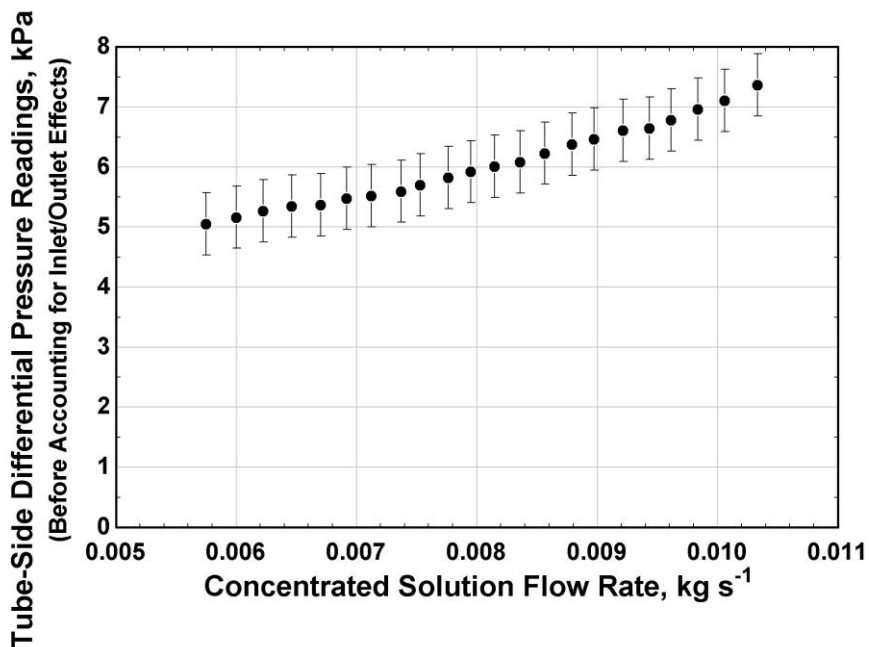
**Figure 5.21 Heat transfer rate as a function of solution flow rate for the prototype tube-array absorber**

The measured heat transfer rate is relatively unaffected (ranging from  $2.129 \pm 0.218$  to  $2.429 \pm 0.342$  kW) by increasing concentrated solution flow rate from 0.0058 to 0.0108 ( $\pm 0.1\%$ ). The data points do not reflect the dependence of heat transfer rate on solution flow rate predicted by the model. Over the range of flow rates, the absorber performed poorly compared to the model (47.6% lower heat duty) with the difference between the heat transfer rates increasing at higher flow rates. This clearly indicates a malfunctioning absorber. An attempt to explain this anomalous behavior on the basis of tube-side maldistribution is made in a subsequent section.

The analysis of the tube-side pressure drop in the prototype tube-array absorber is presented here. First, the raw data from the differential pressure transducer are presented. These differential pressure values must be adjusted before comparison with the model predictions because they include inlet/outlet losses as well as superficially high readings from the liquid column in the inlet transducer port. The estimation of these effects is

described, and their values are used to estimate the total tube-side pressure drop solely within the tube-array absorber. Then, the total tube-side pressure drop in the absorber from testing is compared with predictions from the model.

The large flow area for the solution in the tube array results in a low solution mass flux ( $G_{\text{sol}} = 2.4 \text{ kg m}^{-2} \text{ s}^{-1}$ ) and low predicted pressure drop. This marginal change in pressure presents a challenge experimentally because minor and frictional losses in the inlet and outlet tubes of the absorber are expected to account for a significant portion of the differential pressure recorded by the transducer. To compare the total differential pressure across the tube array predicted by modeling with data from testing, the effects of these losses must be accounted for. *Figure 5.22* shows the tube-side differential pressure measured by the transducer before adjustments to determine the total tube-side pressure drop occurring solely within the absorber.



**Figure 5.22** Tube-side differential pressure recorded by pressure transducer before accounting for inlet/outlet losses

During testing, the differential pressure transducer was located at the outlet of the absorber, with an inlet pressure line connecting the transducer to the absorber inlet. It is assumed that this inlet line was filled with liquid during testing due to gravity, superficially increasing the differential pressure recorded by the transducer. This pressure drop can be approximated using the height difference between the inlet and outlet ports.

$$\Delta P_{\text{transducer,line}} = \rho_{1,\text{in}} g h_{\text{abs,in,out}} \quad (5.5)$$

The recorded change in pressure also includes frictional and minor pressure drops in inlet and outlet tubing between the pressure ports and outside the absorber. The minor pressure drop calculation requires a pressure loss coefficient, fluid density, and flow velocity.

$$\Delta P_{\text{in/out,minor}} = \left( \frac{1}{2} \right) K_{1,\text{in/out,total}} \rho_{\text{in/out}} u_{\text{in/out}}^2 \quad (5.6)$$

The frictional pressure drop in the inlet and outlet tubing can be approximated using the Friedel (1979) correlation, given inlet and outlet mass fluxes and fluid properties.

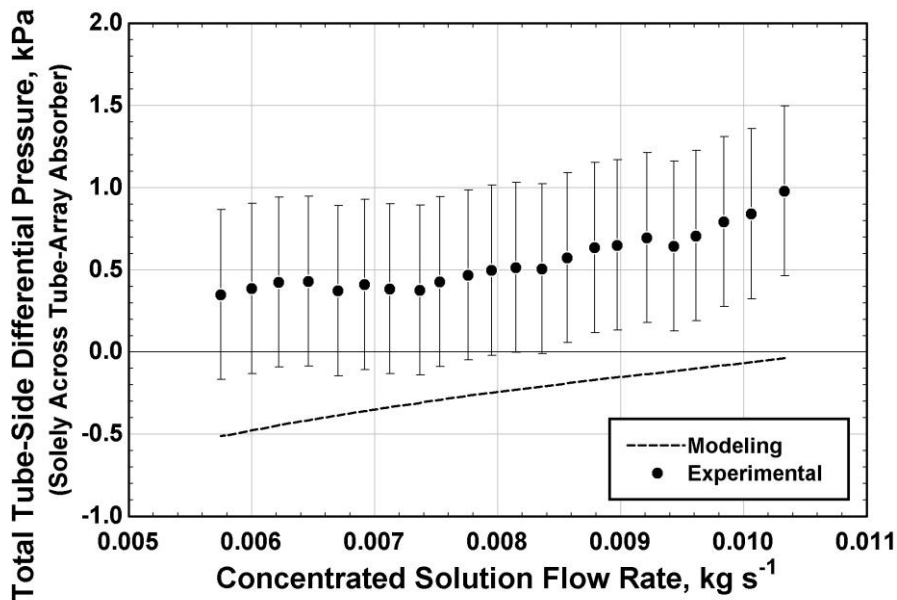
$$\Delta P_{\text{in/out,fric}} = f \left( L_{\text{in/out}}, D_{\text{in/out}}, \rho_{\text{tp,in/out}}, q_{\text{in/out}}, G_{\text{in/out}} \right) \quad (5.7)$$

The total pressure drop to be accounted for in inlet/outlet losses and the liquid level in the transducer line can be determined. As mentioned in Chapter 3, the differential pressure due to expansion/contraction between the header and individual tube array ports is expected to be negligible.

$$\Delta P_{\text{loss,total}} = \Delta P_{\text{in,fric}} + \Delta P_{\text{in,minor}} + \Delta P_{\text{transducer,line}} + \Delta P_{\text{out,fric}} + \Delta P_{\text{out,minor}} \quad (5.8)$$

This total pressure loss varies with solution flow rate, but it is approximately equal to 5.44 kPa at the design condition (0.008 kg s<sup>-1</sup>). Once these losses have been factored into the measured values, the experimental and predicted total tube-side pressure drop solely across the absorber can be compared (*Figure 5.23*). The uncertainty bands indicated in *Figure 5.23* can be misleading. The uncertainty in the measured value (*Figure 5.22*) was

7-10%; after adjustment to account for losses upstream and downstream of the absorber, the uncertainty in total pressure drop is a much larger fraction (53-148%) of the value reported in *Figure 5.23*. Positive values in *Figure 5.23* indicate a total pressure loss across the absorber, while negative values indicate a total pressure gain resulting from gravity.



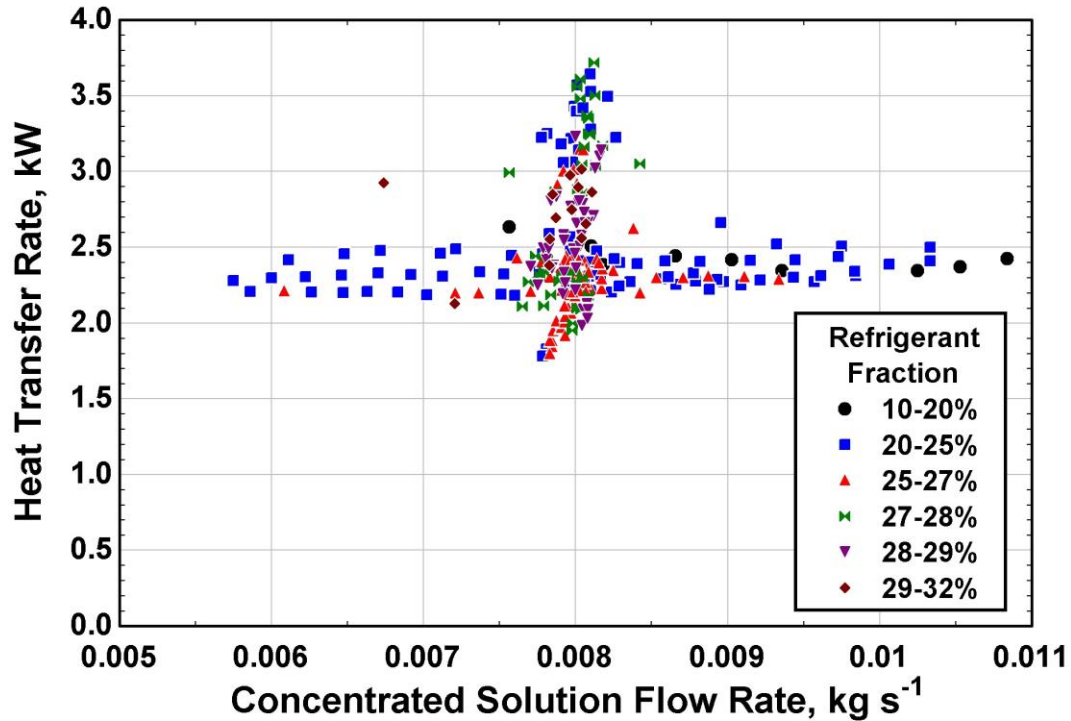
**Figure 5.23 Total tube-side differential pressure in the prototype absorber**

The deviation between the predicted and measured total differential pressure was 0.7-1.0 Pa, corresponding to 102% to 241% of experimental values. The model predicts greater absorption occurring than what was measured; as a result, one would expect a greater gravitational pressure rise in the model predictions due to the lower average quality. This is verified by the lower total differential pressure values in the model compared to the data. It should be noted that the uncertainty in the measured values is a large fraction of the discrepancy between predictions and the data. Also, the measured differential pressure depends on the inlet/outlet fluid assumptions used in the calculation of losses.



### 5.3.6 Refrigerant Fraction

A plot of all measured heat transfer rates as a function of concentrated solution flow rate categorized by refrigerant fraction is shown in *Figure 5.24*.



**Figure 5.24** Prototype heat transfer rates as a function of concentrated solution flow rate, categorized by refrigerant fraction

The vertical cluster of values at the design concentrated solution flow rate (0.008 kg s<sup>-1</sup>) corresponds to adjustments in inlet air and solution temperatures. There is no clear relation between heat transfer rate and refrigerant fraction here, most likely due to the significant underperformance of the absorber resulting from liquid and vapor flow maldistribution.

### **5.3.7 Maldistribution Analysis**

The significant difference between the predicted and measured heat transfer rates in the prototype tube-array absorber warrants additional investigation. Differences in performance could be attributable to one or more of the following phenomena:

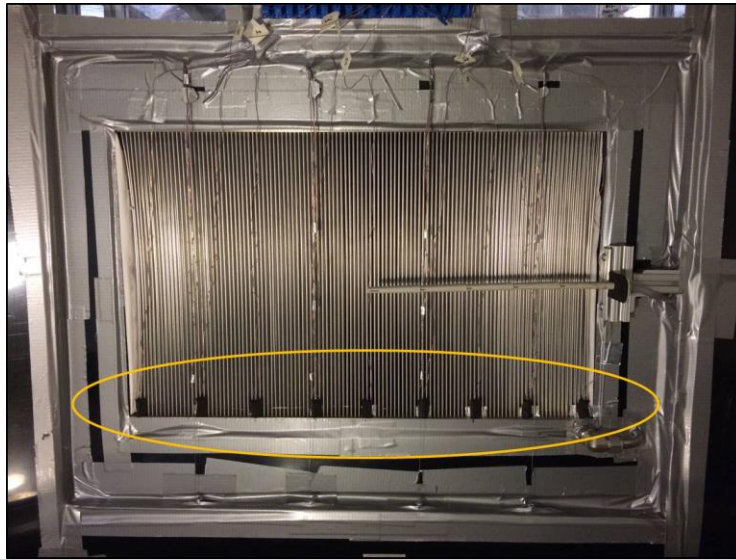
- Maldistribution of solution in the tube array
- Non-uniform inlet air temperature and velocity profile
- Subcooling of liquid in the test absorber
- Misalignment of component and distributor tube
- Variation in height of projection of different tubes into inlet header

The assumption of an equal amount of liquid and vapor distributed in each tube port in the array is improbable, particularly in the lateral direction across the face of the absorber. There is a possibility of maldistribution among the eight tube rows aligned in the direction of air flow, but maldistribution is expected to be most severe in the 114-tube rows across the width of the heat exchanger. Although the holes in the distributor were treated with the same drilling and deburring process, it is possible that there are minute differences in the hole edges that cause differential flow in some holes over others. Finally, a liquid level is likely to form in the inlet header, and any variation in the height of tube protrusion into the header will cause liquid to preferentially flow down some tubes over others.

#### **5.3.7.1.      *Experimental Validation***

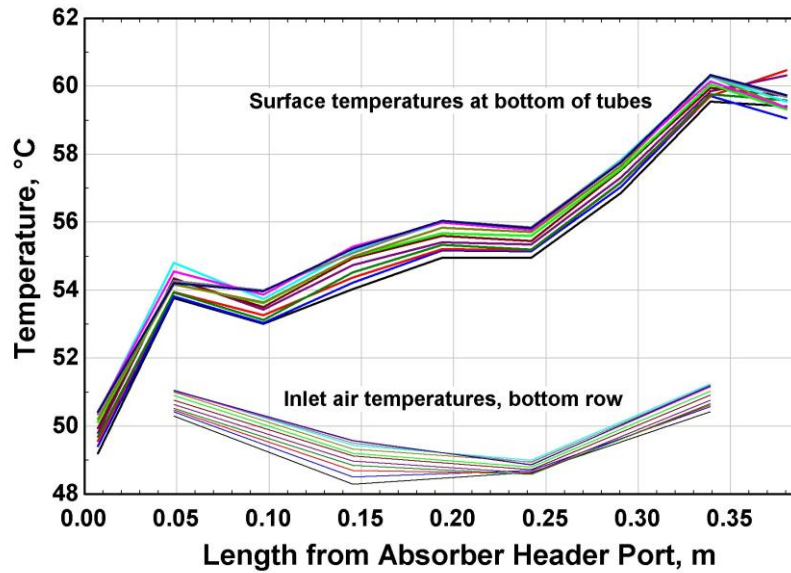
Differences in liquid and vapor flow in the tubes laterally across the face of the heat exchanger would result in differential absorption and variations in solution temperature inside the tubes. This temperature variance is due to the differing heat

capacities and flow rates of the liquid and vapor phases, as well as varying degrees of absorption due to quality differences. This effect would be especially evident at the bottom of the heat exchanger, at which point the liquid and/or vapor has flowed through the major portion of the air flow area. One method to ascertain the possibility of the severely maldistributed flow indicated by the poor performance of this absorber is to collect steady-state wall temperature measurements near the bottom of the tubes (*Figure 5.25*) across the face of the absorber.



**Figure 5.25 Thermocouple probes mounted on outer walls of tubes to record variation in wall temperature**

Nine thermocouples were mounted on the tube walls across the width of the absorber as shown in *Figure 5.25*. A heat sink silicone compound (Chemplex 1381 DE,  $k = 0.75 \text{ W m}^{-1} \text{ K}^{-1}$ ) was used to promote contact between the exposed thermocouple wire and the tube, and a small piece of insulation was used to reduce heat loss from the thermocouple to the air.



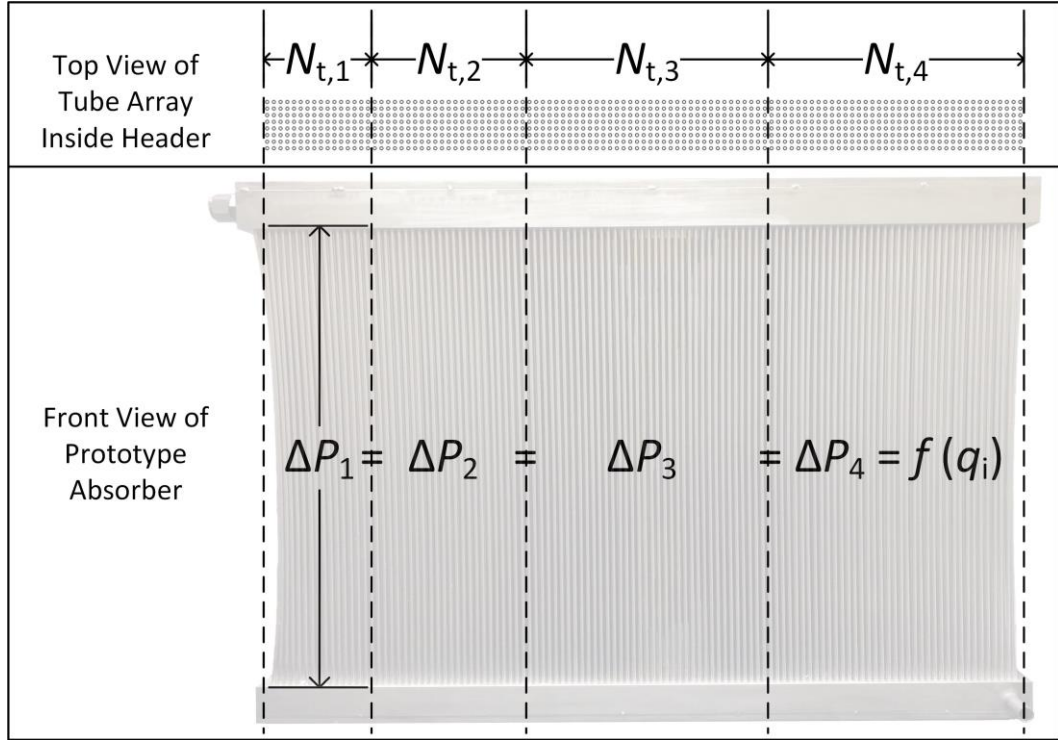
**Figure 5.26 Wall temperature measurements across face of tube-array absorber (each line represents one steady-state data point)**

*Figure 5.26* shows the temperatures recorded on the tube walls across the face of the heat exchanger. Each line represents a steady-state five-minute average of the temperature near design conditions. The temperature disparity is shown to be consistent across all data points. The temperature values are likely to be some average between the wall and air temperature due to imperfect contact of the thermocouple with the wall. Lateral variation of the air temperature would also cause wall temperature differences; therefore, the inlet air temperature at the bottom row of the thermocouple array is plotted in *Figure 5.26* for reference. The disparity in wall temperature measurements is significant ( $\sim 10^{\circ}\text{C}$ ) and is much larger than the inlet air temperature gradient. This confirms the hypothesis of maldistribution of liquid and vapor flow in the tube array playing a role in the poor performance of the absorber.

### **5.3.7.2. Modeling Validation**

Further analysis was conducted to estimate the effect of maldistribution on absorber heat transfer rate. The tube array can be divided into a number of tube bundles laterally (*Figure 5.27*). Each bundle contains a number of tube rows,  $N_{t,i}$ , and the inlet properties are assumed to be uniform in all eight rows along the depth of the header. Therefore, the model is simplified by only considering the first row of tubes. *Figure 5.27* shows the absorber divided into four tube bundles, although any number of bundles could be specified. Most of the distribution cases considered here involved only two tube bundles to minimize the number of assumptions. The model operates such that:

- The pressure drop in each tube bundle is equal.
- The sum of the mass flow rates in the bundles is equal to the total mass flow entering the header.
- One of the following is specified, and the remaining two parameters are permitted to float:
  - Quality in each tube bundle
  - Mass flux in each tube bundle
  - Number of tubes in each bundle



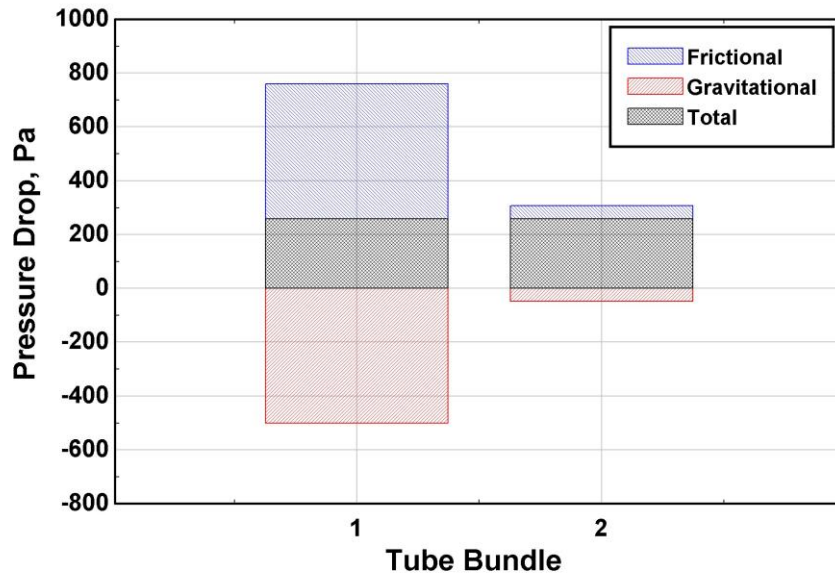
**Figure 5.27 Schematic of maldistribution modeling methodology**

The total pressure drop across each bundle of tubes is specified to be equal, and is composed of frictional (Friedel, 1979) and gravitational components.

$$\Delta P_{sol,total,i} = \Delta P_{fric,Friedel,i} + \Delta P_{grav,i} ; i = \text{Number of tube bundle} \quad (5.9)$$

$$\Delta P_{sol,total,1} = \Delta P_{sol,total,2} = \Delta P_{sol,total,3} = \Delta P_{sol,total,4} \quad (5.10)$$

In the present analysis, the mass flux in each tube bundle is permitted to float, and the quality is specified. Alternatively, the mass flux could be specified For clarity, one potential case of maldistribution is demonstrated, consisting of two tube bundles with qualities of 90% and 10% (mass fluxes of 0.75 and 7.69 kg m<sup>-2</sup> s<sup>-1</sup>, respectively). *Figure 5.28* provides a bar graph of the pressure drop components in each tube bundle for this case.

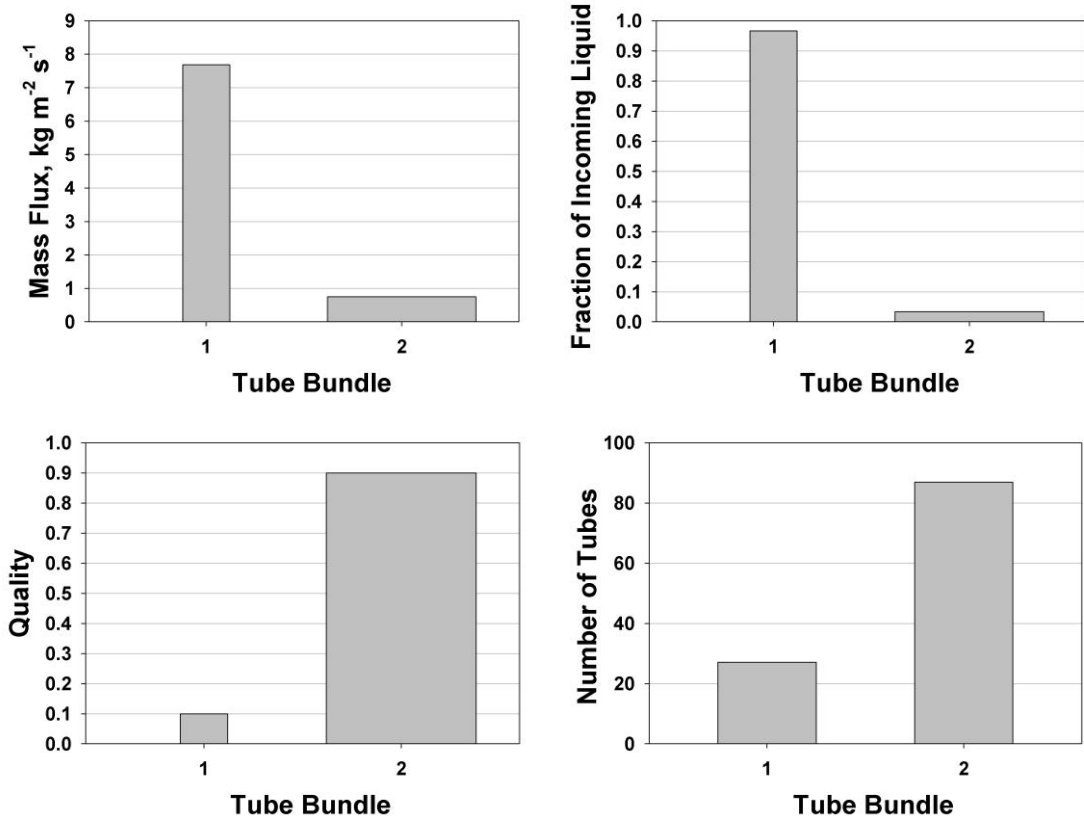


**Figure 5.28 Pressure drop in each bundle of tubes in maldistribution modeling**

For simplicity, the deceleration component of the pressure drop is neglected; it is expected to be minute compared to other differential pressure terms. The sum of the vapor and liquid flow rates in all tube bundles is equal to the inlet vapor and liquid flow rates.

$$\begin{aligned} \dot{m}_{l,\text{total}} &= (\dot{m}_{l,1} + \dot{m}_{l,2}) N_{t,\text{col}} \\ \dot{m}_{v,\text{total}} &= (\dot{m}_{v,1} + \dot{m}_{v,2}) N_{t,\text{col}} \end{aligned} \quad (5.11)$$

Finally, the equations are solved for a number of tubes per bundle and for specific inlet qualities. The user can set qualities, mass fluxes, or numbers of tubes in each bundle, and the model iteratively determines the remaining values. Graphs showing the mass fluxes, liquid distribution, tube bundle qualities, and number of tubes for the 90%/10% quality case are shown in *Figure 5.29*.



**Figure 5.29** Graphs of mass flux (top-left), quality (bottom-left), fraction of incoming liquid (top-right), and number of tube rows (bottom-right) per tube bundle for a representative maldistributed case

The number of tube rows and quality in each bundle was then used in the segmental prototype absorber model to predict the heat transfer rate in each respective bundle. The air flow rate received by each bundle was proportional to the fraction of tubes in the bundle to the total array. The sum of the heat transfer rate in all tube bundles is equal to the total component heat transfer rate.

$$Q_{\text{abs,total}} = Q_{\text{abs,1}} + Q_{\text{abs,2}} \quad (5.12)$$

This process is used to predict the total absorber heat duty that results from a given maldistributed condition. The maldistribution analysis can also be expanded through the use of four, rather than two, tube bundles of varying quality. A series of maldistributed



cases are presented in *Table 5.3* with the predicted absorber duty. The 90%/10% quality case demonstrated above is labeled as case three in *Table 5.3*.

**Table 5.3 Heat transfer in each tube bundle for representative maldistributed conditions**

Case	Number of tubes				Quality				Bundle duty (W)				Total Duty (W)
	(912 total)				1	2	3	4	1	2	3	4	
	1	2	3	4									
1	228	228	228	228	29%	29%	29%	29%	1083	1083	1083	1083	4332
2	137	319	319	137	1%	34%	66%	90%	960	1295	703	263	3221
3	217	695	-	-	10%	90%	-	-	1492	1084	-	-	2576
4	18	72	411	411	2%	10%	90%	98%	234	502	512	688	1936
5	88	824	-	-	5%	95%	-	-	736	1181	-	-	1917
6	45	867	-	-	3%	97%	-	-	448	1209	-	-	1657
7	27	885	-	-	2%	98%	-	-	377	1220	-	-	1597
8	12	900	-	-	1%	99%	-	-	161	1227	-	-	1388

The chosen qualities were selected arbitrarily to give the reader an idea of the reduction in heat transfer possible in different distribution cases. The number of tube rows in each bundle was solved iteratively such that equal pressure drop was predicted throughout the array. Given the possibility of maldistribution in two directions, the large number of tubes (912), and the multitude of potential causes of maldistribution (tube edge finishes, tube height in header, unlevel mounting of distributor, unfavorable diameter/spacing of distributor holes), it is virtually impossible to accurately predict the breakdown of qualities among the tubes. The cases presented in *Table 5.3* serve primarily to indicate the severity of performance degradation one can expect from maldistribution. The analysis predicts that a distribution case similar to case three (90%/10% qualities) would cause heat transfer rates (1.94 kW) comparable to those demonstrated experimentally (2.22 kW), which is significantly less than 4.30 kW predicted at even distribution conditions. Given the experimental demonstration of temperature variation the results of this analysis

of the effect of maldistribution on heat transfer rate, it is likely that flow in the prototype is significantly maldistributed.

Maldistribution is a complex phenomenon that is challenging to prevent and predict. Complete maldistribution analysis and header redesigns are beyond the scope of this work; however, a few suggestions for follow-up investigations are provided. Ideally, temperature measurements on all tubes in the tube array could be obtained to help provide an understanding of where the liquid in the absorber is being distributed. An infrared camera could prove useful in developing a tube-wall temperature profile, although temperatures of the inner tubes and the solution flowing in them would be necessary to get an accurate understanding of absorber performance. Wall temperature information could be added into the segmental model to obtain predicted liquid and vapor flow rates in regions of tubes. Improved distribution may be seen at sufficiently high flow rates, but this would cause a large pressure drop that could hinder heat pump performance. Alternatively, reducing the number of parallel flow paths in the absorber would benefit distribution, but the total heat transfer area would be much lower, keeping other variables constant. Continued studies on predicting and preventing maldistribution in header design would provide insight in future air-coupled absorber designs.

## CHAPTER 6: CONCLUSIONS AND RECOMMENDATIONS

### 6.1 Conclusions

A detailed investigation of air-coupled absorbers for use in a diesel engine exhaust-driven single-effect ammonia-water absorption system was conducted. Heat and mass transfer modeling was used to design round-tube corrugated-fin and compact tube-array absorbers for a 2.64-kW cooling capacity absorption chiller operating at extreme ambient temperatures (51.7°C). A single-pressure ammonia-water test facility was constructed and used in conjunction with a temperature- and humidity-controlled air-handling unit to test the performance of the absorbers at design and off-design operating conditions. Good agreement (0.7-1.9% of  $Q_{\text{abs}}$ ) was found between model predictions and data for the corrugated-fin absorbers at design conditions; however, the tube-array absorber performed extremely poorly (51.6% of  $Q_{\text{abs}}$ ) compared to model predictions. Maldistribution of the two-phase flow in the tube array is the probable cause of the disparity between the prototype absorber data and model predictions.

A thermodynamic cycle model was developed on the *Engineering Equation Solver* (EES) software platform to predict heat pump performance over a range of ambient temperatures, as well as the required heat transfer rate and inlet/outlet conditions for the absorber. A segmental heat- and mass-transfer model was developed for a round-tube corrugated-fin absorber based on the predicted inlet and outlet fluid properties. The model simulated the simultaneous pressure drop, heat exchange, and absorption occurring in the absorber. A model was also developed to predict the performance of a novel, compact absorber composed of a dense array of 912 unfinned 2.16-mm ID tubes. Both

conventional and novel absorbers featured in-house designs customized for the heat pump application under consideration in this study.

The absorbers were tested over a range of air temperatures (35-54.4°C), air flow rates (0.38-0.74 m<sup>3</sup> s<sup>-1</sup>), inlet solution temperatures (92-102°C), concentrated solution flow rates (0.006-0.010 kg s<sup>-1</sup>), and concentrated solution concentrations (38-46%). At design conditions, round-tube corrugated-fin absorbers of 394-FPM and 551-FPM fin densities demonstrated comparable performance ( $Q_{394\text{-FPM,exp}} = 4.521 \pm 0.271$  kW;  $Q_{551\text{-FPM,exp}} = 4.680 \pm 0.260$  kW), and model predicted values slightly under-predicted heat transfer rates with an AAD of 0.7-1.9%. Inlet air temperature, solution temperature, and solution flow rate were shown to have a large impact on corrugated-fin absorber performance, but air-side flow rate had a marginal effect due to unfavorable flow regimes in the corrugated-fin absorbers and internal flow maldistribution in the tube-array absorber. Over the range of tube-side and air-side flow rates, tube-side pressure drop data were slightly over-predicted by the model (11.1-17.7% AAD), and air-side pressure drop was over-predicted by 10.5-27.9% AAD.

The tube-array absorber performed extremely poorly compared to model predictions ( $Q_{\text{prot,exp}} = 2.22 \pm 0.24$  kW;  $Q_{\text{prot,mod}} = 4.30$  kW). To explain the poor performance of the prototype, a maldistribution model was developed, and a series of cases were analyzed. They indicated that unfavorable liquid and vapor conditions could lead to heat transfer rates similar to or below those measured during testing. Poor distribution of liquid and vapor in the tube array was also experimentally corroborated by large differences in measured tube wall temperatures across the face of the absorber. It is

expected that a reduction in the number of flow paths or improved distribution of incoming liquid and vapor in the tube array could lead to improved performance.

## **6.2 Recommendations**

Based on the present study, several avenues are available for the continued development of compact air-coupled heat exchangers for use in low-grade energy driven absorption systems.

### **6.2.1 System-Wide Investigations**

The air-coupled component evaluation in the current investigation was intended to take place at near-uniform air inlet velocity and temperature profiles. While this standardized wind-tunnel testing procedure allows for convenient comparison with other air coils, it is likely to deviate from the conditions expected in a packaged system. As demand grows in residential and small-commercial applications, the packaged absorption heat pump must be delivered in a compact and modular envelope. For the design conditions under consideration, it is likely that the air-coupled heat exchangers in the cycle (the absorber, condenser, and conditioned space heat exchanger) would be oriented on the faces of a rectangular prism to effectively conserve volume and minimize plumbing. Fans would be mounted on the top of the system and would draw air across the absorber and condenser, which would be oriented on two adjacent sides of the prism. As a result, the air flow is likely to enter horizontally through the absorber and condenser before turning upward to exit through the fans. The air would also likely have to flow over baffling or other system components (*e.g.*, pumps, plumbing lines, single-phase heat exchangers) that would affect the flow distribution across the absorber. The performance of the absorber in this flow configuration will be impacted by this non-uniform and multi-

directional air flow profile. Experimental investigations are necessary to validate component performance in packaged-system configurations. Computational Fluid Dynamics (CFD) analyses could also be used to understand air flow patterns across the absorber.

Additional studies pertaining to aspects of full system design can be combined with the present investigation to improve the performance and viability of future heat pumps. Air-coupled condenser development should progress in parallel with absorber design to optimize system performance and reduce fan power consumption and weight. It is likely that the absorber and condenser will reject heat to air drawn by the same set of fans; thus, the air-side pressure drop and flow area of one component will have an impact on the other. It is plausible that banks of absorber and condenser tubes could share the same set of fins to help consolidate the volume of the system intended for air coupling. Experimental investigations of air-coupled condensers, independently and in conjunction with the absorber, would further establish system feasibility. Advanced air coupling design could even enable the use of natural convection as the means of heat rejection as attempted by De Francisco *et al.* (2002).

### **6.2.2 Enhancement of Conventional Heat Exchangers**

For immediate implementation, it appears that conventional round-tube absorbers with patterned fins provide optimal performance at a cost amenable to mass production. Improvements made to these typical geometries for absorption could help enable more widespread waste heat recovery in the near future. The insertion of wire coils, twisted tape, or other conductive packing could be used to reduce hydraulic diameter and potentially enhance mixing during the absorption process for round-tube heat exchangers.

Alternatively, surface enhancements on the inner surface of the tube could promote conditions more favorable to heat and mass transfer. These inserts and enhancements could be implemented as long as the tube-side pressure drop and added mass are acceptable for the application. An expanded inventory of heat transfer and pressure drop data for a variety of fin patterns would broaden the tools available to the air coil designer in predicting absorber performance.

### **6.2.3 Continued Development of Prototype Geometries**

Chapter 4 introduced a series of alternative air coupling designs, including the casting or riveting of a row of steel tubes in aluminum, the brazing of internal fins in flattened tubes for support, and the brazing of milled steel channels into a flat-tube form factor. These or other designs could achieve a hydraulic diameter favorable for heat transfer while enabling the use of compact multi-louvered fins. One follow-up investigation being conducted by the research team includes compact U-bends added to the small-diameter steel tubes to allow for multiple fluid passes over the flow area. These bends would allow for the tube array to be oriented in a staggered arrangement, and the increase in number of passes would reduce the number flow paths and potential for maldistribution. The tube-side pressure drop in the present investigation is sufficiently low to accommodate the increase in pressure drop that would result from this reduction in solution flow area. For a tube-array component to perform effectively, improved header and distributor designs are necessary to prevent maldistribution. Experimental investigations involving the distribution of two-phase flow into a large number of ports could provide insight into future absorber designs. Similar studies could be conducted to

optimize the performance of the mixer while maintaining a sufficiently low pressure drop.

The present investigation expands the understanding of air-coupled absorber performance for the benefit of future absorption heat pump designers. This effort, in combination with the findings of previous and future studies, could enhance the viability of waste heat recovery and reduction of environmental impact through the use of thermally driven absorption cooling and heating systems.



## APPENDIX A: SEGMENTAL HEAT AND MASS TRANSFER MODEL SAMPLE CALCULATIONS

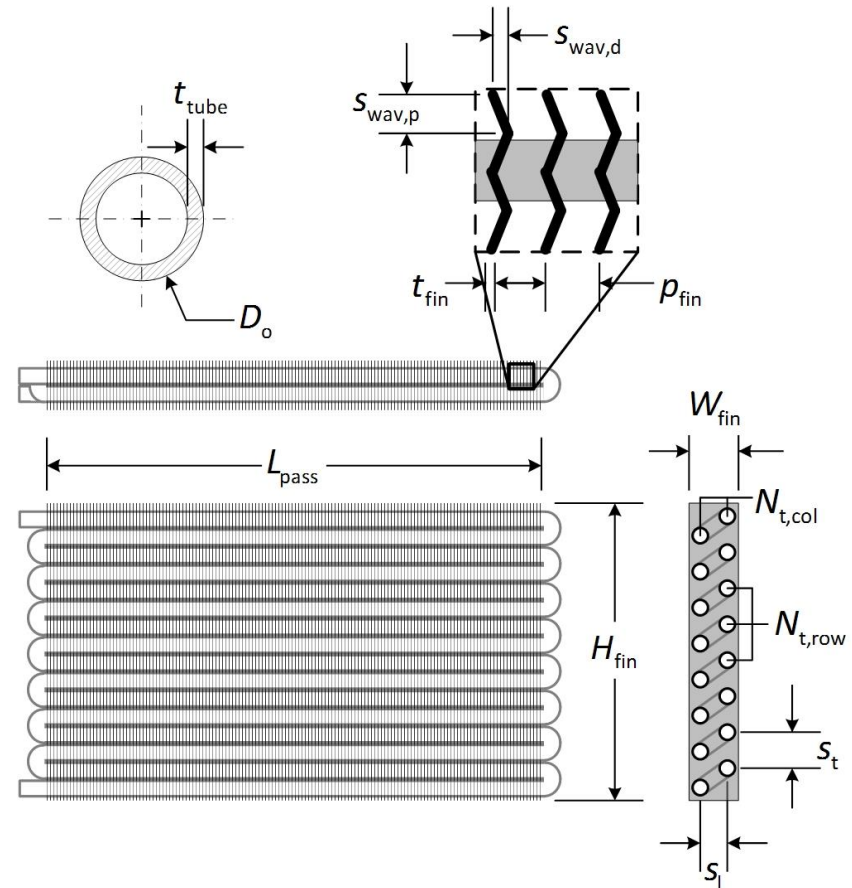
### A.1 Round-Tube Corrugated-Fin Absorber

**Table A.2 Geometric inputs**

Tube-Side Geometry	
$L_{sg}$ (m)	0.025
$N_{sg}$ (-)	528
$D_o$ (m)	0.016
$t_{tube}$ (m)	$1.25 \times 10^{-3}$
$L_{pass}$ (m)	0.610
$N_{t,row}$ (-)	11
$N_{t,col}$ (-)	2
$s_t$ (m)	0.038
$s_l$ (m)	0.033
$\epsilon_{rough}$ (m)	$1.0 \times 10^{-5}$
Tube material	Carbon steel
Air-Side Geometry	
$H_{fin}$ (m)	0.419
$W_{fin}$ (m)	0.066
$t_{fin}$ (m)	$2.41 \times 10^{-4}$
$p_{fin}$ (m)	$2.54 \times 10^{-3}$
$s_{wav,d}$ (m)	$2.79 \times 10^{-3}$
$s_{wav,p}$ (m)	$8.20 \times 10^{-3}$
Fin material	Aluminum

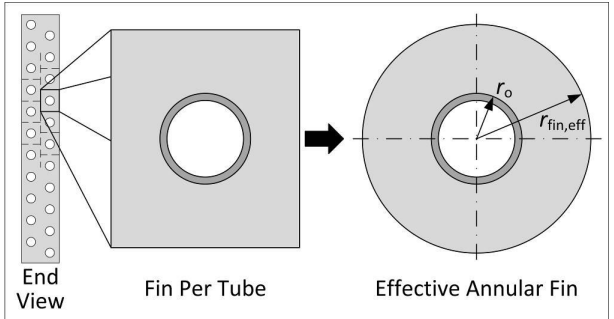
**Table A.1 Inlet conditions**

Refrigerant Vapor Inlet Conditions	
$T_{v,in}$ ( $^{\circ}\text{C}$ )	97.60
$P_{v,in}$ (kPa)	591.8
$x_{v,in}$ (-)	0.877
$\dot{m}_{v,in}$ ( $\text{kg s}^{-1}$ )	$2.32 \times 10^{-3}$
Dilute Solution Inlet Conditions	
$T_{l,in}$ ( $^{\circ}\text{C}$ )	97.49
$P_{l,in}$ (kPa)	591.8
$x_{l,in}$ (-)	0.235
$\dot{m}_{l,in}$ ( $\text{kg s}^{-1}$ )	$5.68 \times 10^{-3}$
Inlet Air Conditions	
$\dot{V}_{air}$ ( $\text{m}^3 \text{s}^{-1}$ )	0.425
$T_{air,in}$ ( $^{\circ}\text{C}$ )	51.67
$P_{air,in}$ (kPa)	101.3
$RH_{air,in}$ (-)	0.18



**Figure A.1 Corrugated-fin absorber geometry schematic**

Segmental Round Finned Tube Heat and Mass Transfer: Sample Calculations		
Inputs	Equations	Results
<b>First 0.025-m segment at the inlet of the 394-FPM corrugated-fin absorber (528 segments total)</b>		
Tube-Side Geometry Intermediate Calculations		
$D_o = 0.016 \text{ m}$ $t_{\text{tube}} = 1.25 \times 10^{-3} \text{ m}$ $N_{\text{t,row}} = 11$ $N_{\text{t,col}} = 2$ $L_{\text{pass}} = 0.610 \text{ m}$ $L_{\text{sg}} = 0.025 \text{ m}$	$D_i = D_o - 2t_{\text{tube}}$	$D_i = 0.013 \text{ m}$
	$A_i = \frac{\pi}{4} D_i^2$	$A_i = 1.41 \times 10^{-4} \text{ m}^2$
	$N_{\text{pass}} = N_{\text{t,row}} N_{\text{t,col}}$	$N_{\text{pass}} = 22$
	$L_{\text{total}} = L_{\text{pass}} N_{\text{pass}}$	$L_{\text{total}} = 13.41 \text{ m}$
	Fraction of segment over total uncoiled tube length, used in finding segmental air flow rate  $Fraction_{\text{sg}} = \frac{L_{\text{sg}}}{L_{\text{total}}}$	$Fraction_{\text{sg}} = 1.89 \times 10^{-3}$
$N_{\text{sg}} = L_{\text{total}} / L_{\text{sg}}$	$N_{\text{sg}} = 528$	
Air-Side Geometry Intermediate Calculations		

Segmental Round Finned Tube Heat and Mass Transfer: Sample Calculations		
Inputs	Equations	Results
$H_{\text{fin}} = 0.419 \text{ m}$ $W_{\text{fin}} = 0.066 \text{ m}$ $N_{\text{pass}} = 22$ $D_o = 0.016 \text{ m}$ $D_{\text{fin,eff}} = 0.04 \text{ m}$ $L_{\text{sg}} = 0.025 \text{ m}$ $t_{\text{fin}} = 2.41 \times 10^{-4} \text{ m}$ $p_{\text{fin}} = 2.54 \times 10^{-3} \text{ m}$ $N_{\text{t,row}} = 11$ $L_{\text{pass}} = 0.610 \text{ m}$	<p>Area of fin per tube, treated as an annular fin of an effective diameter, <math>D_{\text{fin,eff}}</math></p> $A_{\text{annular,fin}} = \frac{\pi}{4} (D_{\text{fin,eff}}^2 - D_o^2) = \left[ \frac{H_{\text{fin}} W_{\text{fin}}}{N_{\text{pass}}} - \left( \frac{\pi}{4} \right) D_o^2 \right]$ 	$A_{\text{annular,fin}} = 1.059 \times 10^{-3} \text{ m}^2$ $D_{\text{fin,eff}} = 0.04 \text{ m}$
	$r_{\text{fin,eff}} = \frac{D_{\text{fin,eff}}}{2}$	$r_{\text{fin,eff}} = 0.02 \text{ m}$
	<p>Finned area per segment, along single serpentine tube</p> $A_{\text{fin,sg}} = 2 \left( \frac{L_{\text{sg}}}{p_{\text{fin}}} \right) \left[ \frac{H_{\text{fin}} W_{\text{fin}}}{N_{\text{pass}}} - \left( \frac{\pi}{4} \right) D_o^2 \right]$	$A_{\text{fin,sg}} = 0.0212 \text{ m}^2$
	<p>Unfinned area per segment (exposed tube)</p> $A_{\text{unfin,sg}} = \pi D_o L_{\text{sg}} \left( 1 - \frac{t_{\text{fin}}}{p_{\text{fin}}} \right)$	$A_{\text{unfin,sg}} = 1.146 \times 10^{-3} \text{ m}^2$
	<p>Total, finned and unfinned, area per segment</p> $A_{\text{total,sg}} = A_{\text{fin,sg}} + A_{\text{unfin,sg}}$	$A_{\text{total,sg}} = 0.022 \text{ m}^2$

Segmental Round Finned Tube Heat and Mass Transfer: Sample Calculations		
Inputs	Equations	Results
	Cross-sectional area available for air flow, for use in air-side pressure drop calculations $A_c = (H_{fin} - N_{t,row} D_o) L_{pass} \left( 1 - \frac{t_{fin}}{p_{fin}} \right)$	$A_c = 0.135 \text{ m}^2$
<b>Fluid Properties</b>		
$P_{v,in} = P_{l,in} = 591.80 \text{ kPa}$	$P_v = (P_{v,in} + P_{v,out})/2$	$P_v = 591.79 \text{ kPa}$
$P_{v,out}^* = P_{l,out}^* = 591.79 \text{ kPa}$	$T_v = (T_{v,in} + T_{v,out})/2$	$T_v = 97.60^\circ\text{C}$
$T_{v,in} = 97.60^\circ\text{C}; T_{v,out}^* = 97.59^\circ\text{C}$	$x_v = (x_{v,in} + x_{v,out})/2$	$x_v = 0.877$
$x_{v,in} = 0.877; x_{v,out}^* = 0.877$	$\dot{m}_v = (\dot{m}_{v,in} + \dot{m}_{v,out})/2$	$\dot{m}_v = 2.318 \times 10^{-3} \text{ kg s}^{-1}$
$\dot{m}_{v,in} = 2.323 \times 10^{-3} \text{ kg s}^{-1}$	$M_{v,avg} = \left( \frac{x_v}{M_{\text{NH}_3}} + \frac{1-x_v}{M_{\text{H}_2\text{O}}} \right)^{-1}$	$M_{v,avg} = 17.15 \text{ kg kmol}^{-1}$
$\dot{m}_{v,out}^* = 2.314 \times 10^{-3} \text{ kg s}^{-1}$	$x_{v,molar} = x_v M_{v,avg} / M_{\text{NH}_3}$	$x_{v,molar} = 0.883$
$M_{\text{NH}_3} = 17.03 \text{ kg kmol}^{-1}$	$Re_v = \frac{\dot{m}_v D_i}{A_i \mu_v}$	$Re_v = 16834$
$M_{\text{H}_2\text{O}} = 18.02 \text{ kg kmol}^{-1}$	$Pr_v = \mu_v C_{p,v} / k_v$	$Pr_v = 0.886$
$T_{l,in} = 97.49^\circ\text{C}; T_{l,out}^* = 97.18^\circ\text{C}$	$P_l = (P_{l,in} + P_{l,out})/2$	$P_l = 591.787 \text{ kPa}$
$x_{l,in} = 0.235; x_{l,out}^* = 0.236$	$T_l = (T_{l,in} + T_{l,out})/2$	$T_l = 97.34^\circ\text{C}$
$\dot{m}_{l,in} = 5.677 \times 10^{-3} \text{ kg s}^{-1}$	$x_l = (x_{l,in} + x_{l,out})/2$	$x_l = 0.235$
$\dot{m}_{l,out}^* = 5.686 \times 10^{-3} \text{ kg s}^{-1}$	$\dot{m}_l = (\dot{m}_{l,in} + \dot{m}_{l,out})/2$	$\dot{m}_l = 5.682 \times 10^{-3} \text{ kg s}^{-1}$
*Determined through iteration		
$D_i = 0.013 \text{ m}$		
$A_i = 1.41 \times 10^{-4} \text{ m}^2$		

Segmental Round Finned Tube Heat and Mass Transfer: Sample Calculations		
Inputs	Equations	Results
With $(P, T, x)$ , all others known: $\mu_v = 1.310 \times 10^{-5} \text{ kg m}^{-1} \text{ s}^{-1}$ ; $\mu_1 = 2.915 \times 10^{-4} \text{ kg m}^{-1} \text{ s}^{-1}$ $C_{p,v} = 2.46 \text{ kJ kg}^{-1} \text{ K}^{-1}$ ; $C_{p,l} = 4.383 \text{ kJ kg}^{-1} \text{ K}^{-1}$ $k_v = 0.036 \text{ W m}^{-1} \text{ K}^{-1}$ ; $k_1 = 0.594 \text{ W m}^{-1} \text{ K}^{-1}$  $k_v, \mu_v$ values from Chapman-Enskog kinetic theory (Mills, 1999) $C_p$ values from <i>EES</i> , using data from Ibrahim and Klein (1993)	$M_{l,avg} = \left( \frac{x_1}{M_{\text{NH}_3}} + \frac{1-x_1}{M_{\text{H}_2\text{O}}} \right)^{-1}$	$M_{l,avg} = 17.77 \text{ kg kmol}^{-1}$
	$x_{l,molar} = x_1 M_{l,avg} / M_{\text{NH}_3}$	$x_{l,molar} = 0.246$
	$Re_1 = \frac{\dot{m}_1 D_i}{A_1 \mu_1}$	$Re_1 = 1854$
	$Pr_1 = \mu_1 C_{p,l} / k_1$	$Pr_1 = 2.151$
Tube-Side Heat Transfer Coefficient		
$\dot{m}_1 = 5.682 \times 10^{-3} \text{ kg s}^{-1}$ $\dot{m}_v = 2.318 \times 10^{-3} \text{ kg s}^{-1}$ $x_1 = 0.235$ $x_v = 0.877$ $M_{\text{NH}_3} = 17.03 \text{ kg kmol}^{-1}$ $M_{\text{H}_2\text{O}} = 18.02 \text{ kg kmol}^{-1}$ $P_{\text{crit,NH}_3} = 11333 \text{ kPa}$ $P_{\text{crit,H}_2\text{O}} = 22064 \text{ kPa}$ $A_1 = 1.41 \times 10^{-4} \text{ m}^2$ $k_1 = 0.594 \text{ W m}^{-1} \text{ K}^{-1}$ $D_i = 0.013 \text{ m}$	$\dot{m}_{\text{sol}} = \dot{m}_1 + \dot{m}_v$	$\dot{m}_{\text{sol}} = 0.008 \text{ kg s}^{-1}$
	$\dot{m}_{\text{sol}} x_{\text{sol,equil}} = \dot{m}_1 x_1 + \dot{m}_v x_v$	$x_{\text{sol,equil}} = 0.421$
	Solved together: $\begin{cases} x_{\text{sol,equil}} = \frac{x_{\text{mol,NH}_3} M_{\text{NH}_3}}{x_{\text{mol,NH}_3} M_{\text{NH}_3} + x_{\text{mol,H}_2\text{O}} M_{\text{H}_2\text{O}}} \\ 1 = x_{\text{mol,NH}_3} + x_{\text{mol,H}_2\text{O}} \end{cases}$	$x_{\text{mol,NH}_3} = 0.435$ $x_{\text{mol,H}_2\text{O}} = 0.565$
	$P_{\text{crit}} = x_{\text{mol,NH}_3} P_{\text{crit,NH}_3} + x_{\text{mol,H}_2\text{O}} P_{\text{crit,H}_2\text{O}}$	$P_{\text{crit}} = 17396 \text{ kPa}$
	$q_{\text{sol}} = \dot{m}_v / (\dot{m}_1 + \dot{m}_v)$	$q_{\text{sol}} = 0.29$
	$G_{\text{sol}} = \dot{m}_{\text{sol}} / A_1$	$G_{\text{sol}} = 56.85 \text{ kg m}^{-2} \text{ s}^{-1}$
	Liquid-only heat transfer coefficient (Dittus and Boelter, 1930)	$\alpha_{lo} = 750.3 \text{ W m}^{-2} \text{ K}^{-1}$
	$\alpha_{lo} = 0.023 \frac{k_1}{D_i} \left( \frac{G_{\text{sol}} D_i}{\mu_1} \right)^{0.8} Pr_1^{0.4}$	

Segmental Round Finned Tube Heat and Mass Transfer: Sample Calculations		
Inputs	Equations	Results
$\mu_l = 2.915 \times 10^{-4} \text{ kg m}^{-1} \text{ s}^{-1}$ $Pr_l = 2.151$	$\alpha_{\text{Shah}} = \alpha_{lo} \left[ (1 - q_{\text{sol}})^{0.8} + \frac{3.8 q_{\text{sol}}^{0.76} (1 - q_{\text{sol}})^{0.04}}{(P_{\text{sol}}/P_{\text{crit}})^{0.38}} \right]$	$\alpha_{\text{Shah}} = 4535 \text{ W m}^{-2} \text{ K}^{-1}$ (Shah, 1979)
	$\alpha_{\text{sol}} = \alpha_{\text{Shah}}$	$\alpha_{\text{sol}} = 4535 \text{ W m}^{-2} \text{ K}^{-1}$
Tube-Side Flow Regime		
$Re_l = 1854$ $Re_v = 16834$ $G_{\text{sol}} = 56.85 \text{ kg m}^{-2} \text{ s}^{-1}$ $q_{\text{sol}} = 0.29$ $\rho_l = 810.1 \text{ kg m}^{-3}$ $D_l = 0.013 \text{ m}$ $f_v = 6.935 \times 10^{-3}$ $\rho_v = 3.416 \text{ kg m}^{-3}$ $\left(\frac{dP}{dz}\right)_l = -2.594 \text{ Pa m}^{-1}$ $\dot{m}_l = 5.682 \times 10^{-3} \text{ kg s}^{-1}$ $v_l = 1.234 \times 10^{-3} \text{ m}^3 \text{ kg}^{-1}$ $A_l = 1.41 \times 10^{-4} \text{ m}^2$ $\dot{m}_v = 2.318 \times 10^{-3} \text{ kg s}^{-1}$ $v_v = 0.293 \text{ m}^3 \text{ kg}^{-1}$	If $Re_{l,v} < 2000$ : $\begin{cases} B_{l,v} = 16 \\ n_{l,v} = 1 \end{cases}$ ; Else: $\begin{cases} B_{l,v} = 0.079 \\ n_{l,v} = 0.25 \end{cases}$	$B_l = 16$ ; $B_v = 0.079$ $n_l = 1$ ; $n_v = 0.25$
	$f_l = B_l Re_l^{-n_l}$	$f_l = 8.628 \times 10^{-3}$
	$f_v = B_v Re_v^{-n_v}$	$f_v = 6.935 \times 10^{-3}$
	Pressure gradient in liquid, used to calculate Martinelli parameter $\left(\frac{dP}{dz}\right)_l = \frac{-2f_l G_{\text{sol}}^2 (1 - q_{\text{sol}})^2}{\rho_l D_l}$	$\left(\frac{dP}{dz}\right)_l = -2.594 \text{ Pa m}^{-1}$
	Pressure gradient in vapor, used to calculate Martinelli parameter $\left(\frac{dP}{dz}\right)_v = \frac{-2f_v G_{\text{sol}}^2 q_{\text{sol}}^2}{\rho_v D_l}$	$\left(\frac{dP}{dz}\right)_v = -82.33 \text{ Pa m}^{-1}$
	Martinelli parameter, used in flow regime mapping $X_{\text{Martinelli}} = \sqrt{\frac{(dP/dz)_l}{(dP/dz)_v}}$	$X_{\text{Martinelli}} = 0.178$ (Lockhart and Martinelli, 1949)
	Superficial liquid velocity $j_l = \dot{m}_l (v_l / A_l)$	$j_l = 0.050 \text{ m s}^{-1}$

Segmental Round Finned Tube Heat and Mass Transfer: Sample Calculations		
Inputs	Equations	Results
$\rho_l = 810.1 \text{ kg m}^{-3}$ $g = 9.81 \text{ m s}^{-2}$ $\dot{m}_{\text{sol}} = 0.008 \text{ kg s}^{-1}$ $\dot{m}_{l,\text{in}} = 5.677 \times 10^{-3} \text{ kg s}^{-1}$ , $\dot{m}_{v,\text{in}} = 2.323 \times 10^{-3} \text{ kg s}^{-1}$ $h_{l,\text{in}} = 263.5 \text{ kJ kg}^{-1}$ , $h_{v,\text{in}} = 1633 \text{ kJ kg}^{-1}$ $\dot{m}_{l,\text{out}} = 5.686 \times 10^{-3} \text{ kg s}^{-1}$ , $\dot{m}_{v,\text{out}} = 2.314 \times 10^{-3} \text{ kg s}^{-1}$ $h_{l,\text{out}} = 260.9 \text{ kJ kg}^{-1}$ , $h_{\text{sol},\text{out}}^* = 657.6 \text{ kJ kg}^{-1}$ *Determined through iteration	Superficial vapor velocity $j_v = \dot{m}_v (v_v / A_i)$	$j_v = 4.822 \text{ m s}^{-1}$
	Factor specified by Taitel and Dukler (1976) for flow regime mapping $F_{\text{TD}} = \sqrt{\frac{\rho_v j_v^2}{(\rho_l - \rho_v) D_i g}}$	$F_{\text{TD}} = 0.866$
	$K_{\text{TD}} = \sqrt{\frac{\rho_v j_v^2 j_l}{v_l (\rho_l - \rho_v) D_i g}}$	$K_{\text{TD}} = 37.29$
	$T_{\text{TD}} = \sqrt{\frac{-dP/dz_l}{(\rho_l - \rho_v) g}}$	$T_{\text{TD}} = 0.018$ (Taitel and Dukler, 1976)
	If $(\text{Re}_l < 2000) \ \& \ (\text{Re}_v < 2000): C = 5$ If $(\text{Re}_l < 2000) \ \& \ (\text{Re}_v > 2000): C = 12$ If $(\text{Re}_l > 2000) \ \& \ (\text{Re}_v < 2000): C = 10$ If $(\text{Re}_l > 2000) \ \& \ (\text{Re}_v > 2000): C = 20$	$C = 12$
	$\dot{m}_{\text{sol}} h_{\text{sol},\text{in}} = \dot{m}_{l,\text{in}} h_{l,\text{in}} + \dot{m}_{v,\text{in}} h_{v,\text{in}}$	$h_{\text{sol},\text{in}} = 661.1 \text{ kJ kg}^{-1}$
	$\dot{m}_{\text{sol}} h_{\text{sol},\text{out}} = \dot{m}_{l,\text{out}} h_{l,\text{out}} + \dot{m}_{v,\text{out}} h_{v,\text{out}}$	$h_{v,\text{out}} = 1632 \text{ kJ kg}^{-1}$
Tube-Side Pressure Drop		
<i>Frictional Pressure Drop According to Friedel (1979)</i>		
$G_{\text{sol}} = 56.85 \text{ kg m}^{-2} \text{ s}^{-1}$ $D_i = 0.0134 \text{ m}$ $\mu_v = 1.310 \times 10^{-5} \text{ kg m}^{-1} \text{ s}^{-1}$	$\text{Re}_{v0} = \frac{G_{\text{sol}} D_i}{\mu_v}$	$\text{Re}_{v0} = 58088$
	If $\text{Re}_{v0} < 2000: \begin{cases} B_{v0} = 16 \\ n_{v0} = 1 \end{cases}$ ; Else: $\begin{cases} B_{v0} = 0.079 \\ n_{v0} = 0.25 \end{cases}$	$B_{v0} = 0.079$ $n_{v0} = 0.25$

Segmental Round Finned Tube Heat and Mass Transfer: Sample Calculations			
Inputs	Equations	Results	
$\mu_1 = 2.915 \times 10^{-4} \text{ kg m}^{-1} \text{ s}^{-1}$ $\mu_1$ from empirical correlations from Meacham (2002) based on graphical data from Herold <i>et al.</i> (1996) $q_{\text{sol}} = 0.29$ $\rho_1 = 810.1 \text{ kg m}^{-3}$ $\rho_v = 3.416 \text{ kg m}^{-3}$ $g = 9.81 \text{ m s}^{-2}$ $\sigma_1 = 0.036 \text{ N m}^{-1}$ $\sigma_1$ from empirical correlations from Meacham (2002) based on graphical data from Herold <i>et al.</i> (1996) $\dot{m}_{\text{sol}} = 0.008 \text{ kg s}^{-1}$ $A_1 = 1.41 \times 10^{-4} \text{ m}^2$ $\dot{m}_{1,\text{in}} = 5.677 \times 10^{-3} \text{ kg s}^{-1}$ $x_{1,\text{in}} = 0.235$ $\dot{m}_{v,\text{in}} = 2.323 \times 10^{-3} \text{ kg s}^{-1}$ $x_{v,\text{in}} = 0.877$ $\dot{m}_{1,\text{out}} = 5.687 \times 10^{-3} \text{ kg s}^{-1}$	Vapor-only friction factor, used in tube-side pressure drop calculations $f_{\text{vo}} = B_{\text{vo}} \text{Re}_{\text{vo}}^{-n_{\text{vo}}}$	$f_{\text{vo}} = 5.089 \times 10^{-3}$	
	$\text{Re}_{1\text{o}} = \frac{G_{\text{sol}} D_1}{\mu_1}$		$\text{Re}_{1\text{o}} = 2611$
	If $\text{Re}_{1\text{o}} < 2000$ : $\begin{cases} B_{1\text{o}} = 16 \\ n_{1\text{o}} = 1 \end{cases}$ ; Else: $\begin{cases} B_{1\text{o}} = 0.079 \\ n_{1\text{o}} = 0.25 \end{cases}$		$B_{1\text{o}} = 0.079$ $n_{1\text{o}} = 0.25$
	Liquid-only friction factor $f_{1\text{o}} = B_{1\text{o}} \text{Re}_{1\text{o}}^{-n_{1\text{o}}}$		$f_{1\text{o}} = 0.011$
	First parameter specified by Friedel (1979) for tube-side frictional pressure drop calculation $C_{\text{F1}} = (1 - q_{\text{sol}})^2 + q_{\text{sol}}^2 \left( \frac{\rho_1}{\rho_v} \right) \left( \frac{f_{\text{vo}}}{f_{1\text{o}}} \right)$		$C_{\text{F1}} = 9.674$
	Second parameter specified by Friedel (1979) for tube-side frictional pressure drop calculation $C_{\text{F2}} = q_{\text{sol}}^{0.78} (1 - q_{\text{sol}})^{0.224} \left( \frac{\rho_1}{\rho_v} \right)^{0.91} \left( \frac{\mu_v}{\mu_1} \right)^{0.19} \left( 1 - \frac{\mu_v}{\mu_1} \right)^{0.7}$		$C_{\text{F2}} = 27.44$
	$Fr = \frac{G_{\text{sol}}^2}{g D_i \rho_{\text{tp}}^2}$		$Fr = 180.8$



Segmental Round Finned Tube Heat and Mass Transfer: Sample Calculations		
Inputs	Equations	Results
$x_{l,out} = 0.236$ $\dot{m}_{v,out} = 2.313 \times 10^{-3} \text{ kg s}^{-1}$ $x_{v,out} = 0.877$ $\phi_{lo,Friedel} = 8.338$ $f_{lo} = 0.011$ $L_{sg} = 0.025 \text{ m}$ $L_{inlet,outlet} = 0.406 \text{ m}$ $L_{total} = 13.41 \text{ m}$	$We = \frac{G_{sol}^2 D_i}{\rho_{tp} \sigma_l}$	$We = 102.4$
	Liquid-only two-phase multiplier specified by Friedel (1979) $\phi_{lo,Friedel} = \sqrt{C_{F1} + \frac{3.24 C_{F2}}{Fr^{0.045} We^{0.035}}}$	$\phi_{lo,Friedel} = 8.338$ (Friedel, 1979)
	$\left( \frac{dP}{dz} \right)_{Friedel} = \phi_{lo,Friedel}^2 \left( \frac{2 f_{lo} G_{sol}^2}{\rho_l D_i} \right)$	$\left( \frac{dP}{dz} \right)_{Friedel} = 457.9 \text{ Pa m}^{-1}$
	Frictional pressure drop across segment $\Delta P_{fric,Friedel} = \left( \frac{dP}{dz} \right)_{Friedel} \cdot L_{sg} + \left( \frac{dP}{dz} \right)_{Friedel} \cdot L_{inlet,outlet} \left( \frac{L_{sg}}{L_{total}} \right)$	$\Delta P_{fric,Friedel} = 11.99 \text{ Pa}$
<i>Tube-Side Pressure Drop Due to Deceleration</i>		
$\phi_{lo,Friedel} = 8.338$ $f_{lo} = 0.011$ $G_{sol} = 56.85 \text{ kg m}^{-2} \text{ s}^{-1}$ $\rho_l = 810.1 \text{ kg m}^{-3}$ $D_i = 0.013 \text{ m}$ $L_{sg} = 0.025 \text{ m}$ $L_{inlet,outlet} = 0.406 \text{ m}$	$q_{sol,in} = \frac{\dot{m}_{v,in}}{\dot{m}_{v,in} + \dot{m}_{l,in}}; q_{sol,out} = \frac{\dot{m}_{v,out}}{\dot{m}_{v,out} + \dot{m}_{l,out}}$	$q_{sol,in} = 0.290$ $q_{sol,out} = 0.289$
	$q_{sol} = (q_{sol,in} + q_{sol,out})/2$	$q_{sol} = 0.290$
	Void fraction at inlet of segment in the form of Butterworth (1975) with constants from Lockhart and Martinelli (1949) $VF_{in} = \left[ 1 + 0.28 \left( \frac{1 - q_{sol,in}}{q_{sol,in}} \right)^{0.64} \left( \frac{\rho_v}{\rho_l} \right)^{0.36} \left( \frac{\mu_l}{\mu_v} \right)^{0.07} \right]^{-1}$	$VF_{in} = 0.921$

Segmental Round Finned Tube Heat and Mass Transfer: Sample Calculations		
Inputs	Equations	Results
$L_{\text{total}} = 13.41 \text{ m}$ $\dot{m}_{\text{v,in}} = 5.677 \times 10^{-3} \text{ kg s}^{-1}$ $\dot{m}_{\text{v,out}} = 2.323 \times 10^{-3} \text{ kg s}^{-1}$ $\dot{m}_{\text{l,out}} = 5.687 \times 10^{-3} \text{ kg s}^{-1}$ $\dot{m}_{\text{l,in}} = 2.313 \times 10^{-3} \text{ kg s}^{-1}$ $\rho_{\text{v}} = 3.416 \text{ kg m}^{-3}$ $\mu_{\text{l}} = 2.915 \times 10^{-4} \text{ kg m}^{-1} \text{ s}^{-1}$ $\mu_{\text{v}} = 1.310 \times 10^{-5} \text{ kg m}^{-1} \text{ s}^{-1}$ $s_{\text{t}} = 0.038 \text{ m}$ $N_{\text{t,row}} = 11$ $\dot{m}_{\text{sol}} = 0.008 \text{ kg s}^{-1}$ $\rho_{\text{sol, equil}}^* = 11.67 \text{ kg m}^{-3}$ *Approximated at $(P_{\text{sol}}, h_{\text{sol}}, x_{\text{sol, equil}})$	Void fraction at outlet of segment $VF_{\text{out}} = \left[ 1 + 0.28 \left( \frac{1 - q_{\text{sol, out}}}{q_{\text{sol, out}}} \right)^{0.64} \left( \frac{\rho_{\text{v}}}{\rho_{\text{l}}} \right)^{0.36} \left( \frac{\mu_{\text{l}}}{\mu_{\text{v}}} \right)^{0.07} \right]^{-1}$	$VF_{\text{out}} = 0.921$
	Pressure drop due to flow deceleration $\Delta P_{\text{dec}} = G_{\text{sol}}^2 \left[ \frac{q_{\text{sol, out}}^2}{\rho_{\text{v}} VF_{\text{out}}} - \frac{(1 - q_{\text{sol, out}})^2}{\rho_{\text{l}} (1 - VF_{\text{out}})} \right] - G_{\text{sol}}^2 \left[ \frac{q_{\text{sol, in}}^2}{\rho_{\text{v}} VF_{\text{in}}} - \frac{(1 - q_{\text{sol, in}})^2}{\rho_{\text{l}} (1 - VF_{\text{in}})} \right]$	$\Delta P_{\text{dec}} = 2.14 \text{ Pa}$
<i>Tube-Side Pressure Rise Due to Gravity</i>		
$s_{\text{t}} = 0.038 \text{ m}$ $N_{\text{t,row}} = 11$ $L_{\text{total}} = 13.41 \text{ m}$	Effective angle of tube inclination (negative is downward) $\gamma = \tan^{-1} \left[ -s_{\text{t}} \left( \frac{N_{\text{t,row}} - 0.5}{L_{\text{total}}} \right) \right]$	$\gamma = -1.71^\circ$

Segmental Round Finned Tube Heat and Mass Transfer: Sample Calculations		
Inputs	Equations	Results
$VF = 0.921$ $\rho_1 = 810.1 \text{ kg m}^{-3}$ $\rho_v = 3.416 \text{ kg m}^{-3}$ $L_{sg} = 0.025 \text{ m}$	Gravitational pressure rise $\Delta P_{\text{grav}} = [(1-VF)\rho_1 + VF \cdot \rho_v] g \sin(\gamma) L_{sg}$	$\Delta P_{\text{grav}} = -0.50 \text{ Pa}$
<i>Tube-Side Pressure Drop Due to Minor Losses</i>		
$q_{\text{sol}} = 0.29$ $\rho_1 = 810.1 \text{ kg m}^{-3}$ $\rho_v = 3.416 \text{ kg m}^{-3}$ $\dot{m}_{\text{sol}} = 0.008 \text{ kg s}^{-1}$ $K_{L,UBend} = 0.2$ , from Cengel and Cimbala (2006) $A_1 = 1.41 \times 10^{-4} \text{ m}^2$ $L_{\text{pass}} = 0.61 \text{ m}$ $L_{sg} = 0.025 \text{ m}$	Two-phase density used in minor loss predictions $\rho_{\text{tp}} = \left( \frac{q_{\text{sol}}}{\rho_v} + \frac{1-q_{\text{sol}}}{\rho_1} \right)^{-1}$	$\rho_{\text{tp}} = 11.67 \text{ kg m}^{-3}$
	Two-phase velocity used in minor loss predictions $u_{\text{sol}} = \dot{m}_{\text{sol}} / (\rho_{\text{tp}} A_1)$	$u_{\text{sol}} = 4.87 \text{ m s}^{-1}$
	Minor losses in segment (U-Bend in each pass is divided evenly over segments in the pass) $\Delta P_{\text{sol,minor}} = \frac{1}{2} K_{L,UBend} \rho_{\text{tp}} u_{\text{sol}}^2 \left( \frac{L_{sg}}{L_{\text{pass}}} \right)$	$\Delta P_{\text{sol,minor}} = 1.51 \text{ Pa}$
<i>Total Tube-Side Pressure Drop</i>		
$\Delta P_{\text{grav}} = -0.50 \text{ Pa}$ $\Delta P_{\text{sol,minor}} = 1.51 \text{ Pa}$ $\Delta P_{\text{dec}} = 2.06 \text{ Pa}$ $\Delta P_{\text{fric,Friedel}} = 11.99 \text{ Pa}$	Total tube-side pressure drop in segment $\Delta P_{\text{sol,sg}} = \Delta P_{\text{fric,Friedel}} + \Delta P_{\text{dec}} + \Delta P_{\text{grav}} + \Delta P_{\text{sol,minor}}$ $\Delta P_{\text{sol,sg}} = 11.99 \text{ [Pa]} + 2.14 \text{ [Pa]} - 0.50 \text{ [Pa]} + 1.15 \text{ [Pa]} = 14.78 \text{ [Pa]}$	$\Delta P_{\text{sol,sg}} = 14.78 \text{ Pa}$
	$P_{\text{sol,out}} = P_{\text{l,out}} = P_{\text{v,out}} = P_{\text{l,in}} - \Delta P_{\text{sol,sg}}$	$P_{\text{sol,out}} = 591.774 \text{ kPa}$
<b>Air-Side Heat Transfer Coefficient</b>		

Segmental Round Finned Tube Heat and Mass Transfer: Sample Calculations		
Inputs	Equations	Results
$p_{\text{fin}} = 2.54 \times 10^{-3} \text{ m}$ $t_{\text{fin}} = 2.41 \times 10^{-4} \text{ m}$ $\dot{V}_{\text{air}} = 0.425 \text{ m}^3 \text{ s}^{-1}$ $L_{\text{pass}} = 0.61 \text{ m}$ $H_{\text{fin}} = 0.419 \text{ m}$ $D_o = 0.016 \text{ m}$ $D_o = 0.016 \text{ m}$ $t_{\text{fin}} = 2.41 \times 10^{-4} \text{ m}$ $s_t = 0.038 \text{ m}$ $s_l = 0.033 \text{ m}$ $A_c = 0.135 \text{ m}^2$ $u_{\text{fr}} = 1.663 \text{ m s}^{-1}$ $\sigma = 0.905$ $s_{\text{wav,p}} = 8.202 \times 10^{-3} \text{ m}$ $s_{\text{wav,d}} = 2.794 \times 10^{-3} \text{ m}$ $\mu_{\text{air}} = 2.076 \times 10^{-5} \text{ kg m}^{-1} \text{ s}^{-1}$ $N_{\text{t,col}} = 2$ $j_N = 0.018$ $\text{Re}_{\text{D,Kim}} = 2518$	Fin spacing $s = p_{\text{fin}} - t_{\text{fin}}$	$s = 2.299 \times 10^{-3} \text{ m}$
	Frontal flow velocity $u_{\text{fr}} = \frac{\dot{V}_{\text{air}}}{L_{\text{pass}} H_{\text{fin}}}$	$u_{\text{fr}} = 1.663 \text{ m s}^{-1}$
	Fin contraction ratio from Kim <i>et al.</i> (1997b) $\sigma = s / (s + t_{\text{fin}})$	$\sigma = 0.905$
	Fin collar diameter from Beecher and Fagan (1987) $D_c = D_o + 2t_{\text{fin}}$	$D_c = 0.016 \text{ m}$
	Fraction of channel volume occupied by tube from Kim <i>et al.</i> (1997b) $\beta = \frac{\pi D_c^2}{4s_t s_l}$	$\beta = 0.167$
	Mean air velocity, used in air-side heat transfer coefficient calculations (Kim <i>et al.</i> , 1997b) $u_m = \frac{u_{\text{fr}}}{\sigma(1-\beta)}$	$u_m = 2.206 \text{ m s}^{-1}$
	Max air velocity based on minimum cross-sectional flow area, used in air-side heat transfer coefficient calculations (Kim <i>et al.</i> , 1997b) $u_{\text{max}} = \dot{V}_{\text{air}} / A_c$	$u_{\text{max}} = 3.149 \text{ m s}^{-1}$
	Geometric parameter used to account for additional fin area provided by waves, relative to flat fin (Kim <i>et al.</i> , 1997b) $\sec \theta = \sqrt{(s_{\text{wav,p}}^2 + s_{\text{wav,d}}^2)} / s_{\text{wav,p}}$	$\theta = 18.81^\circ$

Segmental Round Finned Tube Heat and Mass Transfer: Sample Calculations		
Inputs	Equations	Results
$Pr_{\text{air}} = 0.702$ $D_h = 4.131 \times 10^{-3} \text{ m}$ $k_{\text{air}} = 0.030 \text{ W m}^{-1} \text{ K}^{-1}$	Volumetric hydraulic diameter, used in air-side heat transfer coefficient calculation (Kim <i>et al.</i> , 1997b) $D_h = \frac{2s(1-\beta)}{(1-\beta)\sec\theta + 2s\beta/D_c}$	$D_h = 4.131 \times 10^{-3} \text{ m}$
	Air-side Reynolds number based on hydraulic diameter $Re_h = \frac{\rho_{\text{air}} u_m D_h}{\mu_{\text{air}}}$	$Re_h = 445.5$
	Reynolds number used in air-side heat transfer predictions from Kim <i>et al.</i> (1997b) $Re_{D,\text{Kim}} = Re_h \left( \frac{D_c}{D_h} \right) \left( \frac{u_{\text{max}}}{u_m} \right)$	$Re_{D,\text{Kim}} = 2518$
	Colburn “ <i>j</i> ” factor based on number of tube rows in air-flow direction (Kim <i>et al.</i> , 1997b) $N_{t,\text{col}} \geq 3: j_N = j_3 = 0.394 Re_{D,\text{Kim}}^{-0.357} \left( \frac{s_t}{s_1} \right)^{-0.272} \left( \frac{s}{D_c} \right)^{-0.205} \left( \frac{s_{\text{wav,p}}}{s_{\text{wav,d}}} \right)^{-0.558} \left( \frac{s_{\text{wav,d}}}{s} \right)^{-0.133}$ $N_{t,\text{col}} = 1, 2; Re_{D,\text{Kim}} \geq 1000: j_N = j_3 (0.978 - 0.010 N_{t,\text{col}})$ $N_{t,\text{col}} = 1, 2; Re_{D,\text{Kim}} < 1000: j_N = j_3 (1.350 - 0.162 N_{t,\text{col}})$	$j_N = 0.0177$ (Kim <i>et al.</i> , 1997b)
	Nusselt number according to Kim <i>et al.</i> (1997b) $j_N = \frac{Nu_{\text{Kim}}}{Re_{D,\text{Kim}} Pr_{\text{air}}^{1/3}} \frac{D_c}{D_h}$	$Nu_{\text{Kim}} = 10.01$
	Air-side heat transfer coefficient $\alpha_{\text{Kim}} = \frac{Nu_{\text{Kim}} k_{\text{air}}}{D_h}$	$\alpha_{\text{Kim}} = 72.3 \text{ W m}^{-2} \text{ K}^{-1}$

Segmental Round Finned Tube Heat and Mass Transfer: Sample Calculations		
Inputs	Equations	Results
	$\alpha_{\text{air}} = \alpha_{\text{Kim}}$	$\alpha_{\text{air}} = 72.3 \text{ W m}^{-2} \text{ K}^{-1}$
Air-Side Pressure Drop		
$\rho_{\text{air}} = 1.015 \text{ kg m}^{-3}$ $u_{\text{max}} = 3.149 \text{ m s}^{-1}$ $D_o = 0.016 \text{ m}$ $\mu_{\text{air}} = 2.076 \times 10^{-5} \text{ kg m}^{-1} \text{ s}^{-1}$ $A_c = 0.135 \text{ m}^2$ $s_t = 0.038 \text{ m}; s_f = 0.033 \text{ m}$ $H_{\text{fin}} = 0.419 \text{ m}; W_{\text{fin}} = 0.066 \text{ m}$ $N_{\text{pass}} = 22$ $A_{\text{Eu}}^* = 0.33$ $B_{\text{Eu}}^* = 98.9$ $C_{\text{Eu}}^* = -1.48 \times 10^4$ $D_{\text{Eu}}^* = 1.92 \times 10^6$ $E_{\text{Eu}}^* = -8.62 \times 10^7$ $C_z^* = 0.740$ *Determined from Zukauskas <i>et al.</i> (1968). Shown in Hewitt (1990). $s_t = 0.038 \text{ m}$	Air-side Reynolds number, defined by Zukauskas <i>et al.</i> (1968) $\text{Re}_{\text{D,Z}} = \frac{\rho_{\text{air}} u_{\text{max}} D_o}{\mu_{\text{air}}}$	$\text{Re}_{\text{D,Z}} = 2444$
	Finned friction factor $f_{\text{air,fin}} = 0.508 (\text{Re}_{\text{D,Z}})^{-0.521} (s_t/D_o)^{1.318}$ (Gray and Webb, 1986)	$f_{\text{air,fin}} = 0.028$
	Total finned surface area in absorber, used in air-side pressure drop calculation $A_{\text{fin,total}} = 2 \left( H_{\text{fin}} W_{\text{fin}} - \frac{N_{\text{pass}} \pi D_o^2}{4} \right) \left( \frac{L_{\text{pass}}}{P_{\text{fin}}} \right) + \frac{2 H_{\text{fin}} t_{\text{fin}} L_{\text{pass}}}{P_{\text{fin}}}$	$A_{\text{fin,total}} = 11.23 \text{ m}^2$
	Fin portion of air-side pressure drop for flat fins $\Delta P_{\text{air,f,flat}} = \frac{1}{2} f_{\text{air,fin}} \rho_{\text{air}} u_m^2 \left( \frac{A_{\text{fin,total}}}{A_c} \right)$ (Gray and Webb, 1986)	$\Delta P_{\text{air,f,flat}} = 11.59 \text{ Pa}$
	Fin portion of air-side pressure drop for wavy fins $\Delta P_{\text{air,f,wavy}} = 1.9 \Delta P_{\text{air,f,flat}}$ (Webb and Gupte, 1990)	$\Delta P_{\text{air,f,wavy}} = 22.03 \text{ Pa}$
	Ratio of transverse tube spacing to tube outer diameter $a_t = S_t/D_o$	$a_t = 2.4$

Segmental Round Finned Tube Heat and Mass Transfer: Sample Calculations		
Inputs	Equations	Results
$s_1 = 0.033 \text{ m}$ $Eu_z = 0.271$ $N_{t,col} = 2$ $D_o = 0.016 \text{ m}$ $p_{fin} = 2.54 \times 10^{-3} \text{ m}$ $N_{pass} = 22$ $L_{pass} = 0.61 \text{ m}$ $t_{fin} = 2.41 \times 10^{-4} \text{ m}$ $\rho_{air} = 1.015 \text{ kg m}^{-3}$ $u_{max} = 3.149 \text{ m s}^{-1}$ $A_c = 0.135 \text{ m}^2$ $\Delta P_{f,wavy} = 22.03 \text{ Pa}$ $P_{air,in} = 101.325 \text{ kPa}$	Ratio of longitudinal tube spacing to outer diameter $b_t = S_1/D_o$	$b_t = 2.078$
	Constant used in air-side pressure drop calculation (Zukauskas <i>et al.</i> , 1968) $k_1 = (a_t/b_t)^{-0.048}$	$k_1 = 0.993$
	Euler number for air flow over tube bank $Eu = k_1 \left( A_{Eu} + \frac{B_{Eu}}{Re_{D,Z}} + \frac{C_{Eu}}{Re_{D,Z}^2} + \frac{D_{Eu}}{Re_{D,Z}^3} + \frac{E_{Eu}}{Re_{D,Z}^4} \right)$ (Zukauskas <i>et al.</i> , 1968)	$Eu = 0.366$
	Euler number, corrected for fewer than 10 tubes $Eu_z = C_z Eu$	$Eu_z = 0.271$
	Diagonal tube pitch $s_d = \sqrt{s_1^2 + (s_t^2/4)}$	$s_d = 0.038 \text{ m}$
	Minimum tube pitch, used in pressure-drop over tube bank (Zukauskas <i>et al.</i> , 1968) $s_{min} = \text{Min}(s_t, s_d)$	$s_{min} = 0.038 \text{ m}$
	Friction factor over tubes $f_{air,tube} = Eu_z N_{t,col} \left( \frac{s_{min} - D_o}{\pi D_o} \right)$	$f_{air,tube} = 0.241$
	Total area of bare tubes in absorber $A_{tube,bare} = N_{pass} \pi D_o \left[ L_{pass} - t_{fin} \left( \frac{L_{pass}}{p_{fin}} \right) \right]$	$A_{tube,bare} = 0.605 \text{ m}^2$

Segmental Round Finned Tube Heat and Mass Transfer: Sample Calculations		
Inputs	Equations	Results
	Pressure drop corresponding to air flow over bank of tubes $\Delta P_{\text{air,t}} = \frac{1}{2} f_{\text{air,tube}} \rho_{\text{air}} u_{\text{max}}^2 \left( \frac{A_{\text{tube,bare}}}{A_c} \right)$	$\Delta P_{\text{air,t}} = 4.93 \text{ Pa}$
	Ratio of cross-sectional flow area to frontal area (Kays and London, 1984) $\sigma'_{\text{KL}} = \frac{L_{\text{pass}} (1 - t_{\text{fin}} / p_{\text{fin}}) H_{\text{fin}}}{L_{\text{pass}} H_{\text{fin}}}$	$\sigma'_{\text{KL}} = 0.91$
	Pressure drop due to flow contraction at core entrance $\Delta P_{\text{air,entrance}} = \frac{G_{\text{air}}'^2}{2\rho_{\text{air,in}}} (1 - \sigma_{\text{KL}}'^2 + K_c)$	$\Delta P_{\text{air,entrance}} = 1.22 \text{ Pa}$
	Air-side frictional pressure drop, including tube and fin effects, using the superposition model (Gray and Webb, 1986) $\Delta P_{\text{air,fric}} = \Delta P_{\text{air,t}} + \Delta P_{\text{air,f,wavy}}$	$\Delta P_{\text{air,fric}} = 26.95 \text{ Pa}$
	Pressure drop due to acceleration of flow during heating $\Delta P_{\text{air,accel}} = \frac{G_{\text{air}}^2}{2\rho_{\text{air,in}}} \left( \frac{\rho_{\text{air,in}}}{\rho_{\text{air,out}}} - 1 \right)$	$\Delta P_{\text{air,accel}} = 0.92 \text{ Pa}$
	Pressure rise due to flow expansion at core exit $\Delta P_{\text{air,exit}} = -\frac{G_{\text{air}}'^2}{2\rho_{\text{air,in}}} (1 - \sigma_{\text{KL}}'^2 - K_e) \left( \frac{\rho_{\text{air,in}}}{\rho_{\text{air,out}}} \right)$	$\Delta P_{\text{air,exit}} = -1.03 \text{ Pa}$



Segmental Round Finned Tube Heat and Mass Transfer: Sample Calculations		
Inputs	Equations	Results
	$\Delta P_{\text{air}} = \Delta P_{\text{air,entrance}} + \Delta P_{\text{air,fric}} + \Delta P_{\text{air,accel}} + \Delta P_{\text{air,exit}}$ $\Delta P_{\text{air}} = 1.22 \text{ [Pa]} + 26.95 \text{ [Pa]} + 0.92 \text{ [Pa]} - 1.03 \text{ [Pa]} = 28.06 \text{ [Pa]}$	$\Delta P_{\text{air}} = 28.06 \text{ Pa}$
	$P_{\text{air,out}} = P_{\text{air,in}} - \Delta P_{\text{air}}$	$P_{\text{air,out}} = 101.297 \text{ kPa}$
Mass Transfer		
<i>Effect of Mass Transfer on Condensation</i>		
$\alpha_{\text{sol}} = 4535 \text{ W m}^{-2} \text{ K}^{-1}$ $D_i = 0.013 \text{ m}$ $L_{\text{sg}} = 0.025 \text{ m}$ $C_{\text{p,v}} = 2.451 \text{ kJ kg}^{-1} \text{ K}^{-1}$ $\Delta T_{\text{gl}} = 80.57 \text{ K}$ $\Delta h_{\text{m}} = 2213 \text{ kJ kg}^{-1} \text{ K}^{-1}$ $\alpha_{\text{v}} = 128.9 \text{ W m}^{-2} \text{ K}^{-1}$	$R_{\text{in, film}} = \frac{1}{\alpha_{\text{sol}} \pi D_i L_{\text{sg}}}$	$R_{\text{in, film}} = 0.206 \text{ K W}^{-1}$
	$R_{\text{in, vap}} = q_{\text{sol}} C_{\text{p,v}} \frac{\Delta T_{\text{gl}}}{\Delta h_{\text{m}}} \frac{1}{\alpha_{\text{v}} \pi D_i L_{\text{sg}}}$	$R_{\text{in, vap}} = 0.188 \text{ K W}^{-1}$
	$R_{\text{in}} = R_{\text{in, film}} + R_{\text{in, vap}}$	$R_{\text{in}} = 0.395 \text{ K W}^{-1}$
$Re_{\text{v}} = 16834$ $\varepsilon_{\text{rough}} = 1.0 \times 10^{-5} \text{ m}$ $D_i = 0.013 \text{ m}$	Friction factor for vapor flow according to Churchill (1977) $f_{\text{v, Churchill}} = 8 \left[ \left( \frac{8}{Re_{\text{v}}} \right)^{12} + \left[ 2.457 \ln \left( \frac{1}{\left[ \frac{7}{Re_{\text{v}}} \right]^{0.9} + 0.27 \frac{\varepsilon_{\text{rough}}}{D_i}} \right) \right]^{16} + \left[ \frac{37530}{Re_{\text{v}}} \right]^{16} \right]^{-1.5} \cdot 1/12$	$f_{\text{v, Churchill}} = 0.029$ (Churchill, 1977)

Segmental Round Finned Tube Heat and Mass Transfer: Sample Calculations		
Inputs	Equations	Results
$Re_v = 16834$ $f_{v,Churchill} = 0.029$ $Pr_v = 0.88$ $Nu_v = 47.43$ $k_v = 0.036 \text{ W m}^{-1} \text{ K}^{-1}$ $D_i = 0.013 \text{ m}$ $\dot{m}_v = 2.318 \times 10^{-3} \text{ kg s}^{-1}$ $C_{p,v} = 2.46 \text{ kJ kg}^{-1} \text{ K}^{-1}$ $T_{v,in} = 97.60^\circ\text{C}$ $T_{v,out} = 97.47^\circ\text{C}$ $T_{l,in,int} = 97.42^\circ\text{C}$ $T_{l,out,int} = 97.18^\circ\text{C}$ $A_{int} = 1.025 \times 10^{-3} \text{ m}^2$ $C_{p,NH_3,molar} = 47.97 \text{ kJ kmol}^{-1} \text{ K}^{-1}$ $n_{H_2O}^* = 6.44 \times 10^{-5} \text{ kmol m}^{-2} \text{ s}^{-1}$ *Initially assumed, determined through iteration $C_{p,H_2O,molar} = 44.44 \text{ kJ kmol}^{-1} \text{ K}^{-1}$ $\mu_v = 1.310 \times 10^{-5} \text{ kg m}^{-1} \text{ s}^{-1}$	Nusselt number for vapor flow according to Churchill (1977 (b)) $Nu_v = \left[ 4.364^{10} + \frac{e^{\left[ \frac{2200 - Re_v}{365} \right]}}{4.364^2} + \frac{1}{\left[ 6.3 + \frac{0.079 \left( \frac{f_{v,Churchill}}{8} \right)^{0.5} Re_v Pr_v}{(1 + Pr_v^{0.8})^{5/6}} \right]^2} \right]^{-5} \Bigg]^{1/10}$	$Nu_v = 47.43$ (Churchill, 1977 (b))
	$\alpha_v = Nu_v k_v / D_i$	$\alpha_v = 128.9 \text{ W m}^{-2} \text{ K}^{-1}$
	Sensible heat removed from vapor $q_{v,sens} = \dot{m}_v C_{p,v} (T_{v,in} - T_{v,out})$	$q_{v,sens} = 0.73 \text{ W}$
	$LMTD_v = \left[ (T_{v,in} - T_{l,in,int}) - (T_{v,out} - T_{l,out,int}) \right] / \ln \left( \frac{T_{v,in} - T_{l,in,int}}{T_{v,out} - T_{l,out,int}} \right)$	$LMTD_v = 0.23 \text{ K}$
	$q_{v,sens} = \alpha_v \frac{\phi_T}{1 - e^{-\phi_T}} A_{int} LMTD_v$	$\phi_T = 0.19$
	Heat transfer correction factor required by concentration gradient in vapor $\phi_T = (n_{NH_3} C_{p,NH_3,molar} + n_{H_2O} C_{p,H_2O,molar}) / \alpha_v$	$n_{NH_3} = 4.51 \times 10^{-4} \text{ kmol m}^{-2} \text{ s}^{-1}$

Segmental Round Finned Tube Heat and Mass Transfer: Sample Calculations		
Inputs	Equations	Results
$v_v = 0.293 \text{ m}^3 \text{ kg}^{-1}$	$Sc_v = \frac{\mu_v v_v}{D_{\text{NH}_3\text{H}_2\text{O},v}}$	$Sc_v = 0.533$
$D_{\text{NH}_3\text{H}_2\text{O},v} = 7.2 \times 10^{-6} \text{ m}^2 \text{ s}^{-1}$		
$D_{\text{NH}_3\text{H}_2\text{O},v}$ from expression based on $x$ and $T$ (Frank <i>et al.</i> , 1996)	$\left(\frac{Nu_v}{Sh_v}\right)^3 = \frac{Pr_v}{Sc_v}$	$Sh_v = 40.03$
$P_v = 591.787 \text{ kPa}$		
$T_v = 97.54^\circ\text{C} = 370.69 \text{ K}$	$Sh_v = \frac{\beta_v D_i}{D_{\text{NH}_3\text{H}_2\text{O},v}}$	$\beta_v = 0.022 \text{ m s}^{-1}$
$R = 8.314 \text{ kJ kmol}^{-1} \text{ K}^{-1}$		
$P_1 = 591.787 \text{ kPa}$	Bulk molar concentration	$C_T = 0.192 \text{ kmol m}^{-3}$
$x_1 = 0.235$	$C_T = P_v / RT_v$	
$q_{l,int} = 0$	$P_{l,int} = P_1$	$P_{l,int} = 591.787 \text{ kPa}$
$T_{l,int}^\dagger = 97.30^\circ\text{C}$	$x_{1,int} = x_1$	$x_{1,int} = 0.235$
$^\dagger$ Determined from known $P_{l,int}$ ,	$T_{v,int} = T_{l,int}$	$T_{v,int} = 97.30^\circ\text{C}$
$x_{1,int}$ , $q_{l,int}$	$P_{v,int} = P_v$	$P_{v,int} = 591.787 \text{ kPa}$
$P_v = 591.787 \text{ kPa}$	$M_{v,int} = \left(\frac{x_{v,int}}{M_{\text{NH}_3}} + \frac{1-x_{v,int}}{M_{\text{H}_2\text{O}}}\right)^{-1}$ ; $x_{v,int,molar} = x_{v,int} M_{v,int} / M_{\text{NH}_3}$	$M_{v,int} = 17.14 \text{ kg kmol}^{-1}$ $x_{v,int,molar} = 0.884$
$q_{v,int} = 1$		
$x_{v,int}^{**} = 0.878$		
$^{**}$ Determined from known	Molar flux of vapor being absorbed	$n_{\text{total}} = 5.153 \times 10^{-4} \text{ kmol m}^{-2} \text{ s}^{-1}$
$T_{v,int}$ , $P_{v,int}$ , $q_{v,int}$	$n_{\text{total}} = \beta_v C_T \ln\left(\frac{z - x_{v,int,molar}}{z - x_{v,molar}}\right)$	
$M_{\text{NH}_3} = 17.03 \text{ kg kmol}^{-1}$		
$M_{\text{H}_2\text{O}} = 18.02 \text{ kg kmol}^{-1}$	$n_{\text{NH}_3} = z \cdot n_{\text{total}}$	$z = 0.875$
	$m_{\text{flux,NH}_3} = n_{\text{NH}_3} M_{\text{NH}_3}$	$m_{\text{flux,NH}_3} = 7.68 \times 10^{-3} \text{ kg m}^{-2} \text{ s}^{-1}$

Segmental Round Finned Tube Heat and Mass Transfer: Sample Calculations		
Inputs	Equations	Results
$x_{v,molar} = 0.883$	$\dot{m}_{abs,NH_3} = m_{flux,NH_3} A_{int}$	$\dot{m}_{abs,NH_3} = 7.871 \times 10^{-6} \text{ kg s}^{-1}$
$n_{NH_3} = 4.51 \times 10^{-4} \text{ kmol m}^{-2} \text{ s}^{-1}$	$VF = 1/2(VF_{in} + VF_{out})$	$VF = 0.921$
$VF_{in} = 0.921$	Effective interface diameter based on void fraction	$D_{int} = 0.013 \text{ m}$
$VF_{out} = 0.921$	$D_{int} = \sqrt{VF \cdot D_i^2}$	
$D_1 = 0.013 \text{ m}$	$A_{int} = \pi D_{int} L_{sg}$	$A_{int} = 1.025 \times 10^{-3} \text{ m}^2$
$L_{sg} = 0.025 \text{ m}$	$n_{H_2O} = n_{total} - n_{NH_3}$	$n_{H_2O} = 6.437 \times 10^{-5} \text{ kmol m}^{-2} \text{ s}^{-1}$
$\dot{m}_{l,in} = 5.677 \times 10^{-3} \text{ kg s}^{-1}$	$m_{flux,H_2O} = n_{H_2O} M_{H_2O}$	$m_{flux,H_2O} = 1.16 \times 10^{-3} \text{ kg m}^{-2} \text{ s}^{-1}$
$\dot{m}_{v,in} = 2.323 \times 10^{-3} \text{ kg s}^{-1}$	$\dot{m}_{abs,H_2O} = m_{flux,H_2O} A_{int}$	$\dot{m}_{abs,H_2O} = 1.188 \times 10^{-6} \text{ kg s}^{-1}$
$\dot{m}_{l,out} = 5.686 \times 10^{-3} \text{ kg s}^{-1}$	$\dot{m}_{l,out} = \dot{m}_{l,in} + \dot{m}_{abs,NH_3} + \dot{m}_{abs,H_2O}$	$\dot{m}_{l,out} = 5.686 \times 10^{-3} \text{ kg s}^{-1}$
$\dot{m}_{l,in} = 5.677 \times 10^{-3} \text{ kg s}^{-1}$	$\dot{m}_{l,in} + \dot{m}_{v,in} = \dot{m}_{l,out} + \dot{m}_{v,out}$	$\dot{m}_{v,out} = 2.314 \times 10^{-3} \text{ kg s}^{-1}$
$x_{l,in} = 0.235$	$\dot{m}_{l,out} x_{l,out} = \dot{m}_{l,in} x_{l,in} + \dot{m}_{abs,NH_3}$	$x_{l,out} = 0.236$
$\dot{m}_{abs,NH_3} = 7.871 \times 10^{-6} \text{ kg s}^{-1}$	$\dot{m}_{l,in} x_{l,in} + \dot{m}_{v,in} x_{v,in} = \dot{m}_{l,out} x_{l,out} + \dot{m}_{v,out} x_{v,out}$	$x_{v,out} = 0.877$
$\dot{m}_{v,in} = 2.323 \times 10^{-3} \text{ kg s}^{-1}$		
$x_{v,in} = 0.877$		
$\dot{m}_{v,out} = 2.314 \times 10^{-3} \text{ kg s}^{-1}$		
Thermal Resistance Circuit		
$D_o = 0.016 \text{ m}$	$r_o = D_o/2$	$r_{in} = 7.938 \times 10^{-3} \text{ m}$
$\alpha_{air} = 72.3 \text{ W m}^{-2} \text{ K}^{-1}$	$m_{fin} = \sqrt{\frac{2\alpha_{air}}{k_{fin} t_{fin}}}$	$m_{fin} = 49.99 \text{ m}^{-1}$
$k_{fin}^* = 239.8 \text{ W m}^{-1} \text{ K}^{-1}$		
*Looked up at arithmetic mean between $T_{air,in}$ and $T_{refr,equil}$	$C_2 = \frac{2m_{fin} r_o}{(m_{fin} r_{fin,eff})^2 - (m_{fin} r_o)^2}$	$C_2 = 0.686$

Segmental Round Finned Tube Heat and Mass Transfer: Sample Calculations		
Inputs	Equations	Results
$t_{\text{fin}} = 2.41 \times 10^{-4} \text{ m}$ $r_{\text{fin,eff}} = 0.02 \text{ m}$ $A_{\text{fin,sg}} = 0.021 \text{ m}^2$ $A_{\text{total,sg}} = 0.022 \text{ m}^2$ $\alpha_{\text{sol}} = 4535 \text{ W m}^{-2} \text{ K}^{-1}$ $D_1 = 0.013 \text{ m}$ $L_{\text{sg}} = 0.025 \text{ m}$ $R_{\text{in}} = 0.395 \text{ K W}^{-1}$ $D_o = 0.016 \text{ m}$ $D_i = 0.013 \text{ m}$ $k_{\text{tube}} = 53.06 \text{ W m}^{-1} \text{ K}^{-1}$ *Looked up at arithmetic mean between $T_{\text{ti}}$ and $T_{\text{to}}$ $L_{\text{sg}} = 0.025 \text{ m}$ $R_{\text{in}} = 0.206 \text{ K W}^{-1}$ $R_{\text{out}} = 0.729 \text{ K W}^{-1}$ $\dot{V}_{\text{air}} = 0.425 \text{ m}^3 \text{ s}^{-1}$ $\rho_{\text{air}} = 1.015 \text{ kg m}^{-3}$ $\text{Fraction}_{\text{sg}} = 1.89 \times 10^{-3}$ $C_{\text{p,air}} = 1.068 \text{ kJ kg}^{-1} \text{ K}^{-1}$ $T_{\text{l,in}} = 97.487^\circ\text{C}$	Fin efficiency $\eta_{\text{fin}} = C_2 \frac{K_1(m_{\text{fin}} r_o) I_1(m_{\text{fin}} r_{\text{fin,eff}}) - I_1(m_{\text{fin}} r_o) K_1(m_{\text{fin}} r_{\text{fin,eff}})}{I_0(m_{\text{fin}} r_o) K_1(m_{\text{fin}} r_{\text{fin,eff}}) - K_0(m_{\text{fin}} r_o) I_1(m_{\text{fin}} r_{\text{fin,eff}})}$ $I, K$ : Modified Bessel functions	$\eta_{\text{fin}} = 0.841$
	Overall surface efficiency $\eta_0 = 1 - \left( \frac{A_{\text{fin,sg}}}{A_{\text{total,sg}}} \right) (1 - \eta_{\text{fin}})$	$\eta_0 = 0.849$
	$R_{\text{out}} = \frac{1}{\eta_0 \alpha_{\text{air}} A_{\text{total,sg}}}$	$R_{\text{out}} = 0.729 \text{ K W}^{-1}$
	$R_{\text{cond}} = \frac{\ln(D_o/D_i)}{2k_{\text{tube}} \pi L_{\text{sg}}}$	$R_{\text{cond}} = 0.020 \text{ K W}^{-1}$
	$R_{\text{total}} = R_{\text{in}} + R_{\text{cond}} + R_{\text{out}}$	$R_{\text{total}} = 1.144 \text{ K W}^{-1}$
	$UA = 1/R_{\text{total}}$	$UA = 1.046 \text{ W K}^{-1}$
	$\dot{m}_{\text{air}} = \dot{V}_{\text{air}} \rho_{\text{air,in}}$	$\dot{m}_{\text{air}} = 0.451 \text{ kg s}^{-1}$
	$\dot{m}_{\text{air,sg}} = \dot{m}_{\text{air}} \text{Fraction}_{\text{sg}}$	$\dot{m}_{\text{air,sg}} = 8.535 \times 10^{-4} \text{ kg s}^{-1}$
	$\dot{C}_{\text{sol}} = \dot{m}_{\text{sol}} \left[ \frac{(h_{\text{sol,in}} - h_{\text{sol,out}})}{(T_{\text{sol,in}} - T_{\text{sol,out}})} \right]$	$\dot{C}_{\text{sol}} = 176.6 \text{ W K}^{-1}$
	$\dot{C}_{\text{air}} = \dot{m}_{\text{air,sg}} C_{\text{p,air}}$	$\dot{C}_{\text{air}} = 0.911 \text{ W K}^{-1}$
	$\dot{C}_{\text{min}} = \min(\dot{C}_{\text{air}}, \dot{C}_{\text{sol}})$	$\dot{C}_{\text{min}} = 0.911 \text{ W K}^{-1}$
	$q_{\text{max}} = \dot{C}_{\text{min}} (T_{\text{l,in}} - T_{\text{air,in}})$	$q_{\text{max}} = 41.8 \text{ W}$
	$NTU = UA / \dot{C}_{\text{min}}$	$NTU = 0.9629$

Segmental Round Finned Tube Heat and Mass Transfer: Sample Calculations		
Inputs	Equations	Results
$T_{\text{air,in}} = 51.667^\circ\text{C}$ $\dot{m}_{\text{sol}} = 0.008 \text{ kg s}^{-1}$ $h_{\text{sol,in}} = 661.1 \text{ kJ kg}^{-1}$ $T_{\text{sol,equil}}^* = 97.39^\circ\text{C}$ *Looked up at $(P_{\text{sol}}, h_{\text{sol}}, x_{\text{sol,equil}})$	$\varepsilon = \frac{1}{C_r} \left( 1 - \exp \left[ -C_r \left( 1 - e^{-NTU} \right) \right] \right)$	$\varepsilon = 0.617$
	$\varepsilon = q_{\text{sg}} / q_{\text{max}}$	$q_{\text{sg}} = 25.67 \text{ W}$
	$q_{\text{sg}} = \dot{m}_{\text{sol}} (h_{\text{sol,in}} - h_{\text{sol,out}})$	$h_{\text{sol,out}} = 657.9 \text{ kJ kg}^{-1}$
	$q_{\text{sg}} = \dot{m}_{\text{air,sg}} C_{p,\text{air}} (T_{\text{air,out}} - T_{\text{air,in}})$	$T_{\text{air,out}} = 79.95^\circ\text{C}$
	$q_{\text{sg}} = (T_{\text{sol,equil}} - T_{\text{t,i}}) / R_{\text{in}}$	$T_{\text{t,i}} = 91.50^\circ\text{C}$
	$q_{\text{sg}} = (T_{\text{sol,equil}} - T_{\text{t,o}}) / (R_{\text{in}} + R_{\text{cond}})$	$T_{\text{t,o}} = 90.93^\circ\text{C}$

## A.2 Prototype Tube-Array Absorber

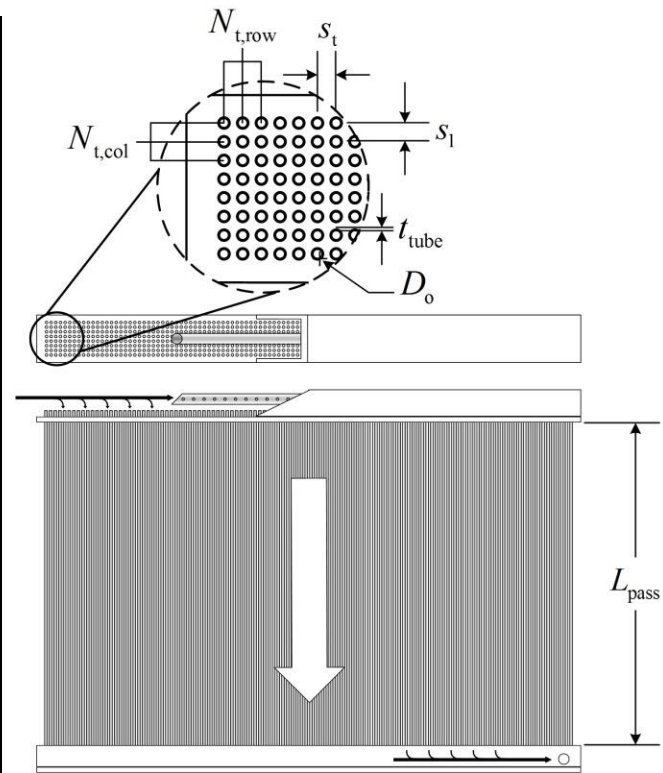
The heat and mass transfer analysis for the prototype tube-array absorber follows a procedure similar to one described above for the round-tube corrugated-fin heat exchanger, with a few differences (geometrical inputs air-side heat transfer and pressure drop).

**Table A.3 Geometric inputs**

Geometry	
$L_{sg}$ (m)	0.025
$N_{sg}$ (-)	15.25 (>200 used in analysis)
$D_o$ (m)	$3.175 \times 10^{-3}$
$t_{tube}$ (m)	$5.08 \times 10^{-4}$
$L_{pass}$ (m)	0.387
$N_{t,row}$ (-)	114
$N_{t,col}$ (-)	8
$s_t$ (m)	$5.588 \times 10^{-3}$
$s_l$ (m)	$5.588 \times 10^{-3}$
$\epsilon_{rough}$ (m)	$1.0 \times 10^{-5}$
Dimensions (m)	$0.71 \times 0.46 \times 0.06$ (W×H×D)
Header Material	303 SS
Tube Material	304 SS

**Table A.4 Inlet conditions**

Refrigerant Vapor Inlet Conditions	
$T_{v,in}$ (°C)	97.60
$P_{v,in}$ (kPa)	591.8
$x_{v,in}$ (-)	0.877
$\dot{m}_{v,in,total}$ (kg s <sup>-1</sup> )	$2.32 \times 10^{-3}$
Dilute Solution Inlet Conditions	
$T_{l,in}$ (°C)	97.49
$P_{l,in}$ (kPa)	591.8
$x_{l,in}$ (-)	0.235
$\dot{m}_{l,in,total}$ (kg s <sup>-1</sup> )	$5.68 \times 10^{-3}$
Inlet Air Conditions	
$\dot{V}_{air}$ (m <sup>3</sup> s <sup>-1</sup> )	0.425
$T_{air,in}$ (°C)	51.67
$P_{air,in}$ (kPa)	101.3
$RH_{air,in}$ (-)	0.18



**Figure A.2 Prototype geometry schematic**

Segmental Prototype Tube-Array Heat and Mass Transfer: Sample Calculations		
Inputs	Equations	Results
<b>First 0.025-m segment of first row of tubes (114 tubes receiving air at 51.7°C) at the inlet of the prototype tube-array absorber (15.25 segments total)</b>		
Tube-Side Geometry Intermediate Calculations		
$\dot{m}_{l,in,total} = 5.677 \times 10^{-3} \text{ kg s}^{-1}$ $\dot{m}_{v,in,total} = 2.323 \times 10^{-3} \text{ kg s}^{-1}$ $N_{t,col} = 8$ $D_o = 3.175 \times 10^{-3} \text{ m}$ $t_{tube} = 5.08 \times 10^{-4} \text{ m}$ $N_{t,row} = 114$	Liquid mass flow rate in one of the eight tube rows, consisting of 114 tubes receiving 51.7°C inlet air. Modeling is iterated for subsequent tube rows to account for changes in air temperature along depth of tube array. $\dot{m}_{l,in} = \dot{m}_{l,in,total} / N_{t,col}$	$\dot{m}_{l,in} = 7.096 \times 10^{-4} \text{ kg s}^{-1}$
	Vapor mass flow rate in one of the eight tube rows, consisting of 114 tubes $\dot{m}_{v,in} = \dot{m}_{v,in,total} / N_{t,col}$	$\dot{m}_{v,in} = 2.904 \times 10^{-4} \text{ kg s}^{-1}$
	$D_i = D_o - 2t_{tube}$	$D_i = 2.159 \times 10^{-3} \text{ m}$
	$A_i = \frac{\pi}{4} N_{t,row} D_i^2$	$A_i = 4.173 \times 10^{-4} \text{ m}^2$
Air-Side Geometry Intermediate Calculations		
$L_{sg} = 0.025 \text{ m}$ $L_{pass} = 0.387 \text{ m}$ $N_{t,row} = 114$ $s_t = 5.588 \times 10^{-3} \text{ m}$ $D_o = 3.175 \times 10^{-3} \text{ m}$	Fraction of segment over total uncoiled tube length, used in finding segmental air flow rate $Fraction_{sg} = \frac{L_{sg}}{L_{pass}}$	$Fraction_{sg} = 0.066$
	$W_{face} = (N_{t,row} - 1)s_t + D_o$	$W_{face} = 0.635 \text{ m}$
	External tube area per segment (exposed to air) $A_{t,o,sg} = \pi D_o L_{sg} N_{t,row}$	$A_{t,o,sg} = 0.029 \text{ m}^2$
	$A_{total,sg} = A_{t,o,sg}$	$A_{total,sg} = 0.029 \text{ m}^2$



Segmental Prototype Tube-Array Heat and Mass Transfer: Sample Calculations		
Inputs	Equations	Results
	Cross-sectional area available for air flow, for use in air-side pressure drop calculations  $A_c = (W_{\text{face}} - N_{\text{t,row}} D_o) L_{\text{pass}}$	$A_c = 0.106 \text{ m}^2$
Fluid Properties		
$P_{v,\text{in}} = 591.80 \text{ kPa}$ $P_{v,\text{out}}^* = 591.78 \text{ kPa}$ $T_{v,\text{in}} = 97.60^\circ\text{C}; T_{v,\text{out}}^* = 95.10^\circ\text{C}$ $x_{v,\text{in}} = 0.877; x_{v,\text{out}}^* = 0.895$ $\dot{m}_{v,\text{in}} = 2.904 \times 10^{-4} \text{ kg s}^{-1}$ $\dot{m}_{v,\text{out}}^* = 2.530 \times 10^{-4} \text{ kg s}^{-1}$ $x_v = 0.886$	$P_v = (P_{v,\text{in}} + P_{v,\text{out}})/2$	$P_v = 591.79 \text{ kPa}$
	$T_v = (T_{v,\text{in}} + T_{v,\text{out}})/2$	$T_v = 96.35^\circ\text{C}$
	$x_v = (x_{v,\text{in}} + x_{v,\text{out}})/2$	$x_v = 0.886$
	$\dot{m}_v = (\dot{m}_{v,\text{in}} + \dot{m}_{v,\text{out}})/2$	$\dot{m}_v = 2.717 \times 10^{-4} \text{ kg s}^{-1}$
	$M_{v,\text{avg}} = \left( \frac{x_v}{M_{\text{NH}_3}} + \frac{1-x_v}{M_{\text{H}_2\text{O}}} \right)^{-1}$	$M_{v,\text{avg}} = 17.14 \text{ kg kmol}^{-1}$
	$x_{v,\text{molar}} = x_v M_{v,\text{avg}} / M_{\text{NH}_3}$	$x_{v,\text{molar}} = 0.891$
	$Re_v = \frac{\dot{m}_v D_i}{A_i \mu_v}$	$Re_v = 107.7$
	$Pr_v = \mu_v C_{p,v} / k_v$	$Pr_v = 0.863$
	$P_l = (P_{l,\text{in}} + P_{l,\text{out}})/2$	$P_l = 591.789 \text{ kPa}$
	$T_l = (T_{l,\text{in}} + T_{l,\text{out}})/2$	$T_l = 94.51^\circ\text{C}$

Segmental Prototype Tube-Array Heat and Mass Transfer: Sample Calculations		
Inputs	Equations	Results
$M_{\text{NH}_3} = 17.03 \text{ kg kmol}^{-1}$ $M_{\text{H}_2\text{O}} = 18.02 \text{ kg kmol}^{-1}$ $\dot{m}_v = 2.717 \times 10^{-4} \text{ kg s}^{-1}$ $D_i = 2.159 \times 10^{-3} \text{ m}$ $A_i = 4.173 \times 10^{-4} \text{ m}^2$ $T_{l,\text{in}} = 97.49^\circ\text{C}; T_{l,\text{out}}^* = 91.53^\circ\text{C}$ $x_{l,\text{in}} = 0.235; x_{l,\text{out}}^* = 0.261$ $\dot{m}_{l,\text{in}} = 7.096 \times 10^{-4} \text{ kg s}^{-1}$ $\dot{m}_{l,\text{out}}^* = 7.470 \times 10^{-4} \text{ kg s}^{-1}$ $P_{l,\text{in}} = 591.80 \text{ kPa}$ $P_{l,\text{out}}^* = 591.78 \text{ kPa}$ *Determined through iteration With $(P, T, x)$ , all others known: $\mu_v = 1.305 \times 10^{-5} \text{ kg m}^{-1} \text{ s}^{-1}; \mu_l = 2.985 \times 10^{-4} \text{ kg m}^{-1} \text{ s}^{-1}$ $C_{p,v} = 2.399 \text{ kJ kg}^{-1} \text{ K}^{-1}; C_{p,l} = 4.392 \text{ kJ kg}^{-1} \text{ K}^{-1}$ $k_v = 0.036 \text{ W m}^{-1} \text{ K}^{-1}; k_l = 0.590 \text{ W m}^{-1} \text{ K}^{-1}$ $k_v, \mu_v$ values from Chapman-Enskog kinetic theory (Mills, 1999) $C_p$ values from <i>EES</i> , using data from Ibrahim and Klein (1993)	$x_1 = (x_{l,\text{in}} + x_{l,\text{out}}) / 2$	$x_1 = 0.248$
	$\dot{m}_1 = (\dot{m}_{l,\text{in}} + \dot{m}_{l,\text{out}}) / 2$	$\dot{m}_1 = 7.283 \times 10^{-4} \text{ kg s}^{-1}$
	$M_{l,\text{avg}} = \left( \frac{x_1}{M_{\text{NH}_3}} + \frac{1-x_1}{M_{\text{H}_2\text{O}}} \right)^{-1}$	$M_{l,\text{avg}} = 17.76 \text{ kg kmol}^{-1}$
	$x_{l,\text{molar}} = x_1 M_{l,\text{avg}} / M_{\text{NH}_3}$	$x_{l,\text{molar}} = 0.259$
	$Re_1 = \frac{\dot{m}_1 D_i}{A_i \mu_l}$	$Re_1 = 12.62$
	$Pr_1 = \mu_l C_{p,l} / k_l$	$Pr_1 = 2.222$

Segmental Prototype Tube-Array Heat and Mass Transfer: Sample Calculations		
Inputs	Equations	Results
Tube-Side Heat Transfer Coefficient		
$\dot{m}_1 = 7.283 \times 10^{-4} \text{ kg s}^{-1}$ $\dot{m}_v = 2.717 \times 10^{-4} \text{ kg s}^{-1}$ $x_1 = 0.235$ $x_v = 0.877$ $x_{\text{sol, equil}} = 0.421$ $M_{\text{NH}_3} = 17.03 \text{ kg kmol}^{-1}$ $M_{\text{H}_2\text{O}} = 18.02 \text{ kg kmol}^{-1}$ $P_{\text{crit, NH}_3} = 11333 \text{ kPa}$ $P_{\text{crit, H}_2\text{O}} = 22064 \text{ kPa}$ $\dot{m}_1 = 7.283 \times 10^{-4} \text{ kg s}^{-1}$ $\dot{m}_v = 2.717 \times 10^{-4} \text{ kg s}^{-1}$ $\dot{m}_{\text{sol}} = 1.00 \times 10^{-3} \text{ kg s}^{-1}$ $A_1 = 4.173 \times 10^{-4} \text{ m}^2$ $k_1 = 0.590 \text{ W m}^{-1} \text{ K}^{-1}$ $D_1 = 2.159 \times 10^{-3} \text{ m}$ $\mu_1 = 2.985 \times 10^{-4} \text{ kg m}^{-1} \text{ s}^{-1}$ $Pr_1 = 2.222$ $P_{\text{sol}} = 591.789 \text{ kPa}$	$\dot{m}_{\text{sol}} = \dot{m}_1 + \dot{m}_v$	$\dot{m}_{\text{sol}} = 1.00 \times 10^{-3} \text{ kg s}^{-1}$
	$\dot{m}_{\text{sol}} x_{\text{sol, equil}} = \dot{m}_1 x_1 + \dot{m}_v x_v$	$x_{\text{sol, equil}} = 0.421$
	Solved together: $\begin{cases} x_{\text{refr, equil}} = \frac{x_{\text{mol, NH}_3} M_{\text{NH}_3}}{x_{\text{mol, NH}_3} M_{\text{NH}_3} + x_{\text{mol, H}_2\text{O}} M_{\text{H}_2\text{O}}} \\ 1 = x_{\text{mol, NH}_3} + x_{\text{mol, H}_2\text{O}} \end{cases}$	$x_{\text{mol, NH}_3} = 0.435$ $x_{\text{mol, H}_2\text{O}} = 0.565$
	$P_{\text{crit}} = x_{\text{mol, NH}_3} P_{\text{crit, NH}_3} + x_{\text{mol, H}_2\text{O}} P_{\text{crit, H}_2\text{O}}$	$P_{\text{crit}} = 17396 \text{ kPa}$
	$q_{\text{sol}} = \dot{m}_v / (\dot{m}_1 + \dot{m}_v)$	$q_{\text{sol}} = 0.272$
	$G_{\text{sol}} = \dot{m}_{\text{sol}} / A_1$	$G_{\text{sol}} = 2.396 \text{ kg m}^{-2} \text{ s}^{-1}$
	Liquid-only heat transfer coefficient (Dittus and Boelter, 1930) $\alpha_{\text{lo}} = 0.023 \frac{k_1}{D_1} \left( \frac{G_{\text{sol}} D_1}{\mu_1} \right)^{0.8} Pr_1^{0.4}$	$\alpha_{\text{lo}} = 65.74 \text{ W m}^{-2} \text{ K}^{-1}$
	$\alpha_{\text{Shah}} = \alpha_{\text{lo}} \left[ (1 - q_{\text{sol}})^{0.8} + \frac{3.8 q_{\text{sol}}^{0.76} (1 - q_{\text{sol}})^{0.04}}{(P_{\text{sol}} / P_{\text{crit}})^{0.38}} \right]$	$\alpha_{\text{Shah}} = 382.1 \text{ W m}^{-2} \text{ K}^{-1}$ (Shah, 1979)
	$\alpha_{\text{sol}} = \alpha_{\text{Shah}}$	$\alpha_{\text{sol}} = 382.1 \text{ W m}^{-2} \text{ K}^{-1}$

Segmental Prototype Tube-Array Heat and Mass Transfer: Sample Calculations		
Inputs	Equations	Results
Tube-Side Pressure Drop		
$\dot{m}_{\text{sol}} = 1.00 \times 10^{-3} \text{ kg s}^{-1}$ $\dot{m}_{\text{l,in}} = 7.096 \times 10^{-4} \text{ kg s}^{-1}$ ; $\dot{m}_{\text{v,in}} = 2.904 \times 10^{-4} \text{ kg s}^{-1}$ $h_{\text{l,in}} = 263.5 \text{ kJ kg}^{-1}$ ; $h_{\text{v,in}} = 1633 \text{ kJ kg}^{-1}$ $\dot{m}_{\text{l,out}} = 7.47 \times 10^{-4} \text{ kg s}^{-1}$ , $\dot{m}_{\text{v,out}} = 2.53 \times 10^{-4} \text{ kg s}^{-1}$ $h_{\text{l,out}} = 224.1 \text{ kJ kg}^{-1}$ , $h_{\text{sol,out}}^* = 573.9 \text{ kJ kg}^{-1}$ *Determined through iteration	$\dot{m}_{\text{sol}} h_{\text{sol,in}} = \dot{m}_{\text{l,in}} h_{\text{l,in}} + \dot{m}_{\text{v,in}} h_{\text{v,in}}$	$h_{\text{sol,in}} = 661.1 \text{ kJ kg}^{-1}$
	$\dot{m}_{\text{sol}} h_{\text{sol,out}} = \dot{m}_{\text{l,out}} h_{\text{l,out}} + \dot{m}_{\text{v,out}} h_{\text{v,out}}$	$h_{\text{v,out}} = 1606 \text{ kJ kg}^{-1}$
<i>Frictional Pressure Drop According to Friedel (1979)</i>		
$G_{\text{sol}} = 2.396 \text{ kg m}^{-2} \text{ s}^{-1}$ $D_i = 2.159 \times 10^{-3} \text{ m}$ $\mu_v = 1.305 \times 10^{-5} \text{ kg m}^{-1} \text{ s}^{-1}$ $\mu_l = 2.985 \times 10^{-4} \text{ kg m}^{-1} \text{ s}^{-1}$ $\mu_l$ from empirical correlations from Meacham (2002) based on graphical data from Herold <i>et al.</i> (1996) $q_{\text{sol}} = 0.272$ $\rho_l = 784.5 \text{ kg m}^{-3}$ $\rho_v = 3.425 \text{ kg m}^{-3}$ $g = 9.81 \text{ m s}^{-2}$	$\text{Re}_{\text{vo}} = \frac{G_{\text{sol}} D_i}{\mu_v}$	$\text{Re}_{\text{vo}} = 396.3$
	If $\text{Re}_{\text{vo}} < 2000$ : $\begin{cases} B_{\text{vo}} = 16 \\ n_{\text{vo}} = 1 \end{cases}$ ; Else: $\begin{cases} B_{\text{vo}} = 0.079 \\ n_{\text{vo}} = 0.25 \end{cases}$	$B_{\text{vo}} = 16$ $n_{\text{vo}} = 1$
	Vapor-only friction factor, used in tube-side pressure drop calculations $f_{\text{vo}} = B_{\text{vo}} \text{Re}_{\text{vo}}^{-n_{\text{vo}}}$	$f_{\text{vo}} = 0.022$
	$\text{Re}_{\text{lo}} = \frac{G_{\text{sol}} D_i}{\mu_l}$	$\text{Re}_{\text{lo}} = 17.33$
	If $\text{Re}_{\text{lo}} < 2000$ : $\begin{cases} B_{\text{lo}} = 16 \\ n_{\text{lo}} = 1 \end{cases}$ ; Else: $\begin{cases} B_{\text{lo}} = 0.079 \\ n_{\text{lo}} = 0.25 \end{cases}$	$B_{\text{lo}} = 16$ $n_{\text{lo}} = 1$
	Liquid-only friction factor $f_{\text{lo}} = B_{\text{lo}} \text{Re}_{\text{lo}}^{-n_{\text{lo}}}$	$f_{\text{lo}} = 0.923$

Segmental Prototype Tube-Array Heat and Mass Transfer: Sample Calculations		
Inputs	Equations	Results
$\sigma_1 = 0.036 \text{ N m}^{-1}$ $\sigma_1$ from empirical correlations from Meacham (2002) based on graphical data from Herold <i>et al.</i> (1996) $\dot{m}_{\text{sol}} = 1.00 \times 10^{-3} \text{ kg s}^{-1}$ $A_1 = 4.173 \times 10^{-4} \text{ m}^2$ $\dot{m}_{1,\text{in}} = 7.096 \times 10^{-4} \text{ kg s}^{-1}$ $x_{1,\text{in}} = 0.235$ $\dot{m}_{\text{v},\text{in}} = 2.904 \times 10^{-4} \text{ kg s}^{-1}$ $x_{\text{v},\text{in}} = 0.877$ $\dot{m}_{1,\text{out}} = 7.47 \times 10^{-4} \text{ kg s}^{-1}$ $x_{1,\text{out}} = 0.261$ $\dot{m}_{\text{v},\text{out}} = 2.53 \times 10^{-4} \text{ kg s}^{-1}$ $x_{\text{v},\text{out}} = 0.895$ $\phi_{\text{lo},\text{Friedel}} = 15.62$ $f_{\text{lo}} = 0.923$ $G_{\text{sol}} = 2.396 \text{ kg m}^{-2} \text{ s}^{-1}$ $\rho_1 = 784.5 \text{ kg m}^{-3}$ $D_1 = 2.159 \times 10^{-3} \text{ m}$ $L_{\text{sg}} = 0.025 \text{ m}$	First parameter specified by Friedel (1979) for tube-side frictional pressure drop calculation $C_{\text{F1}} = (1 - q_{\text{sol}})^2 + q_{\text{sol}}^2 \left( \frac{\rho_1}{\rho_{\text{v}}} \right) \left( \frac{f_{\text{vo}}}{f_{\text{lo}}} \right)$	$C_{\text{F1}} = 6.252$
	Second parameter specified by Friedel (1979) for tube-side frictional pressure drop calculation $C_{\text{F2,down}} = q_{\text{sol}}^{0.8} (1 - q_{\text{sol}})^{0.29} \left( \frac{\rho_1}{\rho_{\text{v}}} \right)^{0.9} \left( \frac{\mu_{\text{v}}}{\mu_1} \right)^{0.73} \left( 1 - \frac{\mu_{\text{v}}}{\mu_1} \right)^{7.4}$	$C_{\text{F2}} = 25.32$
	$\rho_{\text{tp}} = \left( \frac{q_{\text{sol}}}{\rho_{\text{v}}} + \frac{1 - q_{\text{sol}}}{\rho_1} \right)^{-1}$	$\rho_{\text{tp}} = 12.46 \text{ kg m}^{-3}$
	$Fr = \frac{G_{\text{sol}}^2}{g D_i \rho_{\text{tp}}^2}$	$Fr = 1.746$
	$We = \frac{G_{\text{sol}}^2 D_i}{\rho_{\text{tp}} \sigma_1}$	$We = 0.028$
	Liquid-only two-phase multiplier specified by Friedel (1979) $\phi_{\text{lo},\text{Friedel,down}} = \sqrt{C_{\text{F1}} + \frac{48.6 C_{\text{F2,down}} Fr^{0.03}}{We^{0.12}}}$	$\phi_{\text{lo},\text{Friedel}} = 15.62$ (Friedel, 1979)
	$\left( \frac{dP}{dz} \right)_{\text{Friedel}} = \phi_{\text{lo},\text{Friedel,down}}^2 \left( \frac{2 f_{\text{lo}} G_{\text{sol}}^2}{\rho_1 D_i} \right)$	$\left( \frac{dP}{dz} \right)_{\text{Friedel}} = 1526 \text{ Pa m}^{-1}$
	Frictional pressure drop across segment $\Delta P_{\text{fric},\text{Friedel}} = \left( \frac{dP}{dz} \right)_{\text{Friedel}} \cdot L_{\text{sg}}$	$\Delta P_{\text{fric},\text{Friedel}} = 38.76 \text{ Pa}$

Segmental Prototype Tube-Array Heat and Mass Transfer: Sample Calculations		
Inputs	Equations	Results
$\dot{m}_{l,in} = 7.096 \times 10^{-4} \text{ kg s}^{-1}$ $\dot{m}_{v,in} = 2.904 \times 10^{-4} \text{ kg s}^{-1}$ $\dot{m}_{l,out} = 7.47 \times 10^{-4} \text{ kg s}^{-1}$ $\dot{m}_{v,out} = 2.53 \times 10^{-4} \text{ kg s}^{-1}$ $\rho_v = 3.425 \text{ kg m}^{-3}$ $\mu_v = 1.305 \times 10^{-5} \text{ kg m}^{-1} \text{ s}^{-1}$ $\mu_l = 2.985 \times 10^{-4} \text{ kg m}^{-1} \text{ s}^{-1}$ $\dot{m}_{sol} = 1.00 \times 10^{-3} \text{ kg s}^{-1}$ $A_1 = 4.173 \times 10^{-4} \text{ m}^2$ $\gamma = -90^\circ$	$q_{sol,in} = \frac{\dot{m}_{v,in}}{\dot{m}_{v,in} + \dot{m}_{l,in}}; q_{sol,out} = \frac{\dot{m}_{v,out}}{\dot{m}_{v,out} + \dot{m}_{l,out}}$	$q_{sol,in} = 0.290$ $q_{sol,out} = 0.253$
	$q_{sol} = (q_{sol,in} + q_{sol,out})/2$	$q_{sol} = 0.272$
	Void fraction at inlet of segment in the form of Butterworth (1975) with constants from Lockhart and Martinelli (1949) $VF_{in} = \left[ 1 + 0.28 \left( \frac{1 - q_{sol,in}}{q_{sol,in}} \right)^{0.64} \left( \frac{\rho_v}{\rho_l} \right)^{0.36} \left( \frac{\mu_l}{\mu_v} \right)^{0.07} \right]^{-1}$	$VF_{in} = 0.92$
	Void fraction at outlet of segment $VF_{out} = \left[ 1 + 0.28 \left( \frac{1 - q_{sol,out}}{q_{sol,out}} \right)^{0.64} \left( \frac{\rho_v}{\rho_l} \right)^{0.36} \left( \frac{\mu_l}{\mu_v} \right)^{0.07} \right]^{-1}$	$VF_{out} = 0.91$
	$VF = (VF_{in} + VF_{out})/2$	$VF = 0.915$
	Pressure drop due to flow deceleration $\Delta P_{dec} = G_{sol}^2 \left[ \frac{q_{sol,out}^2}{\rho_v VF_{out}} - \frac{(1 - q_{sol,out})^2}{\rho_l (1 - VF_{out})} \right] - G_{sol}^2 \left[ \frac{q_{sol,in}^2}{\rho_v VF_{in}} - \frac{(1 - q_{sol,in})^2}{\rho_l (1 - VF_{in})} \right]$	$\Delta P_{dec} = -0.03 \text{ Pa}$
	Gravitational pressure rise $\Delta P_{grav} = [(1 - VF)\rho_l + VF \cdot \rho_v] g \sin(\gamma) L_{sg}$	$\Delta P_{grav} = -17.39 \text{ Pa}$
	Total tube-side pressure drop in segment $\Delta P_{sol,sg} = \Delta P_{fric,Friedel} + \Delta P_{dec} + \Delta P_{grav}$ $\Delta P_{sol,sg} = 38.76 \text{ [Pa]} - 0.03 \text{ [Pa]} - 17.39 \text{ [Pa]} = 21.34 \text{ [Pa]}$	$\Delta P_{sol,sg} = 21.34 \text{ Pa}$

Segmental Prototype Tube-Array Heat and Mass Transfer: Sample Calculations		
Inputs	Equations	Results
	$P_{\text{sol,out}} = P_{\text{l,out}} = P_{\text{v,out}} = P_{\text{l,in}} - \Delta P_{\text{sol,sg}}$	$P_{\text{sol,out}} = 591.779 \text{ kPa}$
Air-Side Heat Transfer Coefficient		
$\dot{V}_{\text{air}} = 0.425 \text{ m}^3 \text{ s}^{-1}$ $A_c = 0.106 \text{ m}^2$ $\rho_{\text{air}} = 1.056 \text{ kg m}^{-3}$ $u_{\text{max}} = 4.022 \text{ m s}^{-1}$ $D_o = 3.175 \times 10^{-3} \text{ m}$ $\mu_{\text{air}} = 1.974 \times 10^{-5} \text{ kg m}^{-1} \text{ s}^{-1}$ $\text{Pr}_{\text{air}} = 0.739$ $\text{Pr}_s = 0.715$ , looked up at $T_{t,o}$ $C_2 = 0.957$ , looked up at $N_{t,\text{col}}$ $k_{\text{air}} = 0.028 \text{ W m}^{-1} \text{ K}^{-1}$	Maximum air velocity based on minimum cross-sectional flow area, used in air-side heat transfer coefficient calculations $u_{\text{max}} = \dot{V}_{\text{air}} / A_c$	$u_{\text{max}} = 4.022 \text{ m s}^{-1}$
	Reynolds number according to Zukauskas <i>et al.</i> (1968) $\text{Re}_{D,Z} = \rho_{\text{air}} u_{\text{max}} D_o / \mu_{\text{air}}$	$\text{Re}_{D,Z} = 683.1$
	If ( $\text{Re}_{D,Z} < 100$ ): $C = 0.8$ , $m = 0.4$ If ( $100 < \text{Re}_{D,Z} < 1,000$ ): $C = 0.683$ , $m = 0.446$ If ( $1,000 < \text{Re}_{D,Z} < 200,000$ ): $C = 0.27$ , $m = 0.63$ Else ( $\text{Re}_{D,Z} > 200,000$ ): $C = 0.021$ , $m = 0.84$	$C = 0.683$ $m = 0.446$
	Nusselt number for more than 20 rows of tubes according to Zukauskas <i>et al.</i> (1968) $Nu_{D,Nr>20} = C \text{Re}_{D,Z}^m \text{Pr}_{\text{air}}^{0.36} \left( \frac{\text{Pr}_{\text{air}}}{\text{Pr}_s} \right)^{1/4}$	$Nu_{D,Nr>20} = 11.35$
	Nusselt number for fewer than 20 rows of tubes using correction factor $Nu_{D,Nr<20} = C_2 Nu_{D,Nr>20}$	$Nu_{D,Nr<20} = 10.86$
	$\alpha_{\text{air,Zukauskas}} = (Nu_{D,Nr<20} k_{\text{air}}) / D_o$	$\alpha_{\text{air,Zukauskas}} = 94.61 \text{ W m}^{-2} \text{ K}^{-1}$ (Zukauskas <i>et al.</i> , 1968)
	$\alpha_{\text{air}} = \alpha_{\text{air,Zukauskas}}$	$\alpha_{\text{air}} = 94.61 \text{ W m}^{-2} \text{ K}^{-1}$
	Air-Side Pressure Drop	

Segmental Prototype Tube-Array Heat and Mass Transfer: Sample Calculations		
Inputs	Equations	Results
$s_t = 5.588 \times 10^{-3}$ m $s_l = 5.588 \times 10^{-3}$ m $D_o = 3.175 \times 10^{-3}$ m $Re_{D,Z} = 683.1$ $A_{Eu}^* = 0.188, B_{Eu}^* = 56.6$ $C_{Eu}^* = -646, D_{Eu}^* = 6010$ $E_{Eu}^* = -18300$ $C_z^* = 1.046$ *Determined from Zukauskas <i>et al.</i> (1968). Shown in Hewitt (1990). $Eu_z = 0.284$ $N_{t,col} = 8$ $\rho_{air} = 1.056$ kg m <sup>-3</sup> $u_{max} = 4.022$ m s <sup>-1</sup> $W_{face} = 0.635$ m $L_{pass} = 0.387$ m $A_c = 0.106$ m <sup>2</sup> $\rho_{air,in} = 1.061$ kg m <sup>-3</sup> $\rho_{air,out} = 1.051$ kg m <sup>-3</sup> $P_{air,in} = 101.325$ kPa	Ratio of transverse tube spacing to tube outer diameter $a_t = s_t / D_o$	$a_t = 1.76$
	Ratio of longitudinal tube spacing to outer diameter $b_t = s_l / D_o$	$b_t = 1.76$
	Constant used in air-side pressure drop calculation (Zukauskas <i>et al.</i> , 1968) $k_1 = (a_t / b_t)^{-0.048}$	$k_1 = 1.009$
	Euler number for air flow over tube bank $Eu = k_1 \left( A_{Eu} + \frac{B_{Eu}}{Re_{D,Z}} + \frac{C_{Eu}}{Re_{D,Z}^2} + \frac{D_{Eu}}{Re_{D,Z}^3} + \frac{E_{Eu}}{Re_{D,Z}^4} \right)$ (Zukauskas <i>et al.</i> , 1968)	$Eu = 0.272$
	Euler number, corrected for fewer than 10 tubes $Eu_z = C_z Eu$	$Eu_z = 0.284$
	Diagonal tube pitch $s_d = \sqrt{s_l^2 + (s_t^2 / 4)}$	$s_d = 6.248 \times 10^{-3}$ m
	Minimum tube pitch, used in pressure-drop over tube bank (Zukauskas <i>et al.</i> , 1968) $s_{min} = \text{Min}(s_t, s_d)$	$s_{min} = 5.588 \times 10^{-3}$ m
	Frictional pressure drop over tube array $\Delta P_{air,t} = (1/2) Eu_z N_{t,col} \rho_{air} u_{max}^2$	$\Delta P_{air,t} = 19.43$ Pa
	$\Delta P_{air,fric} = \Delta P_{air,t}$	$\Delta P_{air,fric} = 19.43$ Pa
	Frontal face area of absorber $A_{fr} = W_{face} L_{pass}$	$A_{fr} = 0.246$ m <sup>2</sup>



Segmental Prototype Tube-Array Heat and Mass Transfer: Sample Calculations		
Inputs	Equations	Results
	$G_{\text{air}} = \rho_{\text{air}} u_{\text{max}}$	$G_{\text{air}} = 4.267 \text{ kg m}^{-2} \text{ s}^{-1}$
	Pressure drop due to acceleration of flow during heating $\Delta P_{\text{air,accel}} = \frac{G_{\text{air}}^2}{2\rho_{\text{air,in}}} \left( \frac{\rho_{\text{air,in}}}{\rho_{\text{air,out}}} - 1 \right)$	$\Delta P_{\text{air,accel}} = 0.156 \text{ Pa}$
	$\Delta P_{\text{air}} = \Delta P_{\text{air,fric}} + \Delta P_{\text{air,accel}}$ $\Delta P_{\text{air}} = 19.43 \text{ [Pa]} + 0.16 \text{ [Pa]} = 19.58 \text{ [Pa]}$	$\Delta P_{\text{air}} = 19.58 \text{ Pa}$
	$P_{\text{air,out}} = P_{\text{air,in}} - \Delta P_{\text{air}}$	$P_{\text{air,out}} = 101.305 \text{ kPa}$
<b>Mass Transfer</b>		
<i>Effect of Mass Transfer on Condensation</i>		
$\alpha_{\text{sol}} = 382.9 \text{ W m}^{-2} \text{ K}^{-1}$ $D_i = 0.002 \text{ m}$ $L_{\text{sg}} = 0.025 \text{ m}$ $C_{\text{p,v}} = 2.451 \text{ kJ kg}^{-1} \text{ K}^{-1}$ $\Delta T_{\text{gl}} = 80.57 \text{ K}$ $\Delta h_{\text{m}} = 2213 \text{ kJ kg}^{-1} \text{ K}^{-1}$ $\alpha_{\text{v}} = 73.3 \text{ W m}^{-2} \text{ K}^{-1}$ $\text{Re}_{\text{v}} = 107.7$ $\varepsilon_{\text{rough}} = 1.0 \times 10^{-5} \text{ m}$ $D_i = 2.159 \times 10^{-3} \text{ m}$	$R_{\text{in, film}} = \frac{1}{\alpha_{\text{sol}} \pi D_i L_{\text{sg}}}$	$R_{\text{in, film}} = 0.133 \text{ K W}^{-1}$
	$R_{\text{in, vap}} = q_{\text{sol}} C_{\text{p,v}} \frac{\Delta T_{\text{gl}}}{\Delta h_{\text{m}}} \frac{1}{\alpha_{\text{v}} \pi D_i L_{\text{sg}}}$	$R_{\text{in, vap}} = 0.017 \text{ K W}^{-1}$
	$R_{\text{in}} = R_{\text{in, film}} + R_{\text{in, vap}}$	$R_{\text{in}} = 0.150 \text{ K W}^{-1}$
	Friction factor for vapor flow according to Churchill (1977) $f_{\text{v,Churchill}} = 8 \left[ \left( \frac{8}{\text{Re}_{\text{v}}} \right)^{12} + \left( \left[ \frac{2.457 \ln \left( \frac{1}{\left[ \frac{7}{\text{Re}_{\text{v}}} \right]^{0.9} + 0.27 \frac{\varepsilon_{\text{rough}}}{D_i} \right)} \right]^{16} + \left[ \frac{37530}{\text{Re}_{\text{v}}} \right]^{16} \right)^{-1.5} \right]^{1/12}$	$f_{\text{v,Churchill}} = 0.594$ (Churchill, 1977)

Segmental Prototype Tube-Array Heat and Mass Transfer: Sample Calculations		
Inputs	Equations	Results
$Pr_v = 0.863$ $Nu_v = 4.364$ $k_v = 0.036 \text{ W m}^{-1} \text{ K}^{-1}$ $D_i = 2.159 \times 10^{-3} \text{ m}$ $\dot{m}_v = 2.717 \times 10^{-4} \text{ kg s}^{-1}$ $C_{p,v} = 2.399 \text{ kJ kg}^{-1} \text{ K}^{-1}$ $T_{v,in} = 97.60^\circ\text{C}$ $T_{v,out} = 95.10^\circ\text{C}$ $T_{l,in,int} = 97.42^\circ\text{C}$ $T_{l,out,int} = 91.53^\circ\text{C}$ $A_{int} = 0.019 \text{ m}^2$	Nusselt number for vapor flow according to Churchill (1977 (b)) $Nu_v = \left[ 4.364^{10} + \frac{e^{\left[ \frac{2200 - Re_v}{365} \right]}}{4.364^2} + \frac{1}{\left[ 6.3 + \frac{0.079 \left( \frac{f_{v,Churchill}}{8} \right)^{0.5} Re_v Pr_v}{(1 + Pr_v^{0.8})^{5/6}} \right]^2} \right]^{-5/10}$	$Nu_v = 4.364$
$C_{p,NH_3,molar} = 47.97 \text{ kJ kmol}^{-1} \text{ K}^{-1}$ $n_{H_2O}^* = 2.73 \times 10^{-5} \text{ kmol m}^{-2} \text{ s}^{-1} *$ Initially assumed, determined through iteration	$\alpha_v = Nu_v k_v / D_i$	$\alpha_v = 73.33 \text{ W m}^{-2} \text{ K}^{-1}$
$C_{p,H_2O,molar} = 44.44 \text{ kJ kmol}^{-1} \text{ K}^{-1}$ $\mu_v = 1.305 \times 10^{-5} \text{ kg m}^{-1} \text{ s}^{-1}$ $v_v = 0.293 \text{ m}^3 \text{ kg}^{-1}$ $D_{NH_3,H_2O,v} = 7.16 \times 10^{-6} \text{ m}^2 \text{ s}^{-1}$	Sensible heat removed from vapor $q_{v,sens} = \dot{m}_v C_{p,v} (T_{v,in} - T_{v,out})$	$q_{v,removed} = 1.63 \text{ W}$
	$LMTD_v = \left[ (T_{v,in} - T_{l,in,int}) - (T_{v,out} - T_{l,out,int}) \right] / \ln \left( \frac{T_{v,in} - T_{l,in,int}}{T_{v,out} - T_{l,out,int}} \right)$	$LMTD_v = 1.138 \text{ K}$
	$q_{v,removed} = \alpha_v \frac{\phi_T}{1 - e^{-\phi_T}} A_{int} LMTD_v$	$\phi_T = 0.074$
	Heat transfer correction factor required by concentration gradient in vapor $\phi_T = (n_{NH_3} C_{p,NH_3,molar} + n_{H_2O} C_{p,H_2O,molar}) / \alpha_v$	$n_{NH_3} = 8.78 \times 10^{-5} \text{ kmol m}^{-2} \text{ s}^{-1}$

Segmental Prototype Tube-Array Heat and Mass Transfer: Sample Calculations		
Inputs	Equations	Results
$D_{\text{NH}_3\text{H}_2\text{O},v}$ from expression based on $x$ and $T$ (Frank <i>et al.</i> , 1996) $\text{Pr}_v = 0.863$ $P_v = 591.789 \text{ kPa}$ $T_v = 96.35^\circ\text{C} = 369.50 \text{ K}$ $R = 8.314 \text{ kJ kmol}^{-1} \text{ K}^{-1}$ $P_1 = 591.789 \text{ kPa}$ $x_1 = 0.248$ $q_{l,int} = 0, T_{l,int}^\dagger = 94.45^\circ\text{C}$ $\dagger$ Determined from known $P_{l,int}$ , $x_{l,int}$ , $q_{l,int}$ $P_v = 591.789 \text{ kPa}$ $q_{v,int} = 1, x_{v,int}^{**} = 0.892$ $**$ Determined from known $T_{v,int}$ , $P_{v,int}$ , $q_{v,int}$ $M_{\text{NH}_3} = 17.03 \text{ kg kmol}^{-1}$ $M_{\text{H}_2\text{O}} = 18.02 \text{ kg kmol}^{-1}$ $x_{v,molar} = 0.891$ $\beta_v = 0.012 \text{ m s}^{-1}$	$Sc_v = \frac{\mu_v \nu_v}{D_{\text{NH}_3\text{H}_2\text{O},v}}$	$Sc_v = 0.532$
	$\left( \frac{Nu_v}{Sh_v} \right)^3 = \frac{\text{Pr}_v}{Sc_v}$	$Sh_v = 3.72$
	$Sh_v = \frac{\beta_v D_1}{D_{\text{NH}_3\text{H}_2\text{O},v}}$	$\beta_v = 0.012 \text{ m s}^{-1}$
	Bulk molar concentration $C_T = P_v / RT_v$	$C_T = 0.193 \text{ kmol m}^{-3}$
	$P_{l,int} = P_1$	$P_{l,int} = 591.789 \text{ kPa}$
	$x_{l,int} = x_1$	$x_{l,int} = 0.248$
	$T_{v,int} = T_{l,int}$	$T_{v,int} = 94.45^\circ\text{C}$
	$P_{v,int} = P_v$	$P_{v,int} = 591.789 \text{ kPa}$
	$M_{v,int} = \left( \frac{x_{v,int}}{M_{\text{NH}_3}} + \frac{1-x_{v,int}}{M_{\text{H}_2\text{O}}} \right)^{-1}$ ; $x_{v,int,molar} = x_{v,int} M_{v,int} / M_{\text{NH}_3}$	$M_{v,int} = 17.13 \text{ kg kmol}^{-1}$ $x_{v,int,molar} = 0.898$
	Molar flux of vapor being absorbed $n_{\text{total}} = \beta_v C_T \ln \left( \frac{z - x_{v,int,molar}}{z - x_{v,molar}} \right)$	$n_{\text{total}} = 1.152 \times 10^{-4} \text{ kmol m}^{-2} \text{ s}^{-1}$
	$n_{\text{NH}_3} = z \cdot n_{\text{total}}$	$z = 0.763$
	$m_{\text{flux,NH}_3} = n_{\text{NH}_3} M_{\text{NH}_3}$	$m_{\text{flux,NH}_3} = 1.50 \times 10^{-3} \text{ kg m}^{-2} \text{ s}^{-1}$

Segmental Prototype Tube-Array Heat and Mass Transfer: Sample Calculations		
Inputs	Equations	Results
$C_T = 0.193 \text{ kmol m}^{-3}$ $n_{\text{NH}_3} = 8.78 \times 10^{-5} \text{ kmol m}^{-2} \text{ s}^{-1}$ $VF = 0.915$ $D_i = 2.159 \times 10^{-3} \text{ m}$ $L_{\text{sg}} = 0.025 \text{ m}$ $\dot{m}_{\text{l,in}} = 7.096 \times 10^{-4} \text{ kg s}^{-1}$ $\dot{m}_{\text{v,in}} = 2.904 \times 10^{-4} \text{ kg s}^{-1}$ $x_{\text{l,in}} = 0.235$ $x_{\text{v,in}} = 0.877$	Effective interface diameter based on void fraction $D_{\text{int}} = \sqrt{VF \cdot D_i^2}$	$D_{\text{int}} = 2.065 \times 10^{-3} \text{ m}$
	$A_{\text{int}} = \pi D_{\text{int}} L_{\text{sg}}$	$A_{\text{int}} = 0.019 \text{ m}^2$
	$\dot{m}_{\text{abs,NH}_3} = m_{\text{flux,NH}_3} A_{\text{int}}$	$\dot{m}_{\text{abs,NH}_3} = 2.81 \times 10^{-5} \text{ kg s}^{-1}$
	$n_{\text{H}_2\text{O}} = n_{\text{total}} - n_{\text{NH}_3}$	$n_{\text{H}_2\text{O}} = 2.73 \times 10^{-5} \text{ kmol m}^{-2} \text{ s}^{-1}$
	$m_{\text{flux,H}_2\text{O}} = n_{\text{H}_2\text{O}} M_{\text{H}_2\text{O}}$	$m_{\text{flux,H}_2\text{O}} = 4.93 \times 10^{-4} \text{ kg m}^{-2} \text{ s}^{-1}$
	$\dot{m}_{\text{abs,H}_2\text{O}} = m_{\text{flux,H}_2\text{O}} A_{\text{int}}$	$\dot{m}_{\text{abs,H}_2\text{O}} = 9.25 \times 10^{-6} \text{ kg s}^{-1}$
	$\dot{m}_{\text{l,out}} = \dot{m}_{\text{l,in}} + \dot{m}_{\text{abs,NH}_3} + \dot{m}_{\text{abs,H}_2\text{O}}$	$\dot{m}_{\text{l,out}} = 7.470 \times 10^{-4} \text{ kg s}^{-1}$
	$\dot{m}_{\text{l,in}} + \dot{m}_{\text{v,in}} = \dot{m}_{\text{l,out}} + \dot{m}_{\text{v,out}}$	$\dot{m}_{\text{v,out}} = 2.530 \times 10^{-4} \text{ kg s}^{-1}$
	$\dot{m}_{\text{l,out}} x_{\text{l,out}} = \dot{m}_{\text{l,in}} x_{\text{l,in}} + \dot{m}_{\text{abs,NH}_3}$	$x_{\text{l,out}} = 0.261$
$\dot{m}_{\text{l,in}} x_{\text{l,in}} + \dot{m}_{\text{v,in}} x_{\text{v,in}} = \dot{m}_{\text{l,out}} x_{\text{l,out}} + \dot{m}_{\text{v,out}} x_{\text{v,out}}$	$x_{\text{v,out}} = 0.895$	
Thermal Resistance Circuit		
$\alpha_{\text{air}} = 94.61 \text{ W m}^{-2} \text{ K}^{-1}$ $A_{\text{total,sg}} = 0.029 \text{ m}^2$ $\alpha_{\text{sol}} = 382.1 \text{ W m}^{-2} \text{ K}^{-1}$ $D_i = 2.159 \times 10^{-3} \text{ m}$ $L_{\text{sg}} = 0.025 \text{ m}$ $D_o = 3.175 \times 10^{-3} \text{ m}$ $k_{\text{tube}}^* = 14.43 \text{ W m}^{-1} \text{ K}^{-1}$	$R_{\text{out}} = (\alpha_{\text{air}} A_{\text{total,sg}})^{-1}$	$R_{\text{out}} = 0.366 \text{ K W}^{-1}$
	$R_{\text{cond}} = \frac{\ln(D_o/D_i)}{2k_{\text{tube}} \pi L_{\text{sg}}}$	$R_{\text{cond}} = 0.001 \text{ K W}^{-1}$
	$R_{\text{total}} = R_{\text{in}} + R_{\text{cond}} + R_{\text{out}}$	$R_{\text{total}} = 0.517 \text{ K W}^{-1}$
	$UA = 1/R_{\text{total}}$	$UA = 1.935 \text{ W K}^{-1}$
	$\dot{m}_{\text{air}} = \dot{V}_{\text{air}} \rho_{\text{air,in}}$	$\dot{m}_{\text{air}} = 0.451 \text{ kg s}^{-1}$
	$\dot{m}_{\text{air,sg}} = \dot{m}_{\text{air}} \text{Fraction}_{\text{sg}}$	$\dot{m}_{\text{air,sg}} = 0.030 \text{ kg s}^{-1}$

Segmental Prototype Tube-Array Heat and Mass Transfer: Sample Calculations		
Inputs	Equations	Results
*Looked up at arithmetic mean between $T_{t,i}$ and $T_{t,o}$ $\dot{V}_{air} = 0.425 \text{ m}^3 \text{ s}^{-1}$ $\rho_{air,in} = 1.061 \text{ kg m}^{-3}$ $Fraction_{sg} = 0.066$ $C_{p,air} = 1.068 \text{ kJ kg}^{-1} \text{ K}^{-1}$ $\dot{m}_{sol} = 1.00 \times 10^{-3} \text{ kg s}^{-1}$ $h_{sol,in} = 661.1 \text{ kJ kg}^{-1}; h_{sol,out} = 573.9 \text{ kJ kg}^{-1}$ $T_{sol,in,equil}^* = 97.54^\circ\text{C}; T_{sol,out,equil}^* = 93.31^\circ\text{C}$ *approximated at $x_{sol,equil}$ $T_{l,in} = 97.49^\circ\text{C}; T_{air,in} = 51.67^\circ\text{C}$ $T_{sol,equil} = 94.91^\circ\text{C}$	$\dot{C}_{air} = \dot{m}_{air,sg} C_{p,air}$	$\dot{C}_{air} = 30.6 \text{ W K}^{-1}$
	$\dot{C}_{sol} = \dot{m}_{sol} [(h_{sol,in} - h_{sol,out}) / (T_{sol,in} - T_{sol,out})]$	$\dot{C}_{sol} = 20.63 \text{ W K}^{-1}$
	$\dot{C}_{min} = \min(\dot{C}_{air}, \dot{C}_{sol})$	$\dot{C}_{min} = 20.63 \text{ W K}^{-1}$
	$q_{max} = \dot{C}_{min} (T_{l,in} - T_{air,in})$	$q_{max} = 945.1 \text{ W}$
	$NTU = UA / \dot{C}_{min}$	$NTU = 0.094$
	$\varepsilon = 1 - \exp(-C_r^{-1} [1 - \exp(-C_r \cdot NTU)])$	$\varepsilon = 0.087$
	$\varepsilon = q_{sg} / q_{max}$	$q_{sg} = 87.23 \text{ W}$
	$q_{sg} = \dot{m}_{sol} (h_{sol,in} - h_{sol,out})$	$h_{sol,out} = 579 \text{ kJ kg}^{-1}$
	$q_{sg} = \dot{m}_{air,sg} C_{p,air} (T_{air,out} - T_{air,in})$	$T_{air,out} = 54.35^\circ\text{C}$
	$q_{sg} = (T_{sol,equil} - T_{t,i}) / R_{in}$	$T_{t,i} = 83.29^\circ\text{C}$
$q_{sg} = (T_{sol,equil} - T_{t,o}) / (R_{in} + R_{cond})$	$T_{t,o} = 83.16^\circ\text{C}$	

## REFERENCES

- ASHRAE (2007), "Designation and Safety Classification of Refrigerants," *ASHRAE Standards* Vol. 34(2007).
- ASHRAE (2010), "Ammonia as a Refrigerant," *ASHRAE Position Document*(2010).
- Beecher, D. and T. Fagan (1987). Effects of Fin Pattern on the Air Side Heat Transfer Coefficient in Plate Finned Tube Heat Exchangers. Westinghouse Research and Development Center, Pittsburgh, PA (USA)p.
- Bell, K. and M. Ghaly (1973), "An Approximate Generalized Design Method for Multicomponent/Partial Condenser," *AIChE Symp. Ser.*, pp. 72-79.
- Beutler, A., F. Ziegler and G. Alefeld (1996), "Falling Film Absorption with Solutions of a Hydroxide Mixture," *International Absorption Heat Pump Conference, Montreal, Canada*, pp. 303-309.
- Bourouis, M., M. Vallès, M. Medrano and A. Coronas (2005), "Absorption of Water Vapour in the Falling Film of Water–(LiBr+ LiI+ LiNO<sub>3</sub>+ LiCl) in a Vertical Tube at Air-Cooling Thermal Conditions," *International journal of thermal sciences* Vol. 44(5) pp. 491-498.
- Butterworth, D. (1975), "A Comparison of Some Void-Fraction Relationships for Co-Current Gas-Liquid Flow," *International Journal of Multiphase Flow* Vol. 1(6) pp. 845-850.
- Calm, J. M. (2008), "The Next Generation of Refrigerants–Historical Review, Considerations, and Outlook," *international Journal of Refrigeration* Vol. 31(7) pp. 1123-1133.
- Carey, V. P. (1992), "Liquid-Vapor Phase-Change Phenomena."

- Castro, J., C. Oliet, I. Rodríguez and A. Oliva (2009), "Comparison of the Performance of Falling Film and Bubble Absorbers for Air-Cooled Absorption Systems," *International Journal of Thermal Sciences* Vol. 48(7) pp. 1355-1366.
- Cengel, Y. A. and J. M. Cimbala (2006). *Fluid Mechanics*, Tata McGraw-Hill Education.
- Cermak, J., P. Eng and M. Ivanovich (2013), "Fan Efficiency Requirements for Standard 20.1-2013," *ASHRAE*(April 2013).
- Chen, S., F. Gerner and C. Tien (1987), "General Film Condensation Correlations," *Experimental Heat Transfer An International Journal* Vol. 1(2) pp. 93-107.
- Chisholm, D. (1967), "A Theoretical Basis for the Lockhart-Martinelli Correlation for Two-Phase Flow," *International Journal of Heat and Mass Transfer* Vol. 10(12) pp. 1767-1778.
- Chua, H., H. Toh and K. Ng (2002), "Thermodynamic Modeling of an Ammonia–Water Absorption Chiller," *International Journal of Refrigeration* Vol. 25(7) pp. 896-906.
- Churchill, S. W. (1977), "Friction-Factor Equation Spans All Fluid-Flow Regimes," *Chemical Engineering* Vol. 84(24) pp. 91-92.
- Churchill, S. W. (1977 (b)), "Comprehensive Correlating Equations for Heat, Mass and Momentum Transfer in Fully Developed Flow in Smooth Tubes," *Industrial & Engineering Chemistry Fundamentals* Vol. 16(1) pp. 109-116.
- Colburn, A. P. and T. B. Drew (1937). *The Condensation of Mixed Vapors*, American Institute of Chemical Engineers.
- De Francisco, A., R. Illanes, J. Torres, M. Castillo, M. De Blas, E. Prieto and A. Garcá (2002), "Development and Testing of a Prototype of Low-Power Water–

- Ammonia Absorption Equipment for Solar Energy Applications," *Renewable Energy* Vol. 25(4) pp. 537-544.
- Dittus, F. and L. Boelter (1930), "University of California Publications on Engineering," *University of California publications in Engineering* Vol. 2 p. 371.
- Fernández-Seara, J., J. Sieres, C. Rodríguez and M. Vázquez (2005), "Ammonia–Water Absorption in Vertical Tubular Absorbers," *International journal of thermal Sciences* Vol. 44(3) pp. 277-288.
- Fernández-Seara, J., F. J. Uhía and J. Sieres (2007), "Analysis of an Air Cooled Ammonia–Water Vertical Tubular Absorber," *International journal of thermal sciences* Vol. 46(1) pp. 93-103.
- Ferreira, C. I., C. Keizer and C. Machielsen (1984), "Heat and Mass Transfer in Vertical Tubular Bubble Absorbers for Ammonia-Water Absorption Refrigeration Systems," *International Journal of Refrigeration* Vol. 7(6) pp. 348-357.
- Frank, M. J., J. A. Kuipers and W. P. van Swaaij (1996), "Diffusion Coefficients and Viscosities of  $\text{CO}_2 + \text{H}_2\text{O}$ ,  $\text{CO}_2 + \text{CH}_3\text{OH}$ ,  $\text{NH}_3 + \text{H}_2\text{O}$ , and  $\text{NH}_3 + \text{CH}_3\text{OH}$  Liquid Mixtures," *Journal of Chemical & Engineering Data* Vol. 41(2) pp. 297-302.
- Friedel, L. (1979), "Improved Friction Pressure Drop Correlations for Horizontal and Vertical Two-Phase Pipe Flow," *European two-phase flow group meeting, Paper E*, p. 1979.
- Garimella, S. and J. W. Coleman (1998). Design of Cross-Flow Condensers for Ammonia-Water Absorption Heat Pumps. American Society of Heating, Refrigerating and Air-Conditioning Engineers, Inc., Atlanta, GA (United States)p.



- Garimella, S., J. W. Coleman and A. Wicht (1997), "Tube and Fin Geometry Alternatives for the Design of Absorption-Heat-Pump Heat Exchangers," *Journal of Enhanced Heat Transfer* Vol. 4(3).
- Garimella, S. and A. Wicht (1995). Air-Cooled Condensation of Ammonia in Flat-Tube, Multi-Louver Fin Heat Exchangers. American Society of Mechanical Engineers, New York, NY (United States)p.
- Gray, D. and R. Webb (1986), "Heat Transfer and Friction Correlations for Plate Finned-Tube Heat Exchangers Having Plain Fins," *Proceedings of the 8th International Heat Transfer Conference*, pp. 2745-2750.
- Herold, K., R. Radermacher and S. A. Klein (1996). *Absorption Chillers and Heat Pumps*, CRC press.
- Hewitt, G. F. (1990). *Hemisphere Handbook of Heat Exchanger Design*, Hemisphere Publishing Corporation New York.
- Hilpert, R. (1933), "Wärmeabgabe Von Geheizten Drähten Und Rohren Im Luftstrom," *Forschung auf dem Gebiet des Ingenieurwesens A* Vol. 4(5) pp. 215-224.
- Horuz, I. and T. Callander (2004), "Experimental Investigation of a Vapor Absorption Refrigeration System," *International journal of refrigeration* Vol. 27(1) pp. 10-16.
- Ibrahim, O. and S. Klein (1993), "Thermodynamic Properties of Ammonia-Water Mixtures," *TRANSACTIONS-AMERICAN SOCIETY OF HEATING REFRIGERATING AND AIR CONDITIONING ENGINEERS* Vol. 99 pp. 1495-1495.

- Incropera, F. P., D. P. DeWitt, T. L. Bergman and A. S. Lavine (2011). *Fundamentals of Heat and Mass Transfer*, John Wiley & Sons.
- Izquierdo, M., R. Lizarte, J. Marcos and G. Gutiérrez (2008), "Air Conditioning Using an Air-Cooled Single Effect Lithium Bromide Absorption Chiller: Results of a Trial Conducted in Madrid in August 2005," *Applied Thermal Engineering* Vol. 28(8) pp. 1074-1081.
- Jiang, Y. and S. Garimella (2001), "Compact Air-Coupled and Hydraulically Coupled Microchannel Heat Pumps," *International Mechanical Engineering Conference and Exposition, New York, NY. American Society of Mechanical Engineers*, pp. 1-13.
- Kakaç, S., R. K. Shah and W. Aung (1987). *Handbook of Single-Phase Convective Heat Transfer*, Wiley New York et al.
- Kays, W. M. and A. L. London (1984), "Compact Heat Exchangers."
- Keinath, C. M., J. C. Delahanty, S. Garimella and M. A. Garrabrant (2012), "Diesel Engine Waste-Heat Driven Ammonia-Water Absorption System for Space-Conditioning Applications."
- Kim, D. and C. I. Ferreira (2009), "Air-Cooled LiBr-Water Absorption Chillers for Solar Air Conditioning in Extremely Hot Weathers," *Energy Conversion and Management* Vol. 50(4) pp. 1018-1025.
- Kim, K., T. Ameel and B. Wood (1997a), "Performance Evaluations of LiCl and LiBr for Absorber Design Applications in the Open-Cycle Absorption Refrigeration System," *Journal of solar energy engineering* Vol. 119(2) pp. 165-173.

- Kim, N.-H., J.-H. Yun and R. Webb (1997b), "Heat Transfer and Friction Correlations for Wavy Plate Fin-and-Tube Heat Exchangers," *Journal of heat transfer* Vol. 119(3) pp. 560-567.
- Lazzarin, R., A. Gasparella and P. Romagnoni (1996), "Experimental Report on the Reliability of Ammonia-Water Absorption Chillers," *International Journal of Refrigeration* Vol. 19(4) pp. 247-256.
- Llamas-Guillén, S., R. Cuevas, R. Best and V. Gómez (2014), "Experimental Results of a Direct Air-Cooled Ammonia–Lithium Nitrate Absorption Refrigeration System," *Applied Thermal Engineering* Vol. 67(1) pp. 362-369.
- Lockhart, R. and R. Martinelli (1949), "Proposed Correlation of Data for Isothermal Two-Phase, Two-Component Flow in Pipes," *Chem. Eng. Prog* Vol. 45(1) pp. 39-48.
- Meacham, J. and S. Garimella (2002), "Experimental Demonstration of a Prototype Microchannel Absorber for Space-Conditioning Systems," *International Sorption Heat Pump Conference, Shanghai, China*, pp. 270-276.
- Meacham, J. M. (2002). *An Integrated Experimental and Analytical Study of Ammonia-Water Absorption in Microchannel Geometries*, Iowa State University.
- Meacham, J. M. and S. Garimella (2004), "Ammonia-Water Absorption Heat and Mass Transfer in Microchannel Absorbers with Visual Confirmation," *ASHRAE Transactions* Vol. 110(1).
- Medrano, M., M. Bourouis and A. Coronas (2002), "Absorption of Water Vapour in the Falling Film of Water–Lithium Bromide inside a Vertical Tube at Air-Cooling

- Thermal Conditions," *International journal of thermal sciences* Vol. 41(9) pp. 891-898.
- Mills, A. F. (1999). *Basic Heat and Mass Transfer*, Pearson College Div.
- Moya, M., J. Bruno, P. Eguia, E. Torres, I. Zamora and A. Coronas (2011), "Performance Analysis of a Trigeneration System Based on a Micro Gas Turbine and an Air-Cooled, Indirect Fired, Ammonia–Water Absorption Chiller," *Applied Energy* Vol. 88(12) pp. 4424-4440.
- Nagavarapu, A. K. (2012). *Binary Fluid Heat and Mass Exchange at the Microscales in Internal and External Ammonia-Water Absorption*, Georgia Institute of Technology.
- Nagavarapu, A. K. and S. Garimella (2013), "Falling-Film Absorption around Microchannel Tube Banks," *Journal of Heat Transfer* Vol. 135(12) p. 122001.
- Naraghi, M. and B. Chung (1982), "Radiation Configuration Factors between Disks and a Class of Axisymmetric Bodies," *Journal of Heat Transfer* Vol. 104(3) pp. 426-431.
- Ryan, D., R. Long, D. Lauf, M. Ledbetter and A. Reeves (2010), "Department of Energy: Energy Star Water Heater Market Profile."
- Shah, M. (1979), "A General Correlation for Heat Transfer During Film Condensation inside Pipes," *International Journal of Heat and Mass Transfer* Vol. 22(4) pp. 547-556.
- Shah, M. M. (2009), "An Improved and Extended General Correlation for Heat Transfer During Condensation in Plain Tubes," *HVAC&R Research* Vol. 15(5) pp. 889-913.

- Silver, L. (1947), "Gas Cooling with Aqueous Condensation," *Trans. Inst. Chem. Eng* Vol. 25 pp. 30-42.
- Srikhirin, P., S. Aphornratana and S. Chungpaibulpatana (2001), "A Review of Absorption Refrigeration Technologies," *Renewable and sustainable energy reviews* Vol. 5(4) pp. 343-372.
- Taitel, Y. and A. Dukler (1976), "A Model for Predicting Flow Regime Transitions in Horizontal and near Horizontal Gas-Liquid Flow," *AIChE Journal* Vol. 22(1) pp. 47-55.
- Taylor, B. N. and C. E. Kuyatt (1994), "Nist Technical Note 1297," *Guidelines for evaluating and expressing the uncertainty of NIST measurement results* p. 24.
- Touloukian, Y., R. Powell, C. Ho and P. Klemens (1970). Thermophysical Properties of Matter-the Tprc Data Series. Volume 1. Thermal Conductivity-Metallic Elements and Alloys. DTIC Documentp.
- Traviss, D., W. Rohsenow and A. Baron (1973), "Forced-Convection Condensation inside Tubes: A Heat Transfer Equation for Condenser Design," *ASHRAE Trans* Vol. 79(1) pp. 157-165.
- Velázquez, N. and R. Best (2002), "Methodology for the Energy Analysis of an Air Cooled Gas Absorption Heat Pump Operated by Natural Gas and Solar Energy," *Applied Thermal Engineering* Vol. 22(10) pp. 1089-1103.
- Venkatarathnam, G. and S. S. Murthy (2012), "Refrigerants for Vapour Compression Refrigeration Systems," *Resonance* Vol. 17(2) pp. 139-162.

- Wang, C., W. Fu and C. Chang (1997), "Heat Transfer and Friction Characteristics of Typical Wavy Fin-and-Tube Heat Exchangers," *Experimental thermal and fluid science* Vol. 14(2) pp. 174-186.
- Wang, L., G. Chen, Q. Wang and M. Zhong (2007), "Thermodynamic Performance Analysis of Gas-Fired Air-Cooled Adiabatic Absorption Refrigeration Systems," *Applied thermal engineering* Vol. 27(8) pp. 1642-1652.
- Webb, R. and N. Gupte (1990), "Design of Light Weight Heat Exchangers for Air-to-Two Phase Service," *Compact Heat Exchangers: AF estschrift for AL London, Hemi-sphere Publishing Corp., Washington, DC* pp. 311-334.
- White, F. (1991), "Viscous Fluid Flow, 1991," *MacGraw, New York* pp. 335-393.
- Wilke, C. (1950), "A Viscosity Equation for Gas Mixtures," *The journal of chemical physics* Vol. 18(4) pp. 517-519.
- Xu, Y. and X. Fang (2013), "A New Correlation of Two-Phase Frictional Pressure Drop for Condensing Flow in Pipes," *Nuclear Engineering and Design* Vol. 263 pp. 87-96.
- Yin, J., C. Bullard and P. Hrnjak (2002), "Single-Phase Pressure Drop Measurements in a Microchannel Heat Exchanger," *Heat Transfer Engineering* Vol. 23(4) pp. 3-12.
- Ziegler, F. (2002), "State of the Art in Sorption Heat Pumping and Cooling Technologies," *International Journal of Refrigeration* Vol. 25(4) pp. 450-459.
- Zukauskas, A. (1973), "Heat Transfer from Tubes in Crossflow," *Advances in heat transfer* Vol. 8 p. 93.
- Zukauskas, A., V. Makarevicius and A. Slanciauskas (1968), "Heat Transfer in Banks of Tubes in Crossflow of Fluid," *Thermophy* Vol. 1 pp. 47-68.